PROBING LIGHT EMISSION AT THE NANOSCALE WITH CATHODOLUMINESCENCE

Cover image: The front shows the measured polarized angular emission distribution radiated by a vertical indium phosphide nanowire, with the number of rings dictated by the length of the nanowire (3D design by Henk-Jan Boluijt). The back shows the calculated angle-dependent time evolution of transition radiation emitted by an electron impinging on a metallic surface (top image), and a cathodoluminescence excitation map of a silicon photonic crystal waveguide measured at a free space wavelength of λ_0=1425 nm (bottom image).

Ph.D. Thesis University of Amsterdam, June 2016
Probing light emission at the nanoscale with cathodoluminescence
Benjamin Joseph Maarten Brenny

ISBN 978-94-92323-04-0

A digital version of this thesis can be downloaded from http://www.amolf.nl.

PROBING LIGHT EMISSION AT THE NANOSCALE WITH CATHODOLUMINESCENCE

Meten van lichtemissie op de nanoschaal met kathodeluminescentie

ACADEMISCH PROEFSCHRIFT

ter verkrijging van de graad van doctor
aan de Universiteit van Amsterdam
op gezag van de Rector Magnificus
prof. dr. D.C. van den Boom
ten overstaan van een door het college voor promoties
ingestelde commissie,
in het openbaar te verdedigen in de Agnietenkapel
op donderdag 16 juni 2016 te 10:00 uur

door

Benjamin Joseph Maarten Brenny

geboren te Amsterdam

Promotiecommissie

Promotor:	Prof. dr. A. Polman	Universiteit van Amsterdam
Overige Leden:	Prof. dr. M. Kociak	Université Paris Sud
	Prof. dr. ir. O. J. Luiten	Technische Universiteit Eindhoven
	Prof. dr. H. B. van Linden van den Heuvell	Universiteit van Amsterdam
	Prof. dr. W. C. Sinke	Universiteit van Amsterdam
	Prof. dr. F. E. Schreck	Universiteit van Amsterdam

Faculteit der Natuurwetenschappen, Wiskunde en Informatica

This work is part of the research program of the 'Stichting voor Fundamenteel Onderzoek der Materie' (FOM), which is financially supported by the 'Nederlandse organisatie voor Wetenschappelijk Onderzoek' (NWO). It is also funded by NanoNextNL, a nanotechnology program funded by the Dutch ministry of economic affairs, and the European Research Council (ERC).

Contents

1

Introduction

1.1 Light

1.1.1 A short history of light

The science and understanding of light has gone through many stages throughout the centuries, starting out as the study of vision before the development of optical theories and then light as a separate, natural entity governed by laws of physics [1–3]. Today light still captivates both laymen and scientists alike, fueling a rapid expansion of fundamental research and applications.

We can begin the study of light with the Greek theories of vision, who regarded sight as the product of rays traveling between objects and the observer. Intramissionists such as Democritus believed that objects emanated rays while extramissionists such as the Pythagoreans and Euclid believed on the contrary that it was the eye that emitted rays that probed the surrounding world, as shown in Figure 1.1(a). Euclid established the mathematical and geometrical groundwork to study light rays, describing them as straight lines moving through space.

In the medieval period, the Arab scholar Ibn-al-Haitham (Alhacen) discarded the Greek theories and set the foundations for modern optics. He described light as a separate entity that illuminates items and then reflects away, carrying information about the object, as shown in Figure 1.1(b). Light is composed of a multitude of rectilinear rays moving through transparent materials, which allowed Ibn-al-Haitham to examine processes such as reflection, refraction and the "camera obscura". Later, Johannes Kepler built on these principles to explain image formation, allowing him to explain the working principles of concave and convex lenses. Willebrord Snellius and René Descartes both developed the law of refraction before Francesco Grimaldi documented diffraction for the first time and defined light as a fluid substance that moves with great speed, undulating with different frequencies to produce different colors.

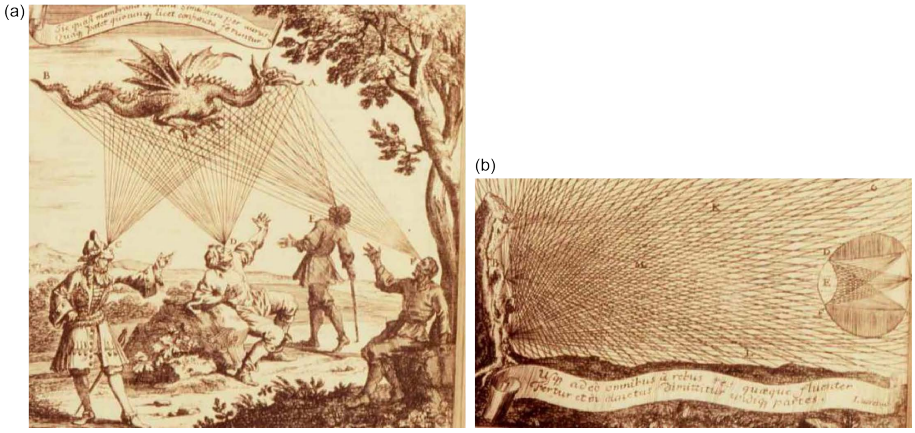

Figure 1.1 – (a) Image representing the Greek extramissionist theory, in which rays come out of the eye to interact with objects. (b) Image showing the theory of Ibn-al-Haitham, in which light hits an object and reflects in all directions, the rays are then perceived by the eye. (Images from [4])

After this the battle over the interpretation of light as a particle or a wave became more explicit, pitting Isaac Newton against Christiaan Huygens. Newton described light as streams of particles of different sizes moving at high speeds in straight lines. Huygens, on the other hand, interpreted light as a high-speed wave or perturbation propagating through an aether that permeates the whole universe, and described the concept of the wavefront for the first time.

Later in the 18th century, experiments on electricity and magnetism by Michael Faraday and others led to the development of new theories, which culminated with James Clerk Maxwell describing electromagnetic fields with four now-famous equations [5], establishing the direct relations between electricity and magnetism. This led to the fundamental realization that light is an electromagnetic wave, composed of rapidly oscillating electric and magnetic components. Many new theoretical and experimental concepts followed, such as polarization, which describes the direction of oscillation of the electric fields and plays an important role in many phenomena.

Experiments on the photoelectric effect in the early 20th century posed problems for Maxwell's wave theory. Metals were shown to emit electrons when irradiated by light, but only if the frequency of the light exceeded a material-specific threshold which also determined the energy of the emitted electrons, while Maxwell's theory predicted a dependence on radiation intensity. Albert Einstein resolved the issue by describing light as a particle with quantized energy, later named the photon [6]. The word photon is derived from the Greek word for light, φῶς (phôs). However, the wave-like properties of light remained, leading to the development of quantum mechanics, which described the particle-wave

duality and a new realm of fascinating effects such as entanglement. During the ensuing decades, research has improved the miniaturization of the objects being used to control and manipulate light, down to the scale of light itself: the nanoscale. At this small scale, light can no longer simply be described by ray optics, but one has to account for different regimes, the near and far fields. Very close to an emitter, within a (few) wavelength(s), the near field is dominant because of bound or evanescent fields, which govern the close-range interactions with other objects and emitters. At longer distances evanescent fields die out and only propagating waves survive, determining how objects interact in the far field.

1.1.2 Nanophotonics

Nanophotonics, the study of light at the nanoscale, has become an important and dynamic field of research in the last decade. At this deep-subwavelength scale, light interacts with matter in complex ways, in which not only the material properties but also their size and shape play a role in determining the interaction. At the nanoscale, one may use these interactions to mold and control different degrees of freedom of light: the temporal and spatial frequencies as well as the phase and polarization. Both fundamental new insights and a plethora of applications have followed from these efforts, a few are described below [7].

To achieve these goals, metallic and dielectric nanoscale geometries are tailored for specific applications. Photonic crystals started the rush, allowing light waves to be guided, slowed down, and even trapped [12–16]. Plasmonics, using (noble) metals to couple light to the oscillations of free electrons, permits even higher degrees of confinement and often a broadband response, albeit in exchange for greater losses [17–19]. Plasmonic structures have been used to great effect in antennas, waveguides and metamaterials [20–25]. Antennas, which connect the electromagnetic near and far fields, have a broad range of applications and can also be composed of dielectrics [26–31]. Although nanostructured materials interact most strongly with the electric field of light, precise engineering allows the enhancement of magnetic effects by using chirality and helicity of structures and/or fields [32–35]. Combining these magnetically active building blocks into 2D metasurfaces or 3D metamaterials allows for even more tailored responses, such as negative refraction [8–10, 21, 36–39]. As the optical components shrink down further, one comes into the quantum regime, opening up a host of new physics and possibilities such as quantum tunneling and single-photon processes [40–45].

All of these nanophotonic architectures and strategies have been used to develop a wide range of devices and applications. Communication/computation technology [11, 46], lasers [23, 47], solid-state lighting [48], solar energy [49–53], sensing and imaging [54–59], medical diagnostics and therapy [60–65], all of these have benefited from the developments in nanophotonics.

These initial successes underlie a vibrant and expanding universe of nanooptics, with exciting new prospects for coupling light to or tuning it with other degrees of freedom, such as mechanical vibrations, electron spins or electron motion [66–

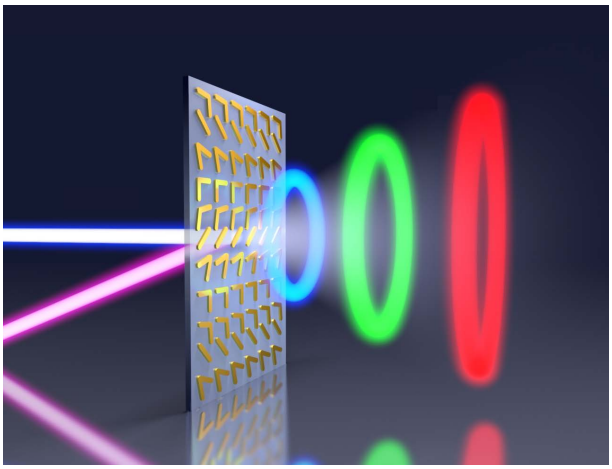

Figure 1.2 – Image of an electrically tunable optical metasurface, an exciting new nanophotonics application under development. Such a metasurface could be used for wavelength multiplexing, creating orbital angular momentum and computing. (Image taken from [7] and inspired by [8–11])

68]. This can be applied to quantum processes, nonreciprocal or topologically insulated optical circuits [69–71], tunable graphene optoelectronic circuits [72, 73] or tunable optical metasurfaces [9–11]. An example of such a possible future application is shown in Figure 1.2. An electrically tunable metasurface could be modulated to achieve a response dependent on wavelength and polarization, for high speed communication and computation.

Light is an essential tool for characterizing the nanoscale world that controls it, but even by using the advantages of the nanophotonic toolbox to shrink the "size" of light, it often remains difficult to study these tiny structures in detail. Far field imaging is limited by Ernst Abbe's optical diffraction limit, which states that light cannot be focused to a spot smaller than $\sim \lambda_0/2$ [74], where $\lambda_0 = 400$–800 nm in the visible spectral range. While near field probes circumvent the Abbe limit, the probe itself perturbs the nanophotonic environment [75–77]. Another cornerstone of nanoscale engineering, the electron, offers an alternative.

1.2 The electron

Similarly to light, the electron has a storied history rife with the particle vs. wave duality. The word comes from the Greek word ἤλεκτρον (ēlektron), meaning "amber", since the Greeks noticed that amber attracted small objects when rubbed by cloth or fur (now known as static electricity). The centuries after the Greeks saw many experiments related to electricity, until the discovery of the electron occurred

during research into electrical discharges in rarified gases during the 19th century. When applying a potential between a cathode and anode in a vacuum tube, a glow would appear from both the gas and the glass of the tube. Experiments by Johann Hittorf, Eugen Goldstein and Sir William Crookes showed that there appeared to be rays moving from the cathode to the anode, creating the glow [78–80]. Placing an object in the path created a shadow, suggesting the rays moved in linear fashion, similar to light, but they could be deflected by using a magnet. British and French scientists viewed the cathode rays as streams of negatively charged particles, while German physicists mostly explained them as wave-like processes in the ether. In 1897, J.J. Thomson performed several experiments that confirmed the existence of negatively charged particles that could also be deflected by electric fields and measured with high accuracy the mass to charge ratio (m/e) [81].

However the exact nature of the particles and their role with respect to atoms was still unknown. Numerous experiments in the ensuing two decades by Ernest Rutherford and others brought about the model of the atom as a positively charged nucleus surrounded by the negatively charged electrons. Niels Bohr posited that the electrons in this atomic model could only exist in quantized energy states, explaining atomic emission lines which tied into Einstein's theory of the quantized photon [82]. Quantum mechanics took hold of the electron, just as it had for the photon, leading to measurements of wave-like behavior such as diffraction, the discovery of spin and processes such as superconductivity or the (quantum) spin Hall effect.

Both the photon and the electron are characterized by the particle-wave duality but, since the electron has mass, it can reach much higher momenta and correspondingly smaller wavelengths. This large energy and momentum allows for different interactions with materials and enables new light generation mechanisms. As was mentioned earlier, the relatively large wavelength of light complicates detailed studies of subwavelength nanophotonic structures. In contrast, the short wavelength of the electron wave function allows for a much smaller probe: the de Broglie wavelength is ~7 pm for a 30 keV electron ($\sim \lambda_{optical}/10^5$). Electron microscopy exploits this to great effect for imaging nanoscale objects.

Electrons were first used for imaging purposes in the 1930's, by pioneers such as Ernst Ruska, Max Knoll and Manfred von Ardenne. The first electron microscopes used electrons transmitted through ultrathin samples, but the scanning electron microscope (SEM) that could image solid samples soon followed [83–87]. In an electron microscope, electrons have to be emitted, accelerated, focused and scanned over the sample of interest [88–90]. Emission sources can either use heat (thermionic emitter) or a large electrical potential gradient (field emitter) to extract electrons from a filament and use them to form a beam. The electrons are then accelerated by an anode; the acceleration voltage determines the energy and velocity of the electrons and is typically in the 1–30 kV range for a SEM. A higher electron energy corresponds to a shorter wavelength, thus affecting the resolution. Electromagnetic lenses are used to generate magnetic fields to focus the electron beam. In the final lens, coils deflect and scan the focused

electron beam over the sample surface in order to construct, point by point, an image from emitted electrons. One can detect different electron-based signals, but the most common are low-energy secondary electrons (< 50 eV) that carry information about the surface topology (forming the typical SEM image) or backscattered electrons that contain information about the atomic number and thus the composition of the sample being studied. The high-energy electrons can also generate electromagnetic radiation, which is our main point of interest: the goal of this thesis is to use electrons as a probe to generate and study the radiative properties of nanophotonic materials, structures, and devices, far below Abbe's optical diffraction limit.

1.3 Light from electrons: cathodoluminescence

Cathodoluminescence (CL), the optical radiation emitted into the far field by a polarizable material upon excitation by a high-energy free electron, was observed long before the electron itself was known. The glow in the vacuum tubes used to study the cathode rays was the first example of CL, hence the name [91]. In essence, the electron beam is a natural source for optical excitation [92]. Just as for light, it creates a time-varying electric field that can interact with a medium, but unlike continuous wave (CW) light where the field is varying at a fixed frequency, the electron is a point charge with a field evolution that is tightly confined in space and time. Additionally, while a plane wave has E and H fields perpendicular to the trajectory of the light, the electron has an electric field component along the trajectory ($E_{\parallel}$), and radially perpendicular to it ($E_{\perp}$), with H being azimuthally oriented. In vacuum, the electric fields of a moving electron correspond to a single oscillation, corresponding to broadband frequency components spanning the UV, visible and infrared spectral regimes. This is shown schematically in Figure 1.3. In a given medium the electron-matter interaction will become more complex due to dispersion and absorption, lengthening the time-evolution and reducing the spread in frequency. Nonetheless, CL retains a broadband character, making it a suitable candidate to study a wide selection of materials and structures.

Fast electrons carry large energies and momenta, allowing them to interact with a sample through a multitude of mechanisms and leading to several different radiation processes. We can divide these into coherent and incoherent categories [92]. Figure 1.4(a) shows a schematic of electron-sample interaction, with CL being emitted to the far field carrying information about the radiative properties. Transmitted electrons contain information about all loss mechanisms, both radiative and non-radiative, which can be determined by electron energy loss spectroscopy (EELS). In this thesis we will only discuss CL.

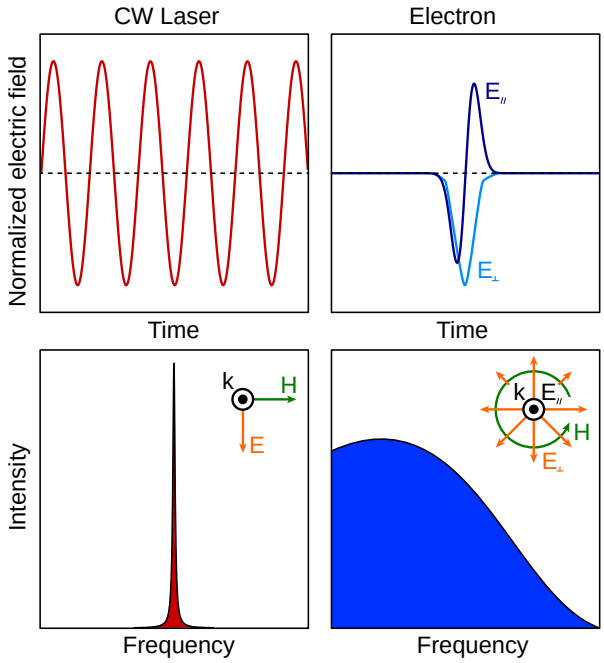

Figure 1.3 – Schematic comparison of laser beam and electron excitation. The electric field of light from a CW laser is constantly oscillating in time (top-left), resulting in a narrow spectral range (bottom-left). The electric fields of a passing electron in vacuum correspond to one optical cycle (top-right), and thus a broad spectral range (bottom-right). The insets describe the field orientations for a plane wave (bottom-left) and the electron (bottom-right). The electric field of the electron has components both along the trajectory and perpendicular to it.

1.3.1 Cathodoluminescence processes

Coherent radiation

The evanescent electric fields of the moving electron can coherently couple to far field radiation when interacting with a polarizable material. The main types of coherent radiation are Cherenkov radiation (CR), diffraction radiation, transition radiation (TR), and the generation of plasmons. The emission is called coherent because it has a fixed phase relation with the fields of the impinging electron. The different coherent mechanisms can also interfere with each other [92].

Cherenkov radiation occurs when the velocity of the electrons exceeds the phase velocity of light in the medium, allowing the evanescent fields of the electron to couple to far field emission [93, 94]. CR is emitted along the forward direction, in a cone with a well defined angle determined by the electron velocity and the refractive index of the material. This process is famous for causing the blue glow in

nuclear reactors and is also used to detect subatomic particles, *e.g.* neutrinos.

Diffraction radiation occurs when an electron passes close to a structured surface without crossing it [95]. This is also named Smith-Purcell emission for the special case of an electron moving parallel to a grating or row of (nano)particles [96].

Transition radiation is perhaps the most general of the processes, occurring whenever an electron (or other charged particle) transits the interface between two different media [92, 97, 98]. The moving charge polarizes the media near the interface, leading to surface currents and charges that radiate into the far field. A simplified explanation in the case of metals is that the electron produces an image charge, as shown schematically in Figure 1.4(b). In all cases, the excitation corresponds very closely to a time-varying vertical electric dipole radiating into the far field, leading to a toroidal angular emission pattern (blue line in Figure 1.4(b)). Due to the highly localized excitation of the electrons and their large momenta, they can directly excite guided waves that require high in-plane momentum, such as surface plasmon polaritons (SPPs) at metal interfaces [99] (in red in Figure 1.4(b)) or waveguide modes in dielectric/semiconductor waveguides.

Finally, the evanescent electric fields of the electron can couple to localized electromagnetic modes, such as plasmon resonances [100–102] or Mie resonances [103]. Only the (induced) field parallel to the electron trajectory, at the position of the electron, can do work and produce losses such as light emission. In this way, the electron will transfer most of its energy under the influence of vertical electric fields (the electron beam is vertically oriented in the SEM). Because of this, electron beam excitations are highly sensitive to vertically polarized or oriented modes, such as SPPs, transverse magnetic (TM) waveguide modes and localized modes with a strong vertical electric field component. Field components perpendicular to the electron trajectory can also contribute however, as they can polarize the sample or structure and induce fields parallel to the trajectory that can then act back on the electron. The CL probability is, to first order, proportional to the radiative local density of optical states (LDOS) integrated along the trajectory, but it can be affected by other components and positions that act back on the electron. In certain cases, such as a high quality waveguide for example, light may be generated but not collected by the setup, leading to a dark CL signal despite the presence of a high full LDOS. While EELS is proportional to the full LDOS (both radiative and non-radiative parts), CL probes only the radiative component [104, 105].

Incoherent radiation

Fast electrons can also excite incoherent radiation in a medium, for which there is no fixed phase relation with the electric field of the incident electron. In this case, the incoming electron excites valence electrons in the material to higher energy levels through inelastic collisions [92, 106, 107]. This process can lead to x-ray emission and generates electron-hole pairs that radiatively recombine to emit luminescence in the UV/visible/infrared spectral range. A broad range of excitations, both

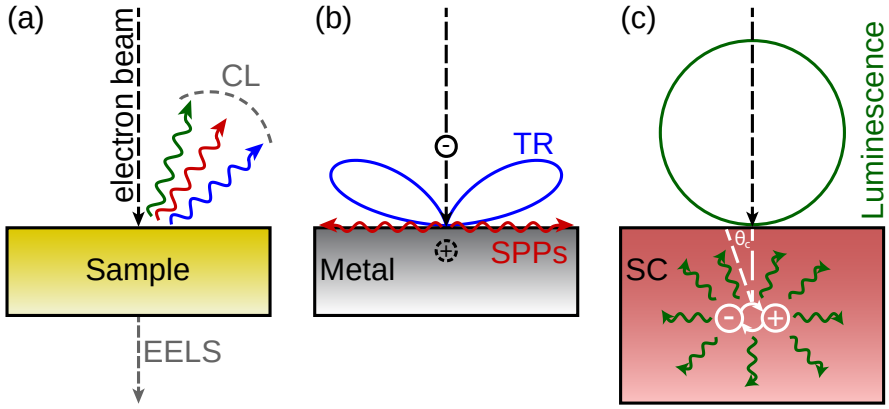

Figure 1.4 – (a) Schematic showing the electron beam spectroscopies that can be used to study a sample when exciting it with a beam of fast electrons. The energy lost by transmitted electrons is measured by EELS, while the generated broadband electromagnetic radiation that is named CL can be measured by optical detection techniques, and comprises different radiation processes. (b) Schematic of coherent CL excitation mechanisms on a metallic sample. The electron can generate transition radiation (blue) and SPPs (red) at the surface. (c) Schematic of incoherent CL excitation in a semiconductor, where the electron can generate electron-hole pairs that radiatively recombine. The random emission direction inside the material combined with the narrow escape angle leads to a Lambertian angular emission pattern.

above and inside the band gap can be probed in this way: band edge recombination in semiconductors, exciton recombination, intermediate defect or donor/acceptor states and traps as well as intra-4f transitions in rare-earth ions can be probed by CL [108–111]. CL is often used to study the dependence of these radiative processes as a function of temperature, local environment, dopant or defect concentration, stress and strain, among other quantities [107, 112–117].

The electron beam is a powerful method to provide nanoscale information about the optical and electronic properties of luminescent materials. By choosing the electron beam energy one can control the lateral extent of the beam as well as the penetration depth, allowing for 3D characterization within certain limits, and determining electronic properties such as carrier diffusion or surface recombination velocities [107].

Figure 1.4(c) shows a schematic representation of electron-hole pair recombination in a semiconductor, with the radiation being emitted isotropically inside the material. A majority of the light will be internally reflected, as only the portion emitted within the critical angle can escape. The emitted intensity has a cosine dependence on the zenithal angle due to refraction at the interface, resulting in a Lambertian angular emission pattern (shown in green) [118, 119].

Due to the large momentum of the electron and its azimuthal symmetry, it can

efficiently excite transitions that are symmetry- or momentum-forbidden for plane wave excitation. In addition, the impact excitation cross sections for electrons are often higher than corresponding optical excitation cross sections [107], and a single incident electron can excite multiple electron-hole pairs, as the necessary ionization/excitation energy is typically only a few times the band gap energy [120, 121]. For most materials the band gap is on the order of a few eV, while the incident electron will usually have an energy of several keV. The large number of slower secondary electrons created by the primary electrons are also usually energetic enough to excite transitions in the optical range. All of these effects contribute to an emission probability for incoherent radiation that is usually several orders of magnitude higher than for coherent radiation.

1.3.2 Electron-matter interactions

Optical characterization of nanoscale samples using CL is advantageous for several different reasons. The technique is contactless, usually damage-free and broadly applicable to a wide range of materials. The only limitation for samples is that they must be sufficiently conductive to carry away the charge from the electron beam. Insulators can be prepared with thin conductive layers (e.g. carbon or gold) in order to circumvent this issue. Next, the large number of coherent and incoherent processes that take place over a broadband wavelength range allow for studying a wide scale of radiative mechanisms and the interaction between them. Additionally, measurements are usually performed inside an electron microscope, allowing for great control in the electron beam energy, current, spot size, positioning, and the possibility to correlate structural and optical properties. Finally, perhaps the most important advantage is the high spatial excitation resolution, which allows for deep-subwavelength characterization.

The achievable spatial resolution depends on multiple parameters. Both the electron beam itself and the interaction with the sample play an important role. For the beam, an obvious variable is the spot size of the focus at the sample surface, which depends on the beam energy and current (increasing for larger current). Typical diameters for the beam spot on the sample surface are 1–20 nm.

In addition, the evanescent electric field profile of the electron plays an important role, especially for coherent processes, as it extends away from the beam, increasingly so for larger energies. The field amplitude diverges at the electron position and falls off as a modified Bessel function of the second kind (0^{th}-order for the component parallel to the trajectory and 1^{st}-order for the perpendicular component) [92]. Due to the high gradient of the fields close to the electron trajectory, there is a large contrast in the interaction strength in that region. For larger distances, we can use the asymptotic behavior of the Bessel functions for large values and define a characteristic field extent: the Bohr cutoff ($v\gamma/\omega$) [92]. Here v is the electron velocity, γ is the Lorentz factor and ω is the frequency. The corresponding distance for the intensity is $v\gamma/2\omega$ [123, 124]. From this formula we can determine an "effective" diameter of the beam (twice the intensity cutoff), finding ~33 nm for

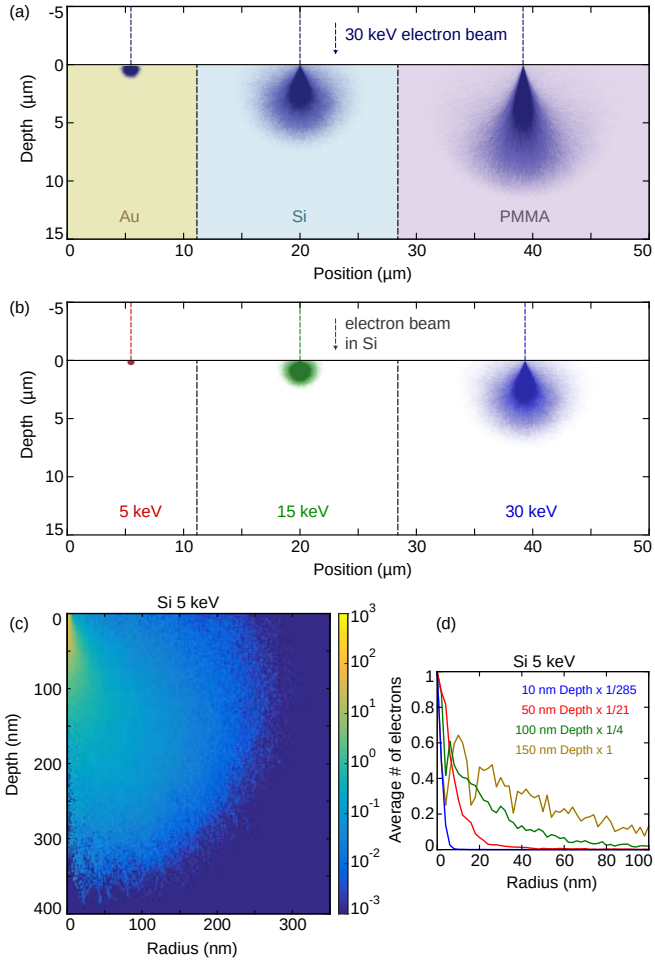

Figure 1.5 – (a) Primary electron beam trajectories in different materials calculated with the Monte Carlo simulation software Casino [122] for 10^4 30 keV electrons impinging on Au, Si and PMMA. The superimposed partially transparent trajectories give a representation of the electron-matter interaction volume, shape and density. (b) Calculations as in (a), for Si at 5, 15 and 30 keV. (c) Histogram of the average number of electrons per 2×2 nm bin as a function of depth and radius for the 5 keV electron beam in Si. (d) Cross-cuts of (c) for different depths, showing the average number of electrons per bin as a function of radius, normalized to the same scale for comparison of the electron beam divergence (curves are multiplied by the factors shown in the figure). Both the color bar of (c) and the vertical axis of (d) correspond to the average number of electrons per bin.

a 30 keV electron and ~118 nm for a 300 keV electron, at a wavelength $\lambda_0 = 600$ nm. Due to the divergence of the fields at the electron position, the resolution will be higher than implied by the Bohr cutoff. The field extent can be used as an advantage however, as it allows for aloof excitation of nanostructures without the electron trajectory actually passing through the structure.

Once the beam enters the material, the interaction volume of the electrons with matter will also affect the resolution, increasing the lateral and depth ranges from which radiation is being emitted. The direct interaction region due to the primary incident electrons only represents a lower bound to this volume, since both charge carriers and photons from CL emission processes can diffuse and be recycled over larger distances [107, 125]. Determining an exact spatial excitation resolution is a complex affair necessitating a convolution of all these parameters, which is strongly dependent on the beam and sample properties.

To exemplify the importance of electron-matter interactions on the resolution and extent of CL emission, we use the Monte Carlo method based software Casino [122] to calculate electron trajectories in different materials, as shown in Figure 1.5. We simulate 10^4 electrons in each case, distributed as a 10 nm wide Gaussian incident beam, and plot all of the primary electron trajectories for different electron energies and materials. In (a) we compare Au, Si and polymethyl methacrylate (PMMA, a low density polymer used in lithography) for 30 keV electrons. We clearly see the interaction volume increasing in size by an order of magnitude and changing in shape as we go from the metal to the polymer, due to the lower material density and atomic number which both affect the electron scattering. The pear shape we see for PMMA and Si is well-known for low-atomic-number materials ($Z \leq 15$) while the hemisphere observed for Au is characteristic of large atomic numbers ($Z \geq 40$) [107]. In between these two regimes a spherical shape is expected.

In addition to the cloud formed by the primary electrons, the backscattered electrons also play a role in the resolution, as they can cover a non-negligible area when scattering out of the material. In the case of Au ~50 % of the electrons are backscattered, for Si this is ~14 % and ~4 % for PMMA. This is in agreement with the fact that materials with higher atomic number backscatter more primary electrons. The cascade of secondary electrons generated by the incident beam can also affect the interaction volume as they can diffuse through the material and excite incoherent processes, but typically they do not extend much further than the primary electron cloud due to their low energy.

Figure 1.5(b) compares 5, 15 and 30 keV electron trajectories in Si. In this case the shape of the interaction volume does not change strongly (we note a slight change due to the saturation of the trajectories) while a tenfold increase in the extent of the electron penetration is observed when comparing 5 and 30 keV.

In order to quantify the distribution of the electrons inside the material in more detail, we study the case for Si at 5 keV more closely, binning horizontal planes for each depth and then performing an azimuthal average to obtain the average number of electrons as a function of depth and radius, in 2×2 nm bins. This is

shown in Figure 1.5(c), in which we clearly see that the majority of the electrons is stopped in a small region very close to the impact position (50–100 nm depth and 25–50 nm radius), with a slower dropoff outside of this region, up to the maximum extent of the interaction volume at ~400 nm depth and ~300 nm radius.

Figure 1.5(d) shows cross-cuts of (c) at different depths, in order to visualize the divergence of the electron beam as it moves deeper into the sample. The curves are noisy due to the relatively small number of electrons used. While the full width at half maximum (FWHM) of the beam is ~10 nm at 10 nm depth (unchanged from the input beam), it increases to ~20 nm at 50 nm depth and ~40 nm at 150 nm depth. Therefore electron-matter interactions play an important role in determining the resolution and emission characteristics of CL.

1.4 Outline of this thesis

Cathodoluminescence is a powerful, versatile and high resolution tool for the nanoscale characterization of optical and electronic properties of nanophotonic materials. In this thesis we describe different CL spectroscopy techniques, adding new functionalities to the angle-resolved CL imaging spectroscopy (ARCIS) setup that has been developed previously. This allows us to study different properties of the light emission from a variety of metallic and dielectric nanostructures, discerning the behavior of these nanophotonic structures in even greater detail.

In **Chapter 2**, we describe the angle-resolved cathodoluminescence imaging polarimetry and spectroscopy setup that is used throughout the thesis, giving an overview of all the different detection schemes available.

In **Chapter 3**, we develop a theoretical framework to describe the time-evolution of coherent CL processes that occur for an electron impinging on a single planar interface between vacuum and a given material. We show how the incident electron induces electric fields at the interface that can be emitted to the far field as transition radiation or guided along the surface as surface plasmon polaritons.

Chapter 4 shows how angle-resolved measurements can be used to recognize and separate coherent and incoherent CL emission. While metals display only dipolar TR and most luminescent materials exhibit Lambertian luminescence emission, Si shows both processes in a wavelength-dependent fashion that we can quantify and separate.

Chapter 5 introduces angle-resolved CL imaging polarimetry as a new powerful addition to the CL toolbox, allowing us to determine the full polarization state of light being emitted from CL processes. As proof of concept we study plasmonic bulls-eye and spiral antennas that exhibit strongly polarized emission as well as bulk Si and GaAs samples in which we separate polarized and unpolarized contributions.

In **Chapter 6**, we use CL polarimetry to study vertically grown InP nanowires of different height. We determine that the angular emission is height dependent and is dominated by azimuthally polarized rings. The emission is modeled as an incoher-

ent sum of randomly oriented dipoles radiating above a substrate, indicating that the CL luminescence emission scatters from the top of the wires. The sensitivity of measurements and calculations to the extent of the emission region enables a probe of the carrier diffusion length.

In **Chapter 7**, we apply CL polarimetry to horizontal GaAs nanowires of different diameter. Polarization-resolved measurements indicate that the emission behavior is dominated by the TM01 waveguide mode for both wires. The difference in diameter leads to a difference in modal dispersion, creating a subtle transition between leaky behavior and guided behavior. This is demonstrated by a change in directionality when exciting the nanowire end facets.

Chapter 8 describes CL spectroscopic tomography, a new technique that allows the 3D characterization of optical properties at the nanoscale. We study a metal-dielectric resonator, measuring 2D CL maps for different orientations and using the method of filtered back projection to reconstruct a 3D image of the CL emission. This allows us to discern material luminescence and plasmonic modes that are spatially and spectrally separated.

Finally, in **Chapter 9**, the CL techniques previously used in (and near) the visible spectral range are applied to the near-infrared spectral range and used to study modal fields in Si photonic crystal waveguides. We discern sharp resonances that are very strongly linearly polarized and exhibit distinct spatial distributions. The dominant emission feature corresponds to the odd (antisymmetric) TE waveguide mode of the system, demonstrating that we can couple to high-quality in-plane modes.

This thesis provides fundamental new insights into electron-induced light emission processes. It cements the status of CL spectroscopy as an essential tool in the nanophotonic and materials characterization arsenal, able to elucidate many important degrees of freedom of light at the nanoscale, for a wide range of structures and applications.

2

Angle-resolved cathodoluminescence imaging polarimetry and spectroscopy

In this chapter we will discuss the setup that is used to perform angle-resolved cathodoluminescence imaging polarimetry and spectroscopy. It combines different functionalities to determine spectrally resolved spatial maps, angular emission patterns and the full polarization state of the emission, for different spectral ranges.

2.1 Cathodoluminescence in a scanning electron microscope

Our cathodoluminescence microscope is based on a scanning electron microscope (SEM, FEI XL-30) with a Schottky field emission gun (SFEG) electron source, as shown in Figure 2.1(a). The inside of the SEM chamber can be seen in Figure 2.1(b). Beam energies are in the 1–30 keV range, and we typically use electron currents in the 0.1–30 nA range. The primary light collection inside the microscope is performed by an off-axis aluminium paraboloid mirror that is mounted on a micromanipulation stage composed of piezoelectric stepper motors and a titanium leaf spring system designed at AMOLF [123, 126, 127]. The mirror position above the sample is shown in Figure 2.1(b), with the inset displaying the mirror in greater detail. The mirror is composed of 6061 aluminium, has a parabola coefficient of a=0.1, a 1.46π sr acceptance angle and a focal distance of 0.5 mm. The end facet is

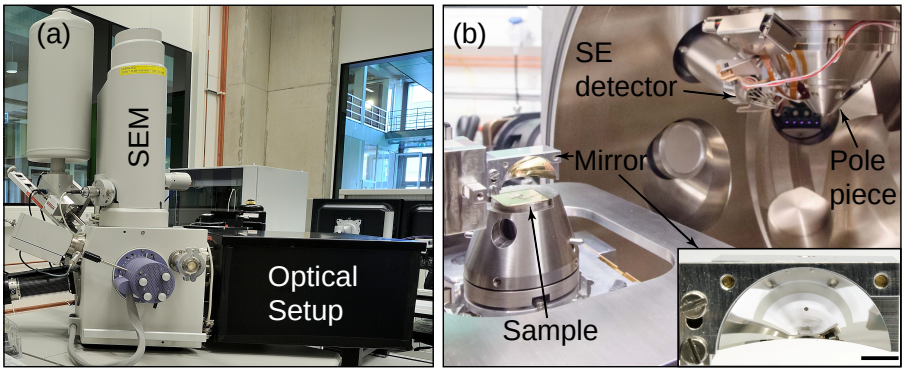

Figure 2.1 – (a) Photograph of the cathodoluminescence setup with the FEI XL-30 SFEG SEM and the box containing the optical components of the setup. (b) Photograph of the piezoelectric mirror stage mounted inside the SEM, showing the positions of the mirror, sample and holder, secondary electron (SE) detector and pole piece of the SEM that emits the electron beam. The inset on the bottom-right shows the parabolic mirror in greater detail (scale bar is 5 mm). (Design by Iliya Cerjak and Hans Zeilemaker, photograph in (a) and inset in (b) by Henk-Jan Boluijt, photograph in (b) by Mark Knight)

23 mm wide and 11 mm tall, which determines the size of the light beam traveling to the optical setup. The mirror has a 600 µm diameter hole above the focal point for the electron beam to pass through. The mirror is aligned using the micromanipulation stage so that the focus of the electron beam and the mirror coincide and the mirror reflects a parallel light beam. The stage moves in the horizontal plane (x and y) and has two axes of rotation (tilt and yaw), while vertical positioning relative to the sample is controlled by the height of the SEM stage, offering five degrees of freedom for precise alignment (see [127] for more details). The emitted radiation collected by the mirror is directed out of the microscope through a quartz vacuum window into the box containing the optical setup (Figure 2.1(a)). This window is the only fixed optical transmission element in the setup and is compatible with a wavelength range of $\sim \lambda_0 = 200$–2500 nm. For measurements further in the infrared, alternative materials (such as ZnSe) could be used for the window.

2.2 Optical setup

The optical setup contains a variety of detection schemes, for different spectral ranges. Figure 2.2(a) shows a photograph of the different components, numbered according to the schematic representation in Figure 2.2(b). All of the components along the optical beam path can be flipped in and out, allowing for easy switching between detection methods, which are spectroscopic and/or angle-resolved. Figure 2.3 provides a schematic overview of the different detection

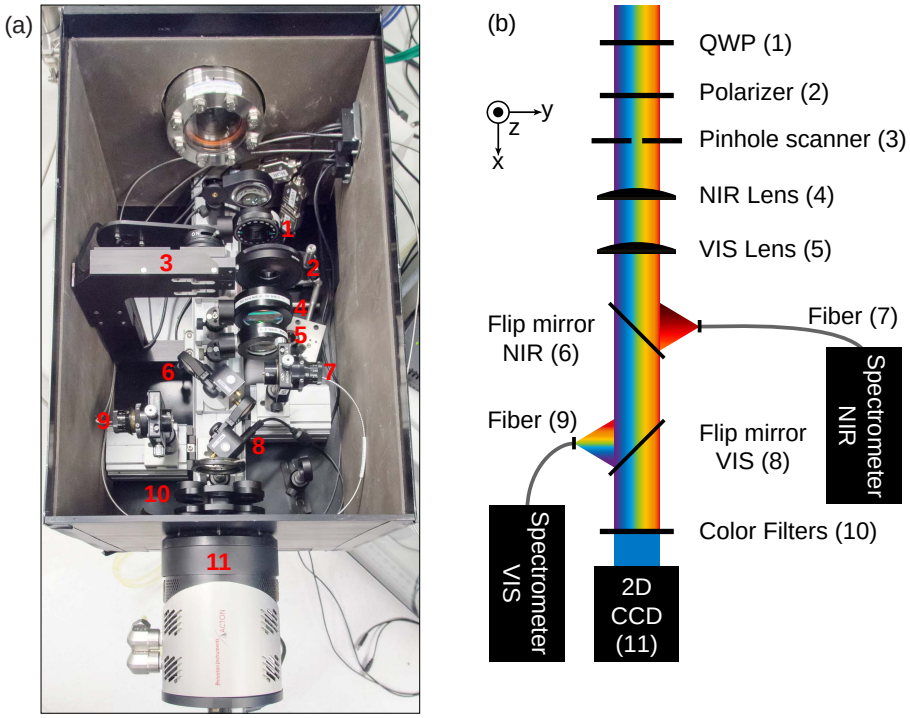

Figure 2.2 – (a) Photograph of the inside of the optics box. The main components of the optical setup are numbered. (b) Schematic of the optical setup showing the different detection methods available, with component numbers corresponding to (a). (photograph in (a) by Mark Knight)

schemes to clarify which components are used in each case. For visible (VIS) spectroscopy (Figure 2.3(a)), the CL emission is focused onto a 550 µm-diameter-core multimode fiber (OZ Optics QMMJ-55-IRVIS-550/600-3AS-2) with NA=0.22 using an achromatic lens (Edmund Optics 32-923, 40 mm diameter, 160 mm focal length, MgF_2 coating): components 5 and 9 in Figure 2.2. The fiber feeds into a Princeton Instruments (PI) Acton SP2300i spectrometer with a liquid-nitrogen-cooled (LN) back-illuminated silicon CCD array (PI Spec-10 100B, 1340×100 pixels), which was used in Chapters 5–7. A front-illuminated array was used (PI Spec-10 100F, 1340×100 pixels) for data in Chapters 4 and 8.

For spectroscopy in the near infrared (NIR) spectral range (Figure 2.3(b)) an achromatic lens (Edmund Optics, 47-318, 50 mm diameter, 150 mm focal length, NIR-II coating) focuses light onto the fiber (same type as for the VIS measurements): components 4 and 7. A PI Acton SP2300i type of spectrometer is connected to a LN-cooled InGaAs photodiode array (PI OMA V 1.7, 1×1024 pixels). For the VIS and NIR spectroscopy modes we use protected silver flip mirrors

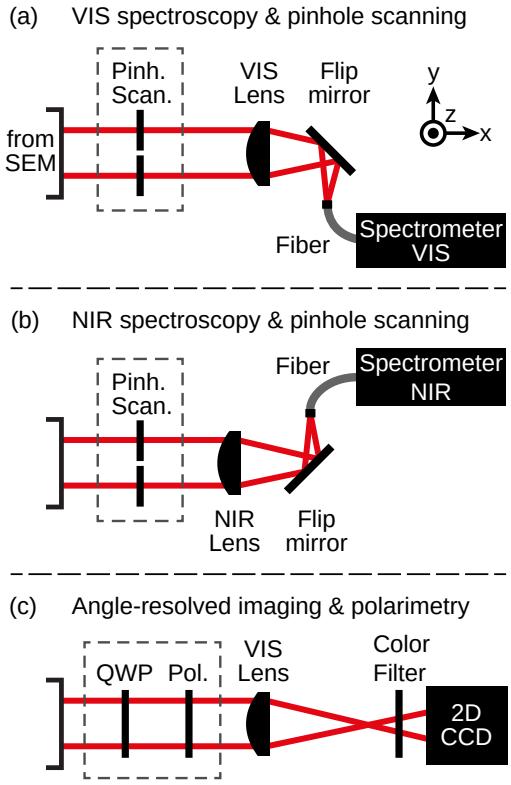

Figure 2.3 – Schematics of the main detection schemes showing which components are used for the different types of measurements. (a) Spectroscopic mode for measurements in the VIS spectral range, with the possibility of adding the pinhole scanner for angular-filtered collection. The coordinate system used throughout the thesis is included. (b) Spectroscopic mode for measurements in the NIR spectral range, again optionally adding the pinhole scanner. (c) Angle-resolved imaging mode in which one projects the beam onto the 2D PIXIS camera. It is possible to use color filters to select a certain wavelength and to add the QWP and polarizer to perform polarimetry measurements.

(Thorlabs PF10-03-P01) to direct the beam onto the fibers: components 6 and 8.

For angle-resolved imaging, we use a 2D back-illuminated, Peltier-cooled, silicon CCD array (PI, PIXIS 1024B, 1024×1024 pixels, component 11). To align the mirror we direct the entire beam untouched onto the PIXIS camera to be most sensitive to misalignments, but for angle-resolved measurements we use the VIS achromatic lens to demagnify the beam (Figure 2.3(c)), see Section 2.4 for more details. To take angle-resolved data for specific wavelengths, we use 40 nm optical bandpass filters covering the wavelength range λ_0 = 400–900 nm in steps of 50 nm (Andover Corporation P/N: xxxFS40-25, xxx corresponding to the center wave-

length: component 10). After component 10 in Figure 2.2(b) we show the effect of a filter in the blue spectral range. To achieve a higher spectral resolution for angle-resolved measurements we have developed a 2D pinhole scanner that filters selected emission angles and can be combined with the spectrometers (component 3, see Section 2.6). Finally, we can use a quarter-wave plate and linear polarizer in combination with any of the previous elements to perform polarization-resolved measurements: components 1 and 2. This is especially useful when using the angle-resolved imaging mode, as will be explained in Section 2.5. A commercial version of the cathodoluminescence setup has been developed by DELMIC B.V., including a software package (ODEMIS) to control both the electron microscope and optical detectors for integrated measurements (see http://www.delmic.com for more information).

2.3 Scanning cathodoluminescence spectroscopy

We perform measurements by using the ODEMIS software to raster-scan the electron beam over a region of interest, simultaneously collecting spectra in a synchronized fashion. In this way we obtain a 3D dataset with a full spectrum for each excitation position. The SE detector can also be used during the scan to build up a SEM image concurrently with the spectral scan, to compare the geometry and light emission, similarly to correlative microscopy.

2.3.1 Visible spectral range

Measurements with the VIS achromatic lens and Si spectrometer are possible in the λ_0 = 360–1100 nm range, with sensitivities of 10–15 % in the λ_0 = 400–950 nm range (such values are expected given the losses in the optics, gratings and camera). All measurements use hardware binning of the CCD pixels (full vertical binning and 4 times horizontally, resulting in a 335×1 array) and a camera temperature of T=−120 °C to improve the signal-to-noise ratio (SNR). Hardware binning both reduces readout noise and increases readout speed. We use either a 150g/mm grating with a 500 nm blaze or a 150g/mm grating with an 800 nm blaze. Typical integration times of 0.1–1 s/pixel are used, allowing a 200×200 nm structure to be scanned with 10 nm spatial resolution in under 7 minutes. Such measurements are used in Chapters 4–8.

2.3.2 Near infrared (NIR) spectral range

The NIR achromatic lens and InGaAs array allows us to measure in the λ_0 = 800–1600 nm range, but the sensitivities are lower than in the visible (0.1–0.01 %). This is due in part to the inability to hardware bin and the smaller chip area, but there is also a small misalignment of the spectrometer. As a result, measurements in the NIR such as those shown in Chapter 9 are more time-consuming. We use either a

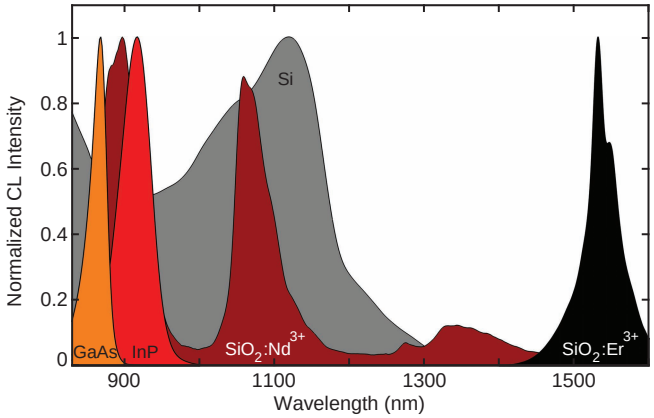

Figure 2.4 – Normalized CL spectra at room temperature for different semiconductors and dielectrics emitting in the NIR regime. The GaAs, InP and Si spectra were measured on bulk samples, while the SiO_2:Er^{3+} was a doped thin film on top of Si and the SiO_2:Nd^{3+} was composed of doped colloids.

150g/mm grating with a 1250 nm blaze, a 150g/mm grating with an 2000 nm blaze or a 600g/mm grating with an 1600 nm blaze. This wavelength regime allows for studying a variety of materials, notably semiconductors and rare earths, that are useful for applications such as telecommunication. Figure 2.4 shows normalized CL spectra of GaAs, InP, Si, SiO_2:Nd^{3+}, and SiO_2:Er^{3+}, measured at room temperature. We see sharp emission peaks due to band edge electron-hole recombination from the semiconductors and intra-4f transitions in the rare-earth ions. Only the spectrum from Si is broad, as a result of the indirect band gap of Si.

2.3.3 System response

For both spectroscopic detection schemes, it is necessary to take into account the wavelength-dependent sensitivity of the system to correct the shape of measured spectra. We use transition radiation (TR) from aluminium (Al) to calibrate the setup. TR is a reproducible source of CL that can be accurately modeled using the dielectric function of the substrate. We use a smooth single-crystal wafer of ⟨100⟩ Czochralski-grown Al, from which surface plasmon polaritons (SPPs) generated by the electron beam are symmetry-forbidden from coupling out to free space, leaving only TR to be emitted and measured.

Figure 2.5 (a) shows the calculated and measured Al TR spectrum (for λ_0 = 400–900 nm). The calculated TR intensity is expressed in units of photon emission probability per incoming electron per unit bandwidth, and is based on the equations described in section IV.C of Ref. 92. In this work, Maxwell's equations are solved for an electron incident perpendicularly to a planar substrate; the moving electron

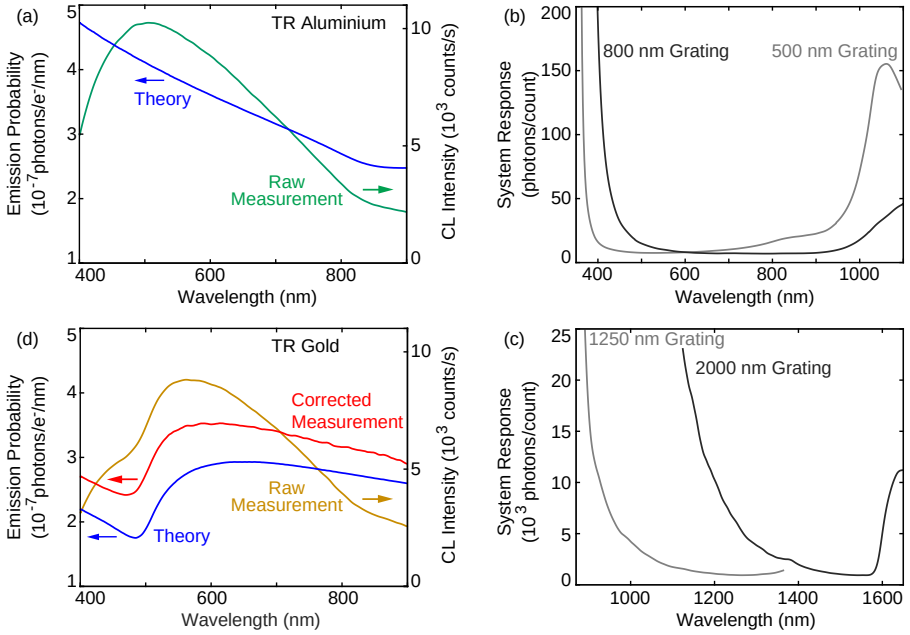

Figure 2.5 – (a) Theoretical (blue) and measured (green) TR spectra for single crystalline Al. These are used to determine the system response of the CL setup. (b) System response (in photons per CCD count) as a function of wavelength for the two gratings of the VIS spectrometer. The responses from different grating positions overlap well and have been stitched together. (c) System response (in photons per CCD count) as a function of wavelength for the two gratings of the NIR spectrometer. Here we only show a specific center wavelength for each grating (1100 nm for the 1250 nm blazed grating and 1400 nm for the 2000 nm blazed grating). (d) Theoretical (blue), raw (yellow) and corrected (red) TR spectra for single crystalline Au.

induces surface charges and currents that generate TR. The angle- and wavelength-dependent TR intensity can be analytically calculated for a given electron energy and material permittivity. We use Al because the permittivity (measured by ellipsometry) varies smoothly in the visible and NIR spectral ranges, leading to a smooth TR spectrum. Other metals such as Au and Cu display stronger spectral features due to intraband transitions that become dominant in the UV but also affect the relevant visible spectral band.

The measurement was performed using the 500 nm blazed grating centered at $\lambda_0 = 650$ nm with the VIS spectrometer, a beam energy of 30 keV and a current of 32 nA. Sample holders with integrated Faraday cups were developed to accurately measure the current *in situ* so that we can quantitatively compare measurements at different beam currents. The measured spectral shape is very different from the calculated one; it is dominated by the spectral response of the spectrometer and

CCD array. We divide the theoretical TR spectrum by the measured one to obtain the system response, repeating the process for a wide set of center wavelengths for the different gratings in both the VIS and NIR spectrometers.

Figure 2.5 (b,c) shows the system response derived in this way for the different gratings of the two spectrometers. For the VIS case there is very good overlap of the system response for different center wavelengths, so we can stitch and interpolate the response over the whole wavelength range of interest ($\sim \lambda_0$ = 360–1100 nm). At the short wavelengths where the sensitivity of the camera drops off completely, the system response increases up to ~700. For the NIR spectrometer, we show the 1250 nm blazed grating for a center wavelength of 1100 nm and the 2000 nm blazed grating for a center wavelength of 1400 nm (the measurable spectral range is $\sim \lambda_0$ = 800–1600 nm). The system response values reach $\sim 4 \times 10^5$ photons per CCD count at the shortest wavelengths, due again to a cutoff in camera sensitivity. As a results of the slight spectrometer misalignment mentioned earlier, different grating positions do not result in an overlapping system response.

We can now multiply any measured spectrum by the system response to obtain the absolute CL emission intensity given the measured beam current. We show this for a smooth single-crystal wafer of ⟨111⟩ Czochralski-grown Au in Figure 2.5 (d), comparing the calculated TR spectrum to both the raw and system corrected CL spectrum. The dips and peaks at λ_0 = 500 nm and λ_0 = 600 nm are well reproduced in the measurement, but there is an intensity difference of ~20 % between measurement and calculation. The difference is mainly attributed to errors in the determination of the current (~1–5 %) and variations in the optical alignment (~10 %), so regular monitoring of the system alignment is required. Errors in the dielectric function used for the calculations, the angular sensitivity and acceptance angles of the mirror and SPP scattering from the surface can also contribute, but are expected to be minor effects (~1 %). We conclude that we can obtain absolute emission intensities to within ~20 %.

2.4 Angle-resolved cathodoluminescence imaging

The angular distribution of CL provides important information to characterize the properties of nanophotonic materials and structures. The paraboloid mirror emits a parallel beam that contains all of the information about the emission angles, as in Fourier imaging. In our case, emitted CL is characterized by a zenithal angle θ=0–90° (0° being normal to the sample surface) and an azimuthal angle φ=0–360° (0° is the paraboloid vertex). Radiation at each emission angle will reach the mirror at a unique point and be reflected to a unique path in the parallel beam. We measure with the 2D PIXIS camera, using the VIS achromatic lens to demagnify the beam by a factor of 2.16 so that the image fills the CCD chip, with every point in the image corresponding to a unique path in the beam and thus to a specific emission angle. This makes it possible to transform the measured image to an angular emission profile. We hardware-bin the CCD pixels 4 times both horizontally

and vertically to improve the signal-to-noise ratio, obtaining images with 256×256 pixels that are 52 µm on each side. Optionally an iris can be used just before the color filters to help remove extraneous contributions to the signal, including parasitic reflections from the optical elements. For more details about the alignment of the mirror and the conversion to the angular patterns, see [127, 128].

2.5 Polarimetry

Polarization is an important degree of freedom in CL. Measuring the polarization of the emitted light is not straightforward in our case, due to the curved shape of the paraboloid mirror that modifies the polarization upon reflection. As a result, the polarization distribution in the beam emanating from the mirror does not correspond to the distribution in the sample plane. In angle-resolved mode we can correct for the effect of the reflection at each angle to retrieve the polarization in the sample plane. Only the central part of the mirror conserves the polarization direction, so using a slit is necessary for polarization contrast in spectral measurements when all of the light is focused onto the fiber [129, 130]. To measure the full polarization of the light, we combine a linear polarizer (LP) with a quarter-wave plate (QWP) to form a rotating plate polarimeter. This allows us to measure the Stokes parameters of the emitted radiation, which in turn determine all electric field components, fully characterizing the polarization [131, 132]. In practice we measure the intensities transmitted by six different positions of the QWP and LP (horizontal, vertical, 45°, 135°, right- and left-handed circular) and use the Mueller matrix formalism to fully correct for the geometrical and polarization distortions of the mirror [132–134]. We give a full explanation of the polarimetry method with its application to plasmonic structures and semiconductor bulk materials in Chapter 5, and apply the technique to characterize semiconductor nanowires in Chapters 6 and 7. We can apply the polarimetry measurements to the spectral detection modes as well, if we use a slit as described above. To allow measurements over a broad range of wavelengths, we combine an ultra-broadband linear polarizer with achromatic QWPs appropriate for different spectral ranges (see the overview in Table 2.1).

2.6 Pinhole scanner

The angle-resolved imaging described in Section 2.4 allows for good angular resolution, but poor spectral resolution as a result of the limited number and bandwidth of the optical filters. In order to combine high angular and spectral resolution we have developed a 2D pinhole scanner that can spatially select a small portion of the beam, effectively filtering momentum-space and then measuring the light intensity with either spectrometer (design by Iliya Cerjak). This detection scheme is similar to previous implementations in CL [135, 136] and is useful to study structures with complex dispersion relations that show strong angular variation with

Type	Wavelength range	Diameter	Part #
Polarizer	300–4000 nm	50 mm	Moxtek PUBB01A50M
QWP	465–610 nm	30 mm	Edmund Optics 48-497
QWP	610–850 nm	30 mm	Edmund Optics 65-919
QWP	690–1200 nm	25 mm	Thorlabs AQWP10M-980
QWP	1100–2000 nm	25 mm	Thorlabs AQWP10M-1600

Table 2.1 – Details of the different components used for the rotating plate polarimeter. A broadband polarizer can be used in conjunction with various QWPs to cover the VIS and NIR spectral regimes.

wavelength, such as photonic or plasmonic crystals. Figure 2.6 (a) shows a photograph of the pinhole scanner. It is composed of an anodized Al frame containing two motorized translation stages (Thorlabs MTS25/M-Z8E) with a range of 25 mm and a minimum step size of 0.05 µm, connected to a flippable blade with interchangeable pinholes. We can choose between pinholes with 100, 150, 290 and 500 µm diameter, depending on the angular resolution that is needed and the signal intensity that can be reached. The effective pixel area used in the measurements with the PIXIS camera corresponds to that of a 60 µm pinhole. For structures with low signal intensity, long integration times are needed, so measuring the full 2D angular range will be very time-consuming. However, when studying structures with a fixed emission symmetry, it is possible to use that symmetry to scan only a subset of angular space, mitigating a long measurement duration. A further advantage is that the pinhole scanner can be used to perform angle-resolved measurements in the NIR regime, which is not possible with the PIXIS camera. The software necessary to perform integrated pinhole scanning spectral measurements has been developed at AMOLF by Sander van de Haar and Sjoerd Wouda.

We show an example of a pinhole scanner measurement in Figure 2.6(b) and compare it to corresponding measurements with the PIXIS camera in Figure 2.6(c). We observe the emission from a silicon-on-insulator sample with a 220 nm thick Si layer on top of a 1 µm thick SiO_2 layer on a Si substrate. The SiO_2 emits different bright spectral peaks as a result of defect luminescence [115, 117], which can interfere in the top Si layer, leading to the emission of different rings, their number decreasing for longer wavelengths. We used a 290 µm diameter pinhole (component 3 in Figure 2.2), placed just before the VIS lens and raster-scanned it in the plane perpendicular to the optical beam, covering an area slightly larger than the mirror. To distinguish the low intensity features in the pinhole data more precisely, we show the intensity on a base 10 logarithmic scale. For the measurements with the PIXIS camera a linear scale is used.

We compare the pinhole and PIXIS data for three different wavelengths: λ_0 =

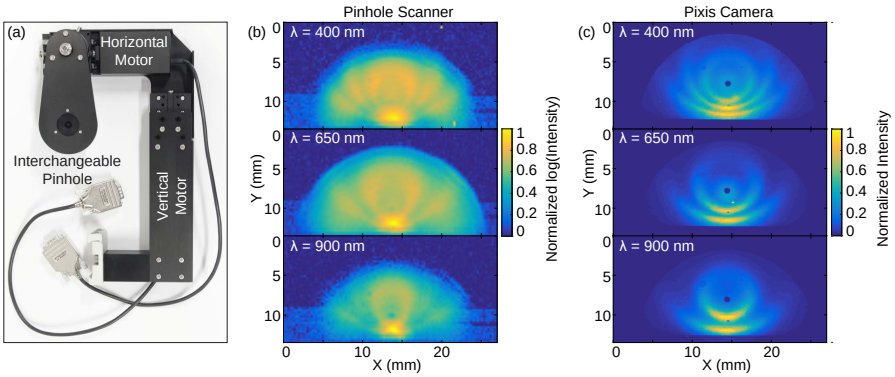

Figure 2.6 – (a) Photograph of the pinhole scanner showing the motor stages and pinhole on the blade that can be flipped up out of the way of the optical beam. (b) Pinhole scanner measurement of the emission from a silicon-on-insulator (SOI) sample. A pinhole with 290 µm diameter was used to scan over the entire area of the mirror and we show the normalized CL intensity (log scale) at $\lambda_0 = 400$, 650 and 900 nm. (c) Normalized emission intensity patterns from the SOI sample measured with the 2D PIXIS camera using bandpass filters at the same wavelengths as in (b). Each panel covers an area slightly larger than the beam area exiting the mirror. (photograph in (a) by Mark Knight)

400, 650 and 900 nm. The pinhole data has been averaged over a 20 nm bandwidth, half that of the filters, but this difference does not have a significant effect on the data. We see qualitative agreement of the number of features and their positions. However, in the PIXIS data we see smooth crescent shapes that gradually decrease in intensity from the bottom center of the mirror outwards. In the pinhole data that is not the case, the bottom center exhibits a large bright feature and we do not resolve the different crescents as clearly. Moving outwards the intensity first decreases slightly before increasing again so we recover the arms of the crescent shapes. Transforming the data from both measurements to θ and φ will thus not give the same result. While the angles of the features are in the right ranges, the pinhole data are not azimuthally symmetric, whereas they are symmetric for the PIXIS data.

The discrepancy is due in part to the large pinhole size that prevents us from resolving the features in as much detail. However, two other factors also contribute: aberrations in the mirror and the difficulty in perfectly focusing the mirror. The mirror has been polished by diamond turning, but still contains deviations from an ideal parabolic shape (the curve accuracy is $\lambda/2$), the effect of which is most severe in the bottom center of the mirror where the curvature is the strongest. This causes scattering and small deviations in reflection leading to diverging rays within the reflected beam. In addition, the mirror alignment is not exact so the entire beam will show a small amount of focusing or defocusing.

When imaging with the PIXIS, these effects are corrected by employing the achromatic lens to make an image of the mirror, focusing the diverging rays back together at the plane of the CCD. With the pinhole however we filter in momentum space before using the lens, in a different plane, so we are more sensitive to these small discrepancies. Both the angular distribution and the intensity contrast between different parts of the mirror are affected, due to the dependence of the aberrations on the mirror curvature.

A smaller pinhole will help mitigate the problem in angular resolution (at the cost of signal-to-noise ratio), while placing the pinhole scanner in the same plane as the PIXIS camera or scanning the fiber can solve the problem of the diverging/aberrated beam. A more flexible solution is to combine the pinhole scanner with lenses to scan the same conjugate plane imaged by the PIXIS.

Even though detailed measurements over the full 2D angular range of the mirror are not feasible yet, important emission features can be recognized and structures with specific directional emission symmetry can be differentiated. Angular resolution in the NIR is now also possible, so the pinhole scanner is already a powerful addition to the capabilities of the CL setup. Further improvements are expected to unlock its full potential.

3

Femtosecond plasmon and photon wave packets excited by a high-energy electron on a metal or dielectric surface

Swift electrons generate coherent transition radiation (TR) when crossing a material surface, as well as surface plasmon polaritons (SPPs) when the material is metallic. In this chapter we present analytical and numerical calculations that describe the time- and space-dependent electric fields of TR and SPPs induced by 30–300 keV electrons on a Drude metal surface. The generated SPPs form wave packets a few hundred femtoseconds in duration. High-frequency components close to the plasmon resonance are strongly damped, causing the wave packets to shift to lower frequencies as they propagate further. TR is emitted to the far field as ultrashort wave packets consisting of just a few optical cycles, with an intensity and angle dependence that is strongly related to the material permittivity. The excitation reaches its peak amplitude within a few femtoseconds and then drops off strongly for longer times. From a correlation between material permittivity and the calculated emission behavior, we determine qualitative predictions of the TR evolution for any given material. The results presented here provide key insights into the mechanisms enabling swift electrons to serve as nanoscale optical excitation sources.

3.1 Introduction

Electron beam spectroscopies such as cathodoluminescence (CL) spectroscopy and electron energy-loss spectroscopy (EELS) have gained much attention in nanophotonics research because of their ability to resolve optical excitations with nanometer precision. Just like photons, electrons carry electromagnetic fields, allowing them to optically excite polarizable matter. In fact, due to their short de Broglie wavelengths and correspondingly high momenta, electrons can be used as a highly localized optical excitation source with a spatial resolution unattainable using optical excitation techniques [92, 102, 124, 137–140]. Many advances have been made in the theoretical descriptions of the interactions between electrons and matter that generate radiation [92, 105, 141–145]. These electron-light-matter interactions occur on the femtosecond time scale, and have only recently been studied in the time domain, in an indirect way using adapted electron microscopes that combine EELS with synchronized ultrafast optical excitations [146, 147]. Most work thus far has focused on exploring the frequency and momentum domains, measuring and simulating spectral responses. Accordingly, analytical theory and simulation techniques have not been applied to investigate the time evolution of CL processes in detail, although time-domain simulation methods have been gaining traction [148, 149].

In this chapter, we develop a theoretical framework to study the temporal, spatial, and spectral evolution of radiation excited by swift electrons impinging on a metallic or dielectric surface. We investigate in detail the time evolution of coherent excitation and emission of transition radiation (TR) and surface plasmon polaritons (SPPs). We examine the space, time, and frequency dependence of the electric fields of the moving electron and how they interact with matter to generate radiation. We start by deriving the external fields of an electron in a homogeneous medium, showing the time and position-dependent behavior of the electric field components. We then examine an electron impinging on a planar surface, interacting with the medium to induce fields that produce radiation emitted into the far field. The general formalism is derived in frequency and momentum space, after which the time and space dependence is obtained by Fourier-transforming the fields. First, we investigate SPPs and study the generation and propagation of these excitations on the femtosecond time scale, for metals described by a Drude dielectric response. We determine the evolution of the SPP wave packet as it propagates away from the point of excitation. We then explore TR, which is composed of far field emission characterized by ultrashort wave packets that strongly depend on the emission direction. We study both the time and frequency dependence of TR and elucidate the interrelation between the material permittivity and TR emission. This allows us to formulate qualitative predictions of TR emission behavior.

3.2 Electron external field

A point charge moving with constant velocity in vacuum possesses an electromagnetic field that represents an evanescent source of radiation. Inside a homogeneous medium the field can be described quite simply, allowing us to study both the time and spectral dependence of the electron field components. We focus on an electron traveling in a straight-line trajectory along the z-axis, with a constant velocity vector $\mathbf{v} = v\hat{\mathbf{z}}$, passing by the origin $R{=}z{=}0$ at time $t{=}0$. The direction perpendicular to the trajectory is denoted as $\mathbf{R}{=}R\hat{\mathbf{R}}$, with the position vector defined as $\mathbf{r}{=}(\mathbf{R},z)$. The electron charge density is given by $\rho(\mathbf{r},t){=}{-}e\,\delta(\mathbf{r}-\mathbf{v}t)$. This can be Fourier transformed to ($\mathbf{q}$–ω) space as $\rho(\mathbf{q},\omega){=}{-}2\pi e\,\delta(\omega-\mathbf{q}\cdot\mathbf{v})$. In our derivations we use Gaussian units and follow the notation used in Ref. 92, but focus only on the electric fields $\mathbf{E}$ (the magnetic field $\mathbf{H}$ can be obtained using the Maxwell-Faraday equation). The equations take into account retardation effects (c is finite and the electron velocity can reach a sizable fraction of c). We also use linear response theory, which assumes that the induced field is linear with the external field of the electron, and consequently, the photon emission probability scales as the square of the external charge ($-e$ for the electron). Maxwell's equations can be solved in momentum–frequency space, leading to the following expression for the electric field of the moving electron:

$$\mathbf{E}(\mathbf{q},\omega) = -\frac{8\pi^2 ie}{q^2-k^2\epsilon}\left(\frac{k}{c}\mathbf{v}-\frac{\mathbf{q}}{\epsilon}\right)\delta(\omega-\mathbf{q}\cdot\mathbf{v}), \tag{3.1}$$

where ϵ is the permittivity of the homogeneous medium and $k{=}\omega/c$ is the free space wave number. The momentum $\mathbf{q}$ of the electron can be decomposed as $\mathbf{q}{=}(\mathbf{Q},q_z)$, in components perpendicular ($\mathbf{Q}$) and parallel (q_z) to the trajectory, with $q_z=\omega/v$. The latter expression, which expresses energy conservation for transfers of frequency and wave vector from the electron to the material, is the nonrecoil approximation [92]. It holds for $\hbar q^2/m_e \ll \omega$, which is valid for photon-energy exchanges $\hbar\omega \ll 1$ MeV, as is usually the case in the study of photonic nanostructures. Integrating $\mathbf{E}(\mathbf{q},\omega)$ over the z component of $\mathbf{q}$ results in

$$\mathbf{E}(\mathbf{Q},z,\omega) = \frac{4\pi ie}{v\epsilon}\,\frac{\mathbf{q}-\mathbf{v}k\epsilon/c}{q^2-k^2\epsilon}\,e^{i\omega z/v}. \tag{3.2}$$

The electron dispersion $\omega{=}qv$ lies outside the light cone in free space $\omega{=}kc$, so the electron does not radiate and the electric field decays exponentially away from the trajectory. In contrast, the electron velocity can exceed the speed of light inside a material, so the electron can couple to excitations in the medium, leading to the emission of Cherenkov radiation; we will not study this here. Performing the Fourier transform over $\mathbf{Q}$ to obtain the electric field in real space, we obtain [150]

$$\mathbf{E}(\mathbf{r},\omega) = \frac{2e\omega}{v^2\gamma_\epsilon\epsilon}\,e^{i\omega z/v}\left[\frac{i}{\gamma_\epsilon}K_0\left(\frac{\omega R}{v\gamma_\epsilon}\right)\hat{\mathbf{z}}-K_1\left(\frac{\omega R}{v\gamma_\epsilon}\right)\hat{\mathbf{R}}\right], \tag{3.3}$$

where γ_e=$1/\sqrt{1-e v^2/c^2}$ is the Lorentz contraction factor and K_m are modified Bessel functions of the second kind [151]. The fields diverge at the origin, so close to the trajectory there is a large contrast in the field strength. Further away from the trajectory, the field amplitude decays with the Bohr cutoff ($v\gamma_e/\omega$) as a characteristic decay length [92, 124]. Using Eq. (3.3) we can determine the spectral components of the electric field at different points in space. To determine the electric field as a function of time, we Fourier-transform Eq. (3.3) as

$$\mathbf{E}(\mathbf{r},t) = \int \frac{d\omega}{2\pi}\, \mathbf{E}(\mathbf{r},\omega)\, e^{-i\omega t}. \tag{3.4}$$

Direct numerical integration is used below for the fields produced when the electron crosses an interface. For the swift electron moving in vacuum ($\gamma_e \to \gamma$), the $E(\mathbf{r},t)$ fields can be determined directly from $\rho(\mathbf{r},t)$ and the Liénard-Wiechert potentials [150], leading to

$$\mathbf{E}(\mathbf{r},t) = -\frac{\gamma}{(R^2+\gamma^2(z-vt)^2)^{3/2}}\Big[R\hat{\mathbf{R}} + (z-vt)\hat{\mathbf{z}}\Big]. \tag{3.5}$$

For illustration, we study an electron traveling through vacuum, with an energy of 30 keV, corresponding to a velocity of $v = 0.328\ c = 98.45$ nm/fs. The results are displayed in Figure 3.1, with a schematic of the electron, the coordinate system, and the field orientations as an inset in (a). We show the evanescent decay of the field away from the trajectory of the electron in Figure 3.1(a), calculating the total electric field intensity (time-integrated over the entire pulse) as a function of radial distance R, for the two field components E_R and E_z. The asymptotic behavior of the fields is clear, with a difference of 8 orders of magnitude in the intensity between R=1 nm and R=100 nm. The E_R field component, perpendicular to the trajectory, has a higher intensity than the E_z component. The strong gradient in the field intensity observed here is responsible for the very high excitation resolution of electron beam spectroscopies.

Figure 3.1(b) shows the electric field components as a function of time, for distances R=10 nm and R=100 nm away from the electron trajectory. The E_z component is asymmetric while the E_R component is symmetric, both displaying a single oscillation. For a distance of R=10 nm, the field transient occurs within ~2 fs, highlighting the extremely short pulse felt by an observer close to the moving electron. At R=100 nm, the field amplitudes have decayed by a factor 100 and the transient spreads out in time by a factor 10. This is due to the fact that further away from the trajectory, the distance between moving electron and observer varies more slowly with time.

Figure 3.1(c) displays the electric field in the frequency domain. Spectra for the two field components are shown for R=10 nm and the total intensity for R=10 nm and R=100 nm. The different field components display characteristic spectral shapes, with E_z vanishing for small frequencies while E_R has a maximum. At R=10 nm, the spectral range extends well beyond 10 eV; at R=100 nm the intensity has decayed by a factor 100 and the spectrum is confined to ~1 eV.

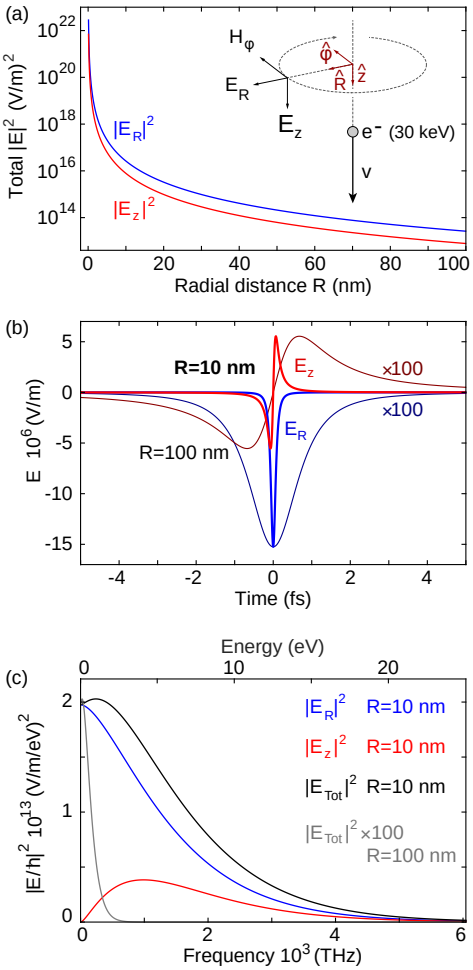

Figure 3.1 – Electric field produced by a 30 keV electron in vacuum. (a) Total (time-integrated) electric field intensity of the radial (E_R, in blue) and vertical (E_z, in red) components, as a function of radial distance to the electron trajectory R, showing the diverging intensity close to the electron trajectory at R=0 nm. The inset shows a schematic of the moving electron with the coordinate system and orientation of the field components. We evaluate the electric fields for a given radial distance R, height z, and time t or frequency ω. (b) Electric field amplitudes of the E_R (blue) and E_z (red) components as a function of time, for distances of R=10 nm (thick lines) and R=100 nm (thin lines, amplitudes multiplied by 100), and with the minimum electron–observer distance at t=0. (c) Electric field intensity in the frequency domain, as a function of frequency and corresponding energy, for the E_R (blue), E_z (red), and $E_{\rm tot}$ (black) components at a distance of R=10 nm, compared to the total intensity for R=100 nm (gray, multiplied by a factor of 100).

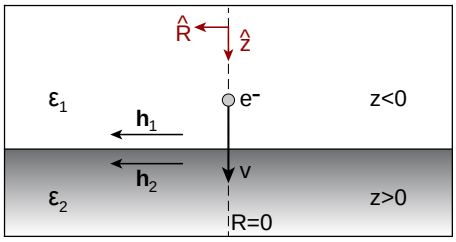

Figure 3.2 – Schematic of the electron traversing the interface between two media, showing the coordinate system, as well as the permittivities ϵ_j and surface currents $\mathbf{h}_j$ on either side of the interface.

These calculations show that an electron moving through vacuum generates ultrashort electric field pulses, with energies extending beyond 10 eV close to its trajectory. The field strength and spectral content decays when moving further away. Since these fields are evanescent, they cannot couple directly to far field radiation. Next, we study an electron impinging on a dielectric medium, leading to processes that can emit radiation.

3.3 An electron impinging on a planar surface

When an electron reaches and traverses the interface between two media it generates transition radiation (TR), as well as surface plasmon polaritons (SPPs) in the case of a metal. In general, the electric field can be described by separating the contributions of the external field of the electron in each medium (as if it were an infinite homogeneous medium) and the field that is induced at the surface. The induced field is created by surface charges and currents induced by the approaching electron

$$\mathbf{E} = \mathbf{E}_j^{\text{ext}} + \mathbf{E}_j^{\text{ind}}.$$

Figure 3.2 shows a schematic of the geometry studied here. The induced field can be expressed in terms of the surface currents $\mathbf{h}_j$ as [92, 143, 152]

$$\mathbf{E}^{\text{ind}}(\mathbf{Q}, z, \omega) = \frac{2\pi i}{q_{zj}}\, ike^{iq_{zj}|z|}\left[\mathbf{h}_j - \frac{1}{k^2\epsilon_j}\left(\mathbf{Q}, \text{sign}(z)q_{zj}\right)\left(\left(\mathbf{Q}, \text{sign}(z)q_{zj}\right)\cdot\mathbf{h}_j\right)\right], \tag{3.6}$$

where $q_{zj}=\sqrt{k^2\epsilon_j - Q^2}$. From the boundary conditions (i.e. the continuity of the **E** and **H** components parallel to the surface), it follows that the currents only have components of parallel momentum **Q** and can be written as $\mathbf{h}_j = D\mu_j\hat{\mathbf{Q}}$. The

induced electric field takes the form

$$\mathbf{E}_j^{\mathrm{ind}}(\mathbf{Q},z,\omega) = \frac{2\pi}{k\epsilon_j}\, D\,\mu_j\, e^{sign(z) i q_{zj} z}\Big[- q_{zj}\hat{\mathbf{R}} + sign(z) Q \hat{\mathbf{z}}\Big], \tag{3.7}$$

where

$$D = \frac{2ieQ/c}{\epsilon_1 q_{z2} + \epsilon_2 q_{z1}}, \tag{3.8}$$

$$\mu_1 = \frac{\epsilon_1 q_{z2} - \epsilon_1 \omega/v}{q^2 - k^2\epsilon_2} - \frac{\epsilon_1 q_{z2} - \epsilon_2 \omega/v}{q^2 - k^2\epsilon_1}, \tag{3.9}$$

and

$$\mu_2 = \frac{\epsilon_2 q_{z1} + \epsilon_1 \omega/v}{q^2 - k^2\epsilon_2} - \frac{\epsilon_2 q_{z1} + \epsilon_2 \omega/v}{q^2 - k^2\epsilon_1}. \tag{3.10}$$

We can now combine the external and reflected fields together to obtain the complete expressions for the electron electric fields on both sides of the interface, for both field components. Recall from Eq. (3.2) that the external field contains components $\mathbf{q} - \mathbf{v}k\epsilon/c$, with $\mathbf{q}$=($\mathbf{Q}, \omega/v$). We obtain the following expressions for $\mathbf{E}(\mathbf{Q},z,\omega)$:

$$\mathbf{E}_R = \frac{4\pi i e}{v\epsilon_1}\,\frac{\mathbf{Q}}{q^2 - k^2\epsilon_1}\, e^{i\omega z/v} - \frac{2\pi}{k\epsilon_1}\, q_{z1}\, D\,\mu_1\, e^{-iq_{z1}z}\,\hat{\mathbf{Q}}, \qquad z<0, \tag{3.11a}$$

$$\mathbf{E}_z = \frac{4\pi i e}{v\epsilon_1}\,\frac{\frac{\omega}{v}(1-\frac{v^2}{c^2}\epsilon_1)}{q^2 - k^2\epsilon_1}\, e^{i\omega z/v} - \frac{2\pi}{k\epsilon_1}\, Q\, D\,\mu_1\, e^{-iq_{z1}z}\,\hat{\mathbf{z}}, \qquad z<0, \tag{3.11b}$$

$$\mathbf{E}_R = \frac{4\pi i e}{v\epsilon_2}\,\frac{\mathbf{Q}}{q^2 - k^2\epsilon_2}\, e^{i\omega z/v} - \frac{2\pi}{k\epsilon_2}\, q_{z2}\, D\,\mu_2\, e^{iq_{z2}z}\,\hat{\mathbf{Q}}, \qquad z>0, \tag{3.11c}$$

$$\mathbf{E}_z = \frac{4\pi i e}{v\epsilon_2}\,\frac{\frac{\omega}{v}(1-\frac{v^2}{c^2}\epsilon_2)}{q^2 - k^2\epsilon_2}\, e^{i\omega z/v} + \frac{2\pi}{k\epsilon_2}\, Q\, D\,\mu_2\, e^{iq_{z2}z}\,\hat{\mathbf{z}}, \qquad z>0. \tag{3.11d}$$

In order to obtain the fields as a function of space and time, we Fourier-transform back from ($\mathbf{Q}$–ω) space:

$$\mathbf{E}(\mathbf{r},t) = \int \frac{d^2\mathbf{Q}}{(2\pi)^2}\, e^{i\mathbf{Q}\cdot\mathbf{R}} \int \frac{d\omega}{2\pi}\, e^{-i\omega t}\, \mathbf{E}(\mathbf{Q},z,\omega). \tag{3.12}$$

The integral over $\mathbf{Q}$ can be partially simplified by removing the azimuthal component of $\mathbf{Q}$ to leave only the radial part, so that we obtain a single integral over Q. This approach differs between the two field components, since $\mathbf{E}_z$ contains no vectorial component of $\mathbf{Q}$ but $\mathbf{E}_R$ does. We find for $\mathbf{E}_z$ that

$$\int \frac{d^2\mathbf{Q}}{(2\pi)^2}\, e^{i\mathbf{Q}\cdot\mathbf{R}} = \int_0^\infty \frac{Q}{2\pi}\, dQ\, J_0(QR),$$

while for $\mathbf{E}_R$

$$\int \frac{d^2\mathbf{Q}}{(2\pi)^2}\, e^{i\mathbf{Q}\cdot\mathbf{R}}\, \mathbf{Q} = \int_0^\infty \frac{Q}{2\pi}\, dQ\; i\; J_1(QR).$$

We apply these identities to Eq. (3.12), and integrate from 0 to ∞ both over Q and ω. We further use causality ($E(\omega)$=$E^*(-\omega)$) to reduce the fields to

$$\mathbf{E}_z(\mathbf{r},t) = \int_0^\infty \frac{Q}{2\pi}\, dQ\, J_0(QR) \int_0^\infty \frac{d\omega}{\pi}\, \mathrm{Re}\{e^{-i\omega t}\, \mathrm{E}_z(Q,z,\omega)\}\, \hat{\mathbf{z}}, \tag{3.13a}$$

$$\mathbf{E}_R(\mathbf{r},t) = \int_0^\infty \frac{Q}{2\pi}\, dQ\, J_1(QR) \int_0^\infty \frac{d\omega}{\pi}\, \mathrm{Im}\{-e^{-i\omega t}\, \mathrm{E}_R(Q,z,\omega)\}\, \hat{\mathbf{R}}, \tag{3.13b}$$

where $E_z(Q,z,\omega)$ and $E_R(Q,z,\omega)$ are given by Eq. (3.11) (replacing $\mathbf{Q}$ by Q). Now that we have derived this general formalism, these integrals can be solved numerically to study SPP and TR generation. From these equations, we can derive analytical expressions for the electric field components in the far field. We demonstrate this in the following sections.

3.4 Surface plasmon polaritons

The excitation of surface plasmon polaritons by fast electrons was discovered several decades ago [153, 154] and has since been demonstrated in a broad variety of experiments [99, 137, 155, 156]. In studying the excitation of SPPs, we can ignore the external electric field as it decays evanescently and thus does not generate radiation. In our formalism, plasmons are revealed by the induced electric fields [Eq. (3.7)] and more specifically, they originate in the pole of the denominator of D: $\epsilon_1 q_{z2} + \epsilon_2 q_{z1}$=0. This equation leads to the plasmon dispersion relation

$$Q_{\mathrm{SPP}} = k\, \sqrt{\frac{\epsilon_1 \epsilon_2}{\epsilon_1 + \epsilon_2}}. \tag{3.14}$$

We now use the plasmon-pole approximation [92, 143, 157], retaining only the contribution of the plasmon pole at Q=Q_{SPP}. For large distances ($R \gg \lambda$), one can perform the integral over Q from Eq. (3.13), allowing us to derive analytical expressions for the fields of the SPPs. Using this method, D becomes

$$D \approx \frac{C}{Q - Q_{\mathrm{SPP}}}, \tag{3.15}$$

where the denominator arises from a Taylor expansion around the plasmon pole

$$\epsilon_1 q_{z2} + \epsilon_2 q_{z1} \approx -Q_{\mathrm{SPP}}\Big(\frac{\epsilon_1}{q_{z2}} + \frac{\epsilon_2}{q_{z1}}\Big)(Q - Q_{\mathrm{SPP}}) = \frac{(Q - Q_{\mathrm{SPP}})}{A},$$

leading to

$$C = \frac{2eiQA}{c}.$$

To determine the SPP electric fields in space as a function of frequency, we can rewrite the frequency domain part of Eq. (3.13), making the plasmon pole explicit, and perform the integral over Q

$$\mathbf{E}_{\mathrm{SPP}}(\mathbf{r},\omega) = \int_0^\infty dQ\, J_m(QR)\, \frac{f(Q,z,\omega)}{Q-Q_{\mathrm{SPP}}} \approx 2\pi\, \frac{i}{2}\, f(Q_{\mathrm{SPP}},z,\omega)\, H_m^{(1)}(Q_{\mathrm{SPP}}R), \quad (3.16)$$

where $H_m^{(1)}$ is a Hankel function of the first kind. By combining Eq. (3.16) with Eq. (3.11), we can consolidate an expression for the frequency-dependent SPP fields in a relatively compact way, and find

$$\mathbf{E}_{\mathrm{SPP}}(\mathbf{r},\omega) = \frac{2\pi e i A Q_{\mathrm{SPP}}^2}{ck\epsilon_j}\, \mu_j\, e^{\mathrm{sign}(z) i q_{zj} z} \left[\mathrm{sign}(z)\, i Q_{\mathrm{SPP}} H_0^{(1)}(Q_{\mathrm{SPP}}R)\hat{\mathbf{z}} + q_{zj} H_1^{(1)}(Q_{\mathrm{SPP}}R)\hat{\mathbf{R}}\right]. \quad (3.17)$$

This equation is applicable on both sides of the interface that the electron traverses. As in the previous section, the final step to obtain the time-dependent electric fields is to Fourier transform over the frequency domain

$$\mathbf{E}_{\mathrm{SPP}}(\mathbf{r},t) = \int_0^\infty \frac{d\omega}{\pi}\, \mathrm{Re}\{\mathbf{E}_{\mathrm{SPP}}(\mathbf{r},\omega)\, e^{-i\omega t}\}. \quad (3.18)$$

We calculate the time- and frequency-dependent SPP electric fields for a 30 keV electron impinging on a Drude metal under normal incidence, with a permittivity described by $\epsilon(\omega)=\epsilon_0 - \omega_{\mathrm{p}}^2/(\omega^2 + i\eta\omega)$. The Fourier transform is performed numerically by summing over energies in the range $\hbar\omega=[10^{-6}-100]$ eV, divided into 10^6 steps. We choose $\hbar\omega_{\mathrm{p}}=1$ eV and $\hbar\eta=0.05$ eV. The corresponding plasmon dispersion relation is shown in Figure 3.3(a), the SPPs being excited for frequencies $\omega \leq \omega_{\mathrm{SPP}}$.

Figure 3.3(b) shows the time evolution of an SPP wave packet, as observed for a height $z=-10$ nm above the metal surface, at a radial distance $R=10$ µm from the electron trajectory ($R \gg \lambda$). After ~30 fs we clearly observe an increase in amplitude and an oscillating wave packet that then decays, for both field components. As expected for the TM polarized SPPs, $E_z > E_R$. The wave packet has a duration of a few hundred femtoseconds, and considering the distance R and the time of the onset, is propagating close to the speed of light. This is to be expected at large distances, as the lowest frequency components close to the light line propagate with the lowest loss and the slower, high-frequency components are strongly damped, see $\mathrm{Im}\{k_{\mathrm{SPP}}\}$ in Figure 3.3(a). In Figure 3.7 of the Supporting information we show the full time evolution and spectral behavior over a 60 µm range.

In Figure 3.3(c) we compare the time evolution of the SPP wave packet at R=1, 10, and 100 µm, as is shown in Figure 3.3(c). The period of the oscillations in the wave packet increases for further distances, corresponding to the shift to lower

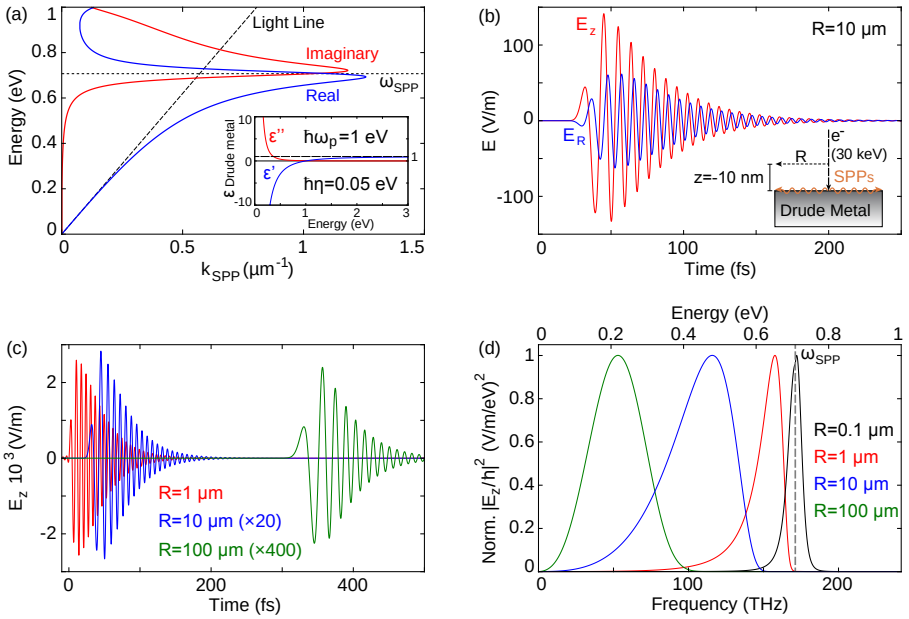

Figure 3.3 – Electric field of surface plasmon polaritons (SPPs) excited by a 30 keV electron, propagating along the surface of a Drude metal. (a) Dispersion relation of the SPPs for a Drude metal with $\hbar\omega_p$=1 eV and $\hbar\eta$=0.05 eV, showing the energy as a function of the real and imaginary parts of the SPP wave vector k_{SPP}. The diagonal dashed line denotes the light cone and the horizontal one the SPP resonance frequency ω_{SPP}. The inset shows the permittivity ϵ of the Drude metal as a function of energy. (b) Electric field amplitudes of the SPP wave packet, showing the E_R (blue) and E_z (red) components as a function of time, evaluated for a height 10 nm above the metal surface and a distance R=10 μm away from the electron impact position (see inset). The time t=0 corresponds to the electron crossing the interface. (c) Comparison of the E_z SPP amplitude as a function of time for a fixed height z=−10 nm at different distances of 1 μm (red), 10 μm (blue, multiplied by 20), and 100 μm (green, multiplied by 400). (d) Comparison of the intensities of the E_z SPP field component in the frequency domain, each normalized to the maximum value at the same distances as in (c). Data for R=0.1 μm (in black) are also shown. The SPP resonance frequency ω_{SPP} is indicated.

frequencies. The wave packet reaches its maximum amplitude within a single optical cycle, as expected for the single-cycle excitation (Figure 3.1(b)). It then decays within ~200 fs after the initial onset, the duration determined by the damping rate η. In Figure 3.8 of the Supporting information we compare the SPP wave packet evolution for different material parameters and electron energies.

To compare the time evolution to the spectral behavior, we calculate the frequency dependent fields in Figure 3.3(d). Data for a distance of R=100 nm are also shown in Figure 3.3(c). All spectra have been normalized to their maximum:

5.1×10^{12}, 5.7×10^{9}, 7.4×10^{6}, and 2.3×10^{4} $(\mathrm{V/m/eV})^2$ for R=0.1, 1, 10, and 100 μm, respectively. Close to the electron trajectory, for R=100 nm, the SPP spectrum is very sharp and peaks at ω_{SPP}. For larger distances, the spectrum broadens and shifts to lower frequencies, as expected from the frequency-dependent damping discussed above.

3.5 Transition radiation

Transition radiation (TR) is the most general form of radiation excited by an electron interacting with matter, as it occurs for any swift electron (or charged particle) crossing the boundary between two different media [94, 97, 98, 158, 159]. The most simple and intuitive way to view TR is that the electromagnetic fields of the electron are "in equilibrium" with their environment, obeying the equations for a homogeneous medium outlined above. If the two media are different however, the fields of the electron must have adjusted to the new electromagnetic properties of the second material. This modification of the fields as the electron transitions between the media is then accompanied by radiation. Jackson describes TR as portions of the electromagnetic field that must shake it off as radiation [150, 160]. An alternate intuitive explanation is provided by the method of image charges. The negatively charged electron produces a positive image charge below the surface, inducing an effective dipole normal to the surface which vanishes and radiates when the electron passes through the interface. This problem can be treated by describing the field lines of two moving charges of opposite sign that instantaneously stop (at the interface) or start (moving away from the interface) [161–163]. More generally, the approaching electron induces surface charges and currents which polarize the atoms in the material close to the trajectory. These polarization charges react and create an induced field which can radiate out to the far field as transition radiation.

The emission actually must originate from the induced field, just as for SPPs, since the homogeneous fields decay evanescently away from the trajectory of the moving electron and do not couple directly to far field radiation, so we can discount them in the derivation of the TR fields. Using the general formalism derived for the single interface, we can write the $\mathbf{E}(\mathbf{r},\omega)$ fields, taking only the integral over Q from Eq. (3.12) applied to the components of Eq. (3.11):

$$\mathbf{E}(\mathbf{r},\omega) = \int_0^\infty \frac{Q}{2\pi}\, dQ\, J_m(QR)\, \frac{2\pi}{k\epsilon_j}\, D\, \mu_j\, e^{iq_{z1}|z|} \left(sign(z) Q\hat{\mathbf{z}} - iq_{zj}\hat{\mathbf{R}} \right). \tag{3.19}$$

TR is emitted to the far field, so taking the limit for large distances, $kr \longrightarrow \infty$, we can evaluate the integral over Q for the two different field components. Here we examine only the upper hemisphere ($z < 0$, see Figure 3.2), taken to be vacuum:

$$\int_0^\infty dQ\, J_0(QR)\, e^{iq_{zj}|z|}\, f(Q) \approx -i\, \frac{q_{zj}}{Q}\, \frac{e^{ikr}}{r}\, f(Q)\hat{\mathbf{z}}, \tag{3.20a}$$

$$\int_0^\infty dQ\, J_1(QR)\, e^{iq_{zj}|z|}\, f(Q) \approx -\frac{q_{zj}}{Q}\, \frac{e^{ikr}}{r}\, f(Q)\hat{\mathbf{R}}. \tag{3.20b}$$

Applying this approximation to Eq. (3.19) leads to a compact expression for the spectral components of the TR electric field:

$$\mathbf{E}_{\mathrm{TR}}(\mathbf{r},\omega) = i\frac{q_{z1}}{k} D\mu_1 \frac{e^{ikr}}{r}\left(Q\hat{\mathbf{z}} + q_{zj}\hat{\mathbf{R}}\right). \tag{3.21}$$

The fields for the lower hemisphere can be obtained by analogy, using the corresponding components from Eq. (3.11). Making use of the geometrical relations between R, z and r as well as Q, q_{z1} and k, we can define an angle θ that determines the emission direction with respect to the surface normal: $\cos\theta = q_{z1}/k = z/r$ and $\sin\theta = Q/k = R/r$. Making use of these relations, we can rewrite the vectorial part of Eq. (3.21) as

$$\left(Q\hat{\mathbf{z}} + q_{zj}\hat{\mathbf{R}}\right) = k\left(\frac{R}{r}\hat{\mathbf{z}} + \frac{z}{r}\hat{\mathbf{R}}\right) = k\,\hat{\theta}.$$

This helps to further simplify Eq. (3.21), which reduces to

$$\mathbf{E}_{\mathrm{TR}}(\mathbf{r},\omega) = i q_{z1} D\mu_1 \frac{e^{ikr}}{r}\hat{\theta}. \tag{3.22}$$

We can rewrite this with a more explicit dependence on θ, finding a result very similar to that for the magnetic field as derived in Ref. 92:

$$\mathbf{E}_{\mathrm{TR}}(r,\theta,\omega) = ik\,\cos\theta\, D\mu_1 \frac{e^{ikr}}{r}\hat{\theta}. \tag{3.23}$$

We can evaluate this expression for $Q = k\,\sin\theta$. The asymptotic part $f(Q)$ of Eq. (3.20) can be used to obtain the TR emission probability by integrating over the upper hemisphere, leading to

$$\Gamma_{\mathrm{TR}}(\omega) = \frac{1}{2\pi\hbar k}\int_0^{\pi/2} \sin\theta\, d\theta \left| ik\,\cos\theta\, D\mu_1 \right|^2. \tag{3.24}$$

Finally, Eq. (3.23) can also be used to determine the TR electric field as a function of time by performing the Fourier transform over frequency,

$$\mathbf{E}_{\mathrm{TR}}(r,\theta,t) = \int_0^\infty \frac{d\omega}{\pi}\, \mathrm{Im}\{\mathrm{E}_{\mathrm{TR}}(r,\theta,\omega)\, e^{-i\omega t}\}\hat{\theta}. \tag{3.25}$$

For a non-dispersive medium, this can be simplified even further, since there are no longer any frequency-dependent components except for the $e^{-i\omega t}$ term. The

integral over ω then results in a $\delta(r-ct)$ term. In particular, for a perfect electric conductor, the TR electric field in space and time reduces to [162]

$$\mathbf{E}_{\mathrm{TR}}(r,\theta,t) = \frac{2ev\sin\theta}{rc}\,\frac{\delta(r-ct)}{1-(\frac{v}{c})^2\cos^2\theta}\,\hat{\theta}. \tag{3.26}$$

We evaluate Eq. (3.25) numerically, since it is generally applicable for any material. We use a fixed distance r_0=$\sqrt{2}$ µm from the origin (so that -z=R=1 µm for θ=45°) for different combinations of R and z to obtain a suitable distributions of angles θ. We use a 30 keV electron impinging on the same Drude metal as for the SPP calculation, with $\hbar\omega_{\mathrm{p}}$=1 eV and $\hbar\eta$=0.05 eV, summing over frequencies in the range ω=[$1e^{-6}-100$] eV/$\hbar$, divided into 10^6 steps. We find a large range of frequencies are necessary to obtain good convergence ($\omega \sim 100$ eV/$\hbar$), although the main features are resolved even with a smaller range ($\omega \sim 10$ eV/$\hbar$). These values are, however, related to the frequency dependence of the material permittivity. The larger the range in frequencies over which ϵ displays features, the larger the range needed in the calculation for good convergence.

Figure 3.4 displays the results of these time-resolved calculations. Figure 3.4(a) shows the TR electric field intensity (on a log scale) as a function of the emission angle θ and normalized time T=$t-r_0/c$. We find a sharp intensity feature for T=0, corresponding to the moment the electron traverses the interface. For all angles we observe the highest intensity just after T=0, following which it decays for larger times. Just as for the SPPs, TR forms a very short wave packet of electromagnetic field that travels through space. Comparing different angles, we clearly observe different regimes. For angles up to ~60° there are distinct oscillations in the intensity, which propagate longer at lower angles. For angles above ~60° we no longer see these oscillations, but instead a uniform decay in intensity.

To study the time evolution in more detail, we directly compare the time trace for different angles (denoted by the horizontal white dashed lines), showing the TR electric field amplitude on a linear scale, in Figure 3.4(b). The inset shows a schematic of the process, with the simple model of the negative electron inducing a positive mirror charge that creates a vertical dipole. Indeed, the angular emission pattern of TR displays two lobes (representing a cross cut through a toroidal three-dimensional pattern), similar to the emission from a vertical point dipole above the interface. Examining the TR wave packets, it is obvious that for all angles there is no discernible emission before T=0. The radiation only begins at T=0, rising rapidly to a maximum within a few femtoseconds, before decaying within ~30 fs (for the material parameters used here). TR thus consists of extremely short-lived wave packets. Comparing the different emission angles, we notice a variation in the maximum amplitude, with the smallest and largest angles showing a lower intensity than those in between (by a factor ~2–5). This agrees with the expected dipolar emission pattern that also exhibits low intensity for small and large angles with a maximum in between. At small angles of emission, θ=5° and 30°, we observe clear oscillations in time, that have a similar initial period before becoming out of phase after the second optical cycle. For higher emission angles, θ=60° and 80°,

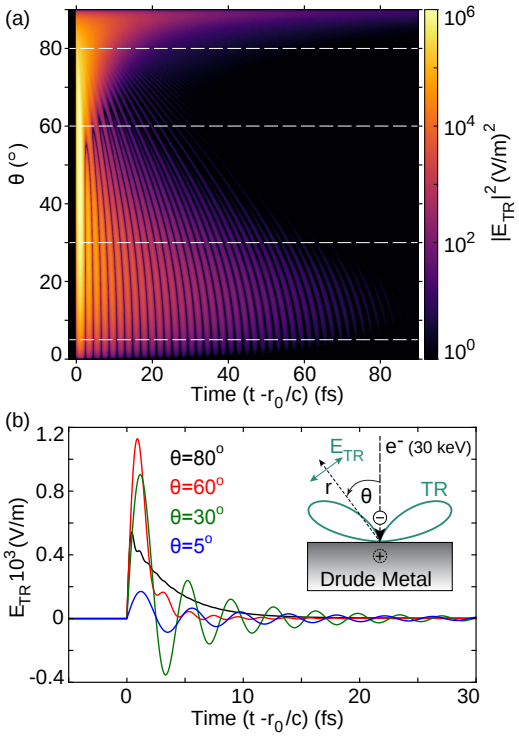

Figure 3.4 – Electric field of transition radiation (TR) excited by a 30 keV electron, propagating away from the same Drude metal as in Figure 3.3, as a function of time. (a) The TR electric field intensity, shown on a logarithmic scale, as a function of the emission angle θ and of the normalized time $T = t - r_0/c$, with r_0=$\sqrt{2}$ µm the position at which the field is calculated for each angle (see inset schematic in (b)). (b) Comparison of the TR electric field amplitude as a function of the normalized time for four different emission angles, corresponding to the dashed lines in (a). The inset shows a schematic of the TR excitation and emission process.

the oscillations are critically damped and the time evolution displays a single slow decay from the initial amplitude maximum.

In order to gain insight into this strong angle-dependent, short-lived behavior, we calculate the TR electric field as a function of frequency. Figure 3.5(a) shows the TR intensity as a function of frequency and emission angle. The intensity is limited to certain sections of $\theta-\omega$ space. For the Drude metal with $\hbar\omega_p$=1 eV, the permittivity approaches unity above an energy of several eV, so the electron will not perceive a transition in that energy range. The intensity is also depleted at the smallest and largest angles for most of the frequency range. Examining Eq. (3.23), we find that it contains a $\cos\theta$ term and a $\sin\theta$ term (due to Q), so E_{TR} is expected to go to 0 for angles close to 0 and $\pi/2$. Physically, these angles correspond to either

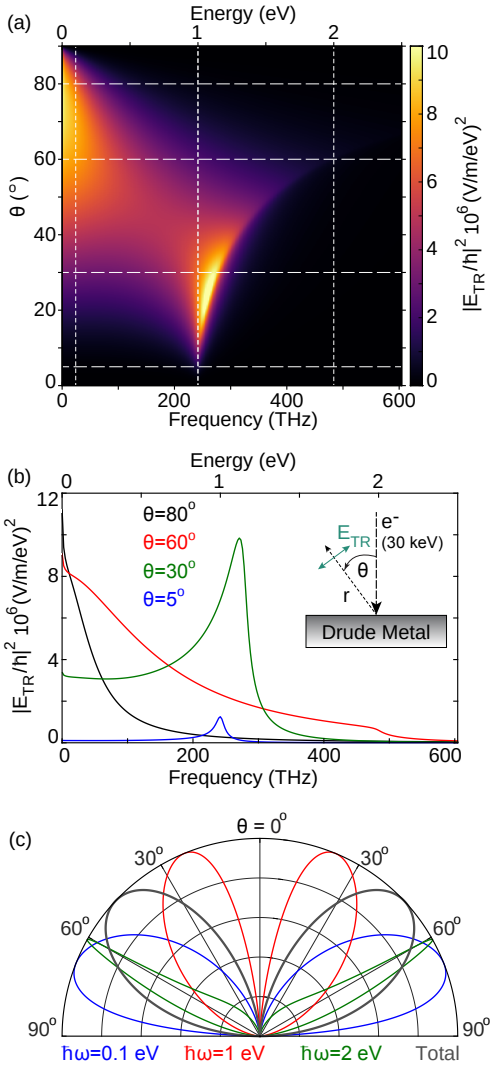

Figure 3.5 – Electric field of TR in the frequency domain, excited by a 30 keV electron impinging on the same Drude metal as in Figures 3.3 and 3.4, evaluated at the same distance $r_0=\sqrt{2}$ µm as in Figure 3.4. (a) TR electric field intensity as a function of emission angle θ and frequency/energy. (b) Comparison of the TR electric field spectra for different emission angles, denoted by the horizontal dashed lines in (a). The inset shows a schematic of the TR excitation and emission geometry. (c) Normalized TR electric field intensity as a function of emission angle, for the total integrated intensity (gray) and for different frequencies, denoted by the vertical dashed lines in (a).

very small Q or q_{zj}, indicating that the light modes are more delocalized (in space) and the coupling between the electrons and the impact region is smaller, leading to lower TR intensity.

At low frequencies and large angles (grazing to the surface) there is a broad and intense feature that occurs when the real and imaginary parts of ϵ_2 reach very large magnitudes (ϵ_2=ϵ_D of the Drude metal). At small angles (close to the surface normal) there is a sharp, bright peak that starts at ω=ω_p and then bends off to higher frequencies and larger angles before disappearing around θ=40°. This feature occurs when $|\epsilon_D|$ displays a sharp kink and can be a result of an accumulation effect comparable to Van Hove singularities [164, 165]. The kink in $|\epsilon_D|$ bears resemblance to divergences in the density of states that lead to anomalies in optical absorption spectra. An additional explanation, described by Ferrell[166] and Stern[167] for metal foils, is that the incoming electron drives plasma oscillations of electrons at the surface, which radiate at the plasma frequency ω_p. This emission is only expected when $\mathrm{Im}\{\epsilon\}$ is much smaller than 1, which is the case here. In the Supporting information we show that the effect indeed disappears for increasing loss.

We attribute the sudden depletion of the TR intensity of this feature for $\omega > \omega_\mathrm{p}$ to the coupling strength between the electron and the material becoming focused in the forward direction, into the metal. The dispersion relation of the light inside the metal is given by $q = k\sqrt{\epsilon_D}$ while the parallel wave vector of the emitted radiation is $Q \leq q$. The boundary for coupling the energy into the metal instead of the far field of the upper hemisphere should thus be determined by $\sin\theta = Q/k = \sqrt{\epsilon_D}$, so $\theta = \arcsin(\sqrt{\epsilon_D})$. We find excellent agreement with the data, shown later on in Figure 3.6 and Figure 3.11 of the Supporting information. This explanation is consistent with the behavior of the μ_1 term (Eq. (3.9)) that appears in Eq. (3.23): the first denominator $q^2 - k^2\epsilon_D$ goes to 0 for $q = k\sqrt{\epsilon_D}$, leading to the divergent behavior that we observe.

These results indicate that the frequency dependent permittivity of the Drude metal leaves a strong imprint on the TR emission. We will study this dependence on permittivity in more detail in Figure 3.6. Additionally, we study the effect of different material parameters and electron energies on the TR emission explicitly in both the time and frequency domains in Figures 3.9, 3.10, and 3.11 of the Supporting information.

In Figure 3.5(b) we examine the corresponding spectra for the same angles as shown in Figure 3.4(b) (denoted by the horizontal white dashed lines). For θ=5°, we note a low intensity but a clear peak in the spectrum at the plasma frequency ω_p. For θ=30° the spectrum is still dominated by this peak that has moved to slightly higher frequencies, but there is a noticeable increase at lower frequencies as well. We can now say that the oscillations in time from Figure 3.4 for small angles correspond roughly to the plasma frequency. For larger angles the frequency of oscillations increases. For θ=60° a broad, decreasing spectral band is observed up to ~2 eV. At θ=80°, a narrower spectral band is distinguished, falling off well below 1 eV. These data correspond to the time evolution that is observed at large angles, which does not exhibit clear oscillations but instead a strongly decaying signal.

Examining the frequency extent of the spectra more closely, they are most confined for the largest and smallest angles (Figures 3.5(a,b)) where the fields are more delocalized. Correspondingly, the TR is more spread out in time. For angles around θ=50–70°, the fields extend over a much wider range of frequencies and are very localized in time, corresponding to stronger coupling between the electrons and the impact region.

In addition to studying the spectra for given angles, we can determine the angular profile at different frequencies, which can also be measured in experiments [119, 128]. Figure 3.5(c) shows the normalized intensity as a function of θ for the frequencies corresponding to the vertical white dashed lines in Figure 3.5(a), as well as the total intensity summed over all frequencies. We clearly observe the characteristic dipolar lobes, which vary in orientation and width for different frequencies. As expected there are broader lobes at grazing angles for low frequencies and narrower lobes close to the surface normal at ω=ω_p. For higher frequencies the distribution moves back to higher angles and becomes sharper.

Figure 3.6 examines the relation between TR emission and material permittivity by comparing the absolute value of ϵ to the total intensity (summed over all angles) and to the angle of maximum intensity θ_{max}, as a function of frequency/energy. The incoming medium is vacuum. We first study the Drude metal with $\hbar\omega_\mathrm{p}$=1 eV and $\hbar\eta$=0.05 eV for a 30 keV electron (Figure 3.6(a)). For low frequencies, $|\epsilon_D|$ and the total intensity show the same decreasing trend when approaching ω_p; the two then show opposite behavior in the frequency range where $|\epsilon_D| < 1$. θ_{max}, meanwhile, displays the same trend as ϵ_D across the whole frequency range, decreasing and increasing in lockstep. We examine the angle $\theta = \arcsin(\sqrt{\epsilon_D})$ for frequencies $\omega > \omega_\mathrm{p}$, indicated by the gray dashed line. As discussed above, this should indicate the boundary between regions where the radiation is coupled in the backward (upper hemisphere) or forward (into the metal) directions. The resulting angle exhibits excellent agreement with θ_{max}, indicating that the sudden depletion of TR can indeed be attributed to coupling into the metal. This is dependent on the specific material permittivity; we show there is good agreement for different parameters in Figure 3.11 of the Supporting information.

In order to further explore these trends, we examine the same variables for silicon in Figure 3.6(b), again using a 30 keV electron. In the $\hbar\omega$=[0–20] eV range, the permittivity ϵ_{Si} of silicon displays a strong double peak around 4 eV and $\mathrm{Re}\{\epsilon_{Si}\} < 0$ from 4 eV to 16 eV. $|\epsilon_{Si}|$ and θ_{max} follow the same trend over the entire frequency range, while the total TR intensity again exhibits the same trend as $|\epsilon_{Si}|$ for frequencies where $|\epsilon_{Si}| > 1$ and an opposite trend for frequencies where $|\epsilon_{Si}| < 1$. As for the Drude model, the minimum of $|\epsilon_{Si}|$ and θ_{max} corresponds to a peak in the total intensity.

Determining a direct relation between ϵ and all aspects of the TR emission is difficult because ϵ appears multiple times in the equations, but it is possible to get an intuitive understanding of the behavior. Looking back at the definition of TR, it is essentially a "reflected" field induced by the approaching electron that has to adapt to its new electromagnetic environment. The term μ_j from the equations

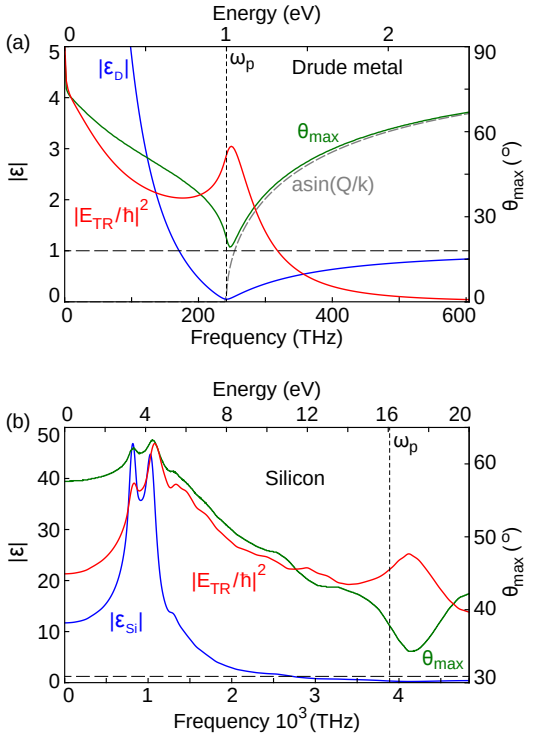

Figure 3.6 – Dependence of TR on the material permittivity ϵ. (a) Absolute value of the permittivity of the Drude metal ($\hbar\omega_p$=1 eV and $\hbar\eta$=0.05 eV), as a function of frequency/energy (in blue) compared to the normalized total TR electric field intensity (integrated over all angles, in red) and the angle of maximum emission intensity θ_{max} (in green). The TR intensity spectrum is normalized to the same maximum as $|\epsilon|$, the vertical dashed line denotes the plasma frequency, and the horizontal dashed line indicates $|\epsilon|$=1. The gray dashed line corresponds to $\theta = \arcsin(Q/k) \sim \arcsin(\sqrt{\epsilon})$. (b) Same as for (a), but now for silicon, with a permittivity that displays typical features of a dielectric but also contains a metallic region.

even bears some resemblance to the Fresnel equations. Just as for reflection of light, one can understand that the higher the contrast between the two media, the more the field of the electron will have to "shake off" components and induce a strong response [168]. The ratio between the permittivities of the two materials can go both ways however. What we observe in Figure 3.6 is that for both $|\epsilon| \gg 1$ and $|\epsilon| \ll 1$ the TR intensity is high due to the large contrast from 1. The angle of maximum emission θ_{max} consistently follows the same trend as $|\epsilon|$. In the Supporting information we study this in more detail.

3.6 Conclusions

We have shown that transition radiation and surface plasmon polaritons excited by swift electrons are composed of ultrashort, femtosecond time-scale wave packets. We have studied the time, space, and frequency dependence of the electric fields of the electron, both in vacuum and when traversing a metallic or dielectric surface, providing intuitive physical insight into these ultrafast processes. The external field of the swift electron in vacuum comprises a single oscillation, similar to a single optical cycle, and thus represents an ultrabroadband optical excitation spectrum. In vacuum the fields evanescently decay away from the electron trajectory and cannot directly couple to radiation. When impinging on a polarizable material however, the electron induces fields at the surface that can radiate out to the far field.

We first studied the surface plasmon polaritons propagating along the surface of a Drude metal, finding that the plasmon wave packets are several hundred femtoseconds in duration (depending on the material parameters). The SPPs decay strongly and red-shift in frequency as they propagate away from the point of excitation. This redshift is due to the fact that high-frequency components close to the plasmon resonance are strongly damped.

We have also examined transition radiation, the far-field emission which occurs when a charged particle traverses the interface between two different media. Using the Drude metal as an example, we find that TR wave packets are strongly dependent on the emission angle and ultrashort in duration, lasting only a few tens of femtoseconds (again depending on the material parameters). The TR intensity and emission angle dependence is correlated with well-defined trends in the permittivity of the material. Given the frequency dependence of ϵ for a certain dielectric, the TR emission can be qualitatively predicted.

The theoretical insights and predictions presented here further our knowledge and understanding of electron-light-matter interactions at the nanoscale and can be applied to study fundamental physical processes occurring at the femtosecond time scale.

3.7 Supporting information

3.7.1 Full time, frequency and material dependence of SPPs

In Section 3.4 of the main text, we discuss how a fast electron impinging on a metal surface can excite surface plasmon polaritons (SPPs). These propagate along the surface as femtosecond-scale wave packets, decaying in intensity with gradually decreasing frequencies as they travel further away from the excitation position. We have shown the time evolution and spectral behavior of the SPP electric fields for a selection of distances in Figure 3.3.

In order to give a more complete overview of the traveling waves, we display a full range of distances here in Figure 3.7. We first examine the intensity of the E_z

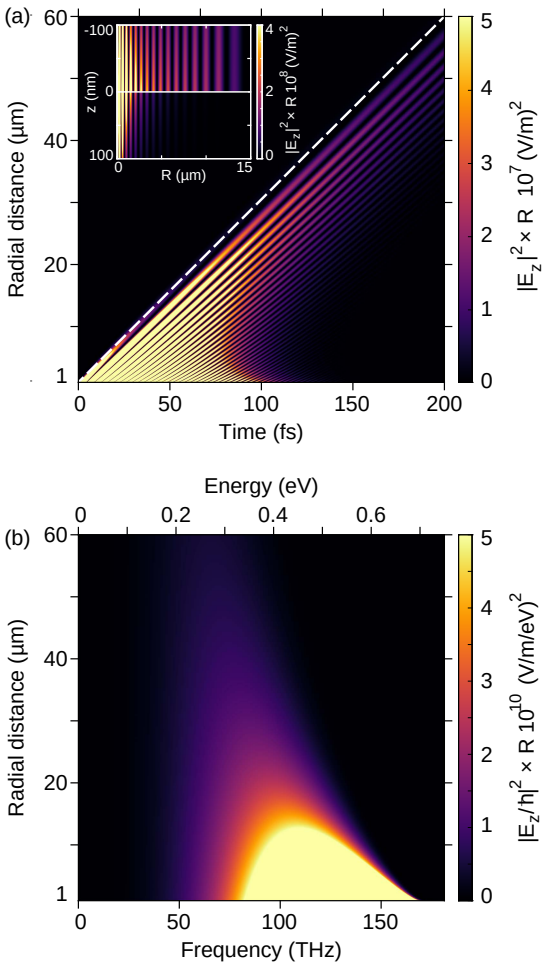

Figure 3.7 – Electric field E_z of surface plasmon polaritons (SPPs) excited by a 30 keV electron, propagating over the surface of a Drude metal ($\hbar\omega_p$=1 eV and $\hbar\eta$=0.05 eV), calculated at a distance z=−10 nm from the surface, as in Figure 3.3. (a) Intensity of the SPP E_z field component multiplied by the radial distance R, as a function of time t and radial distance R away from the electron trajectory. The color scale is saturated in order to distinguish the oscillations of the SPP wave packet over the entire range, the maximum intensity (at the origin) is 2.4×10^{11} (V/m)^2. The diagonal white dashed line represents the light cone. The inset shows a 2D R–z snapshot at t=50 fs of the E_z intensity multiplied by R. (b) The corresponding intensity of the SPP E_z field component in the frequency domain multiplied by the radial distance R, as a function of the frequency and radial distance R. We again saturate the color scale to distinguish the redshift of the frequencies over the entire range, the maximum intensity (at the origin) is 5.5×10^{14} (V/m/eV)^2.

component as a function of time t (up to 200 fs) and radial distance R (up to 60 µm), in Figure 3.7(a). We multiply the intensity by the radial distance R to compensate for its $1/R$ dependence. The color scale is saturated in order to view the features over the entire range. Since the SPP travels as a wave packet over the surface, it displays oscillations both as a function of time and of the distance R, moving at a speed given by the slope in the figure. We observe clear waves oriented diagonally, with slopes corresponding to velocities close to but slower than the speed of light (white dashed line). Very close to the origin, the oscillations in time are much faster and the slopes are smaller (corresponding to lower velocities) than for further distances. This is in agreement with the expected behavior of the SPPs given their dispersion, as discussed in the description of Figure 3.3.

The inset of Figure 3.7(a) exhibits a snapshot of the SPP E_z intensity (multiplied by R) at t=50 fs, as a function of R and z. We observe, as can be expected, that the field intensity decays for increasing R and $|z|$ and that there is more intensity at the incoming vacuum side ($z < 0$). The period of the oscillations also increases with R, in accordance with the damping that leads to smaller Q_{SPP} (longer wavelengths) as the SPPs propagate further away from the point of excitation.

Figure 3.7(b) displays the corresponding information in the frequency domain, with the intensity of the E_z component (multiplied by R) plotted as a function of frequency and the same radial distance range. For small R we find that the spectrum extends up to the plasmon resonance ω_{SPP} ~0.7 eV (see Figure 3.3(d)). For increasing distance, the spectrum gradually shifts to lower frequencies, peaking near ~0.25 eV for R=60 µm.

To gain a better understanding of the SPP dependence on material properties and the energy of the exciting electron, we compare the time evolution of four different cases in Figure 3.8(a) and the corresponding frequency response in Figure 3.8(b). The calculations use the same radial distance R=10 µm and height z=−10 nm. We start with the same properties used before throughout the main text and in Figure 3.7: $\hbar\omega_{\mathrm{p}}$=1 eV and $\hbar\eta$=0.05 eV, $\mathrm{E_{e^-}}$=30 keV (blue lines). We then double the plasma frequency to $\hbar\omega_{\mathrm{p}}$=2 eV (gray lines), or increase the electron energy to $\mathrm{E_{e^-}}$=300 keV (green lines), or increase the loss to $\hbar\eta$=0.25 eV (red lines).

Examining the decay duration of the SPP wave packets in Figure 3.8(a), it appears that changing the plasma frequency and electron energy does not have a strong effect. Increasing the damping η (by a factor of 5), however, noticeably shortens the wave packet duration to ~50 fs and also decreases the maximum field amplitude. Examining the frequency response in Figure 3.8(b) we find a correspondingly lower intensity, combined with a redshift. This is to be expected, since η governs the absorption or damping in the Drude metal. Calculations for other combinations of ω_{p} and η (not shown here) demonstrate that the wave packet duration does not decrease linearly with an increase in η. Using a higher plasma frequency results in a slight reduction in the decay duration.

Increasing the electron energy tenfold only has a significant effect on the field amplitude, which grows by roughly a factor of 2. The period of the oscillations also slightly increases. Both of these differences are also observed in the frequency

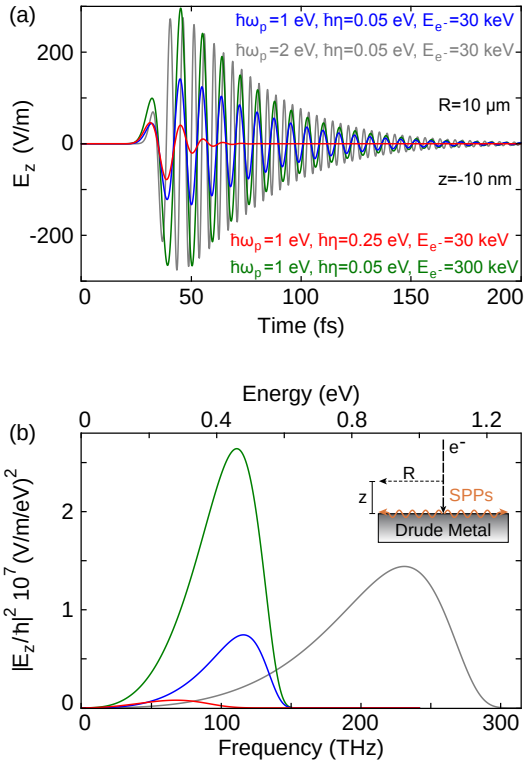

Figure 3.8 – Comparison of the SPP electric field for different Drude metals and electron energies, all for the same radial distance R=10 μm and fixed height z=−10 nm. We compare the parameters used in main text ($\hbar\omega_p$=1 eV and $\hbar\eta$=0.05 eV, E_{e^-}=30 keV, in blue) to a more energetic exciting electron ($\hbar\omega_p$=1 eV and $\hbar\eta$=0.05 eV, E_{e^-}=300 keV, in green), a Drude metal with more losses ($\hbar\omega_p$=1 eV and $\hbar\eta$=0.25 eV, E_{e^-}=30 keV, in red) and a Drude metal with a higher plasma frequency ($\hbar\omega_p$=2 eV and $\hbar\eta$=0.05 eV, E_{e^-}=30 keV, in gray). We show the time dependence of the E_z SPP amplitude as a function of time t (a) as well as the E_z SPP intensity as a function of frequency (b). The inset in (b) shows a simplified schematic of the SPP excitation and emission process.

domain, with a higher intensity and small redshift for the 300 keV electron. The field strength enhancement results from the fact that at higher velocities, the fields extend further (as determined by the Bohr cutoff $v\gamma_e/\omega$). This increases the volume of polarized material, which leads to a stronger induced field and a higher generation rate of SPPs. The very slight difference in the time evolution and corresponding frequency can be related to a different degree of retardation.

Increasing the plasma frequency by a factor of two leads to a clear increase in the field amplitude and corresponding intensity in the spectra. A higher number of conduction electrons are involved for higher plasma frequencies ($\omega_p^2 \propto N_e$) and

according to the f-sum rule, light extinction (the sum of absorption and scattering) generally scales with N_e [169–171]. The interaction strength and SPP generation thus increases with plasma frequency. Overall, we find that changing the material properties has a much stronger effect on the SPP behavior than varying the energy of the incident electron. We will now examine if the same holds true for TR.

3.7.2 Full comparison of TR for different material/electron parameters

Section 3.5 of the main text describes how a fast electron impinging on a second medium (a Drude metal) will generate transition radiation (TR) as it transits through the interface and the electric fields change to adapt to their new environment. TR takes the form of ultrashort wave packets a few tens of femtoseconds in duration, that are highly dependent on the emission angles and material permittivity. Here in Figures 3.9, 3.10 and 3.11 we study the effect of different material properties and electron energy on the TR emission behavior.

In the main text, we have examined the time, angle and frequency dependence of TR emission for one specific instance ($\hbar\omega_p$=1 eV and $\hbar\eta$=0.05 eV, E_{e^-}=30 keV). Figure 3.9 compares the time evolution and spectra for those parameters, at θ=5° and θ=60°, to three additional cases. We either change the electron energy to 300 keV, or increase the loss in the Drude metal tenfold to $\hbar\eta$=0.5 eV, or double the plasma frequency to $\hbar\omega_p$=2 eV. For completeness, Figures 3.10 and 3.11 display the field intensity in the time and frequency domains, for all emission angles. First examining the time-dependent behavior in Figures 3.9(a,b), we find that for increased damping, the field amplitude oscillations die out more rapidly, while for the higher plasma frequency the field amplitude is increased and oscillates about twice as fast. For the higher electron energy, we observe an increase in amplitude, accompanied with a slight change in the frequency of the oscillations. The increase in field strength can be intuitively understood for the same reason as for the SPPs: the electron fields extend further away, polarizing a larger volume of material. The wave packet decay duration and the frequency of oscillations are also directly related to η and ω_p respectively, as we saw for the SPPs in Figure 3.8.

Figures 3.9(c,d) show the corresponding data for θ=5° and 60° in the frequency domain. For the increased η the spectra are less intense, especially for θ=5°, where the peak close to ω=ω_p has broadened and red shifted slightly. For $\hbar\omega_p$=2 eV the peak at θ=5° has increased in intensity and blue shifted to twice the frequency, as expected. The same trend holds for θ=60°. As for the SPPs, the increase in intensity can be related to the higher conduction electron density and the f-sum rule. The calculation with 300 keV electron energy shows the same general spectral behavior as for 30 keV, with a higher intensity and a stronger contribution from low frequencies, for both angles. This agrees well with the time evolution, where we observe that the wave packet for 300 keV lags very slightly and oscillates a little slower than for 30 keV (by ~0.2 fs). Overall, we find that the dependence of TR on material parameters and electron energy is very similar to that of the SPPs.

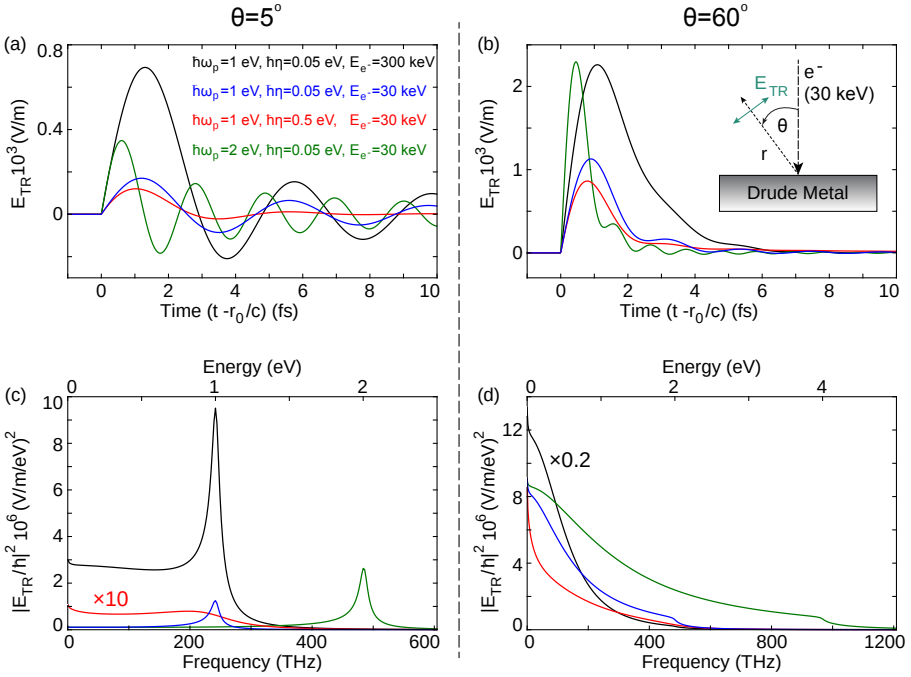

Figure 3.9 – Comparison of the TR electric field for different Drude metals and electron energies. We compare the parameters used in the main text ($\hbar\omega_p$=1 eV and $\hbar\eta$=0.05 eV, E_{e^-}=30 keV, in blue) to a more energetic exciting electron ($\hbar\omega_p$=1 eV and $\hbar\eta$=0.05 eV, E_{e^-}=300 keV, in black), a Drude metal with more losses ($\hbar\omega_p$=1 eV and $\hbar\eta$=0.5 eV, E_{e^-}=30 keV, in red) and a Drude metal with a higher plasma frequency ($\hbar\omega_p$=2 eV and $\hbar\eta$=0.05 eV, E_{e^-}=30 keV, in green). We show the time dependence of the TR electric field amplitude as a function of normalized time ($T=t-r_0/c$) for an emission angle of θ=5° (a) and θ=60° (b). We also show the TR electric field intensity in the frequency domain, as a function of frequency for these same angles (c,d). The red spectrum in (c) has been multiplied by a factor of 10, while the black spectrum in (d) has been multiplied by a factor 0.2. The inset in (b) shows a simplified schematic of the TR excitation and emission process.

Figure 3.10 displays the TR electric field intensity as a function of the emission angle θ and the normalized time $T=t-r_0/c$. As expected, a higher loss factor η leads to TR oscillations that are much more damped, over all emission angles. A higher plasma frequency leads to faster oscillations, except for the most grazing angles where the emission is still critically damped. The faster electron with 300 keV energy mostly leads to an increase in intensity, relatively more noticeable for the higher emission angles.

Figure 3.11 shows the corresponding information in the frequency domain, with panels (a–d) corresponding to the same parameters as in Figure 3.10. The calculation for higher loss displays a much weaker overall intensity and a

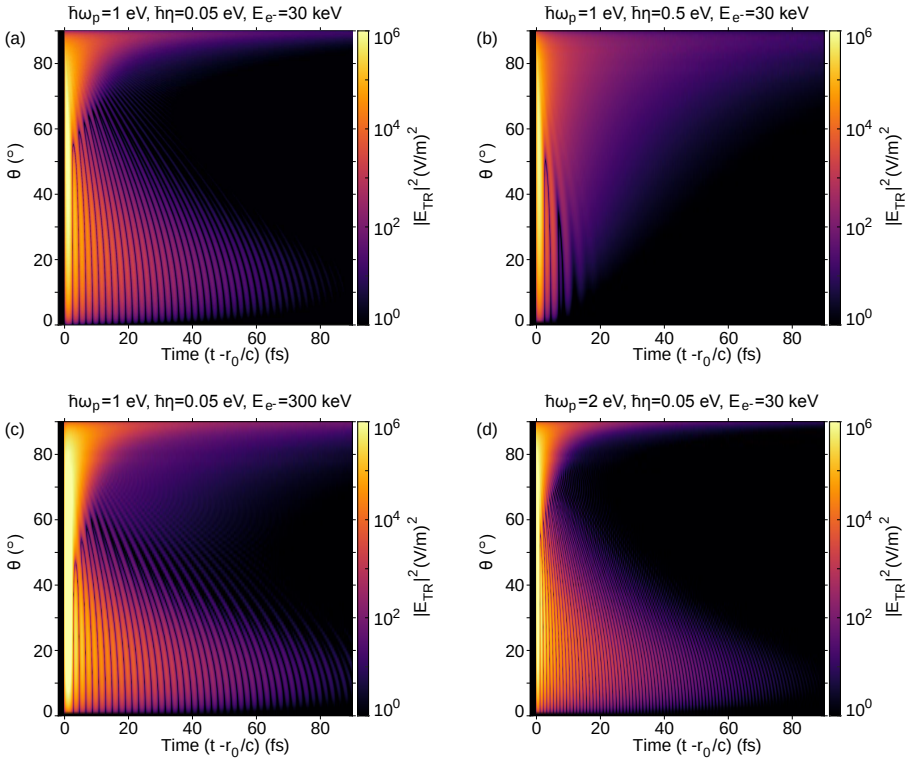

Figure 3.10 – Comparison of the full time evolution of the TR electric fields for the different Drude metals and electron energies from Figures 3.9. We show the TR electric field intensity on a logarithmic scale, as a function of normalized time (T=$t - r_0/c$) and emission angle θ. (a) TR intensity for $\hbar\omega_p$=1 eV and $\hbar\eta$=0.05 eV, E_{e^-}=30 keV. (b) A more lossy Drude metal, $\hbar\omega_p$=1 eV and $\hbar\eta$=0.5 eV, E_{e^-}=30 keV. (c) A more energetic exciting electron, $\hbar\omega_p$=1 eV and $\hbar\eta$=0.05 eV, E_{e^-}=300 keV. (d) A Drude metal with a higher plasma frequency, $\hbar\omega_p$=2 eV and $\hbar\eta$=0.05 eV, E_{e^-}=30 keV.

disappearance of the feature at ω=ω_p, explaining the absence of a well-defined peak for this case in Figure 3.9(c). For the higher electron energy (Figure 3.11(c)) the bright feature at low angles close to ω_p is well-preserved, but we notice a clear relative increase of the intensity at low frequencies, over a wide angular range. The doubled plasma frequency (Figure 3.11(d)) shows a shift of the sharp bright feature at low angles to the new plasma frequency, which is now relatively more intense than the feature at high angles and low frequencies. This change is quite opposite to that observed for the increased electron energy. We discussed in the main text that the TR emission should be depleted when the electron couples its energy into the material instead of radiation into the upper hemisphere. The angle

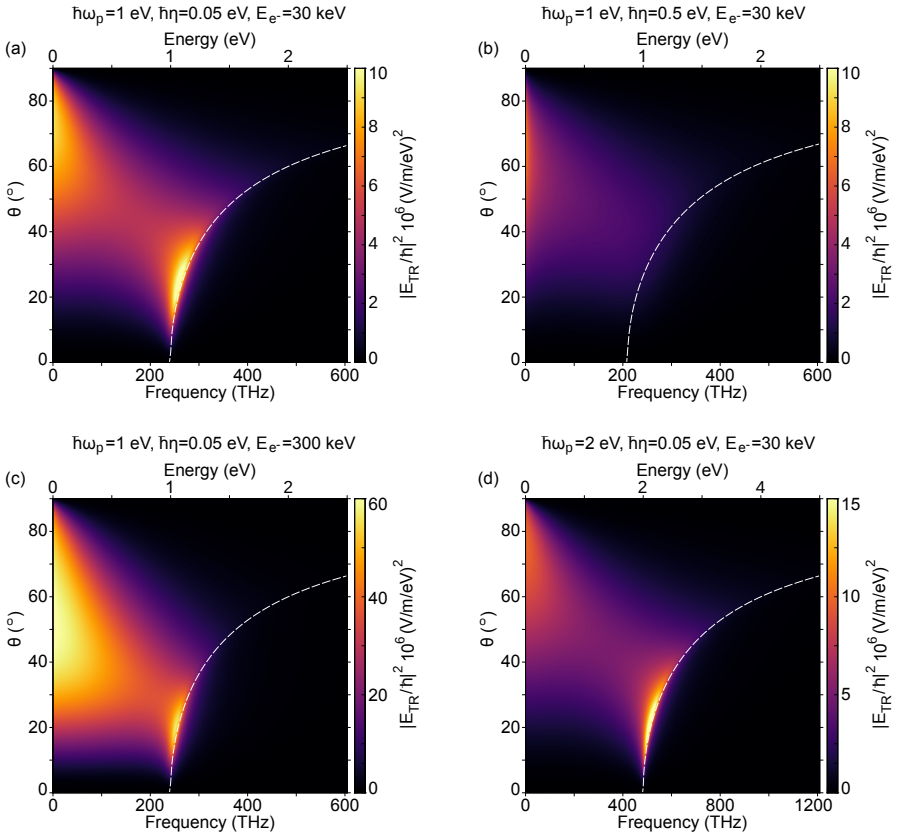

Figure 3.11 – Comparison of the full spectral behavior of the TR electric fields for the different Drude metals and electron energies from Figure 3.9. We show the TR electric field intensity as a function of frequency and emission angle θ. (a) TR intensity for $\hbar\omega_p$=1 eV and $\hbar\eta$=0.05 eV, E_{e^-}=30 keV. (b) A more lossy Drude metal, $\hbar\omega_p$=1 eV and $\hbar\eta$=0.5 eV, E_{e^-}=30 keV. (c) A more energetic exciting electron, $\hbar\omega_p$=1 eV and $\hbar\eta$=0.05 eV, E_{e^-}=300 keV. (d) A Drude metal with a higher plasma frequency, $\hbar\omega_p$=2 eV and $\hbar\eta$=0.05 eV, E_{e^-}=30 keV. The white dashed lines correspond to $\theta = \arcsin(Q/k) \sim \arcsin(\sqrt{\epsilon})$, with ϵ given by the Drude parameters. We note that (a) and (b) are shown on the same scale, but (c) and (d) have different scales.

determining this boundary, $\theta = \arcsin(\sqrt{\epsilon})$, is shown as a white dashed line in all four panels and exhibits excellent agreement with the trend of the TR intensity as it transitions between bright and dark regions for $\omega > \omega_p$. Since we only use the real part of ϵ to determine this angle, we do not account for the strong damping in Figure 3.11(c), which causes the feature to disappear. This is in agreement with Stern[167], who predicts a peak in TR at the plasma frequency when the imaginary part of ϵ is much smaller than 1, which does not apply for the larger η used here. As

for the SPPs, the material parameters have a stronger influence than the electron energy.

3.7.3 Dependence of TR on material permittivity

Figure 3.6 from Section 3.5 describes how the emission behavior of TR correlates with the permittivity of the medium onto which the electron impinges (now denoted as ϵ, the incoming medium always being vacuum). Here we study this relation in more detail. Figure 3.12 displays the results for an artificial frequency-dependent ϵ with specific features, to determine the underlying principles behind the behavior observed in Figure 3.6.

First, Figure 3.12(a) shows the real (ϵ', in blue) and imaginary (ϵ", in red) parts of the artificial permittivity, as a function of frequency. We note such a permittivity does not necessarily satisfy the Kramers–Kronig relations, but is meant to serve as an illustration. ϵ' traces out a positive and then a negative peak before becoming positive again, for ϵ"=0, before repeating the same features with ϵ"=1, finishing with a peak in ϵ" for ϵ'=1. Figure 3.12(b) displays the TR intensity as a function of the frequency and the emission angle. We can observe several features. First, it is clear that the peaks in negative ϵ' lead to more intense TR intensity than peaks in positive ϵ', with a factor ~2 difference. Next, the peak in ϵ" shows a similar intensity to the comparable peak in positive ϵ'. All of the regions where ϵ is close to that of vacuum are very dark, since there is no longer any contrast between the two media. The most noticeable features in Figure 3.12(b) however, are the bright and sharp lobes that occur on both sides of the first negative peak of ϵ', which are very similar to those seen for the Drude metal in Figure 3.5(a). We can now see that these bright regions correspond to ranges in frequency where $1 > \epsilon' > 0$ and ϵ"=0, so that $|\epsilon| < 1$. The feature becomes brighter (not visible on this color scale) and sharper at the smallest emission angles as ϵ' approaches 0, but stops quite abruptly once ϵ' becomes negative, even when $|\epsilon|$ is still below 1. Although not shown here, the edges of these features do correspond to $\theta = \arcsin(\sqrt{\epsilon})$, as was the case for the Drude metal. In the second cycle where ϵ"=1, this feature has completely disappeared, which we attribute to $|\epsilon|$ no longer being smaller than 1 at any point, even when $\epsilon' < 0$. This again agrees with predictions by Stern[167], as discussed in Figure 3.11 and in the main text.

We examine the relation between $|\epsilon|$, the emission intensity and angle more explicitly in Figure 3.12(c), which is similar to Figure 3.6. We show $|\epsilon|$ (in blue), the total TR intensity summed over all angles (in red), normalized to the same maximum value as $|\epsilon|$, and the angle of maximum emission intensity θ_{max} (in green). Overall, we find that θ_{max} and the total intensity follow the same behavior or trend as $|\epsilon|$. The only difference occurs in the region of the bright features in Figure 3.12(b). For $|\epsilon|$ at or just below 1, θ_{max} exhibits a maximum, but this occurs for vanishing intensity, so this is not really significant. As $|\epsilon|$ decreases and becomes closer to 0, θ_{max} again shows the same behavior, also reaching a minimum close to 0. The total intensity however displays the opposite behavior, reaching a maximum, just

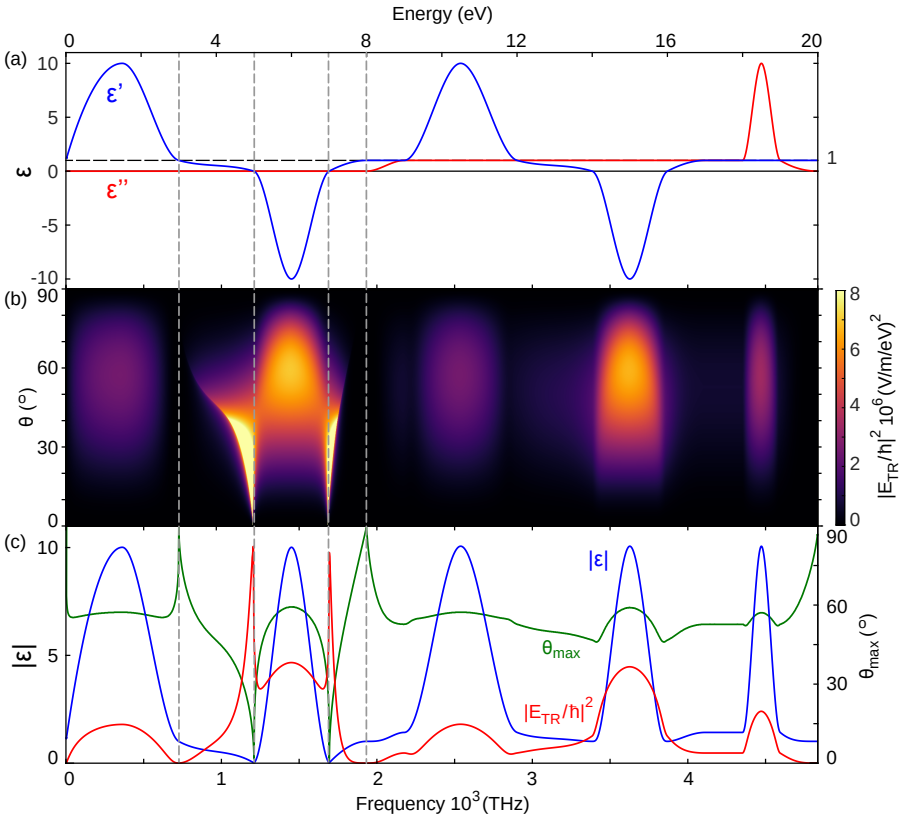

Figure 3.12 – Dependence of TR emission on the permittivity of an artificial material. (a) Real (ϵ', in blue) and imaginary (ϵ", in red) parts of the artificial permittivity as a function of frequency. From left to right we use a positive and a negative peak of ϵ' for ϵ"=0 and repeat for ϵ"=1, ending with a peak in ϵ" for ϵ'=1. The horizontal dashed line denotes ϵ=1. The vertical dashed lines denote the transitions to/from regions in which the absolute value $|\epsilon| < 1$ but $\epsilon' > 0$. (b) TR electric field intensity in the frequency domain, as a function of frequency and emission angle θ for the artificial ϵ from (a). (c) Comparison of the absolute value of the artificial permittivity $|\epsilon|$ (in blue) to the normalized TR electric field intensity (in red) and the angle of maximum emission intensity θ_{max} (in green), all as a function of frequency. The TR intensity is normalized to the same maximum as $|\epsilon|$. We note that θ_{max} goes to 90° at the locations of the dashed lines, but here the intensity goes to 0, so the emission angle is not well-defined.

as was observed in Figure 3.6. All of the observed behavior is consistent with the notion that TR is sensitive to the contrast between the permittivities of the two media, just as for reflection of light. An $|\epsilon|$ much larger than 1 or much smaller than 1 ($|\epsilon|$ close to 0) both lead to very high contrast and correspondingly intense TR emission. There are however additional subtleties, such as the higher intensities

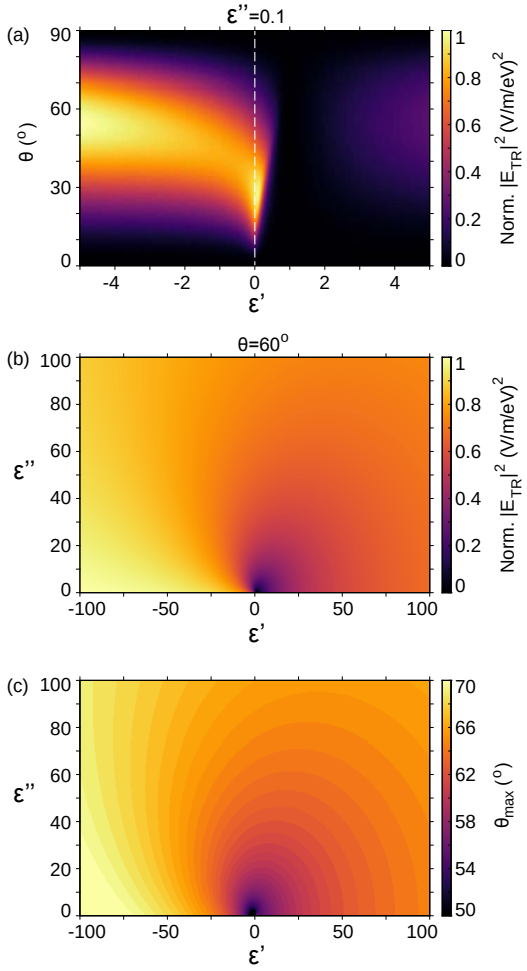

Figure 3.13 – Dependence of TR emission on material permittivity. (a) The TR electric field intensity in the frequency domain normalized to its maximum, as a function of ϵ' and the emission angle θ, for ϵ"=0.1. The dashed line denotes ϵ'=0. (b) The same normalized TR intensity, now shown as a function of ϵ' and ϵ" over a larger range, for θ=60°. (c) The angle of maximum emission intensity θ_{max}, as a function of ϵ' and ϵ". Note the reduced range of angles spanned by the color scale. The color steps visible in the figure are due to the discrete 0.5° steps in θ for which the calculation is performed.

for negative ϵ than for positive values, and the fact that the emission angles also track the behavior of $|\epsilon|$.

Figure 3.13 shows the TR emission behavior plotted explicitly as a function of ϵ,

at a single energy ($\hbar\omega$=1 eV). Figure 3.13(a) displays the TR intensity normalized to the maximum value, as a function of ϵ' and θ, for ϵ"=0.1. The more intense TR for negative ϵ' than for positive ϵ' is clearly observed. The now familiar sharp feature for ϵ' positive but close to 0 is visible as well, but since ϵ"> 0, it is relatively less bright and occurs at higher angles than in Figure 3.12(b). We also observe the transition region from this feature towards high intensities at higher angles for the negative values of ϵ', as well as the disappearance of emission intensity around ϵ'=1 when we lose the contrast with vacuum. In Figure 3.13(b), we examine the normalized TR intensity as a function of ϵ' and ϵ", for an emission angle θ=60°. We again notice the minimum in intensity around ϵ'=1 and ϵ"=0. From this minimum outwards, the intensity increases for increasing $|\epsilon|$, with again the asymmetry of enhanced emission for negative values of ϵ'. Interestingly, for negative ϵ', a higher ϵ" leads to less intensity, while for positive ϵ' a higher ϵ" leads to a very slight increase in intensity. Finally, in Figure 3.13(c), we show the angle of maximum emission θ_{max} as a function of ϵ' and ϵ" (note the reduced scale for the angles). The behavior of smaller emission angles for small values of $|\epsilon|$ close to 0 and increasing angles for increasing $|\epsilon|$ is confirmed. We notice that similarly to the trend in intensity, θ_{max} is larger for negative ϵ' than for positive values.

4

Quantifying coherent and incoherent cathodoluminescence in semiconductors and metals

In this chapter we present a method to separate coherent and incoherent contributions to cathodoluminescence from bulk materials using angle-resolved cathodoluminescence spectroscopy. Using 5 and 30 keV electrons we measure the cathodoluminescence spectra for Si, GaAs, Al, Ag, Au, and Cu. We then determine the angular emission distributions for Al, GaAs, and Si. Aluminium shows a clear dipolar radiation profile due to coherent transition radiation, while GaAs shows incoherent luminescence characterized by a Lambertian angular distribution. Silicon shows both transition radiation and incoherent radiation. From the angular data we determine the ratio between the two processes and decompose their spectra. This method provides a powerful way to separate different radiative cathodoluminescence processes, which is useful for material characterization and in studies of electron-matter and light-matter interactions in metals and semiconductors.

4.1 Introduction

Cathodoluminescence (CL), the radiation excited by a ray of fast electrons, was first studied during the development of cathode tubes [80, 91]. More detailed stud-

ies proliferated after the development of scanning electron microscopes (SEMs), first with a focus on mineralogy and petrology to identify geological samples by examining mineral-specific luminescence [172, 173], later encompassing materials science in general [106, 107, 174]. One can study (band gap) luminescence and other electron transitions across a broad range of energies [108, 175, 176]. The luminescent properties can be used to examine often inaccessible details such as variations in the local composition, local dopant concentration, stress and strain, interfaces, and non-radiative recombination centers such as point or extended defects [111–114]. One can also create and excite such defect states using electron irradiation to study their nature and behavior [116, 117, 177, 178]. Cathodoluminescence studies of nanoscale structures are on the increase as well [109, 110, 179, 180].

In the last decade, CL has gained attention among the nanophotonics community, mostly centered on studies of plasmonic systems, although studies on dielectrics are proliferating. Measuring with a nanoscale excitation probe, especially when combining spectral and angular data, turns CL into a very powerful tool. Optical antennas [26, 101, 102, 130, 181–184], plasmonic nano-cavities [185, 186], waveguides [187–189], and periodic crystals [124, 135, 136] among others have been examined to study their dispersion, radiation profiles, and spatial modal distributions.

A high energy electron beam can generate radiation in a material through a multitude of processes, which can be separated into coherent and incoherent groups [92]. Coherent radiation, so-called because the emitted radiation has a fixed phase relation with the electric field of the incident electron, comprises transition radiation (TR) at the surface, generation of plasmons, and Cherenkov radiation (when applicable). These processes can be used to probe the electromagnetic behavior of nanoscale objects with great precision, but are often quite weak. In metals, TR and plasmon generation are usually the dominant processes. Incoherent radiation such as luminescence generated by electron-hole recombination in semiconductors is usually much stronger and does not interfere with coherent radiation.

CL measurements for material science have generally consisted of spectral measurements, which are very powerful in determining characteristic optical resonances and transitions for a given material. If different radiative mechanisms are at play, however, it is often not possible to separate them. Here, we present the use of angle-resolved CL spectroscopy to separate fundamental CL processes by their characteristic angular emission distributions. We investigate coherent TR and incoherent luminescence that each have very distinctive emission patterns, allowing us to discriminate between them and characterize them separately. We study Al, Ag, Au, and Cu that show strong TR as well as GaAs which shows strong incoherent luminescence. We then focus on partitioning TR and incoherent emission in Si, where we find that both mechanisms strongly contribute to the CL radiation.

4.2 Experiment

We performed measurements on polished p-type (B doping level 10^{15} – 10^{16} cm^{-3}) and n-type (P doping level 10^{15} cm^{-3}) single-crystal Si ⟨100⟩ wafers. No significant differences were found in CL measurements for these two sample types. A single-crystal wafer of Czochralski-grown Al was used to study TR and to characterize the system response of our setup. Thermal evaporation was used to grow layers of Au, Ag, and Cu on a silicon substrate. We used evaporation rates of 0.5 Å/s at a chamber pressure of $\sim 10^{-6}$ mbar. In each case the metal layers are at least 200 nm thick, such that they are optically thick. Finally, a single-crystal slab of GaAs was used as a model for a strongly incoherent emitting material. The dielectric functions of the metal films were measured using variable-angle spectroscopic ellipsometry and compared to values from Palik [190] or Johnson & Christy [191].

The experiments are all performed at room temperature in our Angle-Resolved Cathodoluminescence Imaging Spectroscopy (ARCIS) setup [128]. This consists of a FEI XL-30 SFEG scanning electron microscope (SEM) in which we place an aluminium paraboloid mirror that can be precisely positioned with a piezoelectric micromanipulation stage. We use the focused electron beam to generate radiation in our samples; the mirror collects the emission and directs it out of the microscope to an optical detection system. For spectroscopy measurements we focus the light onto a fiber connected to a spectrometer with a liquid-nitrogen-cooled Si CCD photo-detector. Alternatively, we can image the parallel beam emanating from the paraboloid mirror onto a 2D Si CCD camera, which allows us to determine the angular emission profiles of the emitted radiation [128]. In this case each emission direction from the sample will hit the mirror at a specific location and be directed onto a specific point of the CCD camera. The 2D image is then transformed into a far-field angular radiation pattern. For the angular measurements we use color filters to select certain free-space wavelength ranges (40 nm bandwidth filters, from $\lambda_0 = 400 - 900$ nm in 50 nm steps).

The spectral measurements on the single-crystal Al, evaporated Au, Ag, and Cu were performed at a beam energy of 30 keV and a current of approximately 15 nA. The integration time varied between 0.5 and 4 s. Measurements on single-crystal Si were performed at 5 and 30 keV, with the same nominal current. Data from GaAs was collected at 30 keV, but since the band gap luminescence is extremely bright, we used a much lower current of roughly 0.15 nA. CL count rates were linear with beam current in all cases. We subtract the dark spectrum measured with the electron beam blanked to correct the spectral data, which accounts for thermal and readout noise of the detector. During the measurement we scan the beam over a 200×200 nm square area, in 20 nm steps. A spectrum is measured for each pixel and the data is then averaged. We find that measurements taken on different locations on the samples are very consistent. The correction to account for the spectral sensitivity of the system is described further on. For angular measurements, the same currents and energies were used as for the spectral measurements, while the integration times were 60 s for Al and Si, and 1 s for GaAs. For the angular data

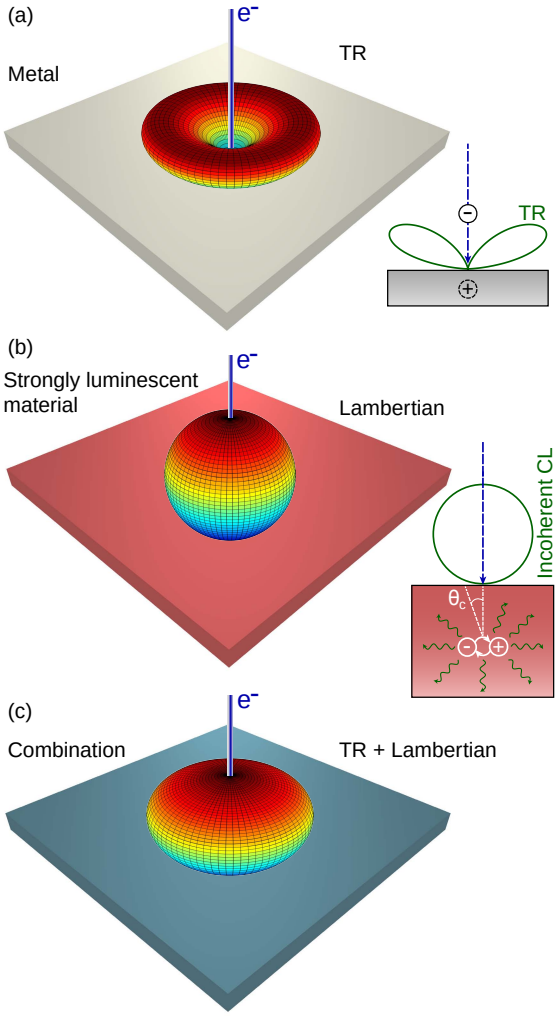

Figure 4.1 – (a) Schematic angular emission profile for electron-beam induced radiation from a metal, in which TR is dominant. The cartoon on the right sketches this process, where the electron creates an image charge in the metal, giving rise to a vertical dipole at the surface which emits radiation with a toroidal angular shape. (b) Schematic angular emission profile for incoherent luminescence generated inside the material with a Lambertian emission profile. The cartoon on the right shows electron-hole recombination emitting light isotropically, only light emitted within the critical angle escapes from the sample. (c) Schematic emission profile for a combination of TR and luminescence, which is the case for Si. The profile is an average of those from (a) and (b).

we took 2-3 measurements for each filter wavelength in order to average them and each measurement is corrected with a dark measurement.

4.3 Results and discussion

A beam of highly energetic electrons can transfer its energy to a material or structure in different ways, leading to a variety of radiative and non-radiative processes. Figure 4.1 provides an overview of radiation processes one commonly encounters in most materials. The typical behavior of metals is shown in (a), where coherent processes such as TR and generation of surface plasmons polaritons (SPPs) are dominant [92, 99]. Due to fast non-radiative recombination of the free electrons, the beam does not tend to excite incoherent luminescence in metals. SPPs can be excited efficiently on a flat surface, but as they cannot radiate to the far field for an unstructured planar surface, the only contribution to measured radiation is from TR, which has a toroidal emission pattern similar to that of a vertical point dipole at the surface as shown in Figure 4.1(a) [92, 99, 128]. The cartoon on the right shows a simplified visualization of this process: the negatively charged electron induces a positive mirror charge in the metal that disappears when the electron transits the interface. The corresponding varying dipole moment then leads to radiation into the far field with an angular emission profile very similar to that of a radiating point dipole placed just above the metal surface. For dielectrics TR generation occurs as well, a polarization charge replacing the image charge, with the dielectric constant determining the magnitude [92].

In the case of many semiconductors and dielectrics, incoherent luminescence is the main source of radiation as it is usually orders of magnitude stronger than coherent emission such as TR. A schematic of such a luminescent material is shown in Figure 4.1(b). The energetic electron can excite a material to a range of excited states over a very broad spectral range. The impact excitation cross sections for these transitions are higher than many optical excitation cross sections [107]. Because of the high incident energy and the formation of an electron cascade, a single incident electron can lead to multiple material excitations. Creation of an electron-hole pair by an incident electron typically requires a few times the energy of the band gap [120, 121], so excitations in the visible and infrared can be generated by both the primary and secondary electrons. The low-energy secondary electrons and decelerated incident electrons have higher excitation cross sections than the primary electrons, as their localized fields can couple more strongly to such excitations than the more delocalized fields of fast electrons [92]. As this kind of CL radiation is caused by spontaneous emission, it is not coherent with the electric field of the incident electron and will not interfere with radiation that is coherent such as TR. The emission is usually due to the radiative recombination of electron-hole pairs and excitons which can recombine to the ground state or to intermediate excited defect states, which then decay to the ground state through radiative or non-radiative pathways. Incoherent emission typically occurs isotropically inside

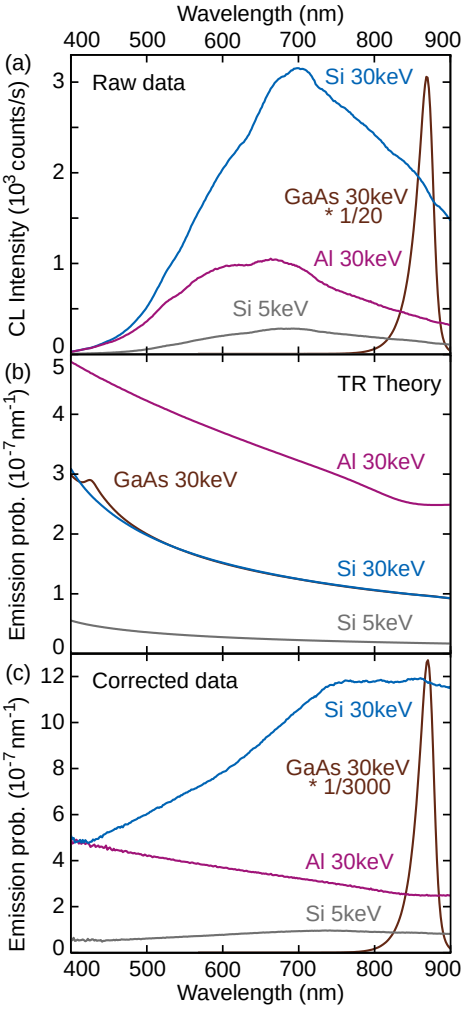

Figure 4.2 – (a) Measured cathodoluminescence spectra from bulk samples of single crystalline Al, GaAs, and Si. Data was taken at 30 keV; for silicon also at 5 keV. The beam current for Al and Si was 15 nA, for GaAs 0.15 nA. The GaAs spectrum is divided by a factor of 20. (b) Calculated TR emission probability as a function of wavelength for Al, GaAs, and Si. (c) The spectra of Al, GaAs, and Si corrected by the system response using the TR data for Al as a reference. In this case the GaAs spectrum is divided by a factor of 3000.

a material. The resulting CL emission distribution exiting the material is Lambertian, with a cosine dependence on the zenithal angle, as shown in Figure 4.1(b). The cosine dependence occurs due to the refraction of light and follows directly

from Snell's law [118]. The cartoon in Figure 4.1(b) illustrates these processes and also indicates the critical angle beyond which radiation is fully reflected into the substrate. Figure 4.1(c) shows a schematic of the emission pattern determined by a combination of TR and Lambertian profiles. Next, we present the experimental spectra and angular emission profiles for each of the three cases described here. We use Al as a TR emitter, GaAs as a strong incoherent emitter and Si representing both effects.

Figure 4.2(a) shows the CL spectra from bulk crystals of Al, GaAs, and Si at 30 keV. Data for Si at 5 keV is also shown. We observe that the Al and Si spectra show similar, broadband spectral shapes while the GaAs spectrum is much sharper and peaks at about λ_0 = 870 nm, corresponding to the band gap energy (~1.43 eV, or ~867 nm, at 300 K).

Figure 4.2(b) shows the calculated TR spectra for the same three materials, where the TR intensity is expressed in units of photon emission probability per incoming electron per unit bandwidth. The calculation is based on the theoretical formalism described in section IV.C of Ref. [92]. In this approach Maxwell's equations are solved for a swift electron interacting with a material, more specifically the case of an electron normally incident on a planar substrate. The moving charge induces surface charges and currents that lead to a reflected electromagnetic field at the surface that is the source of TR. The emitted TR is angle and wavelength dependent, so one can obtain angular intensity distributions and determine the total spectrum by performing the angular integral over the upper hemisphere. The variables that are of importance for the wavelength and amplitude dependence of TR are the electron energy, beam current and material permittivity. The electron energy affects the TR amplitude because the electric field of a higher energy electron extends further from its trajectory. As a result, a larger volume of material is polarized, inducing more surface currents and increasing the TR response. The TR intensity is given by an emission probability per electron, so the signal increases linearly with the number of electrons. In this way the beam current only affects the amplitude and does so in constant fashion for all wavelengths leading to a fixed factor difference in the spectrum.

As far as the wavelength dependence is concerned, TR is an interface effect based on the reflection of induced fields, so the equations contain information about light dispersion in both media, in a way similar to that of the Fresnel equations. Since in our case one medium is vacuum, the material permittivity of the sample determines the wavelength dependence of TR. Spectral features can be correlated with features in the permittivity. We use optical constants measured by ellipsometry for Al and an average of tabulated values for Si and GaAs. The inset in Figure 4.3 compares the real and imaginary part of the permittivity of Al that we measured by ellipsometry with values from Palik [190]. The trends are similar, but the absolute values of both real and imaginary parts of the permittivity differ; we attribute this to differences between the density and crystallinity of our single crystal compared to samples used by Palik. We can see that the calculated spectra for all three materials follow the same trends as their dielectric function. The TR spectra

of GaAs and Si are quite similar, in agreement with the similar permittivity. We also note that using a lower electron energy leads to a lower TR emission probability for Si.

As the CL signal from Al is purely due to TR, we now use it to calibrate our setup and determine the (relative) system response due to the spectral sensitivity of the setup. This will allow us to normalize the other experimental spectra. We obtain this system response by dividing the theoretical TR spectrum by the measured spectrum from the single crystal Al. We can then multiply the other measured spectra by this correction factor to obtain the emission probabilities for the other materials.

Figure 4.2(c) shows the corrected CL spectra for Al, GaAs, and Si. Clearly, the corrected Si spectrum at 30 keV does not correspond to the theoretical TR spectrum in Figure 4.2(b) at all, as the spectral shape is quite different and the intensities are 2 – 12 times higher than the TR spectrum. At 5 keV, the corrected spectrum for Si also exceeds the TR spectrum. It is clear that the Si spectrum cannot be explained as being only due to TR and since Si is a semiconductor, incoherent radiative processes must play a role even if non-radiative recombination is dominant. We do not expect Cherenkov radiation to play a role even though the refractive index is high enough to satisfy the emission condition, because it is emitted in the forward direction downwards into the substrate where it is fully absorbed.

In Figure 4.3, we examine the CL spectra of Au, Ag, and Cu, for which we expect the spectrum to be dominated by TR. The measured spectra are corrected using TR data from Al in the same way as above. Theoretical TR spectra of Au, Ag, and Cu are also shown as comparison. Several trends can be observed. First of all,

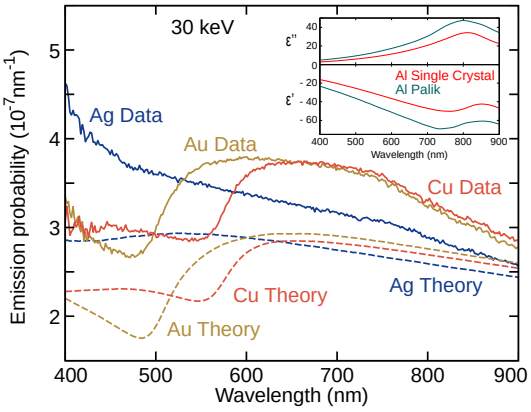

Figure 4.3 – Cathodoluminescence spectra of evaporated Au, Ag, and Cu that have been corrected for the system response (solid curves), compared to the calculated TR spectra (dashed curves), for an electron energy of 30 keV. The inset shows the real and imaginary part of the permittivity of Al measured using ellipsometry together with values from Palik [190].

the experimental TR spectra for Au, Ag, and Cu have quite similar intensities, with clear kinks in the spectra for Au and Cu at λ_0 = 500 and 550 nm respectively. The theoretical spectra show similar trends, the kinks for Au and Cu occur at the same wavelengths as for the experimental spectra. The absolute emission probabilities do not agree well between experiment and theory; they differ by up to ~30 %. We attribute this to variations between measurement sessions of the beam current, as explained in the description of Figure 4.2(b), as well as changes in the system alignment that affect the collection efficiency and thus the intensity. Repeated measurements with the same sample and measurement conditions have shown one can indeed obtain up to ~30 % variations in intensity. Because all of the data is normalized to the intensity of Al, differences in current compared to that of the reference measurement will lead to an offset factor in the spectrum. In this case the current was higher for the measurements than for the reference, so the experimental spectra are a factor higher than the theoretical values. These results show that overall, the experimental data well represent the theoretical spectral features.

Next, we study the angular emission profiles for Al, GaAs, and Si at 30 keV. We find that the radiation profiles are azimuthally symmetric and average the data over an azimuthal range to obtain the polar profiles shown in Figure 4.4. Averaging was done over the azimuthal angle ranges φ = 60 – 120° and φ = 240 – 300°, where φ = 0/360° is the center of the mirror's open end and φ = 180° corresponds to the apex at the back of the mirror. We use these ranges to avoid the open end of the mirror and the apex which contains more aberrations. To further decrease the noise for Al and Si we average the data obtained from the two angular ranges. All angular distributions are normalized to 1; no data is collected in the angular range $\theta = \pm 5°$, corresponding to the hole in the parabolic mirror. The angular resolution is affected by the curvature of the mirror which modifies the solid angle of the emitted radiation compared to its distribution on the CCD camera. As described in Ref. [128] (Fig 2.c), the solid angle per pixel varies between 2–10 $\times 10^{-5}$ sr.

Figure 4.4(a) shows angular profiles for Al (at λ_0 = 400 nm) and GaAs (at λ_0 = 850 nm) together with theoretical curves for TR (Al) and a Lambertian emitter (GaAs). For Al, the measured and calculated data agree very well, with the experimental one being slightly broader, proving the emission from Al is well described by TR. The emission pattern from GaAs corresponds well to the Lambertian profile, confirming that CL from GaAs at the band gap energy is dominated by incoherent luminescence.

Figures 4.4(b–d) show the experimental angular profiles for Si at 30 keV, measured at λ_0 = 400, 550, and 900 nm, respectively. Clearly, at λ_0 = 400 nm the emission pattern is more TR-like while it becomes more Lambertian-like and thus dominated by luminescence for the longer wavelengths. The angular emission from GaAs displays a similar trend (see Figure 4.6 of the Supporting information).

For the case of incoherent luminescence it is important to keep in mind that carrier transport can play a role in determining the emission properties. Diffusion as well as photon recycling can lead to recombination well outside the area of initial generation by the electron beam. Additionally, carrier transport can be anisotropic,

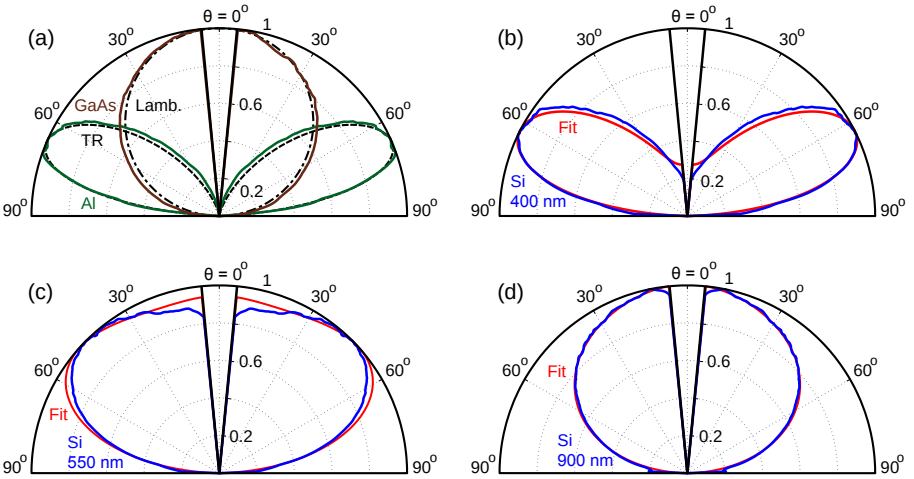

Figure 4.4 – (a) Measured normalized emission patterns as a function of polar angle θ for Al and GaAs (solid lines, measured at 400 and 850 nm, respectively). The theoretical TR pattern for Al and a Lambertian pattern for GaAs are also shown (dashed lines). (b–d) Measured emission patterns of Si at 30 keV for 400, 550, and 900 nm (blue lines) shown together with fits consisting of a combination of Lambertian and TR patterns (red lines). All measurements shown here were performed with a 30 keV electron energy and the resulting data is azimuthally averaged.

further impacting the distribution of recombination and thus affecting the resulting spatial and angular CL profiles [125]. In our case there is very good agreement with the Lambertian profile, so we expect that these effects play a minor role.

To determine the relative contributions of the two processes and separate them, we model the emission pattern as a linear combination of TR and Lambertian profiles for the given wavelengths, with the relative contributions as fit parameters in a least squares fitting routine. The fitted angular profiles are shown in red in Figures 4.4(b–d) and agree well with the measured data. Next, we extend this analysis to the full 400 – 900 nm spectral range in steps of 50 nm, both for 30 and 5 keV electron energies. The relative contributions of TR and incoherent radiation are then determined from the fits for each wavelength; the result is shown in Figure 4.5(a). TR dominates at shorter wavelengths, while incoherent emission dominates at longer wavelengths. Similar trends are observed for 5 and 30 keV. The transition in dominance between the two radiative mechanisms is due to a combination of effects. TR has an increased intensity at shorter wavelengths as one can see from the calculation in Figure 4.2(b), while luminescence which is emitted inside the material will be absorbed much more strongly for short wavelengths than for long wavelengths, so more “red” luminescence will escape the Si. GaAs exhibits similar behavior, but with stronger relative contributions for both processes at ei-

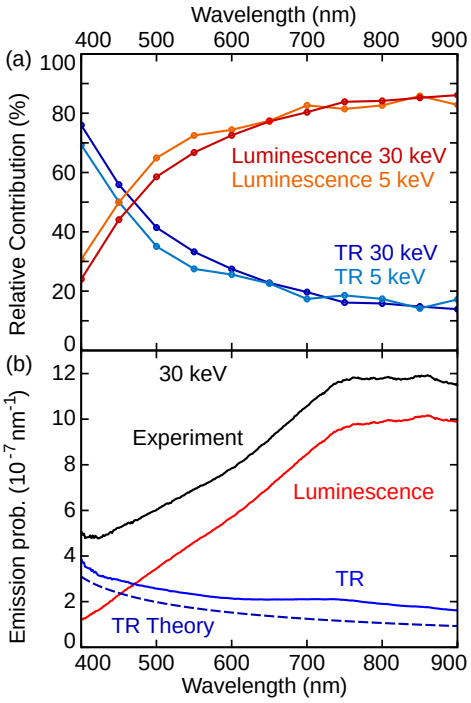

Figure 4.5 – (a) Relative contributions of TR and luminescence derived from fits to the Si emission patterns as in Figure 4.4, both for 5 and 30 keV electron energy (circles). The drawn lines are a guide to the eye. (b) The CL spectrum from Figure 4.2(c) (black) together with TR (blue) and incoherent luminescence (red) contributions for Si at 30 keV derived using the fractions from (a). The theoretical TR spectrum for Si at 30 keV is shown as well (blue dashed line).

ther end of the spectral range, as we demonstrate in Figure 4.7 of the Supporting information.

Now that we have determined the relative contributions of these two radiative processes in Si, we can use this information to decompose the TR and incoherent luminescence spectra. We fit a smooth curve through the data points in Figure 4.5(a) and use this to partition the experimental spectrum for Si at 30 keV from Figure 4.2(c). The total spectrum for Si at 30 keV as well as the separated TR and incoherent contributions are shown in Figure 4.5(b). Comparing the experimentally determined TR contribution with the calculation, the overall behavior as a function of wavelength is well reproduced, while the absolute intensities differ by a factor ~1.5 which we attribute to a difference in beam current, as was discussed earlier.

Figure 4.5(b) shows that the incoherent Si spectrum is spectrally broad, peaks for $\lambda_0 > 750$ nm and extends above the TR spectrum for $\lambda_0 > 470$ nm. We attribute this incoherent spectrum to transitions between defect states in the direct

band gap. Since n-type and p-type samples gave similar results, doping-related luminescence is insignificant. We note that light emission is strongly absorbed in Si, especially in the blue, so the collected spectrum does not directly reflect the emitted incoherent spectrum. Correcting for this effect the relative contribution emitted in the blue spectral range is larger than what is observed in the measured spectrum.

Our data can be compared with experiments at 200 keV performed by Yamamoto et. al. [192] at 200 keV in which the CL spectrum from Si closely follows the calculated TR spectrum, with no discernible incoherent radiation. This is due to the fact that the TR intensity is ~6 times stronger at 200 keV than at 30 keV. Moreover, at 200 keV the penetration depth of the electrons is much larger than at 30 keV (up to ~200 μm versus ~10 μm, as determined using Casino) [193]. Since the incoherent radiation is generated more efficiently as the electrons have decelerated deeper inside the material, it will be strongly absorbed inside the Si for higher electron energies.

4.4 Conclusions

We demonstrated a method to distinguish coherent and incoherent cathodoluminescence processes induced by a beam of fast electrons. We have shown that Al exhibits coherent transition radiation, while GaAs exhibits mainly incoherent band gap luminescence. Si cathodoluminescence is composed of both transition radiation and incoherent radiation. We distinguish the two processes by their characteristic angular profiles, namely dipolar-like lobes for transition radiation and a Lambertian angular distribution for incoherent luminescence. For silicon at 5 and 30 keV, transition radiation dominates around λ_0 = 400 nm, making up ~70 % of the signal while incoherent luminescence becomes increasingly stronger for longer wavelengths, consisting of ~85 % of the signal at λ_0 = 900 nm. Determining the relative strengths of these two effects allows us to decompose the experimental Si cathodoluminescence spectrum to retrieve the spectrum due to transition radiation, which agrees with calculations and the spectrum due to luminescence, which is very broadband.

Using angle-resolved cathodoluminescence to identify, separate and characterize different coherent and incoherent radiative processes is a powerful way to quantify such different forms of radiation in a multitude of materials such as metals and semiconductors. The technique is quite flexible in separating different radiative mechanisms, so long as one measures processes that do not interfere with each other (or do so in a way that can easily be deconvoluted) and have differing angular distributions. The use of antennas, (nano)structured surfaces or non-planar surfaces can all modify the coherent or incoherent distributions, but often in ways that are predictable by calculation or simulation. One can then use the modified angular patterns to separate the processes. For example, a luminescent sample with a hemispherical surface will not display a Lambertian but a hemispherical

angular distribution due to incoherent luminescence. Alternatively, one could separate the coherent emission of an antenna from the luminescence of the substrate. The presented results are relevant for material characterization and for studies of electron-matter and light-matter interaction in general.

4.5 Supporting information

Transition radiation (TR) occurs for electrons impinging on any material, so long as there is a contrast in the permittivity ϵ. Examining the calculated TR emission probability in Figure 4.2(b), we note that the theoretical spectra for Si and GaAs are very similar. It is thus to be expected that GaAs exhibits TR in a similar way to Si. Angle-resolved measurements on GaAs for an electron energy of 30 keV indeed display the characteristic dipolar angular emission distribution of TR, as shown in

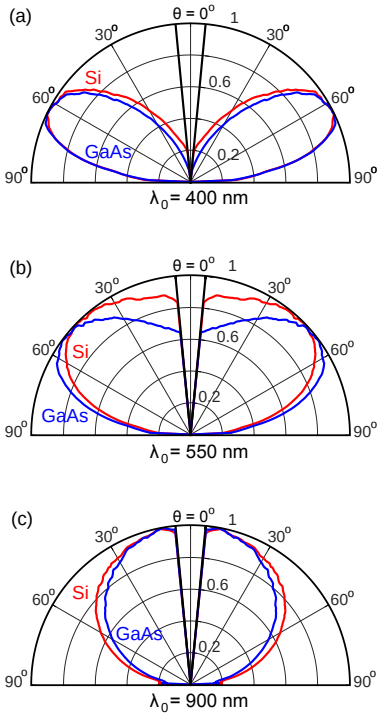

Figure 4.6 – Measured normalized emission patterns as a function of polar angle θ for GaAs (blue lines) and Si (red lines), for wavelengths of 400 (a), 550 (b), and 900 nm (c). Measurements were performed with a 30 keV electron energy and the data is azimuthally averaged. The black lines close to θ=0 denote the angles for which we do not collect any emission with the mirror.

Figure 4.6. Here we compare the normalized emission intensity of GaAs and Si, averaging over the same azimuthal range used for Figure 4.4 ($\varphi = 60 - 120°$ and $\varphi = 240 - 300°$). The two materials follow similar emission trends, being dominated by TR at short wavelengths ($\lambda_0 = 400$ nm in Figure 4.6(a)) and by luminescence at long wavelengths ($\lambda_0 = 900$ nm in Figure 4.6(c)), with a transition in between ($\lambda_0 = 550$ nm in Figure 4.6(b)). We notice, however, that GaAs exhibits stronger extremes for both short and long wavelengths. The angular emission distribution is more dipolar in shape than for Si at both $\lambda_0 = 400$ nm and $\lambda_0 = 550$ nm, while it is more rounded and Lambertian than for Si at $\lambda_0 = 900$ nm.

This difference between the two materials can be viewed more explicitly in Figure 4.7, which shows the relative contribution of TR and luminescence to the total angular emission distribution, determined from fits as described for Figures 4.4 and 4.5. We observe that GaAs has a ~15 % higher relative contribution from TR than Si, for wavelengths up to $\lambda_0 = 700$ nm, after which GaAs has a higher contribution from luminescence instead. These differences can explained quite intuitively. The strong dominance of the Lambertian angular profiles at these longer wavelengths is to be expected, since this matches with the spectral range of the band gap emission peak (see Figures 4.2(a,c)). In this range GaAs emits luminescence that is much more intense than TR by several orders of magnitude, whereas for Si the difference in intensity is much smaller. The luminescence of Si is quite broadband, however, contributing over the entire visible spectral range studied here. In contrast, the luminescence from GaAs is much more spectrally confined to the band gap wavelength, so at shorter wavelengths there is less competition for TR and it will play a relatively stronger role.

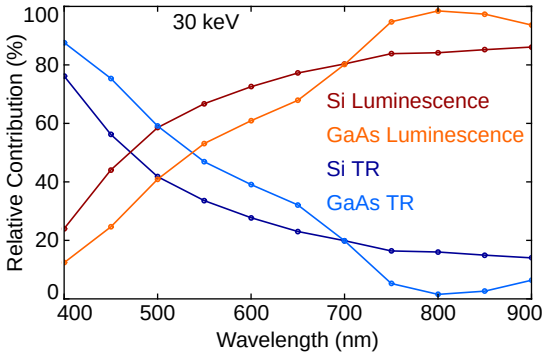

Figure 4.7 – Relative contributions of TR and luminescence as a function of wavelength, derived from fits to the GaAs and Si emission patterns as in Figures 4.4 and 4.6 (circles). The drawn lines are a guide to the eye.

5

Angle-resolved cathodoluminescence imaging polarimetry

Cathodoluminescence spectroscopy (CL) allows characterizing light emission in bulk and nanostructured materials and is a key tool in fields ranging from materials science to nanophotonics. Previously, CL measurements focused on the spectral content and angular distribution of emission, while the polarization was not fully determined. In this chapter we demonstrate a technique to access the full polarization state of the cathodoluminescence emission: the Stokes parameters as a function of the emission angle. Using this technique, we measure the emission of metallic bullseye and spiral nanostructures, showing that handedness as well as nanoscale changes in excitation position induce large changes in polarization ellipticity and helicity. Furthermore, by exploiting the ability of polarimetry to distinguish polarized from unpolarized light, we quantify the contributions of different types of coherent and incoherent radiation to the emission of a gold surface, silicon and gallium arsenide bulk semiconductors. This technique paves the way for in-depth analysis of the emission mechanisms of nanostructured devices as well as macroscopic media.

5.1 Introduction

Among many recent developments in microscopy, optical electron-beam spectroscopy techniques such as cathodoluminescence imaging (CL) have emerged as powerful probes to characterize materials and nanophotonic structures and devices. In one mode of operation of CL, one collects light emitted in response to a beam of energetic electrons ($0.1 - 30$ keV), for example in a scanning electron microscope (SEM). The time-varying evanescent electric field around the electron beam interacts with polarizable matter creating coherent emission, such as surface plasmon polaritons (SPPs) and transition radiation (TR) [92, 139, 194]. The spot size of the focused electron beam and the extent of the evanescent field about the electron trajectory define the interaction resolution to be ~30 nm. A broadband excitation results from the interaction time (approximately 1 fs) set by the high velocity of each electron as a result of its high energy. Aside from coherent emission, incoherent emission can also be generated by both the primary beam and slower secondary electrons, which excite electronic transitions in matter [92, 107]. The relative importance of the coherent and incoherent contributions provides information about the material composition and electronic structure.

Spectral analysis of the cathodoluminescence as a function of the electron beam position allows the local characterization of the structure and defects of semiconductors [108, 113, 116], the functioning of nanophotonic devices [179], and the mapping of optical resonances in plasmonic and metamaterial structures [185]. Recently developed techniques for angle-resolved detection of CL enable the identification of the band structure and Bloch modes of photonic crystals [124, 135, 136, 194, 195], the dispersion of surface plasmons [139, 156], and the directivity and Purcell enhancement of plasmonic nano-antennas [183, 196].

Besides frequency and linear momentum, the vectorial nature of light provides a third degree of freedom rich in information about the physics of light generation and scattering, encoded in the polarization of emitted light. In materials characterization, for instance, polarization provides direct access to the local orientation of emission centers and anisotropies in the host material. In nanophotonics, polarization plays a fundamental role (together with directionality) in determining the interaction between emitters and nanostructures. Furthermore, it is increasingly recognized that mapping and controlling the polarization of light is key to harnessing the wide range of opportunities offered by metamaterials and metasurfaces. Recent breakthroughs in chirality-enhanced antennas [197], photonic topological insulators [198], and the photonic equivalent of the spin-Hall effect [199–202], indicate the emerging importance of mapping the full polarization properties of nanophotonic structures. Polarization measurements of CL emission, however, have been limited to fully polarized emission and in particular to linearly polarized signals [102, 129].

In this chapter we introduce a novel technique to access full polarization information in cathodoluminescence spectroscopy. Based on a polarization analysis method previously demonstrated in optical microscopes [203–206], we integrate

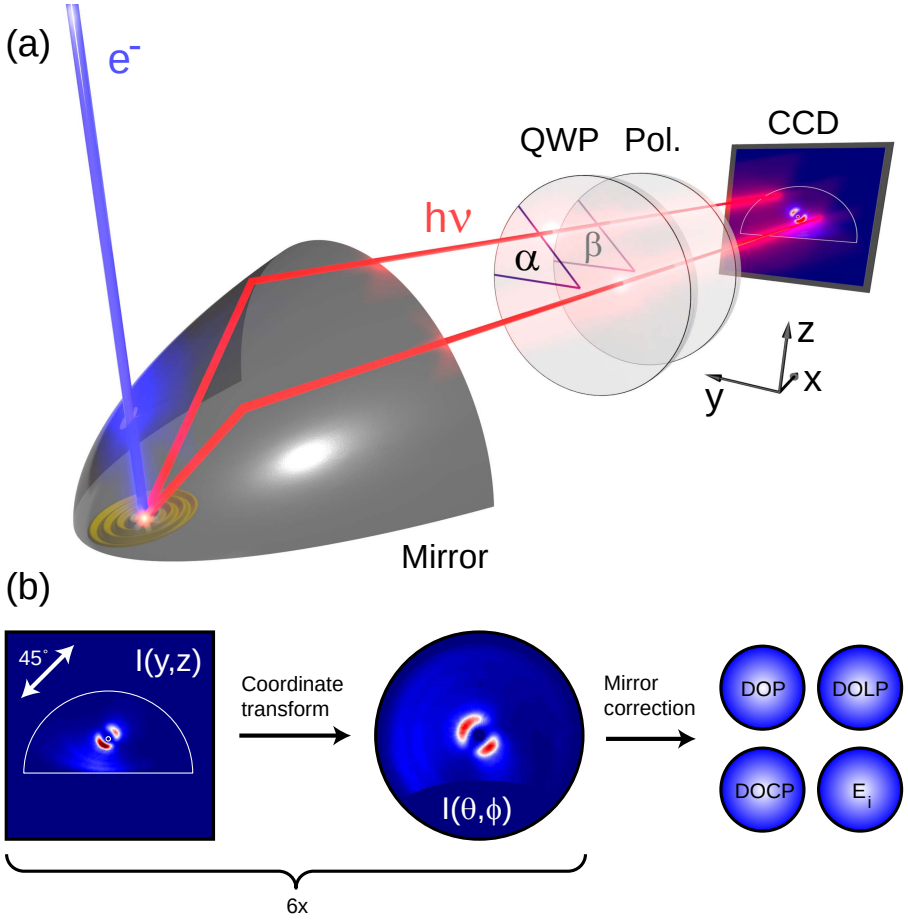

Figure 5.1 – (a) Schematic overview of the cathodoluminescence polarimetry setup. The structure is excited by the electron beam after which the resulting light emission is collected by a parabolic mirror. The light is directed towards a polarimeter composed of a QWP and linear polarizer set at angles α and β respectively. The filtered beam profile is measured by the CCD camera. The CCD image shows data corresponding to a measurement on a bullseye structure with $\alpha = \beta = 45°$. For reference we also show the coordinate system that is used throughout the manuscript. (b) Six measurements with different settings of the polarimeter are required to retrieve the full angle-resolved polarization state of the collected light. In addition to transforming from Cartesian (y, z) coordinates in the detection plane to polar coordinates (zenithal angle θ, azimuthal angle φ) in the emission plane, we corrected for the effect of the mirror on the polarization. Using the retrieved Stokes parameters it is possible to determine any figure of merit for polarization including the total (DOP), linear ($DOLP$) and circular ($DOCP$) degrees of polarization, as well as the electric field components $|E_i|$.

a rotating-plate polarimeter in the detection path of the angle-resolved CL setup. Using the Mueller matrix formalism for the light collection system, we determine the Stokes parameters for CL emission, that is, all parameters required to completely describe the polarization state of the light, which can be polarized, partially polarized or totally unpolarized. We demonstrate the great potential of this new measurement technique by analyzing the angle-resolved polarization state of directional plasmonic bullseye and spiral antennas. Furthermore, exploiting the unique capabilities of CL excitation, we measured the emission from metals and semiconductors. For these materials, we can separate coherent and incoherent emission mechanisms, with further applications in nanoscale materials science.

5.2 CL polarimetry

In our measurements, the 30 keV electron beam from a scanning electron microscope (SEM) excites the sample. An aluminum paraboloid mirror collects and redirects the resulting CL emission out of the SEM. The outcoming beam is focused onto a fiber-coupled spectrometer or projected onto a 2D CCD array [124, 128, 183], as shown in Figure 5.1(a). The wave-vector distribution of the CL emission can be retrieved from the CCD image, as every transverse point in the beam corresponds to a unique emission angle, in a procedure analogous to other Fourier imaging techniques [27, 207–211].

Measuring polarization for all emission angles of CL presents several challenges. First, it requires determining the relative phase difference between field components, a task not achievable with only linear polarizers as in Ref. [129]. Second, the paraboloid mirror performs a non-trivial transformation on the signal as it propagates from the sample to the detector plane. The shape of the mirror introduces a rotation of the vector components of light due to the coordinate transformation and, consequently, a change in the main polarization axes. In addition, the angle and polarization-dependent Fresnel coefficients of the mirror modify the polarization of the light upon reflection [133, 134]. As a function of the angle of incidence, the mirror partially polarizes unpolarized light and transforms linearly to elliptically polarized light in the detection plane.

To address these challenges, we included a rotating-plate polarimeter in the beam path of our CL system, composed of a quarter-wave plate (QWP) and a linear polarizer [131, 212, 213]. Figure 5.1(a) shows the polarizing elements in a schematic of the setup. Depending on their orientation, these two elements act either as a linear polarizer or as a right- or left-handed circular polarizer. As schematically shown in Figure 5.1(b), we measure the intensities I_j transmitted by six different settings of the polarimeter (horizontal, vertical, 45°, 135°, right- and left-handed circular) in order to determine the Stokes parameters of the light:

$$\begin{aligned} S_0 &= I_H + I_V \\ S_1 &= I_H - I_V \\ S_2 &= I_{45} - I_{135} \\ S_3 &= I_{RHC} - I_{LHC}. \end{aligned} \tag{5.1}$$

These four parameters are the most general representation of polarization and can be used to retrieve any polarization-related quantity [131]. The raw polarization-filtered CCD images are projected onto $[\theta,\varphi]$-space as indicated in Figure 5.1(b) using a ray-tracing analysis of the mirror, after which the Stokes parameters in the detection plane are determined. To transform these to Stokes parameters in the sample plane, we determine the Mueller matrix of the light collection system that accounts for the effects of the mirror on the polarization. In addition to the geometrical transformation, the analysis takes into account the Fresnel coefficients of the mirror for *s*- and *p*- polarized light. As a results of the 3D shape of the mirror, each element of the Mueller matrix is a function of the emission angle, i.e., there is a Mueller matrix for each emission angle. The Supporting information describes in more detail how the Mueller matrix was calculated. To benchmark these calculations, we use fully polarized transition radiation (TR) which occurs whenever an electron traverses an interface between two dielectric media. The electron locally polarizes the material close to the interface, giving rise to a well-defined broadband vertically-oriented point-dipole-like source [92, 128, 129], which is perfectly suited to calibrate our CL polarimeter (see Figure 5.6).

The Stokes parameters in the sample plane allow determining *any* figure of merit for polarization. Given that both incoherent and coherent radiation may be generated in CL, the degree of polarization (DOP), and the degrees of linear ($DOLP$) and circular polarization ($DOCP$) will be especially relevant. Defined as the ratios of polarized, linearly or circularly polarized light to total intensity, they are given by $DOP = \sqrt{S_1^2 + S_2^2 + S_3^2}/S_0$, $DOLP = \sqrt{S_1^2 + S_2^2}/S_0$ and $DOCP = S_3/S_0$. Equivalently, the ratio of unpolarized light to total intensity is given by $1 - DOP$ so a DOP smaller than 1 corresponds to partially polarized light.

5.3 CL polarimetry on plasmonic structures

To demonstrate the full potential of angle-resolved CL polarimetry we investigate the emission of a plasmonic bullseye structure with a pitch $d = 600$ nm, milled into a single-crystal gold substrate. Bullseyes are well-known for their ability to strongly direct light scattered by nanoscale apertures [214], generated by fluorescence [209, 215] or thermal emission [216]. Figure 5.2(a) shows a scanning electron micrograph of the structure indicating the excitation position. The electron beam launches a circular surface plasmon polariton (SPP) wave which radiates outwards

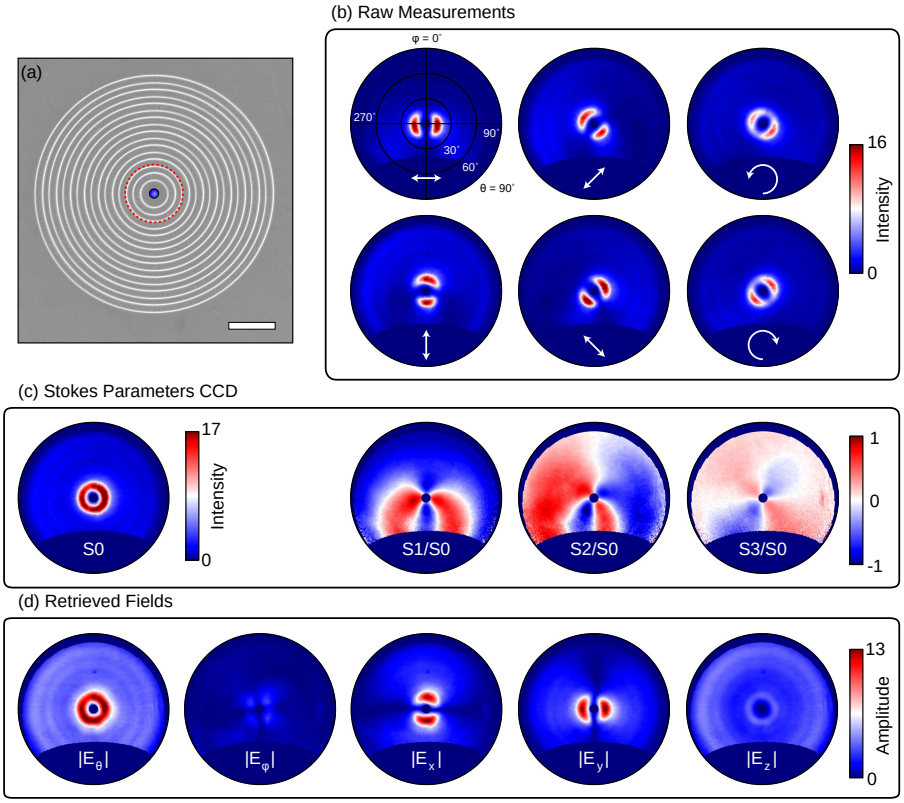

Figure 5.2 – (a) Scanning electron micrograph of a bullseye structure with d = 600 nm. The blue dot indicates the central electron beam excitation position. The red dashed circle indicates which part of the bullseye is shown in detail in Figure 5.3. The scale bar corresponds to 2 µm. (b) Polarization filtered angular CL patterns for different analyzer settings as indicated by the white arrows, measured at λ_0 = 750 nm. (c) Stokes parameters in the detection plane as a function of angle. The S_1, S_2, and S_3 patterns are normalized to S_0 to better show the overall polarization distribution. (d) Spherical and Cartesian absolute field amplitude distributions as a function of angle, retrieved from the experimental data in (b). In all figures, the intensities are given in $10^5 ADUsr^{-1}s^{-1}$ (analog-to-digital units, the equivalent of counts). Amplitudes are in units of $10^2\sqrt{ADUsr^{-1}s^{-1}}$.

and scatters coherently from the grooves of the bullseye. The scattered fields interfere to give rise to directional emission. In our measurements, the emission is spectrally filtered by a 40 nm bandwidth bandpass filter centered at λ_0 = 750 nm (see Figure 5.5 in the Supporting information for full spatial and spectral mapping).

Figures 5.2(b–d) represent the main steps of our polarimetric analysis for CL. Figure 5.2(b) shows the angular intensity patterns measured for the six settings of the polarimeter (indicated by the arrows) after a coordinate transformation of

the raw intensity data. Figure 5.2(c) shows the Stokes parameters in the detection plane calculated using Eq. 5.1 from the patterns in Figure 5.2(b). The leftmost panel corresponds to the total intensity distribution, S_0. The bullseye emits in a narrow doughnut pattern without any azimuthal variations, consistent with the azimuthal symmetry of both excitation position and bullseye structure. The polar angle at which most of the CL is emitted, $\theta = 15°$, corresponds to the grating equation $\theta = \sin^{-1}(k_{SPP} - m2\pi/d)/k_0$. In this spectral regime, the grating order $m = 1$ is the only relevant order, $k_0 = 2\pi/\lambda_0$ and k_{SPP} is the SPP wave-vector, calculated using the optical constants for gold from spectroscopic ellipsometry. The other panels in Figure 5.2(c) show the Stokes parameters S_1, S_2, and S_3 in the detection plane (yz-plane in Figure 5.1) normalized to S_0, such that it is possible to see polarization features outside the areas of very bright emission.

Next, we transform the data collected by the detector to the polarization state of the emitted light in the sample plane, by multiplying the Stokes parameters at the detection plane with the mirror's inverse Mueller matrix. Among the quantities that the Stokes parameters allow retrieving, here we will focus on the electric field components. Figure 5.2(d) shows the reconstructed spherical field vector amplitudes $|E_\phi|$ and $|E_\theta|$ that constitute the natural s- and p- polarization basis relevant to map the far-field generated by a localized radiating object. The figure shows that the $|E_\theta|$ distribution is strong and azimuthally symmetric while $|E_\varphi|$ is close to zero. Therefore, the measured emission of the bullseye is a narrow doughnut beam with a fully linear, radial polarization. Radial polarization is expected for the bulls-eye radiation as SPPs scatter out while maintaining their p-polarized character at the grooves. Additionally, no tangential polarization is allowed for coherent radiation generated by an azimuthally symmetric excitation in an azimuthally symmetric structure.

The polarization can alternatively be cast into Cartesian components. Figure 5.2(d) shows the double-lobe patterns of $|E_x|$ and $|E_y|$, which are rotated 90° relative to each other. The $|E_z|$ component is azimuthally symmetric and shows several emission rings. The outer rings correspond to transition radiation (TR) from the excitation position, which is modulated to yield a fringe pattern due to interference with SPPs scattered off the bullseye grooves. This interference in the far field results from the fact that both TR and SPPs are coherent radiation excited by the same source (same electron) [92, 99]. Since the electric field must be transverse to the propagation direction, the $|E_z|$ component vanishes at near-normal angles and therefore the main SPP emission beam from the bullseye (the narrow ring) appears relatively weak in $|E_z|$. While the emission in the sample plane is completely linearly polarized, a nonzero circularly polarized signal is measured in the detection plane (S_3 in Figure 5.2(c)), which indicates the effect of the mirror and the importance of using the Mueller matrix analysis to correct for it.

We continue by exploring CL polarimetry in a geometry with a different symmetry by launching an off-center circular SPP wave on a bullseye structure. Figure 5.3 shows measurements for electron beam excitation in the center, halfway between the center and the edge, and at the edge of the central bullseye plateau, as indicated

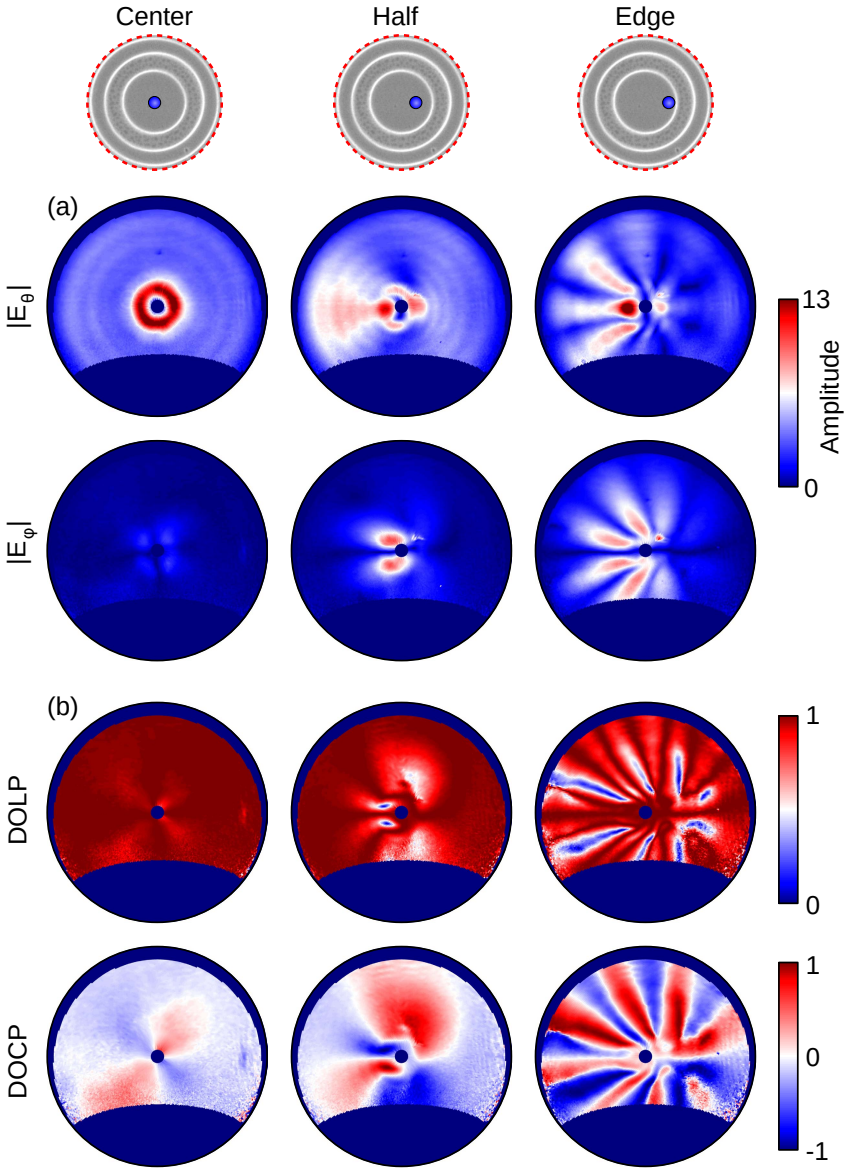

Figure 5.3 – (a) $|E_\theta|$ and $|E_\varphi|$ field amplitudes for central, halfway, and edge excitation on the bullseye plateau. The excitation positions are indicated as blue circles in the SEM micrographs on top, which show the area enclosed by the red dashed circle in Figure 5.2(a). (b) *DOLP* and *DOCP* of the bullseye emission as a function of emission angle for the same excitation positions as in (a).

in the SEM micrographs on top of the figure. Figure 5.3(a) shows $|E_\theta|$ and $|E_\varphi|$ for the three excitation positions. For off-center excitation, the zenithal field distribution $|E_\theta|$ is no longer symmetric, being stronger towards the left than towards the right of the image. This type of asymmetric beaming has also been observed in angular intensity measurements on asymmetric gratings [215], spirals [217], and asymmetrically excited (patch) antennas [102, 218]. Besides the asymmetry, the off-center excitation also leads to a non-zero azimuthal field contribution, $|E_\varphi|$, which is similar in strength to the zenithal field contribution. The excitation position and the center of the bullseye defines a mirror symmetry that expresses itself as a nodal line for $|E_\varphi|$ at $\varphi = 90°$ and $\varphi = 270°$. At far off-center excitation, the azimuthal and zenithal field distributions are very rich in structure and for certain angular ranges the emission becomes elliptically or circularly polarized.

The effect of off-center excitation is most clearly seen in Figure 5.3(b), which shows the degree of linear ($DOLP$) and circular ($DOCP$) polarization. Owing to the mirror symmetry of sample and excitation, the $DOCP$ remains close to zero along the axis of the electron beam displacement. Yet, away from this axis the emission becomes elliptical with opposite handedness on either side of the axis as dictated by mirror symmetry. For edge excitation, the complementary multi-lobe $|E_\theta|$ and $|E_\varphi|$ patterns lead to a rich behavior, where the emission transitions from fully linear to almost fully circular polarization several times. Rather than breaking symmetry by changing the excitation position, it is also possible to study scattering and emission by intrinsic asymmetry and handedness of structures. In Figure 5.7 of the Supporting information we show an extensive analysis of the emission of Archimedean spirals and demonstrate how CL polarimetry can be employed to study the conversion of structural chirality to handed scattering.

The data shown in this section proves that polarimetry analysis of CL, in combination with precise electron beam positioning, provides direct insight into the complex emission behavior of nanophotonic structures. Measuring directionality and polarization of the emission from emitters coupled to single nanostructures is of paramount importance when designing and testing the performance of structures like optical antennas, plasmonic resonators, and metasurfaces.

5.4 CL polarimetry applied to incoherent emitters

In addition to characterizing fully coherent radiation, CL polarimetry allows us to determine whether the measured radiation contains an unpolarized contribution such as in the case of incoherent luminescence from bulk or nanostructured materials. This is shown in Figure 5.4, where we compare azimuthally averaged zenithal cross cuts of the polarized ($S_0 \times DOP$) and unpolarized ($S_0 \times (1 - DOP)$) emission intensities for single-crystal, unpatterned Au, Si and GaAs and compare them to calculations.

The emission from Au is dominated by TR, which is fully coherent and polarized radiation. Figure 5.4(a) shows a measurement at $\lambda_0 = 850$ nm, which com-

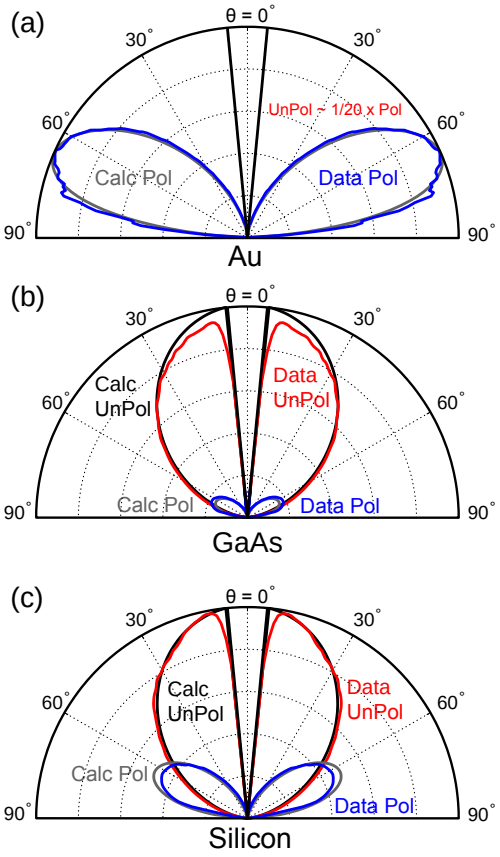

Figure 5.4 – Zenithal cross cuts comparing unpolarized and polarized emission for bulk single crystals of Au at λ_0 = 850 nm (a), GaAs at λ_0 = 850 nm (b) and Si at λ_0 = 650 nm (c). In all cases we compare the unpolarized (red) and polarized (blue) emission from measurements to the unpolarized (black) and polarized (gray) emission determined from calculations. The data is obtained by averaging over an azimuthal range φ = 270° – 90° to improve signal-to-noise ratio, and we scale the angular distributions by the overall emission intensity. For Au, the unpolarized emission component is so small that it is not visible in the plot.

pletely overlaps with a calculated TR emission distribution (see also Figure 5.6 in the Supporting information). In the case of GaAs in Figure 5.4(b), the emission is dominated by very bright incoherent radiative band gap recombination measured at λ_0 = 850 nm. This luminescence is fully isotropic and unpolarized *inside* the material, but large differences between *s*- and *p*- Fresnel transmission coefficients for the semiconductor-vacuum interface partially polarize the emission as seen in the data. Figure 5.4(b) shows that unpolarized light is indeed dominant. The weak polarized emission has a very different angular emission distribution, that agrees

very well with Fresnel calculations (see Figure 5.8 in the Supporting information). Lastly, Si is a material that displays such weak luminescence that it is comparable in intensity to TR [119]. Indeed, the polarized intensity for Si at λ_0 = 650 nm shown in Figure 5.4(c) constitutes ~32 % of the total emission, which is much more significant than for GaAs, although unpolarized emission remains the dominating contribution.

These examples show that angle-resolved polarimetry measurements provide quantitative and precise information about the origin of emission of different materials. This technique enables the separation of polarized and unpolarized emission, and therefore it can be used to determine the different mechanisms that simultaneously contribute to cathodoluminescence (see Figure 5.8 in the Supporting information for a quantitative analysis of TR). Moreover, for the polarized part of the emission we can map the electric field components and their relative phase. Since it does not require any prior knowledge of the sample (unlike the method described in Ref. [119]), this method is very general and can be applied to any (nanostructured) material.

5.5 Conclusions

We have demonstrated 'angle-resolved cathodoluminescence imaging polarimetry' as a new microscopy tool to map the vectorial electromagnetic scattering properties of nanostructured and bulk materials. We determine the complete polarization state of emitted light as a function of angle from six CL intensity measurements in the detection plane, in combination with a mathematical transformation that corrects for the polarizing effect of the CL mirror. As a result of the high resolution of the electron beam excitation, the wave-vector resolved polarization properties of locally excited plasmonic nano-antennas can be extracted with a spatial resolution for the excitation of 20 nm. The angle-resolved polarization measurements of the emission of bullseye and spiral nanoantennas demonstrate how structural symmetry and handedness translate into the helicity of emitted light. These results show that angle-resolved cathodoluminescence polarimetry can be extremely valuable for the development of metallic and dielectric antennas for spin-resolved and chiral spectroscopy as well as for the study of photon spin Hall effects.

Besides its relevance for nanophotonics, we demonstrate that our technique opens new perspectives for materials science not accessible with optical microscopes. Measuring the Stokes parameters generally enables the separation of incoherent and coherent CL generation, as we demonstrated for direct and indirect semiconductor materials. Our measurements on relatively simple samples of Au, GaAs and Si show the potential of the technique for the analysis of bulk materials which could be useful for many material inspection tasks. For optoeletronics, the nanoscale characterization of emission polarization from inorganic LEDs stacks, nanowires and quantum dots stands out in particular. The technique also intro-

duces the possibility of locally studying material anisotropy, birefringence and optical activity.

5.6 Methods

Sample fabrication. We fabricated bullseye and spiral structures by patterning a single-crystal Czochralski-grown Au ⟨100⟩ pellet which was mechanically polished to obtain a sub-10 nm RMS roughness. The patterning was done by using a 30 keV Ga^+ ion beam in a FEI Helios NanoLab dual beam system at 9.7 pA beam current and a dwell time of 10 µs per pixel. In the bullseye design the central plateau has a diameter of 1.2 µm (2 times the pitch, 600 nm) and the duty cycle of the circular grating consisting of 8 grooves is 50%. The spiral design is based on an Archimedean spiral where the first half period of the spiral is omitted. For the spiral we show data both for 600 and 440 nm pitches. Both for the spirals and the bullseyes the groove depth was ~110 nm. The measurements on silicon were performed on a polished p-type (boron doping level $10^{15}-10^{16}$ cm^{-3}) single-crystal ⟨100⟩ wafer. The measurements on GaAs were done on a polished single-crystal ⟨100⟩ wafer.

Measurements. The measurements were performed in a FEI XL-30 SFEG (30 keV electron beam, 30 nA current) equipped with a home-built CL system [124, 128, 183]. To obtain the polarization state of the emission, we perform a series of six measurement of the angular CL pattern using a 2D back-illuminated CCD array. Each measurement was taken with a different setting of the polarimeter, defined by a specific combination of QWP and polarizer angles. Handedness of circularly polarized light was defined from the point of the view of the source, following the IEEE standard. In this case, right-handed circularly polarized light rotates anticlockwise and left-handed circularly polarized light rotates clockwise. We use the known transition radiation pattern from an Au surface to calibrate the optical detection system. A 40 nm bandpass color filter spectrally selected the measured emission. For the bullseye and spiral measurements we used 30 s integration time, which is a good compromise between a small spatial drift of the electron beam and a good signal-to-noise in CL. For the TR emission from single-crystal gold and the measurements on silicon we used 120 s integration time since TR emission and luminescence are position independent and the measurement is not affected by spatial drift of the electron beam. For the measurements on GaAs we used a much lower current (0.9 nA) and integration time (1 s) due to the very bright band gap luminescence. For every setting of the polarimeter, we collected a dark reference measurement where we blank the electron beam (with the same integration time as the CL measurement), which was subtracted from the data in the post-processing stage. Possible sources of errors on the measurements include e-beam drift (in the case of position dependent samples), bleaching/contamination during measurements leading to a reduction in CL signal, fluctuations in current and mirror

alignment.

5.7 Supporting information

5.7.1 Spectral measurements on bullseye

To study the spectral response of the bullseye from Figure 5.2, we raster scan the electron beam over the central part of the structure in 15 nm steps, and collect a CL spectrum for every pixel using a visible/NIR fiber-coupled Czerny-Turner spectrometer [183]. The scan includes the central plateau, the first groove, and part of the first ridge. The spectra are corrected for the system response using the TR emission of the unstructured gold substrate [99]. We then radially average the spectrum to obtain a map showing emitted intensity as a function of wavelength and radius, taking into account the proper Jacobian so we can directly compare the intensities (shown in Figure 5.5(a)). Figure 5.5(b) shows individual spectra for specific radial distances as indicated in (a) by the white dashed lines.

We observe several features in the scan. On the plateau, the emission is quite broadband except for a strong dip in intensity around $\lambda_0 = 650$ nm. The CL intensity increases towards the edge of the plateau, then drops in the groove, and becomes bright on the first ridge again. The observed spectral features can be attributed to a mix of resonant and diffractive effects.

Because the groove is wide enough, it supports a zero-th order standing wave mode on the bottom of the groove around $\lambda_0 = 580$ nm, which is cut-off for longer wavelengths leading to a low intensity in the red [219, 220]. The dip at $\lambda_0 = 650$ nm can be attributed to an interesting experimental artifact related to the diffraction of SPPs. Consistent with the grating equation mentioned in the main text, the bullseye emits very close to the normal at this wavelength. Because the bullseye structure is highly directional, a major part of this diffracted beam is lost through the 600 µm hole in the mirror right above the sample. In fact, one could use this dip to find the wavelength and spatial position at which such a structure attains maximum directionality in the normal direction. In this case, the effect is strongest for the central positions in the bullseye because the beam is exactly normal to the sample as is visible in Figure 5.3(a) for $\lambda_0 = 750$ nm. Even though the dip is strongest in the center of the plateau, it is visible for every radial excitation position in this map (even within the groove), indicating that the extended bullseye geometry always causes a significant fraction of CL emission to be in the normal direction.

5.7.2 Calculation of the Mueller matrices

The Mueller matrix of an optical element accounts for the effect of the element on the polarization state of an incident field [131]. The Mueller matrices of a linear polarizer and a QWP are well-known for example. We use the Mueller formalism to relate the Stokes vector in the detection plane to the Stokes vector describing the

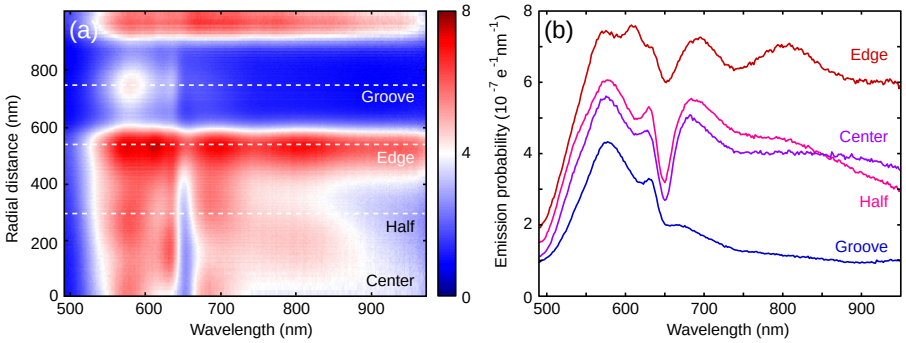

Figure 5.5 – (a) CL intensity as a function of wavelength and radial position from the center of the bullseye. The spectra are corrected for dark noise and the spectral response of the detection system. (b) CL spectra at selected radial positions corresponding to the center, halfway, and the edge of the bullseye plateau. We also show a spectrum for excitation in the center of the first groove. The positions are indicated by the white dashed lines in (a). Notice that the color bar in (a) and the vertical axis in (b) both correspond to emission probability.

sample emission polarization. The resulting Mueller matrix of the mirror contains both geometric and polarizing effects of the mirror in the emission polarization.

To retrieve the Mueller matrix of our light collection system, we calculate how the electric field components E_θ and E_φ in the emission plane transform to E_y and E_z in the detection plane [133, 134]. To that end we calculate how fully isotropic p-polarized and s-polarized emission is projected onto the detection plane by the parabolic mirror. We use the geometrical methods described in section 3 of Ref. [129] to account for the parabolic reflector and we use the full complex Fresnel reflection coefficients to accurately describe the light reflection on the mirror. These coefficients were calculated using tabulated optical constants [190] for the central frequency of the collection bandwidth. Since the reflection angle at the mirror is different for every wave-vector emanating from the sample, each element of the Mueller matrix is a function of the emission angle [133, 134]. Instead of calculating the Mueller matrix, one could also envision experimentally retrieving it. This requires a precisely controlled radial and azimuthal polarization source as standard. While transition radiation could serve as a fully radial source, a fully azimuthal source is not readily available.

The Mueller matrices can be used in two directions. Either one can invert measured data from the detector plane to sample coordinates, or in the opposite direction, one can predict how a given source will appear on the detector plane. For our analysis of TR emission in Figure 5.6, we apply Mueller matrices to theoretical TR emission to predict the measured data for each setting of the polarimeter. In this case, we combine the mirror Mueller matrix with the Mueller matrices of a linear polarizer and a QWP, which are a function of the selected analyzer angles α and β [213]. We note that for fully polarized sources this is analogous to the approach

in Ref. [129] where the Jones matrix of the polarizing element operates on the Jones electric field vector.

5.7.3 Polarimetry of transition radiation emission

Transition radiation (TR) emission occurs whenever an electron traverses an interface between two dielectric media. The electron locally polarizes the material close to the interface, giving rise to a well-defined broadband vertically-oriented point-dipole-like source [92, 128, 129]. This makes it a useful source to test our CL polarimetry technique. Here we perform polarimetry measurements on an unstructured part of the single-crystal Au substrate from which only TR emission is expected, using the same technique used for the bullseye. Figure 5.6(a) shows the TR data at $\lambda_0 = 850$ nm for every polarimeter setting. The top left panel includes the angular coordinate system for reference.

In addition to the TR measurements, we calculated the emission pattern for a z-oriented dipole on top of an Au substrate and its polarization components. The dipolar far-field for $\lambda_0 = 850$ nm was calculated from the asymptotic far-field expressions [221] using ellipsometry data for the optical constants of the gold substrate. We then calculate the expected filtered pattern using the appropriate Mueller matrices for the paraboloid mirror and the polarimeter components. Figure 5.6(b) shows the result of this calculation including the angular acceptance of the mirror, in order to allow a good comparison with the data. The excellent agreement of both angular distributions and relative intensities between data and calculation indicates that TR emission is indeed dipolar and that the mirror correction works well. The fringes in the data are an experimental artifact, probably due to interference between multiple reflections of the optical elements on the detector.

We can use the measurements from Figure 5.6(a) to determine the Stokes parameters in the detection plane of the CCD and then use the Mueller matrix formalism to correct for the effects of the mirror. This allows us to retrieve the Stokes parameters in the sample plane from which we can determine the different field amplitudes. Figure 5.6(c) shows the Stokes parameters in both the detection and sample planes, where S_1, S_2 and S_3 have been normalized by S_0 so that we can clearly observe the polarization distortions due to the mirror. In the detection plane the Stokes parameters display complex patterns that are very similar to those shown earlier for the bullseye in Figure 5.2(c), since both cases are dominated by purely radial polarization. In the sample plane the behavior of the Stokes parameters is much simpler, S_0 has barely changed and S_1 is close to 1 while S_2 and S_3 are very small. Again, TR is expected to be fully radially polarized, so there should be no diagonal (S_2) or circular (S_3) components. The striking difference between the Stokes parameters in the two planes underscores the importance of the Mueller matrix correction to provide accurate results.

Figure 5.6(d) shows the spherical and Cartesian field amplitudes that have been retrieved from the Stokes parameters in sample space. The fields nicely reveal

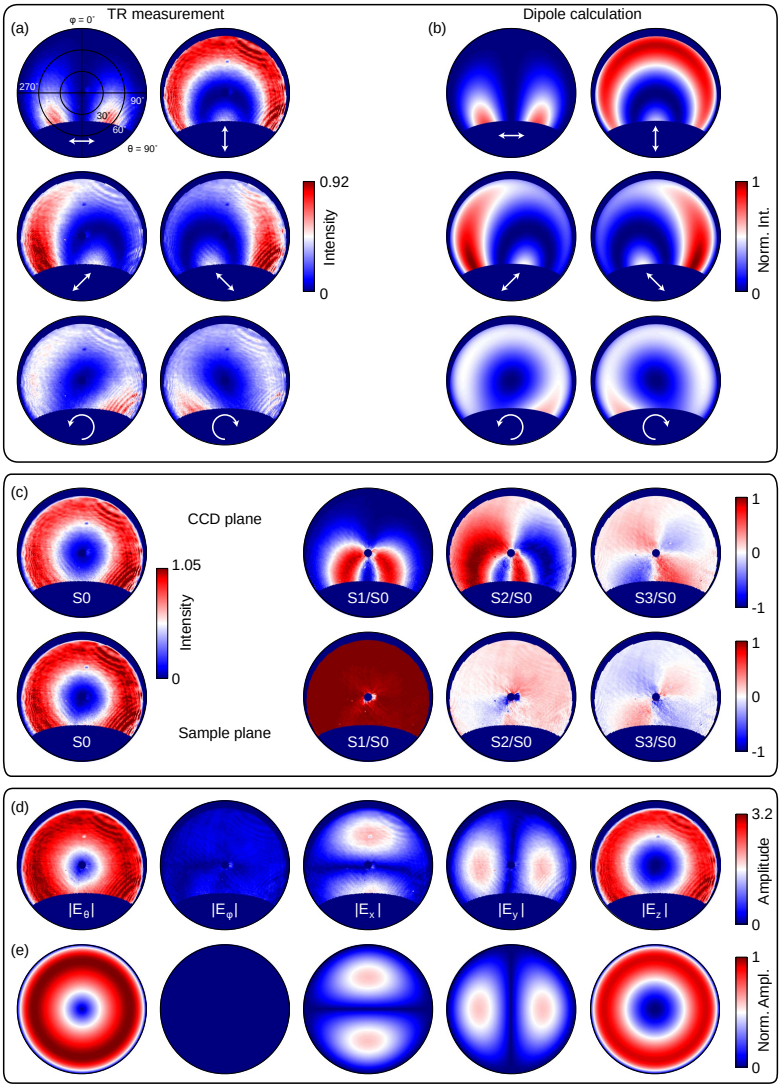

Figure 5.6 – (a) Polarization-filtered angular CL patterns of TR emission for a Au single crystal for different analyzer settings as indicated by the white arrows, measured at λ_0 = 850 nm. (b) Calculated polarization-filtered patterns for a vertically oriented point-dipole source on top of a gold substrate (at λ_0 = 850 nm). (c) Stokes parameters as a function of angle in the CCD plane as well as in the sample plane, after the mirror correction. The S_1, S_2, and S_3 patterns are normalized to S_0 to better show the overall polarization distribution. (d) Spherical and Cartesian field amplitude distributions as a function of angle, retrieved from the experimental data in (a). (e) Calculated field amplitudes for a vertical dipole.

the expected radially polarized nature of the emission. The amplitudes have been plotted using a single color scale to allow a quantitative comparison between the different components. Both the relative amplitudes and amplitude distributions match very well with the calculated dipolar fields shown in Figure 5.6(e). These results demonstrate that cathodoluminescence polarimetry can reliably be used as a quantitative tool for deducing the far-field polarization distribution of a nanoscale emitter.

5.7.4 Spirals

Rather than breaking symmetry by changing the position of excitation, breaking symmetry in scattering and emission by intrinsic asymmetry and handedness of structures is of large current interest. Handed plasmonic structures have been proposed in the study of (inverse) photon spin Hall effects and spin-orbit coupling, the enhancement of enantioselective spectroscopies, and the generation of nanoscale light sources of definite orbital and spin angular momentum inherited from the surrounding structure. We fabricated Archimedean spiral gratings with clockwise (CW) and anti-clockwise (ACW) orientation, shown in Figures 5.7(a,b), which enjoy a growing interest since it was shown that spirals can enhance the extraordinary transmission of single nanoapertures for particular helicities [222], and that spirals transfer polarization and orbital angular momentum to scattered photons [217, 223]. This can result in a polarization-dependent directional beaming [224] and demonstrates strong photon spin-orbit coupling effects [197].

We use CL polarimetry to study the effect of spiral asymmetry and handedness on the far-field polarization, again taking a pitch $d = 600$ nm and $\lambda_0 = 750$ nm. We excite the spirals in their origin as indicated in Figure 5.7. Figures 5.7(c,d) show the Cartesian components of the far-field emission of the spirals, which better reflect the handedness than the spherical fields. Since the groove pitch is the same for spirals and bullseyes, the angular spread of these patterns is similar, however they no longer have a minimum at the surface normal ($\theta = 0$) and the s-like shape in $|E_x|$ and $|E_y|$ clearly reflects the handedness of the spiral.

In contrast with bullseyes excited at their center, the spirals can induce ellipticity in the polarization of the light even when excited in their origin, as shown in Figures 5.7(e,f). This is particularly evident in the region of higher intensity in the vicinity of the normal, where the $DOCP$ is close to ± 1. Thereby, the spirals are highly directional sources of circularly polarized light. Mirrored spirals simply exhibit mirrored patterns (where the y-axis defines the mirror symmetry), conserving intensities and field strengths, while the sign of the $DOCP$ changes. This result indicates that swapping spiral handedness flips the helicity of the output field, in addition to mirroring the distribution of intensity over angle. For spirals with smaller pitch we find similar but even stronger effects of handedness, aided by the fact that their radiation pattern is more strongly off-normal (see Figures 5.7(g–l)). In that case the $|E_z|$ distribution is also clearly chiral.

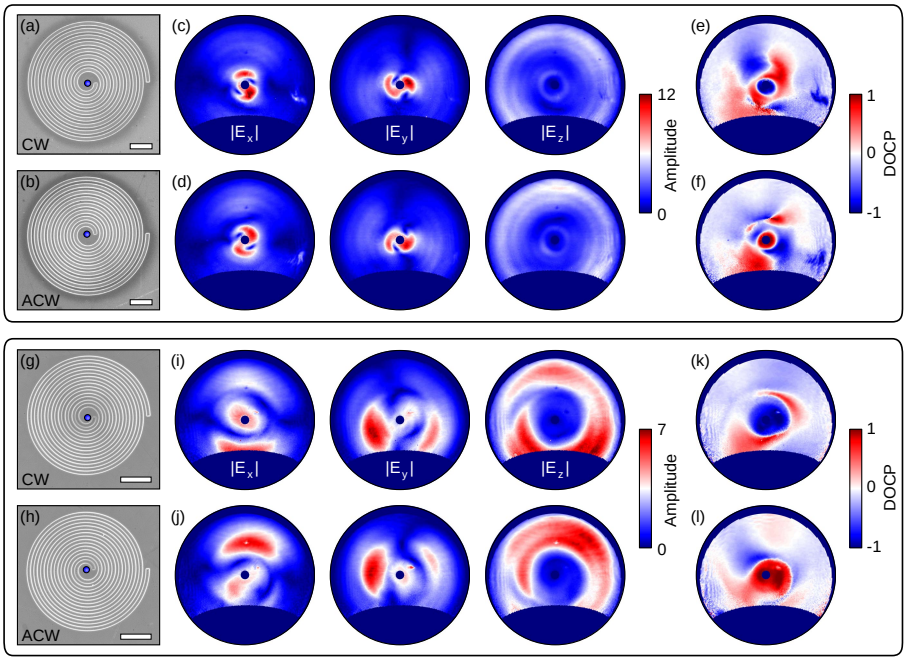

Figure 5.7 – Scanning electron micrographs of a clockwise (a) and anti-clockwise (b) Archimedean spiral grating with d = 600 nm. Amplitude distributions of the Cartesian fields for a CW spiral (c) and an ACW spiral (d). Degree of circular polarization ($DOCP$) for a CW spiral (e) and an ACW spiral (f). Scanning electron micrographs of a CW (g) and an ACW (h) spiral with d = 440 nm. Amplitude distributions of the Cartesian fields for a CW spiral (i) and an ACW spiral (j). Degree of circular polarization ($DOCP$) for a CW spiral (k) and an ACW spiral (l). All measurements were performed at λ_0 = 750 nm. For reference we again indicate the electron beam excitation position with a blue dot. Scale bars in the electron micrographs correspond to 2 µm.

5.7.5 Silicon and GaAs polarimetry

Calculating the contributions of TR, polarized and unpolarized luminescence to the total emission from Si or GaAs requires determining their angular profiles. An essential part of this process are the transmission coefficients T_p and T_s at the sample-vacuum interface, shown in Figure 5.8(a) for the case of Si at λ_0 = 650 nm. The large contrast between the two coefficients at angles above ~ 20° leads to more p-polarized light exiting the Si than s-polarized light, especially near the Brewster angle where the intensity contrast exceeds 4 (see Figure 5.8(a)). This difference in transmission coefficients results in a CL emission profile slightly different than the expected Lambertian cos(θ) profile (blue curve in Figure 5.8(b)). Although the polarizing effect of the interface does not noticeably affect the emission pattern of the total luminescence, the unpolarized luminescence (consisting of equal amounts of

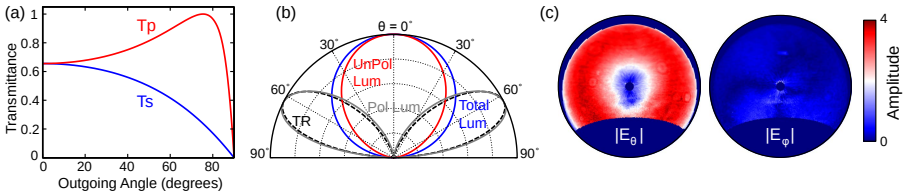

Figure 5.8 – (a) Transmission coefficients T_p and T_s at the sample-vacuum interface at $\lambda_0 = 650$ nm for Si, as a function of the internal angle of emission. (b) Calculated normalized angular emissions patterns of the different contributions to Si CL emission. The total luminescence profile (blue) as well as the unpolarized (red) and polarized (gray) luminescence contributions are shown together with the theoretical TR profile (black dashed line). (c) $|E_\theta|$ and $|E_\varphi|$ field amplitudes of the polarized emission from Si, in units of $10^2\sqrt{ADUsr^{-1}s^{-1}}$.

s- and *p*-polarized light) is markedly narrower. Accordingly, the polarized part of the luminescence is stronger at higher angles and, interestingly, it follows a very similar profile to that of TR for Si at $\lambda_0 = 650$ nm, which has been calculated using formulas derived in Ref. [92]. The same formulas are used to calculate the gray line describing TR from Au at $\lambda_0 = 850$ nm in Figure 5.4(a).

Once the theoretical profiles for the different emission processes are calculated, it is possible to determine their relative contributions to the total emission. The fraction of polarized and unpolarized luminescence is fully specified by the Fresnel equations. This provides enough information to compare calculations to data from GaAs with very good agreement, as that is fully dominated by luminescence. The case of Si is more complex as TR also plays a role, so the polarized emission is comprised of coherent TR as well as polarized luminescence. We determine the ratio of TR and luminescence by fitting the total intensity (S_0) to a linear combination of the two processes. Fresnel calculations predict the polarized and unpolarized contributions to the luminescence so that we can combine all three components. For both the calculations and the experiments we scale the angular distributions by the overall (integrated) emission intensity, and find good (absolute) agreement, as was shown in Figure 5.4(b). The polarized signal constitutes ~32 % of the total emission. More explicitly, we find that TR contributes ~21 % of the total CL intensity, so polarized luminescence contributes ~11 % and unpolarized luminescence ~68 %.

Both the TR and the polarized luminescence should be *p*-polarized, which we verify from the experimental data using the Mueller analysis to remove the unpolarized contribution and determine the radial and azimuthal field amplitudes from the polarized emission. This is shown for Si in Figure 5.8(c), where we indeed observe that almost all of the amplitude is in the $|E_\theta|$ component, i.e. for *p*-polarization. This demonstrates that we can separate the unpolarized and polarized emission even from mostly incoherently radiating semiconductors and still retrieve the correct electric fields for the polarized portion of the emission.

6

Azimuthally polarized cathodoluminescence from InP nanowires

In this chapter we determine the angle and polarization dependent emission from 1.75 μm and 2.50 μm long InP nanowires by using cathodoluminescence polarimetry. We excite the vertical wires using a 5 keV electron beam, and find that the 880 nm band gap emission shows azimuthally polarized rings, with the number of rings depending on the wire height. The data agree well with a model in which spontaneous emission from the wire emitted into the far field interferes with emission reflected off the substrate. The model indicates that the depth range from which the emission is generated is up to 400 nm below the top surface of the wires, well beyond the extent of the primary electron cloud. This enables a probe of the carrier diffusion length in the InP nanowires.

6.1 Introduction

The research field of semiconductor nanowires has grown tremendously in the last two decades, due to the applications in optoelectronic devices such as LEDs [225, 226], lasers [227], photovoltaics [50, 228], photodetectors [229] and more. The electrical properties of nanowires as well as their optical properties, such as the directionality and polarization of emitted radiation [229–234], can be tuned by controlling the morphology, size, crystallinity, composition, and inclusions or

junctions [235–239]. Among the nanowire materials, indium phosphide (InP) has a band gap well-suited for photovoltaic applications, long carrier lifetime and low surface recombination velocity [240].

The light emission properties of semiconductor nanowires have mostly been studied using optical excitation techniques, which are limited in spatial resolution and therefore cannot access all details of the nanoscale emission mechanisms. Cathodoluminescence (CL) spectroscopy is an alternative technique that uses an electron beam as an excitation source, providing high excitation resolution and accessing a broad range of material transitions and defects [111, 113, 179]. Spatially-resolved CL has shown that very thin (~20 nm diameter) InP nanowires exhibit polarized emission [187]. However, the angular distribution of the emitted light, which is crucial for many applications, was not resolved so far.

In this chapter, we characterize the angle- and polarization-dependent emission from InP nanowires by using angle-resolved cathodoluminescence imaging polarimetry [132]. Previous studies of the directionality and polarization of semiconductor nanowires have focused on wires with high-aspect-ratio dimensions, whose behavior is dominated by waveguide modes [230, 233, 234, 241]. In contrast, here we will examine low-aspect-ratio wires. We find that the angular emission from these short wires is dominated by azimuthally polarized rings that are not related to waveguide modes, and demonstrate that the emission and the number of rings are directly related to the wire height. The measurements are well-reproduced by a point dipole scattering and interference model and provide a measure for the carrier diffusion length in the wires.

6.2 Experiment

We measured undoped InP nanowires grown vertically on an InP ⟨100⟩ substrate by a combination of vapor-liquid-solid (VLS) and vapor-solid (VS) methods [234]. Wires with an initial length of 8 µm were mechanically broken, resulting in wires 1.75 ± 0.05 µm (NW1) and 2.50 ± 0.05 µm (NW2) in length. Figures 6.1(a,b) show SEM images for both nanowires, taken for a tilt angle of 55°. We note that both wires are tapered in shape due to the growth process of the base. NW1 and NW2 are 450 and 350 nm wide at the top, respectively, and are both 1.3 µm wide at the bottom of the base. This tapering will cause waveguide modes, which can play a role in short wires as well [242], to be ill-defined.

The spectra and polarization-resolved angular emission patterns of the wires were measured using angle-resolved cathodoluminescence imaging spectroscopy and polarimetry. The emission resulting from exciting the wires with an electron beam from an SEM (5 keV, beam current ~0.4 nA) is collected by an aluminium parabolic mirror and directed to an optical setup. We can measure either the spectrum using a liquid-nitrogen-cooled back-illuminated silicon CCD array (Princeton Instruments Spec-10 100B), or the angular emission profile using a Peltier-cooled back-illuminated 2D silicon CCD array (Princeton Instruments PIXIS 1024B) [128,

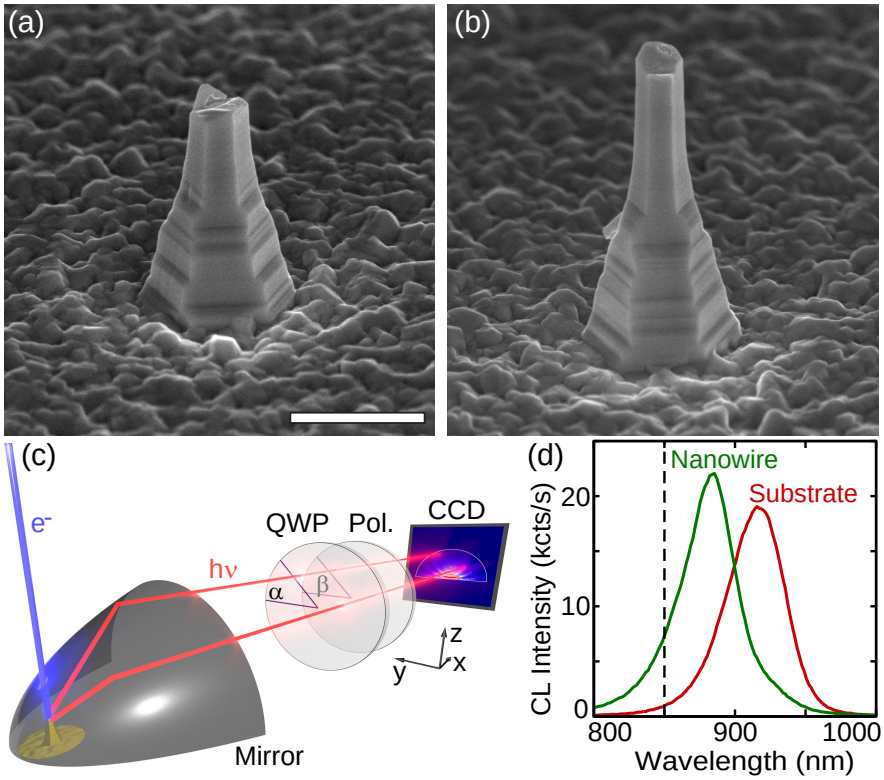

Figure 6.1 – Scanning electron micrographs of the InP nanowires NW1 (a) and NW2 (b), measured at a tilt angle of 55° (scale bar is 1 µm for horizontal dimensions and 1.2 µm for vertical dimensions). NW1 is 1.75 µm tall and 450 nm wide at the top; NW2 is 2.50 µm tall and 350 nm wide at the top; both wires are clearly tapered. (c) Schematic overview of the cathodoluminescence polarimetry setup. The electron beam excites the nanowires, the emitted radiation is collected by a parabolic mirror and sent through a quarter-wave plate (QWP) and linear polarizer. Bandpass filters can be used to select a certain wavelength range and the resulting beam profile is measured by the CCD camera. (d) Measured CL emission spectra of NW2 (green) and substrate (red). The spectrum of NW1 (not shown) does not differ noticeably from that of NW2. The black dashed line at $\lambda_0 = 850$ nm indicates the transmittance maximum of the 40 nm bandwidth bandpass filter used for the angular measurements.

183]. The angular imaging mode, shown schematically in Figure 6.1(c), includes a quarter-wave plate (QWP) and a linear polarizer (Pol.). These allow us to determine the Stokes parameters and therefore the polarization of the emitted radiation, including all electric field components [131]. To achieve this we measure the intensities transmitted by six different combinations of QWP and polarizer positions

(horizontal, vertical, 45°, 135°, right- and left-handed circular) and fully take into account the geometrical and polarization dependent effect of the parabolic mirror on the measured emission [132].

6.3 Results and discussion

The CL spectra of the InP nanowires peak at λ_0 = 880 nm, while the spectrum of the InP substrate is centered at λ_0 = 920 nm, as we show in Figure 6.1(d). This blueshift in the emission spectrum is due to a difference in crystal structure between the wires (mixed wurtzite–zinc blende) and the substrate (zinc blende) [234]. The spectral shape of the nanowire spectrum indicates that the signal from the substrate is minimal for this measurement. This is due to the relatively shallow penetration depth of the 5 keV electrons, as shown in Figure 6.2(a). The superimposed trajectories of 10^4 electrons hitting the center of a 350 nm diameter InP wire are displayed, which were calculated using the Monte Carlo based software Casino [122]. The full interaction volume covers the entire diameter of the wire and reaches a depth of ~250 nm, generating electron-hole pairs in this region until the electrons fully relax. The large majority of excitations will take place in the first 200 nm however, as shown by the dense region in Figure 6.2(a). The energy of the incident electrons decreases as they move further into the material, reducing the energy of the carriers that can be excited.

The angular emission patterns of the wires exhibit a series of rings, as we show in Figures 6.3(a–d), which display the measured angular emission patterns at λ_0 = 850 nm as a function of azimuthal (φ) and zenithal (θ) angles. The dark blue regions in the measurement correspond to the angles at which no light is collected by the mirror. Figure 6.3(a) shows the total intensity (I_{tot}) for NW1, while Figures 6.3(b,c) compare the intensity of the radially polarized field component (I_θ) to that of the azimuthally polarized field component (I_φ) for NW1. Figure 6.3(d) shows I_φ for NW2. These figures show that the emission is dominated by azimuthally polarized rings and that the taller NW2 exhibits more rings than NW1. The intensity trends are similar to those in previous work on the angular emission profiles of plasmonic nanoantennas, which, for a fixed wavelength, exhibit an increasing number of rings for increasing antenna height [243]. The polarization was not resolved in this case however.

In order to analyze the emission patterns, we model the spontaneous emission of the wires as an incoherent sum of point dipoles radiating in free space above a substrate, as shown schematically in Figure 6.2(b). We implement the Green's function formalism and asymptotic far field approximations from Ref. [221] as they are applied in Ref. [244]; the measured far field radiation results from a superposition of the emission of the dipole and its image. We calculate the far field radiation patterns for separate X, Y and Z oriented point dipoles at λ_0 = 850 nm (corresponding to the bandpass filter center wavelength) in vacuum, at a height h above an InP substrate and incoherently add the intensities for different field

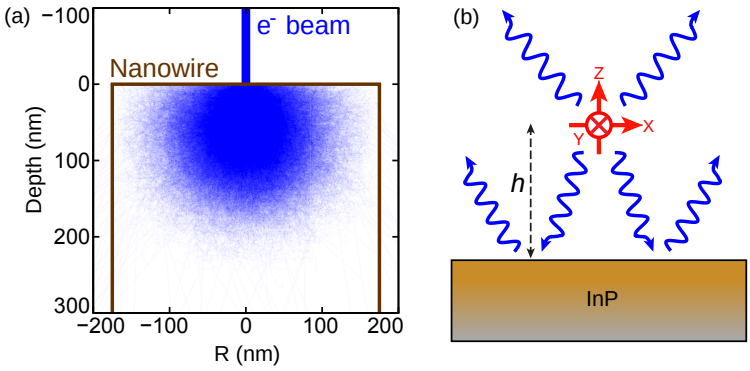

Figure 6.2 – (a) Monte Carlo simulation of 10^4 electrons with 5 keV energy impinging the middle of an InP nanowire, using Casino [122]. All the electron trajectories are shown as superimposed partially transparent lines forming a blue cloud, indicating the interaction density and volume of the primary electrons with the wire. (b) Schematic of the dipole calculation. Separate X, Y and Z oriented dipoles are placed in vacuum at a height h above an InP surface. The direct emission interferes with light reflected off the substrate and the calculation produces the resulting far field radiation patterns for all field components. The field intensities for the three orthogonal dipoles are incoherently added to simulate the behavior of randomly oriented dipoles.

components. We neglect the dielectric body of the nanowire itself, placing the dipoles in vacuum, in order to keep the model simple. We find this to be a valid approach as the emission only overlaps with the nanowire body for a small portion of angular space, namely downwards where it will be guided into the substrate and absorbed. We use equal dipole amplitudes for the three orientations. The angular patterns result from the interference between the directly emitted radiation and the reflection from the substrate, and are therefore sensitive to the dipole height. The overall behavior is dominated by the X and Y dipoles, which combine to produce a strong azimuthal intensity distribution, while the Z dipole has a minor effect. To reflect the electron excitation volume we have averaged the dipole positions over a range of heights, performing a calculation every 10 nm. Measurements and calculations agree best when using a height range of 350 nm, 65–415 nm below the top edge for both nanowires. The calculations accurately reproduce all major features of the measurements such as the number of rings, zenithal emission angles, relative intensities and polarization for both wires, as shown in Figures 6.3(e–h). We find that the averaged calculation is quite sensitive to the chosen height range: moving the range up or down will shift the zenithal position of the rings, while increasing the range will decrease the amplitude of the intensity oscillations. A change of 10 nm or more already results in a noticeably larger difference with the measurement.

Examining I_{tot} for NW1 (Figures 6.3(a,e)), we see in both measurement and

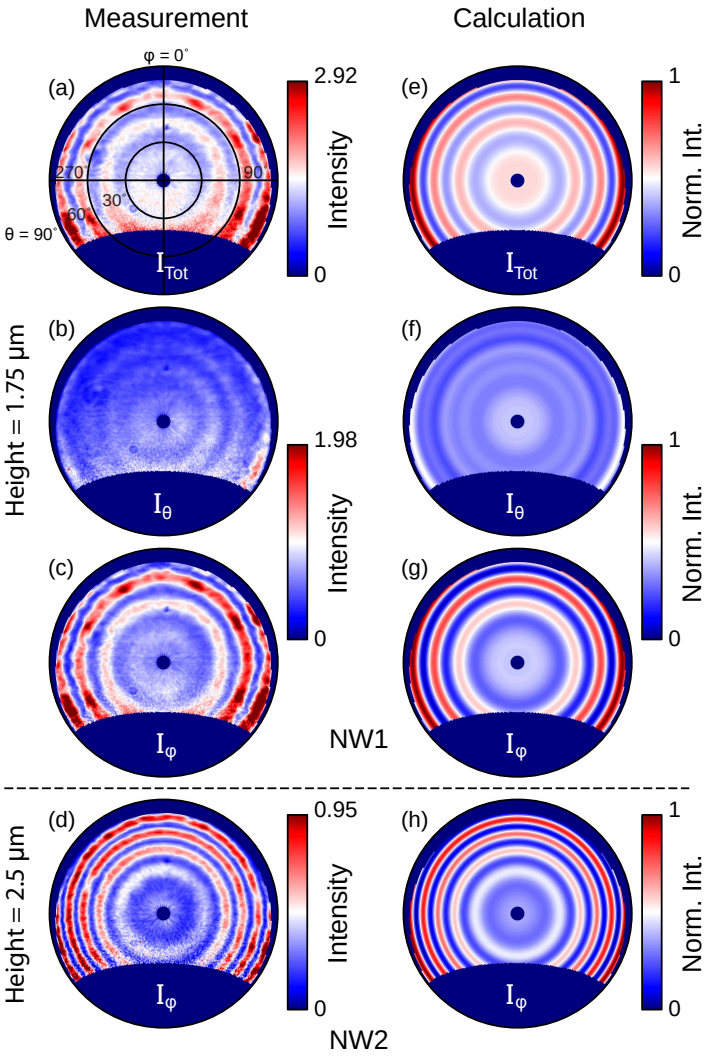

Figure 6.3 – Measured (a, b, c, d) and calculated (e, f, g, h) angular CL polarimetry emission intensities at λ_0 = 850 nm. The patterns were measured for central excitation of the nanowire, and the calculations averaged over a range of heights (65–415 nm below the surface, in steps of 10 nm, for both wires). (a) and (e) show the total intensity I_{tot}, (b) and (f) the radially polarized intensity I_θ, (c) and (g) the azimuthally polarized intensity I_φ, all for NW1. (d) and (h) show I_φ for NW2. The θ and φ polarized intensities for NW1 are shown on the same color scale. The calculations have been normalized to 1, while the measured intensities are given in 10^5 counts sr^{-1} s^{-1}.

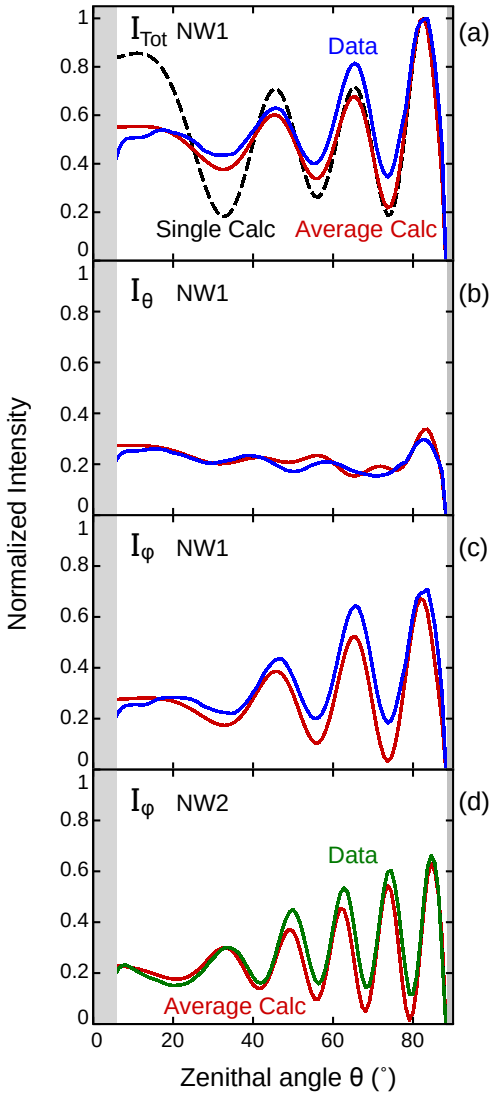

Figure 6.4 – Azimuthally averaged intensities from Figure 6.3, comparing the measurements (blue for NW1, green for NW2) to the averaged calculations (red). All measured and calculated intensities are normalized to their respective total intensity. (a), (b) and (c) show I_{tot}, I_θ and I_φ respectively for NW1, while (d) shows I_φ for NW2. In (a), the black dashed line indicates the calculation for a single height best matched to the measured data (1.52 µm). The gray areas represent the angular range not collected by the mirror.

calculation a region of higher intensity in the center and three rings of increasing intensity for increasing zenithal angle. For I_θ in NW1 (Figures 6.3(b,f)) the features are less pronounced but we notice a thin ring at the outer edge of both measurement and calculation. Figures 6.3(c,g) show the center disk and three rings of increasing intensity for I_φ, as for I_{tot}, confirming the total emission is dominated by the azimuthally polarized contribution. We note that the measured data for I_θ and I_φ are plotted with the same color scale. Finally, for I_φ in NW2 (Figures 6.3(d,h)) five rings are observed, two more than in NW1. In this case we also find good agreement of both zenithal emission angles and relative intensities between measurement and calculation. A full set of measured and calculated angular emission patterns for NW2 can be found in Figure 6.5 of the Supporting information.

To quantitatively compare the measurements and calculations, we azimuthally average the data from Figure 6.3 (taking into account only the angles that are collected by the mirror) and show the result in Figure 6.4. The measured and calculated intensities are normalized to their corresponding total intensity. In Figure 6.4(a) we also show the calculation for a single dipole height for NW1 that most closely reproduces the intensity oscillations. We observe that in the case of a single height, the oscillations at small values of θ have a much larger amplitude than in the data, while there is a very good match for the calculation that averages over a height range. The height range that best fits the data for both nanowires is larger than the extent of the primary electron cloud (~400 nm vs ~200 nm below the top edge of the wires). It is known that carrier diffusion and photon recycling can enlarge the volume of light emission [125]. Carrier diffusion lengths of 160 nm have been measured in doped InP nanowires [245], for our undoped wires a larger diffusion length, on the order of a few hundred nanometers, is expected. Rather than using a simple model in which the carrier generation and light emission is fixed over a depth range, one could take a depth profile of carrier diffusion and recombination in the wires into account. This will allow the CL polarimetry presented here to directly determine the carrier diffusion length. Due to the high sensitivity to height changes of our simple model, on the order of 10 nm, we expect that the diffusion length can be resolved with a similar precision. Measurements using a range of electron beam energies and thus penetration depths could be used to study the diffusion more accurately.

The features of I_θ in Figure 6.4(b) are much less pronounced than those of I_φ in Figure 6.4(c), but in both cases there is very good agreement of the oscillations and the relative intensities, which is also the case for I_φ for NW2 in Figure 6.4(d). A full set of averaged measurements and calculations for NW2 can be found in Figure 6.6 of the Supporting information. A similar background level is observed for both polarizations I_θ and I_φ, indicating that the emission also contains an unpolarized contribution.

6.4 Conclusions

In conclusion, we have demonstrated that InP nanowires, excited by a 5 keV electron beam at their top, display very distinctive angular emission rings that are strongly azimuthally polarized and dependent on wire height. The radiation is not dominated by the intrinsic angular emission of the nanowire itself, due to the tapering and low-aspect-ratio, but by interference of the luminescence with the substrate reflection. A dipolar interference model that calculates the interference between the directly emitted light and light reflected off the substrate reproduces the data well. The luminescence originates from a several hundred nanometer wide range near the top of the wire. The depth range is the same for both wires we studied and is larger than the primary electron cloud, providing a measure for carrier diffusion in the wires. The capability to resolve the spectral, angular and polarization properties of nanoscale excitation processes shows the power of cathodoluminescence polarimetry as a technique to study the highly tunable optical and electrical properties of semiconducting nanostructures with features much smaller than the optical diffraction limit.

6.5 Supporting information

A complete set of angular intensity distribution patterns for NW2 are shown in Figure 6.5, comparing measurements to calculations for I_{tot}, I_θ and I_φ. We find good agreement of both zenithal emission angles and relative intensities between measurement and calculation, just as for NW1. Note for instance the thin ring of high intensities at large angles for I_θ. Here the emission is dominated by azimuthally polarized rings as well, but with five rings instead of the three that are observed for NW1. The azimuthally averaged data from Figure 6.5 are shown in Figure 6.6, again comparing measurement to calculation for I_{tot}, I_θ and I_φ. Figure 6.6(a) shows both the calculation averaged over the height range discussed earlier as well as a calculation for a single dipole height that most closely reproduces the intensity oscillations. We find that for a single height, the oscillations at small values of θ have a much larger amplitude than in the data, while there is a good match for the calculation that averages over a height range. This agrees with the trend observed in Figure 6.4(a). There is also good correspondence of the relative intensities and angular oscillations for I_φ and I_θ, although there are some discrepancies for I_θ. Measurement errors can play a role here, as the intensity oscillations in this case are very weak, and thus difficult to resolve in detail. Overall there is good agreement in reproducing the experimental results with the simple dipole model.

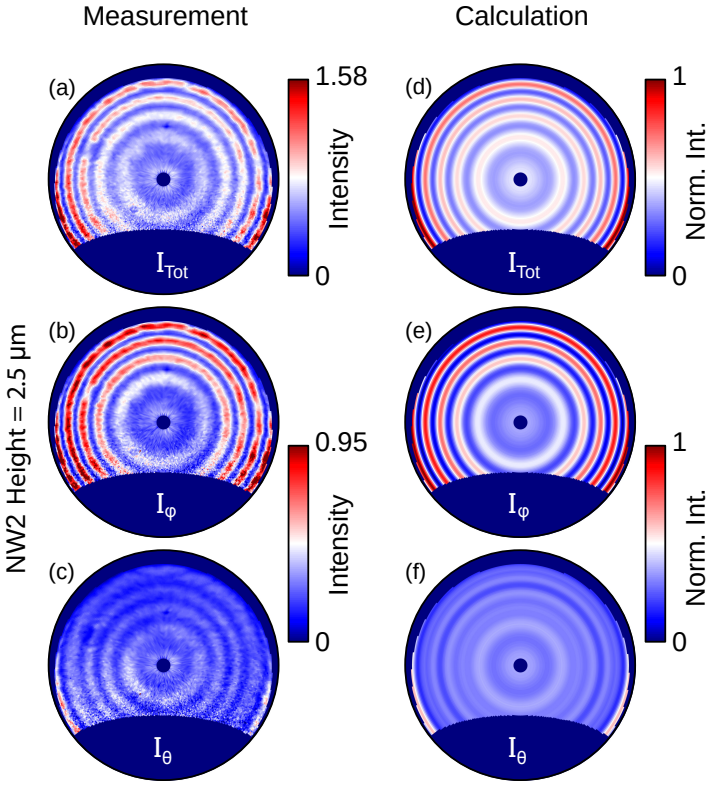

Figure 6.5 – Measured (a, b, c) and calculated (d, e, f) angular CL polarimetry emission intensities at λ_0 = 850 nm for NW2. The patterns were measured for central excitation of the nanowire, and the calculations averaged over a range of heights (65–415 nm below the surface, in steps of 10 nm, for both wires). (a) and (d) show the total intensity I_{tot}, (b) and (e) the azimuthally polarized intensity I_{φ}, (c) and (f) the radially polarized intensity I_{θ}. The θ and φ polarized intensities for NW1 are shown on the same color scale. The calculations have been normalized to 1, while the measured intensities are given in 10^5 counts sr^{-1} s^{-1}.

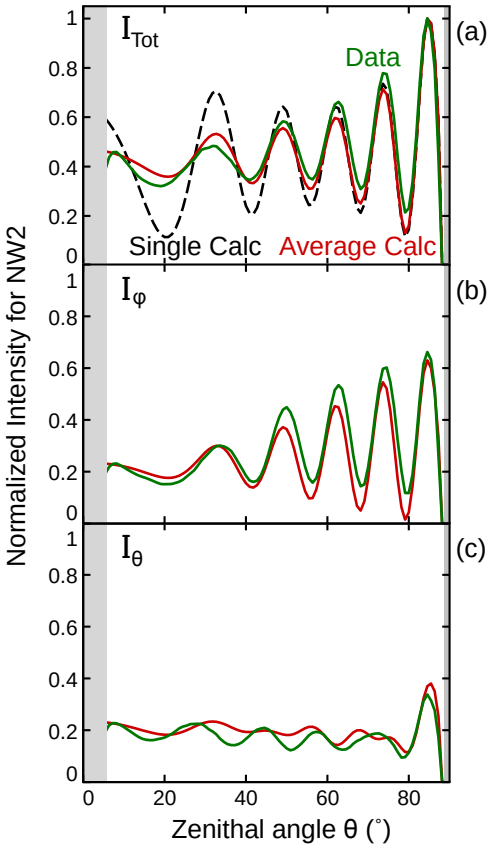

Figure 6.6 – Azimuthally averaged intensities for NW2 from Figure 6.5, comparing the measurements (green) to the averaged calculations (red). All measured and calculated intensities are normalized to their respective total intensity. (a), (b) and (c) show I_{tot}, I_{φ} and I_{θ} respectively. In (a), the black dashed line indicates the calculation for a single height best matched to the measured data (2.27 µm). The gray areas represent the angular range not collected by the mirror.

7

Directional emission from leaky and guided modes in GaAs nanowires measured by cathodoluminescence

We measure the polarization-resolved angular emission distribution from thin and thick GaAs nanowires (diameters ~110 and ~180 nm) with cathodoluminescence polarimetry. The nanowires, which horizontally rest on a thin carbon film, are excited by a 5 keV electron beam and emit band gap luminescence at a central wavelength of 870 nm. The emission can couple to different waveguide modes that propagate along the wire, are dependent on the wire diameter, and determine the directionality and polarization of the emission. Although each measured nanowire can support different modes, the polarized emission is dominated by the TM01 waveguide mode in all cases, independently of wire diameter. When exciting the nanowires close to the end facets, the thin and thick wires exhibit opposite directional emission. The emission from thin nanowires is dominated by a leaky TM01 mode that leads to emission toward the opposite end facet (emission to the right when exciting the left-side edge). For the thick wires, however, the TM01 mode is guided but also lossy due to absorption in the substrate. In such a case, the wires emit toward the excited end facet (to the left when exciting the left-side edge). The emission directionality switches for nanowire diameters in the range of 145–170 nm. We show that the measurements agree well with both a simple 1D current model and numerical simulations.

7.1 Introduction

Semiconductor nanowires have fueled a growing field of integrated nanoscale optoelectronic devices, such as lasers [227, 246, 247], light emitting diodes [225, 226], photovoltaics[50, 228, 248, 249], single-photon detectors [239, 250–252], photodetectors [229], and metamaterials [253, 254]. Both the electrical and optical properties of nanowires are eminently tunable by controlling their size, geometry, or composition, among others [235–237, 255]. The directionality and polarization of emitted radiation from nanowires have been examined in previous studies [229, 232–234] and result from the coupling to leaky and guided waveguide modes [230, 231, 241, 256–258], which can also be described by Mie and Fabry-Pérot resonances [242, 258]. All modes are highly dependent on nanowire diameter.

Most previous studies of semiconductor nanowire emission properties have employed optical excitation methods. While powerful, such techniques lack the nanoscale spatial resolution to uncover all the features of the radiative processes from these nanostructures. Here we use cathodoluminescence (CL) spectroscopy, in which an electron beam acts as a highly localized excitation source and the emitted light is detected [92, 124, 194]. The high spatial excitation resolution of CL is typically determined by the electron beam spot size and the evanescent field extent about the beam path (~10–30 nm) [124], which enables the study of the nanoscale modal behavior of light [103, 136, 139, 185]. In general, CL also allows the characterization of a wide range of material properties [107, 111, 113]. Recently, the ability to measure both the angular and polarization distribution in CL has been demonstrated [132, 259].

In this chapter, we use these new CL features to investigate the angle- and polarization-dependent emission from horizontal GaAs nanowires [132]. We study nanowires of different lengths and diameters that support both leaky and guided modes. Exciting the nanowires along their length, we find that the TM01 mode dominates the polarization-resolved emission for all excited wires, but depending on the diameter, the mode is either leaky or guided. We observe a distinct change of the directionality of the CL emission when exciting the nanowires close to their end facets, which correlates with the nanowire diameter and the nature of the mode. Thinner, leaky wires emit in the opposite direction from thicker, guided wires. The measurements exhibit good agreement with both a simple 1D current model and numerical simulations, which show that the substrate also plays a role in the emission directionality.

7.2 Experiment

GaAs nanowires were grown by self-catalyzed molecular beam epitaxy on silicon [260, 261] and were subsequently mechanically broken and deposited on a holey carbon TEM grid (see Methods7.7). Scanning electron micrographs of the two GaAs nanowires studied here are shown in Figure 7.1(a). The thin NW1 has a

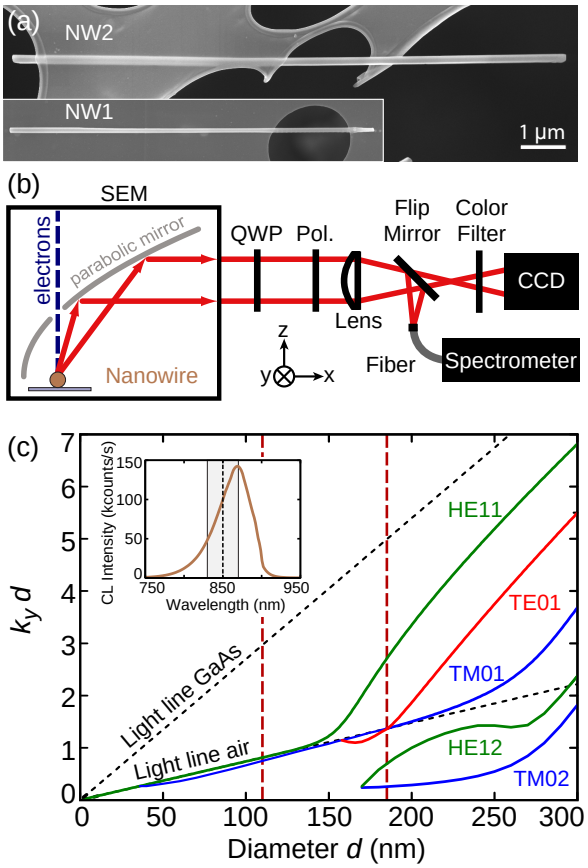

Figure 7.1 – (a) Scanning electron micrographs of the GaAs nanowires NW1 (bottom) and NW2 (top), shown on the same scale. NW1 is 7.9 µm long and 100–120 nm thick; NW2 is 12 µm long and 175–195 nm thick. (b) Schematic overview of the cathodoluminescence polarimetry setup. The electron beam excites the nanowires, the emitted radiation is collected by a parabolic mirror and either focused onto a fiber connected to a spectrometer or sent through a QWP, linear polarizer, and bandpass filter before being imaged onto a 2D CCD camera. (c) Dispersion relation of leaky and guided modes for infinitely long cylinders, showing the real part of the wavevector k_y multiplied by the cylinder diameter d, as a function of d, for GaAs at $\lambda_0 = 850$ nm ($n = 3.6$, $k_0 = 7.39$ µm^{-1}). The vertical red dashed lines indicate the average diameters of the two wires. The inset shows the measured CL emission spectrum from NW2. The spectrum of NW1 (not shown) does not differ noticeably except for a lower intensity. The vertical black dashed line in the inset at $\lambda_0 = 850$ nm indicates the transmittance maximum of the bandpass filter used for the angular measurements, while the gray area indicates the 40 nm bandwidth of the filter.

length of 7.9 µm and a diameter of 100–120 nm, while the thick NW2 has a length of 12 µm and a diameter of 175–195 nm. Both wires are slightly tapered, the right-hand side being thinner, although NW2 does thicken again slightly at the very edge. The nanowires lie horizontally on the ~20 nm thick carbon layer. In the Supporting information we show data for an additional thin and thick wire (SEM images shown in Figure 7.5).

The cathodoluminescence spectroscopy and polarimetry setup [128, 132, 183] is schematically shown in Figure 7.1(b). A parabolic mirror collects the radiation from the nanowires and directs it onto a spectrometer or images it onto a 2D camera to measure the angular intensity distribution for a given wavelength (using a bandpass filter). Polarization-resolved measurements are obtained by using a polarimeter composed of a quarter-wave plate (QWP) and a linear polarizer (Pol.), which determines the Stokes parameters of the emitted radiation. The full polarization can be detected in this way, obtaining information about the degree of polarization and its orientation, ellipticity, and handedness. Essentially, this allows the retrieval of any arbitrary polarization state, including the different electric field components and the phase difference between them[131]. This is not possible using only a linear polarizer. We correct for the geometrical and polarization-dependent transformations of the parabolic mirror on the measured emission [132] (see Methods7.7 for more details about the CL measurements). For the measurements, the nanowires are aligned along the y-axis, as defined by the coordinate system shown in Figure 7.1(b). As we expect directional emission along the nanowire axis, this is the preferred orientation for the mirror to collect the radiation symmetrically. The CL emission spectrum from NW2 is shown in the inset of Figure 7.1(c) and is dominated by band gap recombination centered around $\lambda_0 = 870$ nm. This emission can feed into waveguide modes supported by the nanowire, which depend on its diameter and which can affect the polarization and directionality of the emitted radiation [230, 233, 234, 241].

7.3 Nanowire waveguide modes

Figure 7.1(c) shows the dispersion relation of waveguide modes for infinitely long cylinders [262], calculated for GaAs at $\lambda_0 = 850$ nm ($n = 3.6$, $k_0 = 7.39$ µm^{-1}), the wavelength at which we filter the angle-resolved measurements. We follow the formalism used in Ref. 257 and determine the wavevector k_y along the axis of the nanowire. We show the real part of k_y multiplied by the wire diameter d, as a function of d. The dispersion curves denote transverse electric (TE), transverse magnetic (TM), and magnetoelectric (HE) modes. These modes are characterized as "leaky" if their dispersion lies below the light line of air ($k_y < k_0$), in which case they also possess a non-negligible imaginary part of the wavevector k_y [257]. If the mode dispersion lies above the light line of air but below the light line in GaAs ($k_{GaAs} > k_y > k_0$), the waveguide mode is guided within the nanowire.

The vertical red dashed lines in Figure 7.1(c) display the average diameter of the

two nanowires studied here. For the thin NW1 (and any nanowire with a diameter below 150 nm), only the TM01 and the HE11 modes are supported. Both are very close to the light line in air, but the TM01 mode is slightly below it and thus leaky for these diameters. In the case of the thicker NW2, the TE01, HE12, and TM02 also occur. The latter two are far below the light line in air and thus have a very short propagation length along the nanowire, while the HE11 mode is very clearly guided. The TE01 and TM01 modes are both very close to the light line of air in this region, representing a transition region between a leaky and guided nature for these modes. Which modes will dominate the emission depends on the coupling efficiency between the excitation source and the mode.

The dispersion relation allows us to determine which modes can play a role in the emission from these nanowires and to calculate the wavevector corresponding to each mode for a given diameter. A 1D current model, developed in Ref. 257 and applied in Ref. 234, uses the wavevectors to calculate far-field emission patterns for all electromagnetic field components. The model describes the nanowire as a 1D cavity in vacuum with length L; the emission is produced by a line current excited by a dipole at a given position along the wire. This simple model allows us to retrieve the expected polarization-dependent angular emission patterns for different modes at different wire diameters, which we can compare to measurements.

7.4 CL polarimetry

Measurements and calculations of the angle- and polarization-dependent emission intensity distributions at λ_0 = 850 nm for central excitation of the two nanowires clearly identify the TM01 mode as having the dominant contribution to the emission, as shown in Figure 7.2. For NW1 we compare the measurements (Figures 7.2(a–c)) to the 1D calculation for the TM01 mode (Figures 7.2(d–f)), displaying the Cartesian electric field intensities $|E_x|^2$, $|E_y|^2$ and $|E_z|^2$ as a function of azimuthal (φ) and zenithal (θ) angles. The field orientations are indicated by the coordinate system at the left, and the wires are oriented along the y-axis. A wavevector of $k_y = 6.63 + i\ 1.19\ \mu m^{-1}$ was used for the calculation, as determined from the dispersion relation and nanowire diameter. The dark blue regions around the edges of each image correspond to the angles at which no light is collected by the mirror. The intensity scale is chosen so as to maximize the contrast in the color scale to better view the details of the features. In the case of the calculation, the intensities are normalized to the overall maximum value for each wire. We observe excellent qualitative agreement between measurement and calculation. For $|E_x|^2$ (Figures 7.2(a,d)) there are four bright features at large zenithal angles, while $|E_y|^2$ (Figures 7.2(b,e)) displays bright emission in the center of the mirror and $|E_z|^2$ (Figures 7.2(c,f)) exhibits two lobes to the left and right of the polar image, in the directions of the end facets of the nanowire.

For NW2 we also observe very similar features for both measurements (Figures 7.2(g–i))and calculations (Figures 7.2(j–l)). A wavevector of $k_y = 8.00 +$

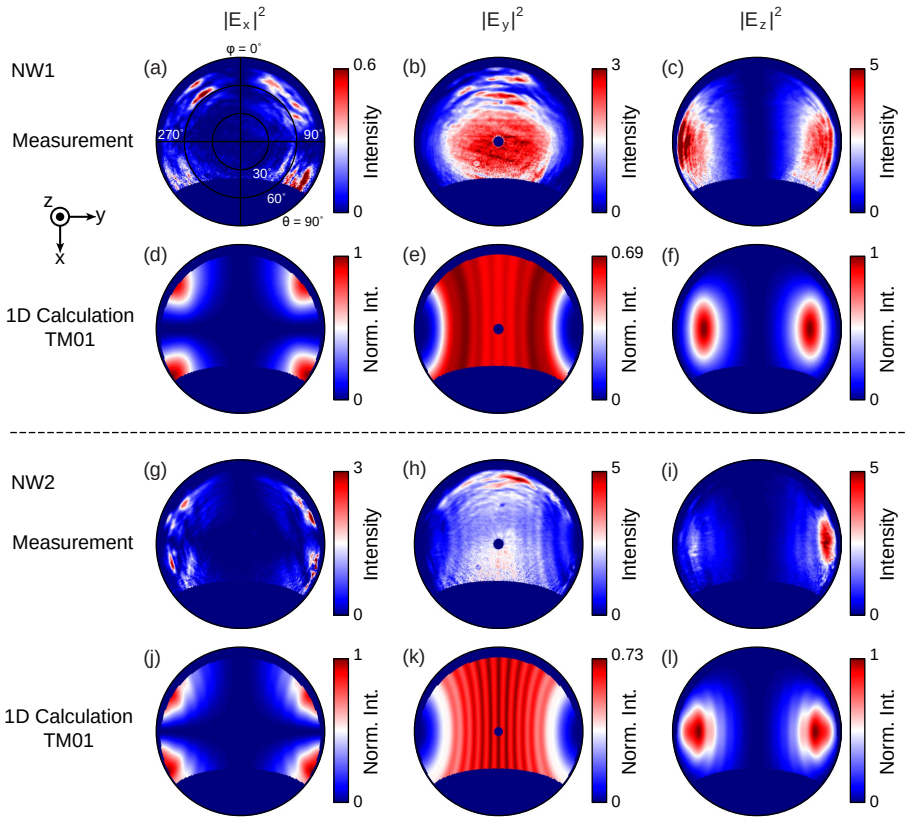

Figure 7.2 – Measured (a–c, g–i) and calculated (d–f, j–l) angular emission distributions of the Cartesian field intensities at λ_0 = 850 nm for NW1 (a–f) and NW2 (g–l), as a function of azimuthal (φ) and zenithal (θ) angles. The patterns were measured and calculated for central excitation of the nanowires. (a, d, g, j) Intensity of the E_x field component; (b, e, h, k) intensity of E_y; and (c, f, i, l) intensity of E_z (the coordinate system is shown in the top left). The calculations for each wire determine the far-field emission profiles for the TM01 mode. We use the full range of the color scale for each panel, but the intensity scales for all three field components of each nanowire are normalized to the maximum value (E_x and E_z are equal). The measured intensities are given in 10^6 counts sr^{-1} s^{-1}.

i 0.50 $\mu\mathrm{m}^{-1}$ was used for the calculation in this case. For $|E_x|^2$ (Figures 7.2(g,j)) we observe four features at slightly higher zenithal angles than for NW1, at the corners of the angular range. $|E_y|^2$ (Figures 7.2(h,k)) shows the brightest intensity in the center, as for NW1, but this time we can also see intensity fringes along the vertical direction, which are due to interference between the emission from the nanowire end facets. The fringes are clearly visible in the experiment, but with lower contrast than in the calculations, which we attribute to imperfections in the mirror and the

nanowire end facets and to limitations on the angular resolution. Finally, $|E_z|^2$ (Figures 7.2(i,l)) again displays two lobes to the left and right, but at higher angles than for NW1, similarly to the behavior of $|E_x|^2$. In the experiment, the two lobes are asymmetric, which we attribute to the slight tapering of the wire. The emission is brighter in the direction of the thinner side. Comparing the relative intensities of calculations and measurements for both nanowires, we find that $|E_x|^2$ is weaker in the measurements than in the calculations. We ascribe this discrepancy to a lower collection efficiency at the edges of the mirror, where the $|E_x|^2$ component is strongest.

Even though the two nanowires have quite different diameters, in both cases we can clearly recognize very similar polarized field distributions that show excellent qualitative agreement with calculations for the TM01 mode. From this we conclude that the emission behavior of both NW1 and NW2 is dominated by the TM01 mode. The fundamental HE11 mode does not appear to play a major role in our case. This has been observed previously[233] and is ascribed to the fact that the fields are localized more outside of the wire for the HE11 mode than for the TM01 mode, which shows relatively more intensity in the center of the wire, allowing it to couple more strongly. For comparison, we include calculations of the far-field emission profiles of the HE11 mode for central excitation of the thin and thick nanowires in Figure 7.8 of the Supporting information. Examining all field components, we find there is much better agreement with the TM01 mode than with the HE11 mode. This confirms that the CL emission couples most efficiently to the TM01 mode. Differences between the two wires are expected, however, because for NW1 the mode is leaky ($Re(k_y) = 6.63 < k_0 = 7.39\ \mu m^{-1}$), while for NW2 it is guided ($Re(k_y) = 8.00 > k_0 = 7.39\ \mu m^{-1}$). To support the data, we show polarization-resolved measurements for an additional thin and thick nanowire in Figure 7.6 of the Supporting information, which exhibit the same type of features for all three field components as the results shown here.

7.5 Directional emission

Next, we study the directional behavior of the nanowire emission for excitation off-center, near the end facets of the wires, observing a distinct difference in the directionality of the emission between NW1 and NW2, as shown in Figure 7.3. We compare the total intensity that both wires emit as a function of the azimuthal and zenithal angles in the case of measurements, calculations and simulations, for excitation at the left edge, center, and right edge. The edge excitation is always a few hundred nanometers away from the end facet, with the exact positions shown by the dashed lines in Figure 7.4. We compare the total intensity measurements to calculations using the dominant TM01 mode. Polarimetry measurements for select positions near the end facets (not shown here) display the same characteristic features as in Figure 7.2, so we do not observe a transition to a different mode at the edges. The measured intensities differ between the wires and excitation positions,

which we attribute to variations in local material quality and size of the interaction volume (due to tapering and different diameters). Here the total emission intensity is brighter when exciting the thicker ends. For the measurements on NW1, central excitation (Figure 7.3(b)) results in two symmetric lobes of higher intensity to the left and right, while excitation at the left edge (Figure 7.3(a)) leads to directional emission to the right side and excitation on the right (Figure 7.3(c)) leads to emission toward the left side. 1D calculations of the total emission intensity from the leaky TM01 mode qualitatively reproduce the emission behavior for excitation in the center and 300 nm from the end facets (Figures 7.3(d–f)). In the measurements, the electron beam excitation at the edges was ~300–500 nm from the end facets.

We attribute the discrepancies in the shape of the emission patterns between measurements and calculations to the fact that the excitation volume can be much larger than the electron beam width (up to a few hundred nanometers). This is due to electron scattering, secondary electron generation, carrier diffusion, and photon recycling, which can play a large role in such a direct band gap material [122, 125, 259]. A large majority of excitations occur very close to the point of impact, but light generation will cover a larger area. The overall spatial resolution is determined by a convolution of all of these effects and will depend on the material properties. For such strongly luminescent materials as GaAs the resolution is not as good as the electron beam size but better than the full interaction volume. This is different from the calculations, which assume a point-source. The presence of the thin holey carbon substrate, which is not taken into account in the calculation, can also affect the emission, as we will now show for NW2.

The measurements on the thicker NW2 (Figures 7.3(g–i)) show the opposite directionality to that of NW1. Excitation at the left edge leads to emission toward the left, while excitation at the right edge produces emission toward the right. The excitation positions were 700 nm (left) and 400 nm (right) away from the end facets (see also the dashed lines in Figure 7.4(b)). For central excitation we observe asymmetrical emission, as was the case for Figure 7.2(i), which we again attribute to the tapering of the wire that creates an inherent asymmetry in the wire and its emission properties. The tapering affects the leaky mode in the thin wire less since radiation is emitted continuously as the mode propagates along the wire. The thicker NW2, on the other hand, supports a guided mode, so light mostly escapes from the end facets and has a longer propagation length, traveling through the wire for multiple round trips. Since the modal properties are very sensitive to the diameter, the gradual variations along the length of the wire will affect the light more strongly.

We first compare the measurements to the 1D calculations of the (guided) TM01 mode, which do not directly take the substrate into account (Figures 7.3(j–l)). We represent absorption at the band edge and losses into the substrate by an imaginary part of k_y of 0.50 i μm^{-1}; this leads to an effective absorption length of 2 μm, much larger than the TM01 wavelength (~220 nm), but shorter than the NW length, thus limiting mode bouncing at the NW edges. We find that for excitation near the edges (500 nm away from the end facet, similarly to the measurement)there is a maximum in emission to the same side as in the measurements, with a weaker feature in

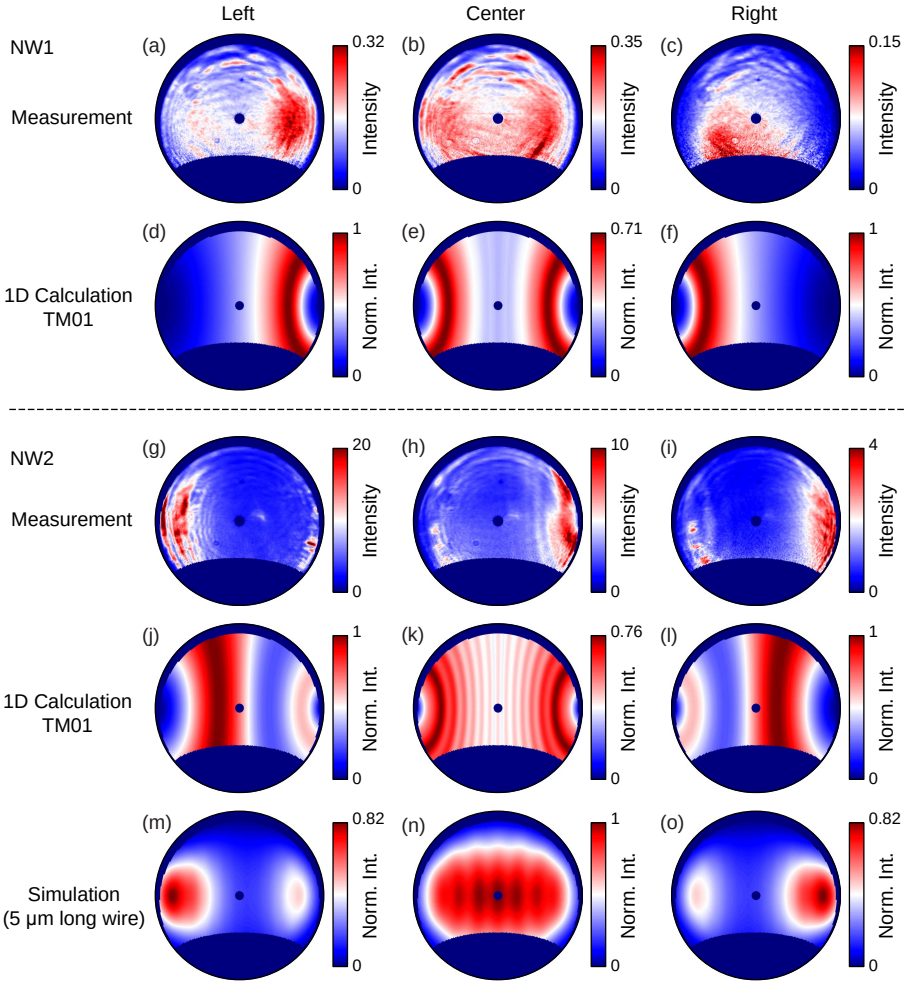

Figure 7.3 – Measured (a–c, g–i), calculated (d–f, j–l) and simulated (m–o) angular emission distributions of the total intensity at $\lambda_0 = 850$ nm for NW1 (a–f) and NW2 (g–o). The patterns were measured and calculated for excitation at the left (a, d, g, j, m), center (b, e, h, k, n), and right (c, f, i, l, o) of the nanowires (see Figure 7.4 for positions). The calculations and simulations for each wire have been normalized to their maximum. The measured intensities are given in 10^6 counts sr^{-1} s^{-1}. The 1D calculation uses the same wire lengths as in the experiment (7.9 and 12 µm), but due to computational constraints the simulated NW2 is shorter (5 µm).

the opposite direction. We note that in the measurements of NW2 there is also a region of higher intensity to the opposite side of the dominant emission. For central excitation, we observe quite good qualitative agreement between experiment and

calculation, taking into account the asymmetry we attribute to tapering of the wire. As shown in Figure 7.3(k), interference fringes from the emission of both facets are expected for this long wire. These are also faintly visible in Figure 7.3(h).

To get a better measure for the effect of the substrate, we perform numerical simulations using COMSOL (see Methods7.7 for more details) on a 180 nm thick and 5 µm long wire on a semi-infinite carbon substrate (Figures 7.3(m–o)). Due to computational constraints, we did not simulate a 12 µm long wire nor the extremely thin substrate. The simulations, however, do show good qualitative agreement with the experiment and provide insight into the role of the substrate on the emission behavior. Central excitation leads to a symmetric emission profile with highest intensity in the central region and interference fringes that are less distinct than for the 1D calculation. Excitation at the edges (500 nm from the end facets) shows emission profiles in good qualitative agreement with the measurements. There is a bright feature on the same side at high angles and a weaker spot on the opposite side. Both the 1D calculations and the simulations predict the measured directionality, which is completely opposite to the behavior of NW1. The features measured for edge excitation closely resemble the simulation, while there is better agreement with the 1D calculation for central excitation. As the substrate is very thin, we can expect it to have a smaller effect than in the simulation that was performed for a semi-infinite substrate. The importance of the substrate as an additional loss channel does not play a large role in the case of the leaky mode ($k_y < k_0$), as there is already a strong inherent leakage. For the thicker wire, simulations without substrate show an emission directionality that is more strongly dependent on excitation position and near the edges becomes opposite to that observed in the measurements (Figures 7.9 and 7.10 of the Supporting information). We conclude that both the guided behavior of the TM01 mode and the additional loss channel due to the substrate play a role in determining the directional emission behavior of the thick nanowire.

The changing directionality observed in the measurements and calculations may be understood in an intuitive manner, when examining the differences between leaky and guided modes. For the leaky mode, leakage of the light along the nanowire dominates the emission. When exciting close to an end facet, light propagating to the edge will partially reflect back, while light going to the opposite side will propagate longer and thus leak out more, leading to a majority of the emission into the opposite direction. For the guided mode, emission from the end facets dominates, while there is loss to absorption into the substrate for light propagating along the wire, so more light will scatter out from the closest edge than from the far edge.

We can study the directional behavior of the emission as a function of the excitation position more closely, taking advantage of the high spatial resolution of CL. As discussed previously, the resolution is not limited to the electron beam size, but still remains subwavelength. Figure 7.4 shows the emission directionality for both wires when scanning the beam along their length. We determine a left-to-right ratio (L-R)/(L+R) by averaging the total intensity over all zenithal angles in 60° azimuthal

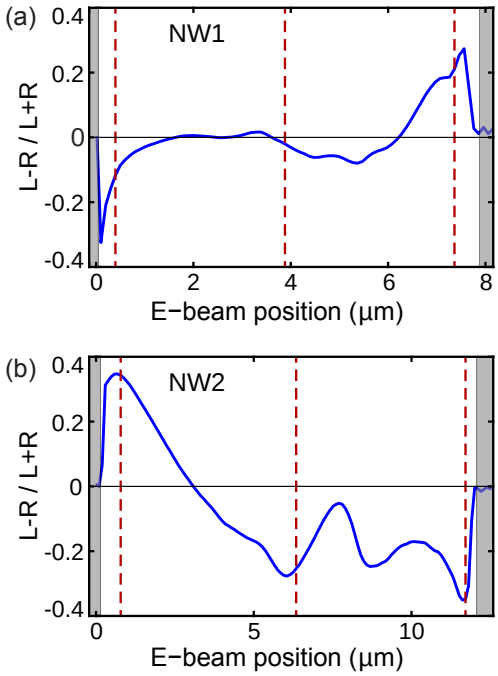

Figure 7.4 – Ratio of the left-to-right directional emission for NW1 (a) and NW2 (b), showing the ratio (L-R)/(L+R) as a function of the electron beam position as it scans along the wire. The gray bands indicate positions that are not on the wire, while the red dashed lines indicate the positions of the left, center, and right measurements shown in Figure 7.3. The leftward and rightward directional intensities were determined by averaging the total intensity over all zenithal angles in 60° azimuthal wedges (φ=240–300° for left and φ=60–120° for right).

wedges on the left and right sides, as these correspond to the regions of highest intensity features. The gray bands correspond to positions that are outside the wires and the dashed lines indicate the positions of the measurements in Figure 7.3.

Comparing NW1 (Figure 7.4(a)) to NW2 (Figure 7.4(b)), we observe that there is no left/right directionality at the very edges for both wires, but that close to the edges the left-to-right ratio reaches a maximum that is reversed for the two wires, as expected from Figure 7.3. Figure 7.10 in the Supporting information shows the left-to-right ratio for simulations of a thick wire, which also exhibit a maximum close to the end facet. Additionally, the simulations with substrate show better agreement with the measurements than the simulations without. The directionality we observe results from interference of waves propagating back and forth in the nanowire, which is dependent on the reflection at the end facets, absorption and leakage during propagation, and also on the excitation position. This peak in

emission close to the end facet is convoluted with the interaction volume of the electrons with the material. At the very edge we do not excite as large a region, which contributes to the decrease in intensity and directionality we observe.

The change in emission directionality observed here is consistent with the additional thin and thick nanowires examined in the Supporting information (Figure 7.7). Comparing all nanowires, the thickest diameter for the leaky behavior in the thinner wires is 145 nm, while the thinnest diameter for the guided behavior in the thicker wires is 170 nm. This indicates that the transition in emission directionality should occur for nanowire diameters in the range of 145–170 nm.

7.6 Conclusions

In conclusion, we have demonstrated that cathodoluminescence emission from GaAs nanowires is strongly directional and depends on the nanowire diameter. The emission excited by the electron beam couples to waveguide modes that determine the polarization and angular distribution of the outcoupled radiation. These waveguide modes are very sensitive to wire diameter, especially as they change in nature from leaky to guided when crossing the light line in air. Polarization-resolved measurements show that the TM01 mode dominates the emission from both nanowires. The thin wire supports a leaky TM01 mode, which displays emission in the direction opposite to the excited edge, while the thick wire supports a guided TM01 mode that exhibits emission in the same direction. The emission directionality switches for nanowire diameters in the range of 145–170 nm. Both the leaky/guided nature of the mode and the presence of the substrate play an important role in determining the emission directionality. Cathodoluminescence polarimetry proves to be a powerful technique to study the angular- and polarization-dependent emission properties of semiconductor nanowires or other nanostructures, with a subwavelength excitation resolution.

7.7 Methods

Sample fabrication. The GaAs nanowires were grown on a Si(111) undoped wafer via a Ga-assisted method in a DCA P600 solid-source MBE machine [260, 261]. Typical growth parameters are as follows: a Ga rate of 0.3 Å/s as flux of 2.5×10^{-6} Torr, a substrate temperature of 640 °C, rotation of the substrate at 7 rpm, and a V/III beam equivalent pressure ratio of 50. The nanowires were removed from the silicon substrate in an isopropanol solution by ultrasonic bath for 1 min. A few drops of the isopropanol solution containing nanowires were transferred to a holey carbon TEM grid (Plano GmbH).

CL measurements. The measurements were performed in a FEI XL-30 SFEG (5 keV electron beam, ~0.1 nA current) equipped with a home-built CL system [124, 128, 183]. The emission excited by the electron beam is collected by an aluminium

paraboloid mirror and directed to an optical setup. We measure either the spectrum using a liquid-nitrogen-cooled back-illuminated silicon CCD array (Princeton Instruments Spec-10 100B) or the angular emission profile using a Peltier-cooled back-illuminated 2D silicon CCD array (Princeton Instruments PIXIS 1024B) [128, 183]. Using a series of six measurements of the angular CL distribution with the 2D CCD array in conjunction with a quarter-wave plate (QWP) and linear polarizer (LP) determines the full emission polarization. Each measurement was taken for a different combination of QWP and LP settings (horizontal, vertical, 45°, 135°, right- and left-handed circular). We correct for the geometrical and polarization dependent response of the paraboloid mirror on the CL emission that it redirects to the optical setup [132]. A 40 nm bandpass color filter was used to spectrally select the measured emission at $\lambda_0 = 850$ nm. Integration times of 0.1–1 s were used depending on sample brightness. For every setting of the QWP and LP, we collected a dark reference measurement where we blank the electron beam (using the same integration time as for the corresponding CL measurement). This reference was subtracted from the data in the postprocessing stage. Possible sources of measurement errors include drift of the electron beam, bleaching/contamination which leads to a reduction in CL signal, and fluctuations in the current and/or the alignment of the mirror.

FEM simulations. The finite-element-method (FEM) simulations of the far-field emission profiles of finite nanowires were performed using the commercial software package COMSOL Multiphysics v4.3b, using the same methods as in Ref. 257 and Ref. 234. For free-standing nanowires the simulation space consisted of a circular cylinder of length L and diameter d that represents the nanowire, enclosed in three concentric spheres of diameter $L+2\lambda_0$, $L+4\lambda_0$, and $L+6\lambda_0$, with their centers coinciding with that of the cylinder. The innermost two spheres were set to be air (n_{air}), while the outermost layer was defined as a perfectly matched layer (PML) to absorb all outgoing radiation and prevent reflections. The material constants of GaAs for the cylinder were taken from Palik [263] ($n_{GaAs} = 3.6$ at $\lambda_0 = 850$ nm). A tetrahedral mesh was used, with maximum element sizes (MES) of 25 nm in the domain of the cylinder and 160 nm for the air domains. The maximum element growth rate was set to 1.35 for all of the domains.

For nanowires on top of a carbon substrate the geometry is modified as follows. The three concentric spheres of the same diameter are divided into two semispherical layered domains through a plane that contains the cylinder axis, and the cylinder is then shifted by $d/2$ from its original position in order to be placed on top of one of the new semispherical spaces, which we refer to as the substrate. The substrate was set to be amorphous carbon ($n_C = 1.987 + i\,0.83$ at $\lambda_0 = 850$ nm) [264], and the rest was set to be air, except for the GaAs cylinder. As the space was divided into two different media, the material properties of the outermost PML must be the same as the adjacent medium. The MES of the tetrahedral mesh was 25 nm for the cylinder, 160 nm for the air, and 90 nm for the substrate. The maximum element growth rate was 1.35, the same as for the free-standing nanowires.

Simulations were highly memory-demanding; in the case of the nanowires of length $L = 5$ µm on top of the substrate, the calculations need ~400 GB. Postprocessing calculations were used to determine the total radiated power at the inner spherical boundary $\sum_{int}$, defined by:

$$P = \int_{\sum_{int}} \langle \mathbf{S} \rangle \cdot \mathbf{n} dS \tag{7.1}$$

where **n** is the outward normal unit-vector to the surface.

7.8 Supporting information

7.8.1 Additional nanowires

The polarization and directional behavior of the GaAs nanowires we have studied is quite robust, including the differences between thinner and thicker nanowires. Here we show data from an additional thin (NW3) and thick (NW4) nanowire. Figure 7.5 shows scanning electron micrographs of these two wires: NW3 has a length of 1.9 µm, a diameter of 135–145 nm and is resting on the copper support of the TEM grid, while NW4 has a length of 13.6 µm, a diameter of 170–195 nm and is lying on the holey carbon film.

We perform polarimetry measurements [132, 259] on both of these nanowires, as shown in Figures 7.6(a–c) for NW3 and (d–f) for NW4. We display the field intensities $|E_x|^2$, $|E_y|^2$ and $|E_z|^2$ as a function of the azimuthal (φ) and zenithal (θ) angles, measured at $\lambda_0 = 850$ nm with a 40 nm bandwidth bandpass filter. This is identical to the measurements in the main text. The coordinate system at the left indicates the field orientations, with the wires oriented along the y axis. The dark blue regions around the edges of each image correspond to the angles at which no light is collected by the mirror. Both wires display very similar intensity features, which also resemble those in Figure 7.2 of the main text, showing good agreement with the expected behavior for the TM01 mode. $|E_x|^2$ exhibits 4 intense lobes in the corners of the polar image, while $|E_y|^2$ displays vertical lines of high intensity, and $|E_z|^2$ shows two bright lobes to the left and right. NW3 is much shorter than the other wires, so there are fewer fringes from the interference between emission from different regions of the wire, and the features are found at angles closer to the surface normal. NW4 is very similar to NW2, showing clear interference fringes for $|E_y|^2$ and having features at higher zenithal angles. All these results show that for different GaAs nanowire lengths (1.9–13.6 µm) and diameters (100–200 nm), the TM01 waveguide mode appears to be the dominant contribution with regards to the emission behavior.

The change in directionality for off-center excitation of the thin and thick nanowires is a quite robust phenomenon, which is also visible in thin NW3 and thick NW4, as shown in Figure 7.7. We display the left-to-right ratio as a function of the electron beam excitation position while scanning along the length of the

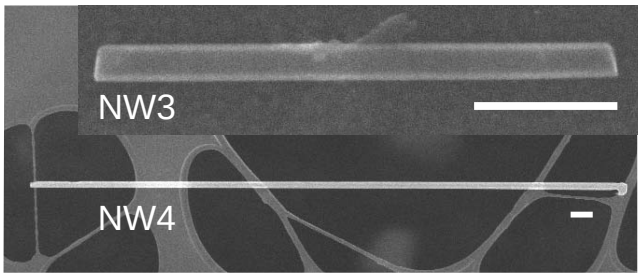

Figure 7.5 – (a) Scanning electron micrographs of the GaAs nanowires NW3 (top) and NW4 (bottom). NW3 is 1.9 µm long, 135–145 nm thick and is lying on the copper support from the TEM grid. NW4 is 13.6 µm long, 170–195 nm thick and is lying on the holey carbon from the TEM grid. The scale bars both represent 500 nm.

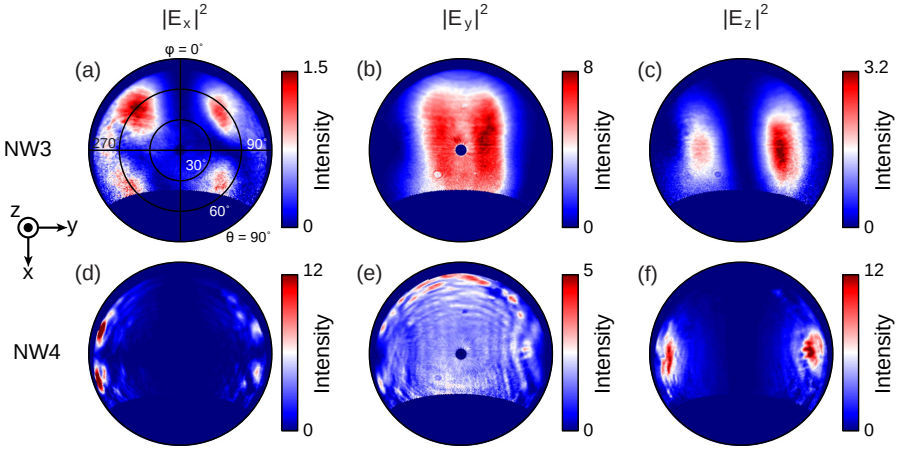

Figure 7.6 – Measured angular emission distributions of the Cartesian field intensities $|E_x|^2$, $|E_y|^2$ and $|E_z|^2$ at λ_0 = 850 nm for NW3 (a-c) and NW4 (d-f). The patterns were measured for central excitation of the nanowires. The intensities are given in 10^6 counts sr^{-1} s^{-1}.

wire, in the same way as for Figure 7.4 of the main text. We observe that thin NW3 has the same behavior as NW1, emitting in the opposite direction to thick NW4, which shows the same behavior as NW2. In all cases, when exciting close to the end facets, the thin nanowires emit in the opposite direction while the thick nanowires emit toward the same direction. Due to the tapering of the wires the directionality is not symmetric around the center. Since NW3 is up to 145 nm thick and NW4 is down to 170 nm thick, it seems the transition from thin/"leaky" behavior to thick/"guided" behavior occurs around a diameter of ~150–160 nm. For all wires

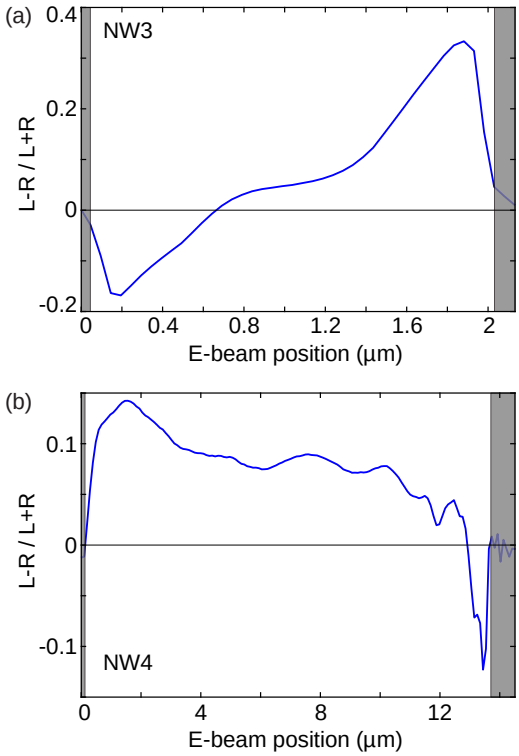

Figure 7.7 – Ratio of the left-to-right directional emission for NW3 (a) and NW4 (b). We show the ratio (L-R)/(L+R) as a function of the electron beam position as it scans along the wire. The gray bands indicate positions that are not on the wire. The leftwards and rightwards directional intensities were determined by averaging the total intensity over all zenithal angles in 60° azimuthal wedges (φ=240–300° for left and φ=60–120° for right).

we note that there is no left/right directionality when we reach the end facet of the wire (the ratio becomes 0).

7.8.2 HE11 mode

The fundamental mode in the nanowires is the HE11 mode [234, 257, 258], so it is to be expected that the CL emission also couples to it. In the main text we found excellent agreement with the TM01 mode, however, indicating that mode dominates the emission behavior. For comparison, we show the calculated angular emission intensity distributions for the HE11 mode in Figure 7.8. The Cartesian field intensities for the thin NW1 and thick NW2 exhibit the same characteristic features. Comparing them to the measurements from Figure 7.2, we find that the

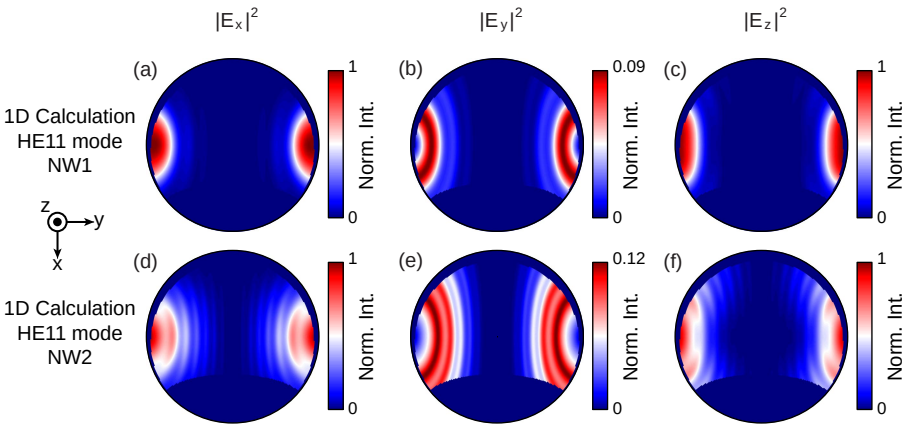

Figure 7.8 – Calculated angular emission distributions of the Cartesian field intensities of the HE11 mode at λ_0 = 850 nm for NW1 (a-c) and NW2 (d-f), as a function of azimuthal (φ) and zenithal (θ) angles. The patterns were calculated for central excitation of the nanowires. (a, d) show the intensity of the E_x field component, (b, e) the intensity of E_y, and (c, f) the intensity of E_z. The calculations for each wire have been normalized to their maximum.

maximum at 90° zenithal angle for the E_z component is similar to the measurements. However, the angular distribution has a slightly different shape and the measurement is not as concentrated at 90° degrees as the calculation. The E_y and (especially) E_x components for the HE11 mode are very different from the measurements. This confirms that the TM01 mode is the dominant contribution. We cannot exclude however that the HE11 mode still plays a minor role in the emission.

7.8.3 Influence of the substrate

Numerical FEM simulations with COMSOL [234, 257, 258] are used to determine the influence of the substrate on the directionality of the thick (guided) nanowires. Due to constraints on the numerical simulations, it was impossible to calculate the behavior of very long wires such as NW2 and NW4. Instead we compare 3 µm and 5 µm long nanowires with a diameter of 180 nm. Figure 7.9 compares the angular total intensity distribution at λ_0 = 850 nm for dipole excitation in the center and 500 nm away from the right-hand edge for these different nanowires with and without a substrate. The intensities are normalized to the maximum for each wire, but we use different scales to show better contrast between the features. For the 3 µm and 5 µm long wires without a substrate (Figures 7.9(a–d)), we observe crescent-shaped features of high intensity, symmetrically for center excitation and off to the left side for excitation at the

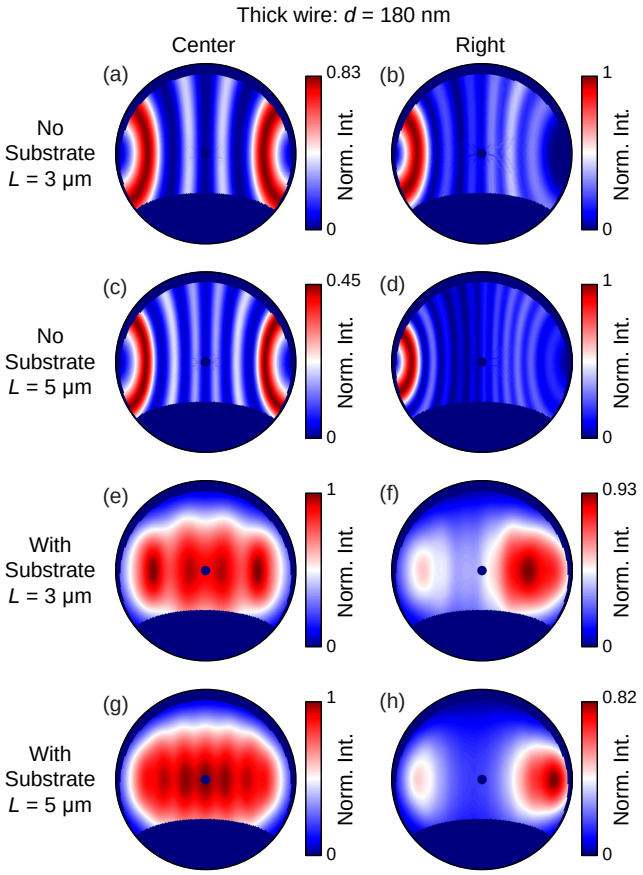

Figure 7.9 – Simulated angular emission distributions of the total intensity at λ_0 = 850 nm for a 3 µm long wire, without (a,b) and with (e,f) a semi-infinite substrate, compared to a 5 µm long wire without (c,d) and with (g,h) the substrate, in all cases for a diameter of 180 nm. The patterns were measured and calculated for excitation at the center (a,c,e,g) and right (b,d,f,h) of the nanowire (500 nm away from the edge, see Figure 7.10 for positions on the 5 µm long wire). The simulations for each wire have been normalized to their maximum.

right-hand edge. For this wire the dominant mode is so close to the light line that the behavior is not very different than for the leaky case in the thinner wire, the wire emits in the opposite direction from the excitation position. For the longer wire we observe more interference fringes, the bright features move outwards to larger zenithal angles and there is a stronger intensity contrast between central and edge excitation than for the shorter wire.

When taking a semi-infinite substrate into account (Figures 7.9(e–h)), we ob-

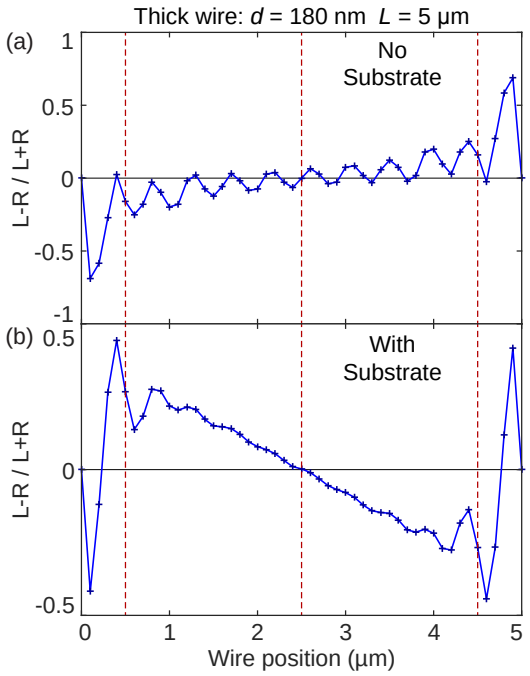

Figure 7.10 – Ratio of the left-to-right directional emission for the simulated 5 µm long wire with 180 nm diameter, (a) without a substrate and (b) on the same semi-infinite carbon substrate used in Figures 7.3(m–o) of the main text. We show the ratio (L-R)/(L+R) as a function of the simulated excitation position as it scans along the wire in steps of 100 nm. The blue crosses indicate the data points, the blue lines are a guide to the eye. The red dashed lines indicate the center and right excitation positions of the simulated angular emission patterns shown in Figure 7.9 (we also show the symmetrically placed left-hand excitation position). The leftwards and rightwards directional intensities were determined by averaging the total intensity over all zenithal angles in 60° azimuthal wedges (φ=240–300° for left and φ=60–120° for right).

serve a distinct change in behavior. For excitation in the center, there is a high intensity over a large angular range around the surface normal and interference fringes are now less pronounced than in the wire without substrate. The main difference is for the edge excitation however, where we clearly distinguish a flip in the directionality, the wire now emits toward the same direction as the excitation position. There is still a non-negligible contribution in the opposite direction, but the dominant intensity is clearly emitted to the right-hand side. This shows that the substrate plays an important role in the nanowire emission behavior, as it breaks the symmetry of the environment of the wire and allows an extra loss channel for light that cannot couple out directly to free space. Comparing the 3 and 5 µm

long wires, we can see that the directional behavior is preserved, so it is robust to changes in the nanowire length. There are more intensity fringes in the long wire for central excitation. In the case of edge excitation, the features move outwards to larger zenithal angles and there is a stronger intensity contrast between central and edge excitation for the long wire. This is the same without a substrate. Extrapolating this behavior to the measured wires predicts good agreement, as we do observe intensity fringes for central excitation and high intensity at the very highest zenithal angles for edge excitation (Figures 7.3(g–i) of the main text). Even though the actual substrate is not semi-infinite, it does play a role in the nanowire emission behavior, which is qualitatively predicted here.

We can also determine the left-to-right ratio for the simulations. Figure 7.10 shows the directionality ratio for different dipole excitation positions along the 180 nm diameter and 5 μm long wire without (a) and with (b) substrate also shown in Figures 7.9. There is good qualitative agreement between the directional behavior of the simulation with substrate and that of the two thick nanowires (NW2 and NW4), with highest directionality when approaching the end facets. A notable difference is a flip of the simulated results toward opposite directionality, similar to the thin wires, for excitation very close to the end facet. This change is not observed in the measurement, which we attribute to the large extent of the electron interaction volume and thus of the excitation region. This will average out the behavior over multiple positions, reducing these sharp changes at the nanowire edges. The simulation without substrate displays a strong dependence on excitation position, the emission directionality flipping frequently from one side to another, which is different from the measured behavior. At the end facet of the substrate-less wire the directionality is opposite to the excitation position, similarly to the behavior of the simulated wire with substrate.

8

Nanoscale optical tomography with cathodoluminescence spectroscopy

Tomography has enabled characterization of the Earth's interior, visualization of the inner workings of the human brain, and three-dimensional (3D) reconstruction of matter at the atomic scale. For tomographic techniques that rely on optical excitation or detection, diffraction generally limits the attainable resolution. In this chapter we introduce a tomographic technique, cathodoluminescence (CL) spectroscopic tomography, to probe optical properties in three dimensions with nanometer-scale spatial and spectral resolution. We first obtain two-dimensional CL maps of a 3D nanostructure at various orientations. Then, we use the method of filtered back projection to reconstruct the CL intensity at each wavelength. The resulting tomograms allow us to locate regions of efficient CL in 3D across visible and near-infrared wavelengths, with contributions from material luminescence and radiative decay of electromagnetic eigenmodes. The experimental signal can be further correlated with the radiative local density of optical states in particular regions of the reconstruction. We demonstrate how CL tomography can be used to achieve nanoscale 3D visualization of light-matter interactions by reconstructing a 3D metal-dielectric nanoresonator.

8.1 Introduction

Tomography enables the determination of a three-dimensional (3D) function from two-dimensional (2D) data. Originally driven by the need for a non-invasive technique to peer inside the human body, the development and application of tomography has had a significant impact on a wide range of disciplines, from medical diagnosis [265] to oceanography [266] and seismology [267]. While conventional tomographic techniques yield 3D structural or chemical information with macroscopic resolution, recent advances in electron microscopy have enabled nanoscale reconstruction of material geometries [268–271]. Notably, electron tomography has been used to reconstruct nanoparticles with atomic-scale resolution [272, 273] and to identify their different chemical constituents in three dimensions [274–277].

Still, optical tomography with subwavelength, nanometer-scale resolution remains a significant challenge. For example, while super-resolution techniques can yield 3D maps of molecular structure [278, 279], they rely on fluorescent tagging and cannot probe intrinsic radiative optical properties of the nanostructure. Nearly all other label-free techniques for probing nanoscale light-matter interactions are inherently 2D: scanning a physical probe such as a nanoscale tip [76, 280–282] or fluorescent emitter [283–287] over an object creates a planar map of the optical modes or local density of optical states (LDOS). Similarly, a focused electron beam can act as a spatially-localized but optically broadband impulse excitation to an object [92, 124, 141, 142, 183, 288], but has historically been used to probe electromagnetic modes in 2D. Capturing the often complex 3D nature of light-matter interactions with nanometer scale spatial and spectral resolution remains a significant challenge.

Recently, the first label-free 3D maps of nanoscale optical modes were obtained by combining 2D electron-energy loss spectroscopy (EELS) with tomographic reconstruction methods [145, 289]. In this paper, we introduce a complementary technique for nanoscale interrogation of optical properties in three dimensions: cathodoluminescence (CL) tomography. While both EELS and CL rely on electron-beam excitation of a sample, they are fundamentally distinct in their detection mechanisms and signal interpretation. First, CL spectroscopy detects light emitted by a sample rather than the energy lost by electrons transmitted through the sample. This optical detection scheme currently allows higher spectral resolution than is afforded by EELS. Second, CL selectively detects radiative optical processes, whereas EELS indiscriminately probes both radiative and non-radiative processes. Therefore, unlike EELS, CL enables direct visualization of material luminescence and radiative decay of electromagnetic modes. Together, the high spectral resolution and selective detection of radiative processes of CL tomography could elucidate, for example, the regions of highest radiative rate enhancement near a nanostructure or the distribution of radiative recombination sites in a semiconductor.

To demonstrate this new tomographic technique, we first obtain a series of CL maps of a 3D metal-dielectric nanostructure at various orientations. Next, we use the method of filtered back projection to reconstruct the CL intensity, which

we correlate with both material luminescence and the radiative local density of optical states. Owing to the high spatial and spectral resolution afforded by CL, our reconstruction provides detailed, 3D spectral maps of radiative optical properties across visible and near-infrared wavelengths.

8.2 Cathodoluminescence spectroscopy and 2D imaging

As an example of CL spectroscopic tomography, we consider a 3D metal-dielectric crescent, or nanocup, shown schematically in Figure 8.1(a). It is composed of a sub-wavelength dielectric core coated with a tapered metallic shell. This structure is well-known for its ability to harvest light over a large bandwidth [290–292], to confine light on the nanoscale [293–297], to support electric and magnetic modes [298, 299], and to serve as the constituent of an extremely broadband negative index metamaterial at optical frequencies [300]. The plasmonic nanocrescent derives many of its interesting optical properties from the asymmetry of its core-shell geometry: the tapered metallic shell yields a broadband optical response, while the metallic discontinuity across the tips enables strong electric and magnetic resonances and field enhancements. Yet, the crescent's rotational symmetry imparts it with a degree of insensitivity to polarization as well as relatively facile fabrication. Additionally, the complex 3D structure of the crescent provides a powerful platform for demonstrating the potential of CL tomography.

Nanocrescents are fabricated by evaporation of Au onto polystyrene spheres. Bright-field transmission electron microscopy (TEM) images of Au-polystyrene crescents are shown in Figures 8.1(b,c). The figures reveal the axial symmetry of individual crescents, as well as their high degree of uniformity.

CL spectroscopy is performed in a scanning electron microscope (SEM) [124, 183]. Figure 8.2 depicts CL measurements of crescents with different orientations, where θ is the angle between the axis of symmetry of the crescent (the z axis) and the incident beam direction. Note that this coordinate system co-rotates with the crescent such that the z axis is always aligned with the axis of symmetry; this axis of rotation is defined as the y axis. An angle of 0° corresponds to a crescent with tips pointing toward the substrate. Figure 8.2(b) shows the result of scanning the electron beam across the center of a crescent oriented at an angle of 90°. As the electron beam passes through the tips of the crescent (darker colored lines), the CL signal peaks at a wavelength of approximately 850 nm. This lowest-energy resonance of the crescent is characterized by strong electric field enhancement near the sharp tips of the structure [293, 297], as confirmed by finite difference time domain (FDTD) simulations (see Figure 8.2(c) and Supporting Figure 8.7). The spatial and spectral characteristics of this tip mode are also well reproduced by numerical simulations of CL via the boundary element method (BEM) [301–303] (see Supporting Figure 8.12). A discussion of the factors that influence the resolution

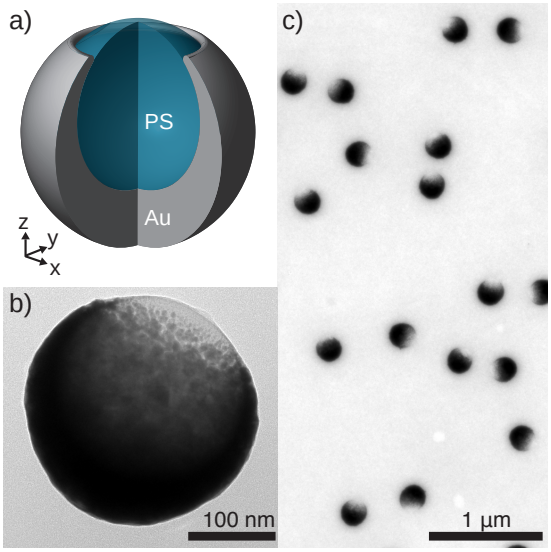

Figure 8.1 – Metal-dielectric crescents (a) Schematic of a crescent consisting of a polystyrene (PS) core (blue) and a Au shell (grey). (b) Bright-field TEM image of an individual crescent. (c) Wide-field TEM image of crescents.

of the CL technique, including determination of electron-sample interactions via Monte Carlo simulations, is provided along with Supporting Figure 8.13.

As the electron beam passes through the base of the crescent (lighter colored lines in Figure 8.2(b)), the CL signal exhibits a broad peak between approximately 550 nm and 700 nm. This broad feature is understood by considering three contributions: the high energy plasmonic resonance supported by the crescent, the contribution of radiation from electron-hole pair recombination in the Au shell, and luminescence from the polystyrene core of the crescent. The higher energy plasmonic modes exhibit significant field intensity near and inside the base of the crescent, as detailed in Supporting Figure 8.10. BEM CL simulations reveal, however, that radiative decay of the high energy modes alone cannot account for the strong signal at short wavelengths observed in the experiments (see Supporting Figure 8.12). By comparing CL spectra to photoluminescence (PL) spectra of both crescents and polystyrene cores, we determine that a significant portion of the CL signal at short wavelengths is due to Au [304–306] and polystyrene luminescence [307] (see Supporting Figures 8.8 and 8.9).

Before tomographic reconstruction, we probe the effect of crescent angle on CL excitation efficiency. CL line scans of various crescents at angles between 0° and 165°, in 15° increments, are collected. The normalized CL intensities at 850 nm are used to form the sinogram shown in Figure 8.2(d). From this sinogram, it is determined that the tip mode at a wavelength of 850 nm is excited for nearly all

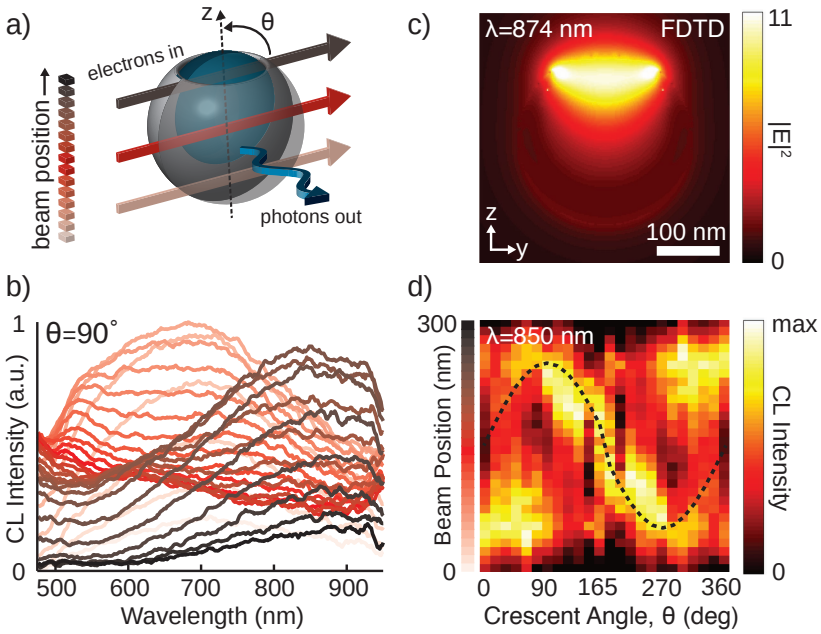

Figure 8.2 – Cathodoluminescence line scans (a) Schematic of the CL line scan, with the beam passing through the central z-axis of the crescent. θ is the angle between the crescent's axis of symmetry and the electron beam. (b) Experimental CL line scan of a crescent oriented at 90°, with darker line colors corresponding to higher beam positions, as indicated in (a). (c) Cross section of the scattered electric field intensity calculated by FDTD simulations for excitation with an x-polarized plane wave propagating in the $-z$ direction at a wavelength of 874 nm, the peak in the extinction efficiency. (d) Experimental sinogram of normalized CL intensity line scans at a wavelength of 850 nm for crescents at various angles, where the vertical axis corresponds to the excitation positions shown schematically in Figure 8.2(a). As a result of the reflection symmetry of the crescent, data from 0° to 165° are flipped and repeated for angles of 195° to 360°. A crescent at 180° was not available. The dashed line overlay denotes the physical position of the center of the gap between the tips of the crescent, derived from the crescent model.

crescent angles, except for the few angles near 0° and 180°. At these angles, the orientation of the electron beam is perpendicular to the tip gap, which results in inefficient excitation of this mode, as the electron beam preferentially couples to out-of-plane electric field components while the tip mode has a strong field oriented across the tips. A sinogram at 550 nm illustrates that CL is excited efficiently near and in the base of the crescent over a broad range of angles, as expected (see Supporting Figure 8.10).

By scanning the beam in the SEM and collecting a spectrum at each position, 2D CL maps are generated at all wavelengths concurrently. Figure 8.3 shows 2D CL

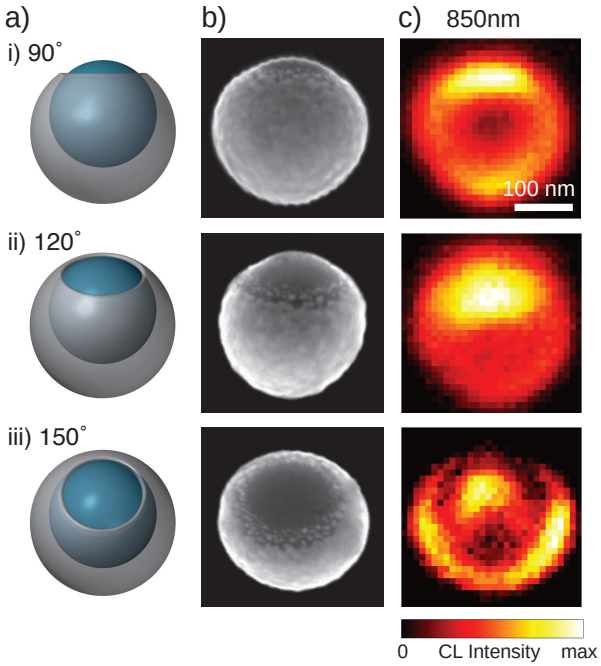

Figure 8.3 – 2D cathodoluminescence maps (a) Schematics of crescents with orientations of (i) 90°, (ii) 120°, and (iii) 150°. (b) SEM images of crescents. (c) 2D maps of the normalized CL intensity of crescents at a wavelength of 850 nm. The scale bar of 100 nm applies to all images.

maps at a wavelength of 850 nm for crescents at different orientations with respect to the electron beam, along with schematic representations and SEM images of the crescents. Note that this series of CL maps is the 2D extension of the 1D line-scans compiled in the sinogram of Figure 8.2(d). They confirm that the various modes can be excited for a wide-range of crescent angles, and allow 2D tracking of radiative optical properties for wavelengths spanning the visible and near-infrared spectrum (see also Supporting Figure 8.11).

8.3 3D reconstruction of monochromatic cathodoluminescence

We now use tomography to map the CL signal from the crescent in three dimensions. The CL maps just discussed, as well as the TEM images, represent 2D projections of a 3D function, and as such tomography can be used to reconstruct the 3D functions. In the case of the bright field TEM image, the intensity of the

signal is related to the integrated thickness and atomic number of the constituent materials. In CL, the intensity of a given pixel in a 2D map (as in Figure 8.3) is proportional to an integral of the CL along the electron's path. In both cases, for accurate reconstruction the generated images should satisfy the projection requirement for conventional tomography, which assumes that the signal must be linear and monotonic with the property of interest.

We first reconstruct the 3D structure of the crescent from a transmission electron micrograph to assist in the interpretation of the CL tomograms. The intensity of the TEM image is related to the integrated thickness and atomic number of the constituent materials, and rigorously satisfies the projection requirement for our non-crystalline samples. We carry out the reconstruction using a crescent oriented at 90°, as in the TEM image of Figure 8.1(b). Note that with this orientation, the crescent's axis of rotational symmetry (z) is perpendicular to the incident electron beam. Since the crescent is assumed to be rotationally symmetric, the single TEM projection of Figure 8.1(b) can be used as a virtual tilt-series spanning the full 360° of rotation [308]. To reconstruct the crescent's structure we use the tomographic method of filtered back projection, which forms a reconstructed image by summing partial reconstructions at various angles [309–311].

Figure 8.4(a) shows the resulting TEM tomographic reconstruction. The black portions of the reconstruction correspond to regions of high atomic number, i.e. gold, whereas the dielectric core appears white, similar to the vacuum background (see also Supporting Figure 8.14). In comparing this 3D tomogram to the original TEM image in Figure 8.1(b), it is clear that reconstruction has resulted in a significantly improved spatial representation of the structure.

To reconstruct the CL signal, we consider two different tilt-series: i) a virtual tilt-series constructed from a single experimental projection utilizing the rotational symmetry of a single crescent, and ii) the experimental tilt-series of crescents described in Figures 8.2 and 8.3. We first use the 2D CL map of Figure 8.3(c)(i) as a virtual tilt-series spanning the full 360° of rotation. For this crescent oriented at 90° with respect to the electron beam (z-axis parallel to the substrate) the excited modes are identical for any angle of rotation of the crescent about the z-axis. While modes that require a z-oriented electron beam are not excited in this configuration, the trajectory dependency of the excitation of all other modes is eliminated, as they will contribute uniformly to the CL signal across all tilt angles, allowing for a scalar reconstruction. Note that this use of symmetry to simplify an otherwise complex vector tomography problem is very similar to what was done in previous EELS tomography work [289]. Furthermore, note that material luminescence is a scalar quantity and thus trajectory independent (within the small particle assumption) and thus strictly satisfies the projection requirement. In summary, we can use the individual crescent oriented at 90° for a virtual tilt-series to directly reconstruct all but the z-component of the CL signal using conventional scalar tomographic methods. Note that this method assumes negligible particle-substrate interactions, a reasonable assumption for a crescent at θ=90°, as shown by simulations provided in Supporting Figures 8.15 and 8.16.

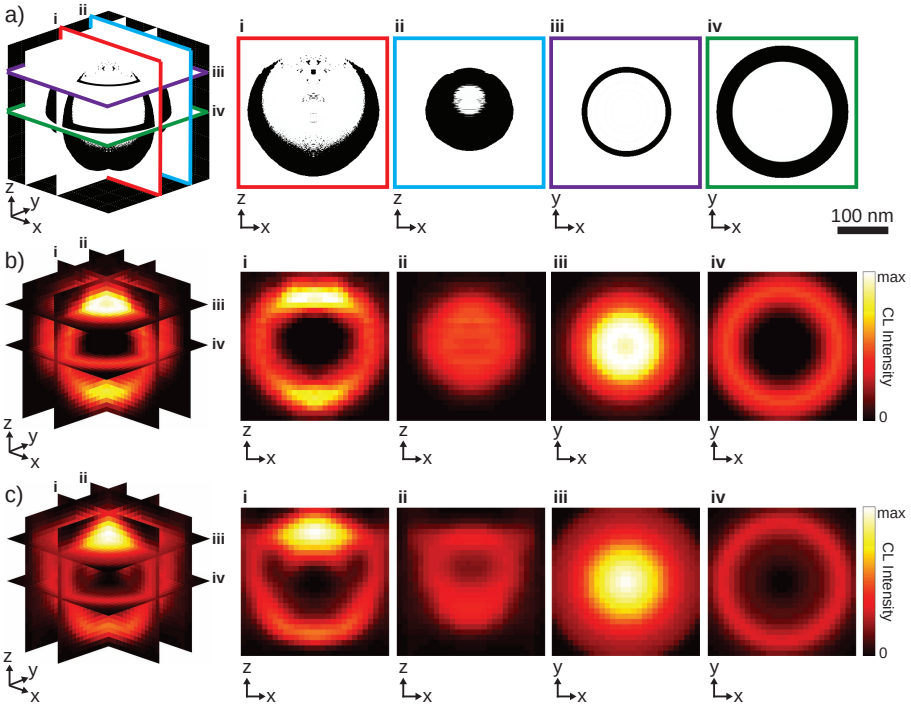

Figure 8.4 – 3D TEM and CL reconstructions (a) TEM tomogram based on a single projection. Panels (i–iv) correspond to different cross sections through the reconstruction, as indicated by the colored outlines. Panel (i) shows an (x, z) cross-section of the reconstruction at the midpoint of the crescent, where the metal shell and the crescent geometry can be distinctly resolved. Panel (ii) shows an off-center (x, z) cross-section of the reconstruction for comparison. Panel (iii) is a horizontal (x, y) cross-section of the reconstruction at the z position where the crescent tips come to a point, whereas panel (iv) is a (x, y) cross-section of the reconstruction at the midpoint of the crescent, clearly showing the metal shell surrounding the inner core. (b) CL tomogram at 850 nm based on a single CL map (reconstruction in (x, y) planes). (c) CL tomogram at 850 nm based on experimental tilt-series consisting of 7 crescents (reconstruction in (x, z) planes).

Figure 8.4(b) shows the result of a 3D tomographic reconstruction of the CL signal at a wavelength of 850 nm based on reconstructing individual (x, y) planes for each value of z (for a step-by-step illustration of this technique, see Supporting Figure 8.17). As shown by these figures, the highest CL signal is localized within the gap region between the tips of the crescent panels (i) and (iii) in particular illustrate the strong field enhancements that are spatially-localized in z near the tips, as expected for this mode based on the FDTD simulations shown in Figure 8.2(c), as well as the BEM simulations provided in Supporting Figure 8.12. Significant CL intensities can also be observed near and around the metallic shell, stemming

mostly from luminescence of the Au itself. A similarly detailed view of the CL reconstruction at a wavelength of 550 nm is provided in Supporting Figure 8.18 for comparison.

To rigorously reconstruct the complete CL signal, including modes excited in all three orthogonal directions, a fully vectorial reconstruction is needed. As no such technique exists at this time, we can approximately reconstruct the full CL signal by carefully considering a tilt-series in which the angle between the electron beam and the z-axis of the crescent is varied. The angular dependence of the excitation of the various modes strictly breaks the projection requirement, but by restricting the range of angles considered we can minimize this effect. Furthermore, we normalize the tilt-series prior to reconstruction at each wavelength to minimize the effect of the variation in excitation efficiency on the reconstruction. Although the resulting tomogram is thus not exact, it still provides useful information about the existence and qualitative 3D distribution of all excitable modes in our structure.

We consider CL maps of crescents at different orientations, some of which were shown in Figure 8.3. Note that this tilt-series is comprised of individual crescents at different orientations with respect to the fixed substrate, similar to single-particle analysis in TEM tomography [312], and thus provides information about a mean object. For this tilt-series, we obtain 2D CL maps for crescents with angles between 75° and 165°, in 15° increments (which, as a result of the reflection symmetry of the crescent, are equivalent to angles between 195° and 285°). We choose these angles because particle-substrate interactions are negligible for these crescent orientations (see Supporting Figures 8.15 and 8.16).

Reconstruction of the CL signal is then performed using the same filtered back projection method as before, except that the reconstruction is done by 2D reconstruction in the (x,z) plane for each value of y. Following the example set by previous work [289], we impose the symmetry of the particle during reconstruction to enhance the quality of the tomogram. Figure 8.4(c) shows the result of the 3D reconstruction of the CL signal at a wavelength of 850 nm based on reconstructing individual (x,z) planes. This experimental multi-crescent reconstruction compares well with the reconstruction from the single projection in Figure 8.4(b), with all of the main features reproduced: the strong field enhancement near the tips in both (i) and (iii), the reduced areal cross section in (ii), and the intensity in and around the Au shell in (iv). The remarkable agreement between the two reconstruction schemes, based on two very different sets of initial data, indicates both the validity of the assumption of negligible particle-substrate interactions for the angles considered here, as well as the merits of the qualitative reconstruction scheme. The quality of the multi-crescent reconstruction is also confirmed by comparing the original CL maps to re-projections of the tomograms at the same angles as were obtained in the experiment (see Supporting Figure 8.20).

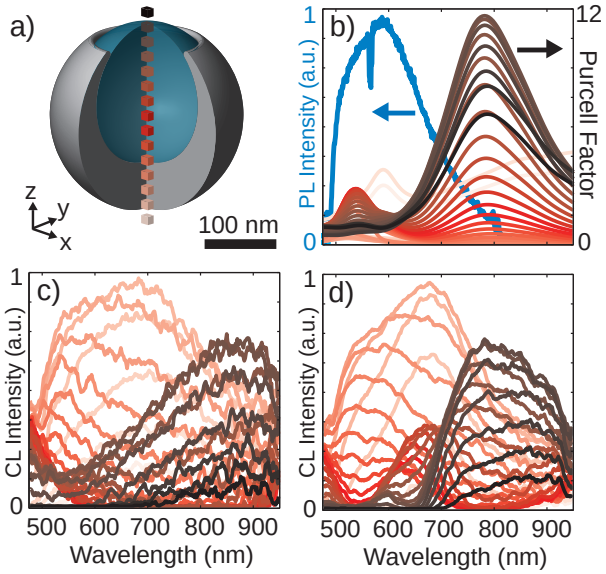

Figure 8.5 – Axial voxel cathodoluminescence spectra (a) Schematic of voxel positions within the crescent along its central axis. Darker colors correspond to higher z positions. (b) Total Purcell factor (average of x, y, and z components) calculated with FDTD along right axis. Average photoluminescence (PL) spectra of six individual crescents excited at 488 nm (blue curve, left axis). (c) Voxel spectra from CL reconstruction based on single CL map (reconstruction in (x, y) planes). (d) Voxel spectra from CL reconstruction based on experimental tilt-series consisting of 7 crescents (reconstruction in (x, z) planes).

8.4 Spectroscopic cathodoluminescence tomography

Since CL is a spectroscopic technique, we can reconstruct the CL signal in three dimensions at all wavelengths in the measured 475–950 nm range. Figure 8.5 plots the reconstructed CL spectra at volumetric pixels, or voxels, along the central axis of the crescent, as indicated in Figure 8.5(a). Figures 8.5(c,d) show the associated spectra for the single- and multi-crescent reconstructions, respectively. By comparing these spectra with the colored voxels in the schematic, it is clear that the CL spectra vary significantly with position. In the metallic base of the crescent (light pink curves), the CL is strong and peaks broadly between 550 nm and 700 nm. In the dielectric between the tips of the crescent (dark curves), the CL signal peaks again, at approximately 800 nm to 850 nm. Aside from the discrepancy between the spectra in the dielectric core of the crescent (red curves), which will be discussed below, the main spectral trends are visible in both the single- and multi-crescent reconstructions.

The spatially-dependent CL can be understood by considering two factors con-

tributing to the intensity of the CL signal in this system: the radiative LDOS within the crescent structure and luminescence from Au and polystyrene. To investigate the radiative LDOS, which is a measure of the number of radiative decay pathways available to an emitter, we use a FDTD method to calculate the radiative rate enhancement, or Purcell factor (PF), at each position along the crescent axis, as shown in Figure 8.5(b). These spectra indicate that the radiative LDOS peaks in the gap region between the tips of the crescent at a wavelength of 782 nm. This calculated result is in very good agreement with the peak seen in this spatial region in the reconstructed CL spectra of Figures 8.5(c,d). Notably, the rapid fall in signal intensity for voxels farther away from the tips is remarkably similar between the calculated PF spectra and the experimental CL spectra. An alternative visualization of this data, along with individual components of the PF, are provided in Supporting Figure 8.21.

Near the metallic base of the crescent, the reconstructed CL signal exhibits a significant and broad peak between 500 nm and 700 nm, which is not fully reproduced in the calculated PF spectra. This feature is also absent from BEM CL calculations shown in Supporting Figure 8.12. Like the BEM calculations, the PF calculations do not account for material luminescence and indeed, PL measurements of individual nanocrescents reveal significant electron-hole pair recombination in the Au shell, as shown in Figure 8.5(b). The PL from the Au shell peaks at a wavelength of 593 nm, with a spectral shape that closely resembles the reconstructed CL. The narrower width of the PL spectrum may be due to the narrowband characteristic of the laser used for PL experiments, compared to the broadband nature of the electron beam as an excitation source in CL, or to the different temporal characteristics of the excitation. Also, note that the sharp feature at 568 nm is related to the dominant Raman line (-CH_3 symmetric stretch, 2886 cm^{-1}) of the PDMS substrate used in this PL experiment [313].

In the dielectric core of the crescent, the multi-crescent reconstruction reveals a peak at around 650 nm not present in the single-crescent reconstruction (compare Figures 8.5(c,d). This peak is due to a mode that is not efficiently excited at 90°, and thus does not show up in the single-crescent reconstruction, which ignores modes that require a z-oriented electron beam for efficient excitation. This mode is identified through plane wave extinction calculations, BEM CL simulations, as well as Purcell factor calculations, which confirm the existence of a mode at approximately 600 nm excited in the center of the crescent for a z-oriented dipole, but not for x- or y- oriented dipoles (see Supporting Figures 8.7 and 8.22). The existence of this peak in the CL tomogram demonstrates the ability of the multi-crescent reconstruction to probe all modes of the system. Lastly, it is interesting to note that the spectra of both reconstruction methods show significant CL signal in the dielectric core of the crescent below 500 nm, rising up to the edge of the spectral window studied here. This signal stems from luminescence of the polystyrene bead itself [307], which peaks at approximately 450 nm (see polystyrene PL spectrum in Supporting Figure 8.9). Taken together, these results demonstrate the high spatial and spectral resolution of the experimental CL reconstructions.

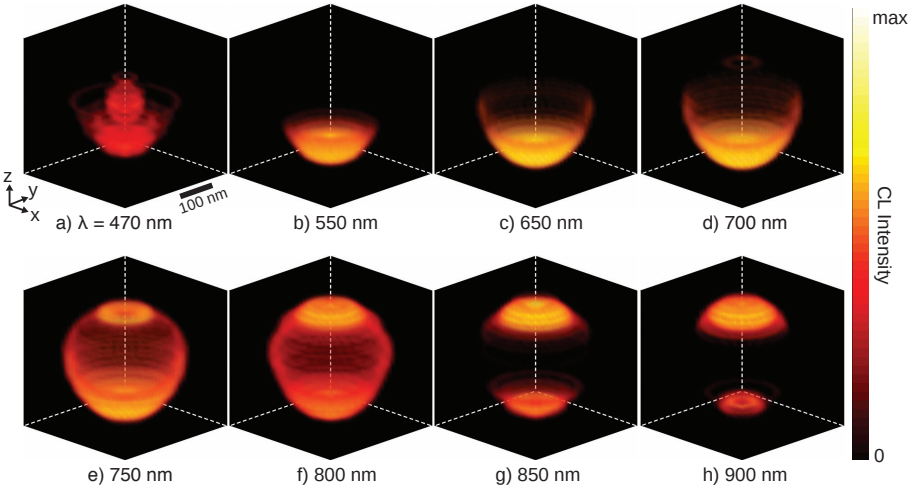

Figure 8.6 – CL spectroscopic tomography Reconstructed CL signal based on a single CL map (reconstruction in (x, y) planes) at wavelengths of (a) 470 nm, (b) 550 nm, (c) 650 nm, (d) 700 nm, (e) 750 nm, (f) 800 nm, (g) 850 nm, (h) 900 nm. The reconstructed intensity corresponds to both the color scale and the transparency of the figure. The scale bar of 100 nm applies to all images.

To obtain a complete sense of the spectral and spatial dependence of the CL signal, three-dimensional reconstructions at wavelengths between 470 nm and 900 nm are shown in Figure 8.6. In these images, the crescent is oriented with its tips at the top of the images. This figure contains tomograms generated from the single crescent at 90°; tomograms generated from the experimental multi-crescent tilt-series show excellent agreement and are provided in Supporting Figure 8.19. These spectroscopic CL tomograms clearly demonstrate how different spectral features contributing to the CL spectrum of a 3D nanostructure can be resolved at a spatial resolution well below the diffraction limit. Videos illustrating these reconstructions are provided online in the Supporting information of [314].

8.5 Conclusions

In conclusion, we have developed CL spectroscopic tomography as a novel technique to probe deeply subwavelength radiative optical properties in three dimensions. The technique allows spectral reconstruction of individual nanoscale volumetric pixels, spanning visible and near-infrared frequencies. The resultant tomograms reveal regions of efficient CL, with contributions from both material luminescence and radiative decay of resonant electromagnetic modes. Looking forward, we envision CL tomographic reconstructions that include momentum- and polarization-resolved information with nanometer-scale voxel resolution.

Additionally, application of CL tomography to systems beyond simple inorganic specimens should be straightforward. For example, this tomographic technique could be used to precisely locate radiative recombination centers in light emitting diodes, probe the nanoscale distribution of defect states in organic photovoltaics, and potentially provide new label-free avenues for biological imaging.

8.6 Methods

Crescent fabrication. Nanocrescents are fabricated by metal evaporation onto dielectric beads. An aqueous solution of 200 nm diameter polystyrene beads (Polysciences, Inc., coefficient of variance = 8%) is deposited onto a glass coverslip coated with polydiallydimethylammonium chloride, a charged polymer used to improve areal coverage. The coverslip is then mounted on a rotation stage that is tilted at an angle of approximately 45 degrees and rotated at 45 rpm during the e-beam evaporation. Au is evaporated at a rate of approximately one angstrom per second until the thickness of the metal at the base of the dielectric beads reaches about 70 nm. For TEM, the crescents are removed from the substrate with a carbon grid coated with an ultra-thin layer of polydimethylsiloxane (PDMS). For CL experiments, the crescents are removed from the original substrate with a PDMS stamp and then transferred onto a clean Si wafer via a transfer printing procedure that, importantly, does not preserve their orientation. The orientation of each crescent is determined by taking SEM images at 0° and 40° stage tilt and comparing the images to a computer-generated tilt-series.

TEM imaging. TEM images were obtained using a FEI Tecnai G2 F20 X-TWIN transmission electron microscope at 200 keV in bright field imaging mode.

CL spectroscopy. CL measurements were performed in an FEI XL-30 SFEG SEM with an aluminum paraboloid mirror attached to a piezoelectric positioning system. The 30 keV electron beam passes through a 600 μm hole in the mirror directly above its focal point. The beam spot diameter was approximately 10 nm, and the typical beam current used was approximately 1 nA. The emitted radiation is collected by the mirror and directed outside the microscope into a spectrometer outfitted with a liquid-nitrogen-cooled Si CCD detector. To generate one-dimensional (1D) and 2D CL maps, the beam is incrementally scanned and a spectrum is collected at each position. For all CL experiments, the electron beam step size and corresponding pixel size, is 10 nm. The CL spectra and sinogram in Figure 8.2, which represent line scans through crescents, are smoothed by averaging the central 3 pixel lines (30 nm) of the 2D map, as well as by averaging over wavelengths in a ±5 nm range. Spectral noise in CL maps and tomograms is reduced by averaging over wavelengths in a ±5 nm range.

Numerical simulations. Plane wave and dipole excitation of the crescent are modeled using three-dimensional finite difference time domain methods, with the software FDTD Solutions by Lumerical Solutions.
Electron-beam excitation is modeled using the boundary element method (BEM) [301–303]. In all cases, the simulated crescent has the following geometrical parameters: 270 nm diameter gold shell (permittivity from CRC Handbook of Chemistry and Physics); 200 nm diameter dielectric core (index = 1.47), offset in the $+z$ direction by 32.5 nm; 145 nm diameter of the tip gap; 5.5 nm radius of curvature of the tips; 1 nm mesh size. The extinction cross section under plane wave excitation is calculated as the sum of the scattering and absorption cross sections using a total-field-scattered-field source approach. The Purcell factor for a given position and orientation is calculated as the ratio of the power emitted to the far field by a dipole to the power emitted by a dipole in free space. The total Purcell factor at a given position is calculated by averaging the contributions from the three orthogonal orientations.

Tomographic reconstruction. The method of filtered back projection is used to reconstruct 3D functions from 2D projections. A ramp filter multiplied by a Hann window is used both to increase contrast and to decrease noise in the reconstructions. Complete details are provided in the Supporting information of [314].

Photoluminescence. PL spectra are collected from individual crescents on a PDMS substrate, using a focused CW Ar-ion laser operated at 488 nm. The PL spectrum shown in Figure 8.5(b) represents the average of six normalized single particle spectra. Dark-field scattering spectra are collected before and after laser illumination to guarantee that the crescents are not damaged during the experiment.

8.7 Supporting information

8.7.1 Nanocrescent mode simulations

The plasmonic modes of the crescent are determined by exciting the structure with plane waves in finite difference time domain (FDTD) simulations. The extinction efficiency, the ratio of the extinction cross section to the geometrical cross section, is calculated for various angles of incidence θ, where θ is the angle between the crescent's axis of symmetry and the polarization of the electric field in the (x, z) plane. The extinction spectra for angles between 0° and 90° in 15° increments are shown in Supporting Figure 8.7(a).

A number of different modes can be identified from the spectra. The lowest energy mode at 874 nm, excited most efficiently at 90°, is characterized by strong

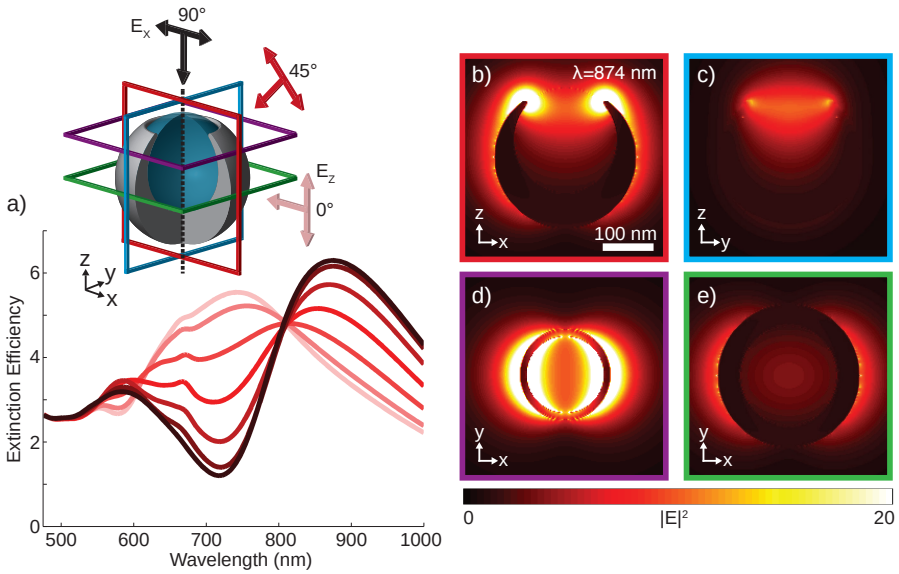

Figure 8.7 – Plane wave excitation (a) The extinction efficiency, calculated using FDTD, for plane waves at angles of incidence between 0° (light pink curve) and 90° (black curve), in 15° increments. The scattered electric field intensity at 874 nm of a crescent at 90° for cross sections of: (b) the central slice in the (x,z) plane, (c) the central slice in the (y,z) plane, (d) a slice through the tips in the (x,y) plane, and (e) a slice through the center in the (x,y) plane. The slices in (b–d) are color-coded according to the schematic in (a). Scale bar of 100 nm applies to all field maps.

electric field enhancement between the sharp tips of the crescent. This mode peaks at approximately 850 nm in the CL experiments, in excellent agreement with the simple model. The nature of this mode is illustrated in Supporting Figures 8.7(b–e), which plot the calculated intensity of the scattered electric field at 874 nm for a crescent oriented at 90° at various slices, as indicated in the color-coded schematic in Supporting Figure 8.7(a). Supporting Figure 8.7(b) plots the central cross section in the (x,z) plane, as defined in the main text. Supporting Figure 8.7(c) plots the central cross section in the (y,z) plane, orthogonal to the direction of electric field polarization. Supporting Figures 8.7(d,e) plot cross sections in the (x,y) plane at the position of the tip gap and at the center of the crescent, respectively. Note that these cross sections correspond to the slices of the reconstruction provided in Figures 8.4 (i), (iii), and (iv) of the main text. It can be recognized from the simulated cross sections shown here, that this mode is characterized by strong field enhancement primarily between the tips of the crescent, which agrees well with the experimental CL tomogram.

The mode at 740 nm is only efficiently excited at 0°, when the electric field is oriented in the z-direction. This mode is also accessible with a z-oriented dipole or

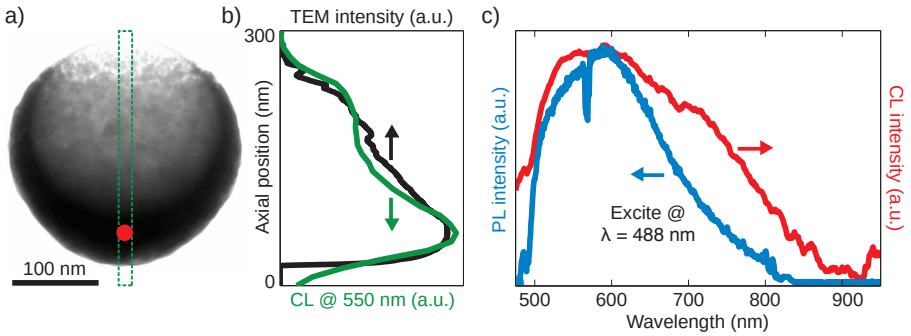

Figure 8.8 – Au luminescence. (a) TEM of crescent. (b) Axial line scans of both TEM intensity (black curve) and CL intensity at 550 nm (green curve) for the region identified by the green box in (a). (c) Average photoluminescence (PL) spectrum of six individual crescents when excited at 488 nm (blue curve), as well as the CL spectrum from inside the base of the crescent at the position identified by the red dot in (a), derived from the CL tomogram.

an electron beam propagating along z, and is thus observed in the multi-crescent tomogram, as described in detail in a later section. The next section describes the highest energy mode, at 580 nm, which is most efficiently excited at 90° and is characterized by an enhanced field near the base of the crescent.

8.7.2 Cathodoluminescence signal at high energies

To understand the peaks in the CL spectra at high energies, we must consider not only the radiative decay of plasmonic modes, but also the luminescence from Au and polystyrene. Radiation in Au occurs when an electron in the d band is excited to an unoccupied state in the sp conduction band. Some fraction of these excited electrons recombine radiatively with the holes in the d band, resulting in emission of a visible photon. This interband transition process is typically studied by exciting the Au with light using photoluminescence (PL) spectroscopy. For smooth Au films [304], the PL quantum yield is as low as 10^{-10}, and this source of radiation is thus often ignored in many CL experiments [92]. It has been shown, however, that nanoparticles of Au exhibit PL quantum yields as high as 0.04, more than eight orders of magnitude higher than Au films [305, 306, 315–318].

To demonstrate that radiation from electron-hole pair recombination in Au contributes to the CL signal of crescents, we consider both CL and PL from crescents in Supporting Figure 8.8. A TEM image of a crescent is shown in Supporting Figure 8.8(a), where, as a result of mass-thickness contrast, the intensity corresponds to the amount of Au at each location. We plot a line scan of the TEM intensity along the central axis in Supporting Figure 8.8(b), where it can be seen that the Au density peaks in the base of the crescent, as expected for this geometry.

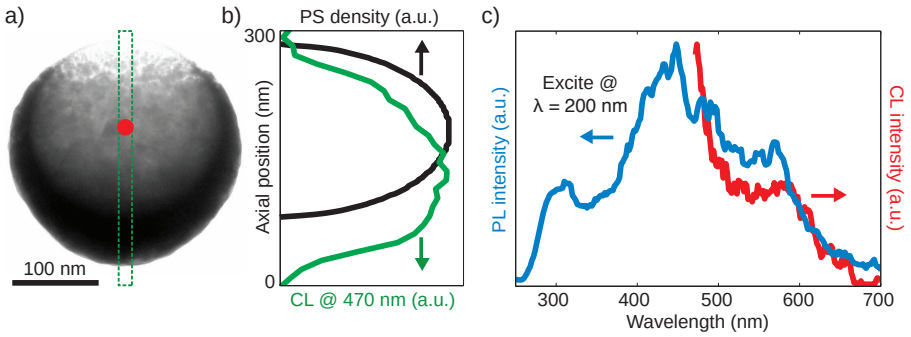

Figure 8.9 – Polystyrene luminescence. (a) TEM of crescent. (b) Axial line scans of both polystyrene (PS) density (from model, black curve) and CL intensity at 470 nm (green curve) for the region identified by the green box in (a). (c) Photoluminescence spectra of 200 nm diameter polystyrene beads (used as the dielectric core of the crescent) when excited at a wavelength of 200 nm (blue curve), as well as cathodoluminescence spectra from inside the polystyrene core of the crescent at the position identified by the red dot in (a), derived from the CL tomogram.

Overlaid in the figure is a line scan of the measured CL intensity along the central axis at a wavelength of 550 nm, where Au is known to fluoresce. By comparing these two curves, we see that the CL intensity at 550 nm tracks the Au density quite well. The fact that this CL signal is correlated with the amount of Au the electron interacts with suggests that luminescence from Au contributes significantly to the CL signal at this wavelength.

To confirm this hypothesis, we measure the PL of individual crescents excited at 488 nm with a CW Ar-ion laser. An average of six single crescent PL spectra is shown in Supporting Figure 8.8(c). The sharp feature at 568 nm is a result of the dominant Raman line (-CH_3 symmetric stretch, 2886 cm^{-1}) of the polydimethylsiloxane (PDMS) substrate used in this experiment [313], which shows up as a dip in the spectrum due to imperfect background subtraction. On top of this spectrum we plot the CL spectrum at the axial position in the base of the crescent where the peak Au density is found in Supporting Figure 8.8(b), as indicated by the red dot in Supporting Figure 8.8(a). This CL spectrum is from the multi-crescent reconstruction, as explained in the text. Both the PL and the CL spectra peak near 595 nm, and exhibit similar spectral shapes. The increased breadth of the CL spectrum may be a result of the broadband nature of the electron beam as an excitation source, as compared to the extremely narrowband characteristic of the laser used for PL experiments, or due to the different temporal characteristics of the excitation.

The strong spatial agreement of Supporting Figure 8.8(b) and spectral agreement of Supporting Figure 8.8(c) suggest that radiation due to electron-hole pair recombination in Au is responsible for a significant portion of the crescent CL signal at short wavelengths.

Another source of CL at the shortest wavelengths probed in this experiment is luminescence from the polystyrene core of the crescent, as shown in Supporting Figure 8.9. A TEM image of a crescent is provided in Supporting Figure 8.9(a) for reference. Once again focusing on the central axis of the crescent, we plot a line scan of the density of polystyrene in Supporting Figure 8.9(b), calculated based on the crescent geometry used in FDTD simulations. This is compared to a line scan of the CL intensity along the central axis at a wavelength of 470 nm, at which polystyrene is known to photoluminesce [307]. While some signal at this wavelength is likely a result of Au luminescence and radiative decay of the high energy plasmonic modes, the shape of the CL spectrum suggests that a portion of the signal is originating from the dielectric core, especially in comparing Supporting Figure 8.9(b) with Supporting Figure 8.8(b).

To confirm that the 200 nm diameter polystyrene beads used as the core of the crescents exhibit PL in this spectral regime, we perform PL measurements of polystyrene beads suspended in water using a Cary Eclipse fluorescence spectrophotometer. The excitation is centered at a wavelength of 200 nm and the emission is collected after a delay of one microsecond to avoid Raman scattering. The PL spectrum, smoothed by averaging over neighboring wavelengths in a ± 5 nm range, is provided in Supporting Figure 8.9(c), and is seen to peak at 450 nm, in good agreement with previous studies. Also plotted in this figure is the CL spectrum from the single-crescent reconstruction, at the axial position at the center of the polystyrene core of the crescent, as indicated by the red dot in Supporting Figure 8.9(a). In comparing these spectra, it is important to keep in mind that the luminescence of polystyrene will be modified by the presence of the Au shell. Although the PL from polystyrene beads is relatively broad, CL signal is only clearly observed within the dielectric bead in the 3D tomograms (Figure 8.6 of the main text) at the shortest wavelengths because radiation from the Au shell becomes dominant beyond 500 nm.

Of course understanding the plasmonic resonances supported by the crescent at these short wavelengths is also important when interpreting the CL signal, as radiative decay of these modes will contribute to the overall CL signal. The nature of the high energy crescent mode is elucidated by plotting the intensity of the scattered electric field at 580 nm, the peak in the extinction efficiency at high energies, when illuminated with a field polarized in the x-direction, as shown in Supporting Figure 8.10(a). It can be seen that the field enhancement is localized to the base of the crescent, both inside and outside of the metal shell. This is in contrast to the lowest energy mode at 874 nm, which exhibits the highest field intensity between the tips of the crescent. The high energy mode localized near the metallic base, while also excited directly by the electron beam, most likely enhances the radiation from Au near the base of the crescent.

The physical localization of this high energy CL signal is confirmed by examining the CL tilt series. CL line scans of crescents at angles between 0° and 165°, in 15° increments, are collected, and the normalized intensities at 550 nm are used to form the sinogram shown in Supporting Figure 8.10(b). Here, the dashed sine

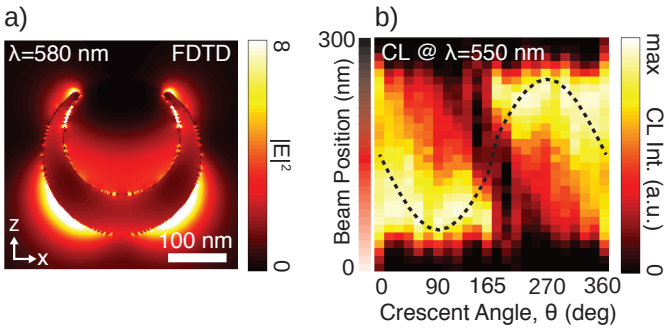

Figure 8.10 – High energy crescent mode (a) Central cross-section of the intensity of the scattered electric field for a plane wave incident along $-z$, polarized along x, at a wavelength of 580 nm. The largest enhancement is concentrated near the base of the crescent at this wavelength. (b) Sinogram of central CL scans at 550 nm. The dashed line tracks the position of the center of the base of the crescent.

curve overlay denotes the physical position of the center of the base of the crescent, derived from the crescent model, which roughly tracks the location of the CL signal, as expected for the high energy crescent mode. The downward sloping streak of low CL intensity in the middle of the sinogram corresponds to regions where the electron passes through relatively little Au, and consequently where less Au luminescence is emitted at this wavelength. This sinogram thus suggests that the high energy CL signal is comprised of both radiative decay of the high energy crescent mode as well as radiation from electron-hole pair recombination in Au.

CL maps of crescents with different orientations help illustrate this point more completely. Supporting Figure 8.11 shows schematics, SEM images, and 2D CL maps at 550 nm for crescents at angles of 90°, 120°, and 150°, respectively. The CL maps allow us to visualize where the most efficient excitation occurs at this short wavelength. As expected, across all crescent angles, the CL signal is highest towards the base of the crescent and where the Au is thickest. Note that these maps are part of a tilt-series of 7 crescents used to reconstruct the CL signal in three dimensions via tomography.

Another way to understand the spatial and spectral dependence of crescent CL is to compare CL line scans of crescents at different angles, as provided in Supporting Figure 8.11(d) for angles of 90°, 120°, and 150°. Here, the color of the different spectra correspond to the different excitation positions indicated in Supporting Figure 8.11(a). At short wavelengths, the CL peaks consistently near the base of the crescent (light pink lines) where the high energy modes are excited and where the metal shell is at its thickest. At longer wavelengths, the peak centered in the 800–850 nm spectral range (dark brown curves) decreases in magnitude for increasing crescent angle. This is a result of reduced coupling to this mode at 180° (or 0°) when the electron beam is parallel to the crescent's axis of symmetry. This mode is

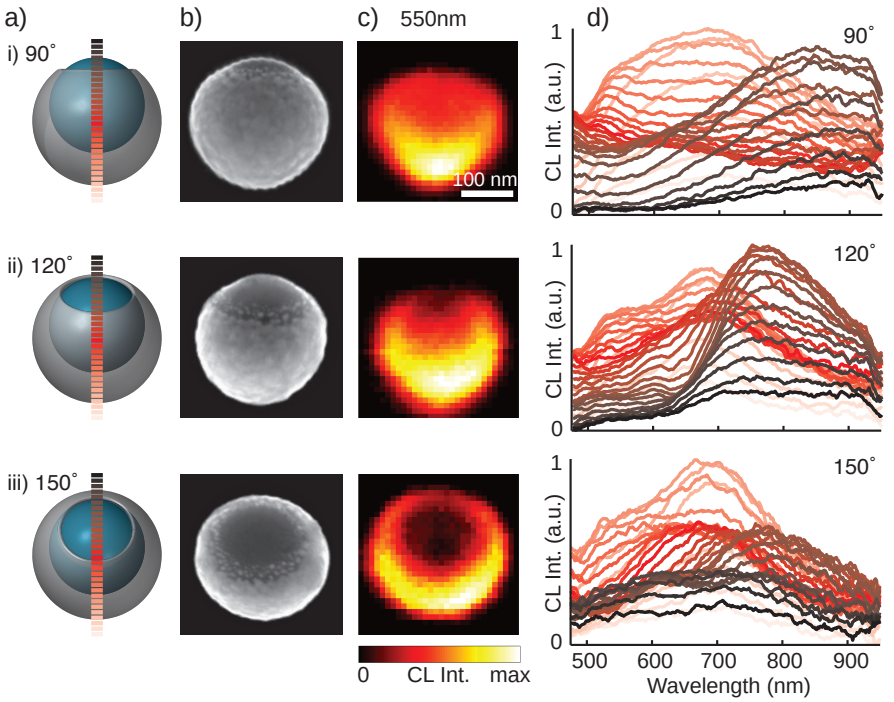

Figure 8.11 – Crescent CL tilt series (a) Schematics of crescents at various orientations, where the angle between the crescent's axis of symmetry and the electron beam is (i) 90°, (ii) 120°, and (iii) 150°. (b) SEM images of crescents. (c) CL maps of crescents at a wavelength of 550 nm. Scale bar of 100 nm applies to all images. (d) Experimental CL line scans of crescents where the line colors correspond to the excitation positions indicated in (a).

excited at most angles, however, and the slight shift in spectral position is likely due to small differences in the geometry of the sharp tips. The excitation of this mode across nearly all crescent angles is most clearly seen in the CL sinogram at 850 nm provided in the main text, which consists of 12 different crescent angles.

8.7.3 Boundary element method simulations of cathodoluminescence

We simulate the CL experiments using the boundary element method (BEM) [301–303]. This technique models the fields generated by the swiftly moving electron and is used to simulate the coherent portion of the CL signal, including radiative decay of electromagnetic eigenmodes and transition radiation. It is important to note, however, that this technique does not reproduce the incoherent portion of the CL signal, namely material luminescence.

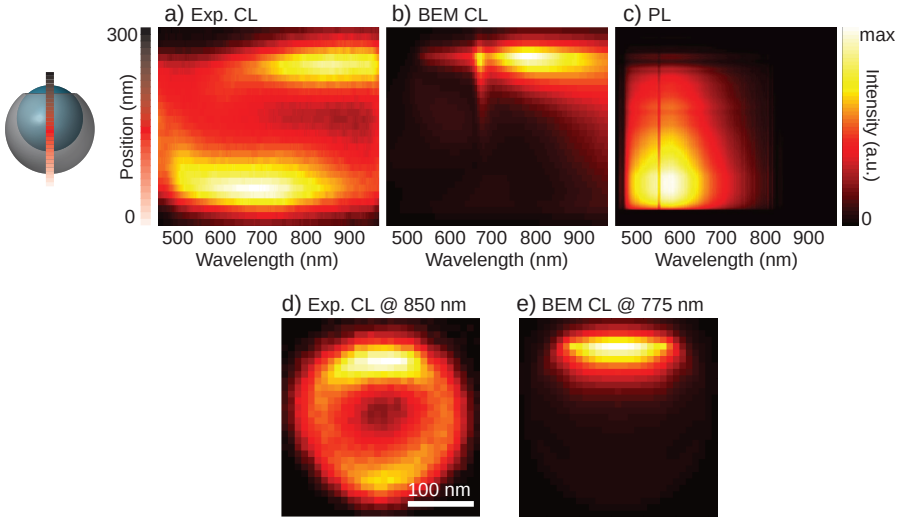

Figure 8.12 – Crescent CL simulations (a) Color map of the experimental CL line scan through the center of a crescent oriented at 90°. (b) The same CL line scan calculated via the boundary element method (BEM). (c) A line scan of the crescent photoluminescence (PL) spectrum weighted by the density of Au as determined by the TEM image. (d) 2D CL map of the crescent at a wavelength of 850 nm. (e) 2D CL map of the crescent at 775 nm calculated via BEM.

The crescent geometry used in the BEM simulations is the same as that used for the FDTD simulations. As a result of geometrical constraints of the code, the crescents are simulated in free space, ignoring the influence of the substrate, which should be minimal as described in a subsequent section.

Supporting Figure 8.12 shows the results of the BEM CL simulations for a crescent oriented at 90°. As a reference, Supporting Figure 8.12(a) is a color map of the experimental CL spectra for electron beam positions along the crescent's central axis, as shown in the schematic. Supporting Figure 8.12(b) represents the same data as calculated via BEM. Note that the bright feature at long wavelengths near the tips of the crescent is present in both the experiments and the BEM CL simulations. This signal is due to the radiative decay of the plasmonic mode of the crescent, illustrated in Figure 8.2(c) in the main text, which is efficiently excited by the electron beam. On the other hand, the feature at shorter wavelengths near the base of the crescent in the CL experiments is absent in the BEM CL simulations. This discrepancy indicates that the high-energy mode illustrated in Supporting Figure 8.10(a) is not efficiently excited by the electron beam. Thus, the short wavelength CL signal at the base of the crescent in the experiments must be due primarily to material luminescence, as this type of signal is not accounted for in the BEM simulations.

The material luminescence at the base of the crescent is best understood by

considering the photoluminescence (PL) of the crescents stemming from the Au shell, as discussed above. Supporting Figure 8.12(c) shows a spatial line scan of the PL spectrum weighted by the density of Au as determined by the TEM image, to serve as a qualitative approximation of the strength of the Au luminescence as a function of beam position in the CL experiment. From this comparison, the Au PL strongly resembles the experimental CL signal at short wavelengths near the base of the crescent. Recall that the increased spectral breadth of this CL signal compared to the PL is most likely a result of the broadband nature of the electron beam as an excitation source, as compared to the extremely narrowband character of the laser used for PL experiments.

We also compare experimental 2D CL maps with maps generated with BEM. The experimental CL map at a wavelength of 850 nm for a crescent oriented at 90° is provided in Supporting Figure 8.12(d). Supporting Figure 8.12(e) shows the BEM CL map at 775 nm, the peak wavelength in the simulations. These maps illustrate the excellent agreement between experiment and theory for the plasmonic tip mode. The weak signal in the metal shell in the experimental map is due to material luminescence, which is not accounted for in the simulations.

8.7.4 Electron-sample interaction simulations

Many factors influence the physical limits of resolution of the CL tomography technique. Most importantly, the lateral resolution of CL imaging is limited by the spot size of the electron beam and the radial extent of the evanescent field associated with the swiftly moving electron. Using an accelerating voltage of 30 kV and a beam spot diameter of approximately 10 nm, as in our case, previous work has found a lateral resolution of 30-40 nm [124].

The resolution in the third dimension will depend on the complex interactions of the electrons with the sample, and is thus highly dependent on the particular sample. To estimate the effect of electron-sample interactions on resolution for the crescents studied here, we have simulated electron trajectories using three-dimensional Monte Carlo software [122]. As a result of constraints of the simulation software, a simplified crescent-like object is considered. The crescent consists of a 270 nm diameter Au sphere with a 200 nm diameter polystyrene sphere enclosed within it. The center of the polystyrene sphere is displaced by 69 nm with respect to the center of the Au sphere, such that the Au shell has a thickness of 1 nm at its thinnest point, which corresponds to the center of the tip gap in the real crescent. A beam diameter of 1 nm is considered.

By tracking the trajectories of 10,000 electrons as they pass through the crescent in a particular orientation, we are able to statistically determine the divergence of the beam. Supporting Figure 8.13 depicts the electron-sample interactions for two representative crescent orientations. This figure indicates that for a 30 keV electron beam, 50% of the electrons deviate from their original path by less than 25 or 80 nm after passing through the entire structure, for vertically or horizontally oriented crescents, respectively. In other words, the beam width averaged over the

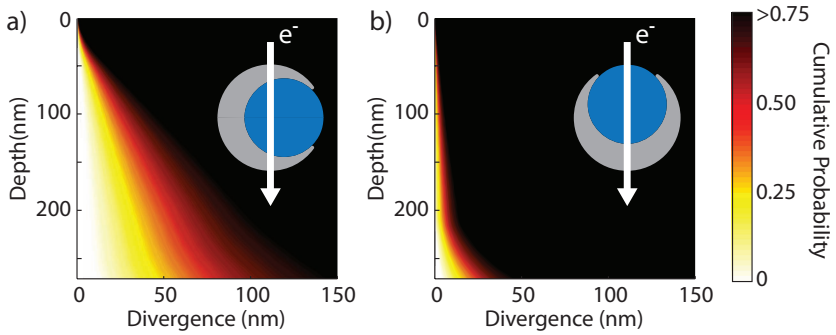

Figure 8.13 – Estimating electron trajectories Statistical analysis of Monte Carlo simulations reveal the divergence of electrons as a function of depth as the 30 keV beam passes through the crescent. A cumulative probability of 0.5 at a divergence of 25 nm indicates that 50% of the electrons have deviated by less than 25 nm at the given depth. A horizontally oriented crescent (a) and a vertically oriented crescent (b) are considered.

entire thickness of the crescent is between 12 and 70 nm. This unavoidable beam divergence will influence the effective lateral resolution of a 2D CL image, and thus the resolution of the 3D tomograms as well. We note, however, that the 2D CL map calculated with BEM in Supporting Figure 8.12, which assumes zero beam divergence, matches the experimental map quite well. Furthermore, the CL voxel spectra in Figures 8.5(c,d) in the main text correspond very well with the local density of optical states (Figure 8.5(b)) calculated for discrete points using FDTD. Generally, the agreement between experiments and theory indicate that beam divergence is not a significant issue for CL tomography of the metal-dielectric crescent. It is worth noting that the divergence of the beam is reduced by an order of magnitude for 300 keV electrons, such as can be obtained in a TEM.

8.7.5 Reconstructed crescent geometry

To define the crescent geometry for modeling purposes, we more closely investigate the geometry of the TEM reconstruction. Based on the reconstruction, we choose the model crescent to consist of a 200 nm diameter dielectric core and a 270 nm diameter Au shell displaced by 32.5 nm. The gap in the tips is chosen to be 145 nm, resulting in tips with a radius of curvature of 5.5 nm. A side-by-side comparison of the central slice of the reconstruction to the central slice of the model is provided in Supporting Figure 8.14. Visual inspection suggests that the simulated geometry (red) is quite similar to the TEM reconstruction (black), aside from the detailed geometry of the tips, which are sharper in the experiment.

To quantitatively compare the two geometries, we project the density of each along two orthogonal axes. The plot at the top of Supporting Figure 8.14 depicts

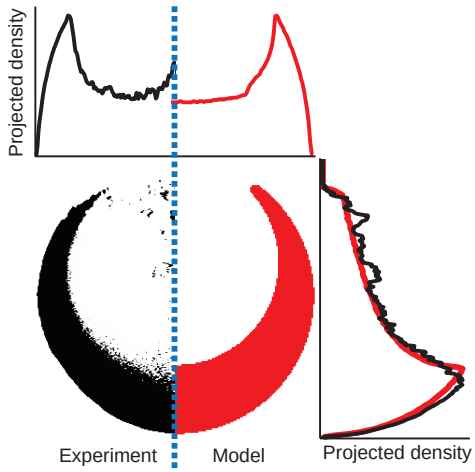

Figure 8.14 – Reconstructed crescent geometry Central slice of the TEM reconstruction (black) and the model used in FDTD (red). Projected densities along the vertical (top) and horizontal (right) directions show excellent agreement between the two geometries.

the projection in the vertical direction, while the plot at the right of the figure depicts the projection in the horizontal direction. These projected densities illustrate the excellent agreement between the model geometry and the experimental TEM reconstruction.

8.7.6 Effect of substrate on crescent tilt-series

To construct a tilt-series of crescents for tomographic reconstruction, we must rely on distinct crescents with different orientations relative to the substrate. This is due to the inability to tilt the sample in the CL SEM. An important assumption of this multi-particle tomography method is that the properties under study are not significantly affected by the substrate. We justify this assumption by considering two important dipole locations, as shown in Supporting Figures 8.16 and 8.15.

The first dipole is located in the metal base of the crescent, 55 nm from the outer edge, as depicted in the schematic inset of Supporting Figure 8.15(a). This dipole location is chosen because of the importance of metal luminescence in the CL signal. The second dipole is located in the dielectric core of the crescent, 72.5 nm from the outer edge along the crescent's axis of symmetry, and oriented perpendicular to the substrate (refractive index = 3.7), as depicted in the schematic inset of Supporting Figure 8.16(a). This dipole location is chosen for its ability to excite both the low energy gap mode at the tips of the crescent, as well as higher energy modes. The angle between the crescent's axis of symmetry and the substrate normal is defined

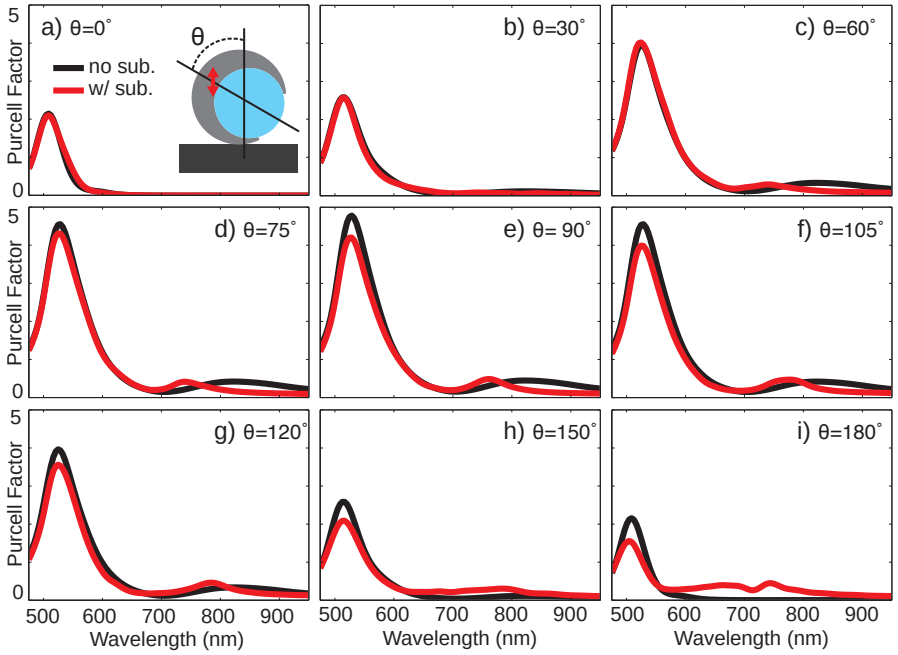

Figure 8.15 – Substrate effects The Purcell factor (PF), or radiative rate enhancement, for a dipole located inside the metal base of the crescent. The angle between the crescent's axis of symmetry and the substrate normal is defined as θ, as shown in the schematic inset. (a–i) Data for angles of 0°, 30°, 60°, 75°, 90°, 105°, 120°, 150°, and 180° are shown. The PF with no substrate (black curves) are compared to the PF with substrate (refractive index n=3.7) for each angle θ (red curves).

as θ. Note that in the absence of particle-substrate interactions, angles of θ and $180° - \theta$ would give the same response.

Supporting Figures 8.15(a–i) and 8.16(a–i) (red curves) plot the Purcell factor, or radiative rate enhancement, spectra for angles of 0°, 30°, 60°, 75°, 90°, 105°, 120°, 150°, and 180°, respectively. The black curves represent the PF when no substrate is present. Supporting Figure 8.15 demonstrates that the substrate has a negligible effect on the LDOS within the base of the metal shell of the crescent. From Supporting Figure 8.16, it can be seen that the substrate diminishes the intensity of the peak near 800 nm for angles close to 0°. For angles of 75° and above, however, the effect of the substrate is minimal, as the spectra with and without substrate agree well. For these reasons, we perform the multi-crescent tomographic reconstruction using a tilt-series composed of crescents at angles of 75° and above.

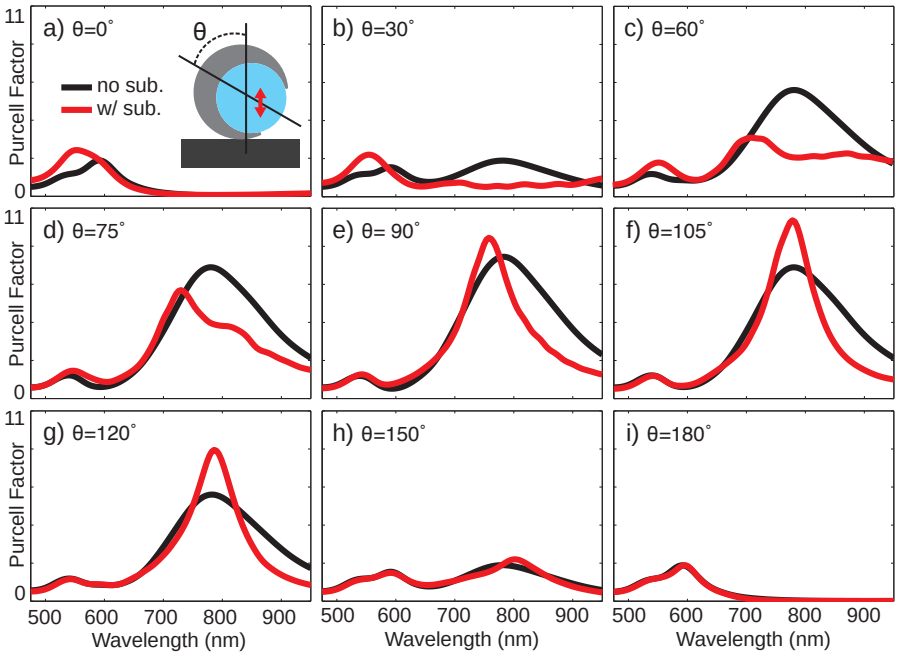

Figure 8.16 – Substrate effects The Purcell factor (PF), or radiative rate enhancement, for a dipole located inside the crescent's dielectric core. The angle between the crescent's axis of symmetry and the substrate normal is defined as θ, as shown in the schematic inset. (a–i) Data for angles of 0°, 30°, 60°, 75°, 90°, 105°, 120°, 150°, and 180° are shown. The PF with no substrate (black curves) are compared to the PF with substrate (refractive index n=3.7) for each angle θ (red curves).

8.7.7 Step-by-step cathodoluminescence reconstruction

To elucidate the reconstruction of the CL signal by the method of filtered back projection, we illustrate the step-by-step process in Supporting Figure 8.17. For simplicity, we explain the reconstruction based on a single CL image, but the method is general and is used for the reconstruction based on the full tilt-series, as well. Supporting Figure 8.17(a) shows the CL map at 850 nm for the crescent oriented at 90°, with its axis of rotational symmetry perpendicular to the incident electron beam. Assuming the crescent is rotationally symmetric and ignoring any substrate effects, we can use this CL map as a virtual tilt-series spanning the full 360° of rotation.

As mentioned before, the 3D reconstruction is accomplished by carrying out a 2D reconstruction in the (x, y) plane at each value of z. For this example, an intermediate value of z is chosen, as highlighted by the blue box in Supporting Figure 8.17(a). This data is a CL line scan through the crescent, perpendicular to its axis of symmetry, as shown by the black curve in Supporting Figure 8.17(b), where

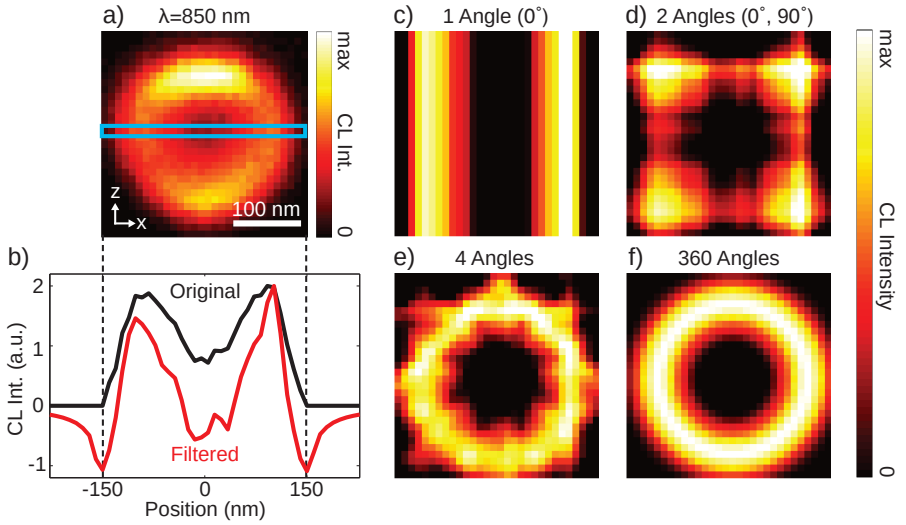

Figure 8.17 – CL reconstruction method (a) 2D CL map at 850 nm of the crescent at 90°. The blue box encloses the z height used in the reconstruction. (b) CL line scan before (black) and after (red) filtering in the frequency domain. (c–f) Reconstructions in the (x, y) plane made with the method of back projection using 1, 2, 4, and 360 angles, respectively.

data points beyond the boundaries of the scan have been set to zero. The red curve in this plot is the CL signal after being filtered in the frequency domain by a ramp filter multiplied by a Hann window (See Supporting information of [314]).

To illustrate the back projection method, reconstructions using an increasing number of angles are provided in Supporting Figures 8.17(c–f). When only a single angle, 0°, is used for the reconstruction (Supporting Figure 8.17(c)), it can be seen that the filtered function is simply smeared across the reconstructed image plane in the vertical direction. When two angles, 0° and 90°, are used (Supporting Figure 8.17(d)), the vertical and horizontal back projections sum to give a square-like pattern. With the four angles 0°, 45°, 90° and 135° (Supporting Figure 8.17(e)), the donut-like form begins to take shape. Supporting Figure 8.17(f) shows the complete reconstruction using 360 angles, or a projection every degree. From these figures it is clear that the accuracy of the reconstruction is dramatically improved through the use of projections at multiple angles. It is also important to note, however, that even with only 4 angles, the general shape of the reconstructed function is apparent. This indicates that the tomogram based on the actual tilt-series data, which makes use of 14 angles, should, in fact, capture the essence of the 3D CL signal.

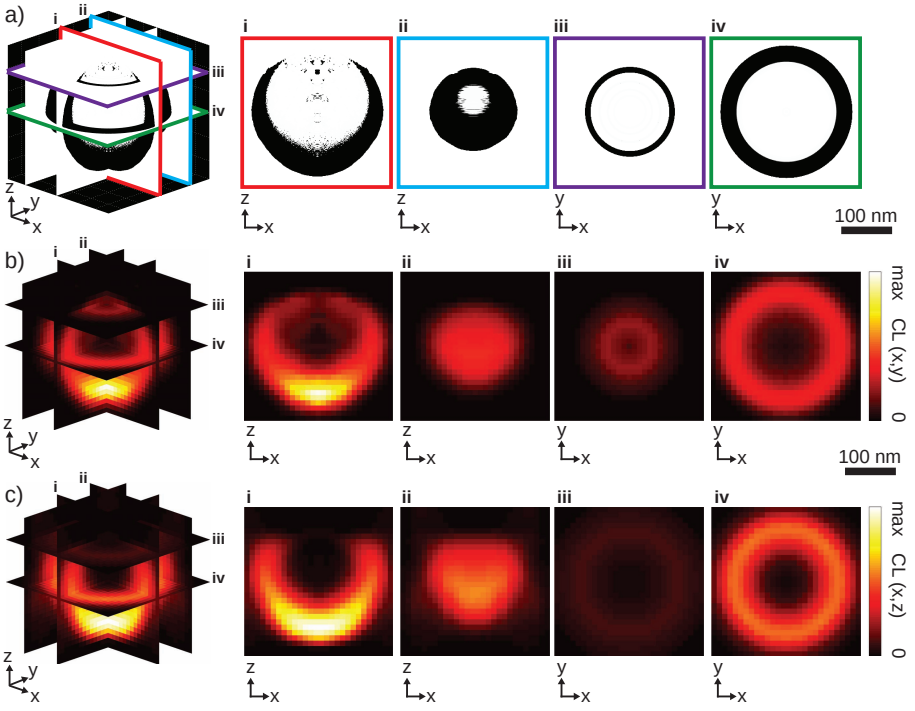

Figure 8.18 – 3D TEM and CL reconstructions at 550 nm (a) TEM tomogram as a visual aid for comparing structure to CL intensity. Panels (i–iv) correspond to different cross sections through the reconstruction, as indicated by the colored outlines. (b) CL tomogram at 550 nm based on a single CL map (reconstruction in (x, y) planes). (c) CL tomogram at 550 nm based on experimental tilt-series consisting of 7 crescents (reconstruction in (x, z) planes).

8.7.8 Cathodoluminescence tomogram at high energy

As mentioned, the tomographic reconstruction of the CL signal is performed at each wavelength. Supporting Figure 8.18 shows the CL tomogram at a wavelength of 550 nm. Supporting Figure 8.18(b) is a tomogram based on a virtual tilt-series, while Supporting Figure 8.18(c) is a tomogram based on an experimental tilt-series, as described in the text and elaborated in the next section. At this wavelength, the CL intensity is primarily localized to the regions of the crescent containing Au (indicated by the black portions of Supporting Figure 8.18(a), a TEM tomogram). This corroborates the assertion that the CL signal at shorter wavelengths is primarily a result of luminescence from the Au shell.

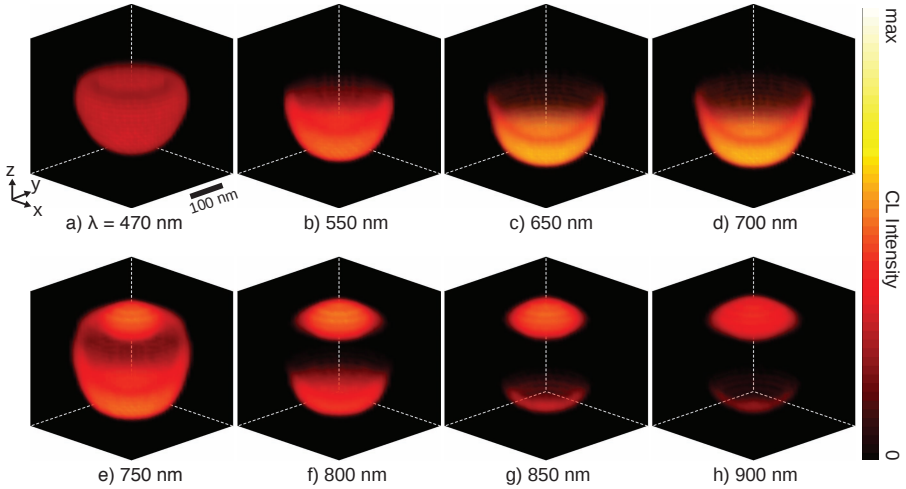

Figure 8.19 – 3D CL Spectroscopic Tomography Reconstructed CL signal based on experimental tilt-series (reconstruction in (x,z) planes) at wavelengths of (a) 470 nm, (b) 550 nm, (c) 650 nm, (d) 700 nm, (e) 750 nm, (f) 800 nm, (g) 850 nm, and (h) 900 nm. The reconstructed intensity corresponds to both the color scale and the transparency of the figure.

8.7.9 Cathodoluminescence tilt-series reconstruction and reprojection

As described in the text, while the rotational symmetry of the crescent allows for a simple reconstruction of the CL signal from a single CL map, this symmetry is not a requirement of the CL tomography method. We also reconstruct the CL signal with the CL maps of crescents at different orientations. For this tilt-series, we consider crescents with angles between 75° and 165°, in 15° increments, ignoring angles between 0° and 60° for the reasons stated above. As a result of the reflection symmetry of the crescent, crescents at angles between 75° and 165° are equivalent to those at angles between 195° to 285°, and thus the tilt series is composed of 14 different angles. To reduce the effect of the angular dependence of the excitation of the various modes, we normalize the intensities of the 2D maps in the tilt-series at each wavelength prior to reconstruction. Thus, although the angular dependence strictly breaks the projection requirement, we minimize the effect and the resulting qualitative reconstruction still provides useful information about the existence and 3D distribution of all excitable modes in our structure. Finally, following the example set by prior work [289], we impose the particles' rotational symmetry during the reconstruction process to enhance the tomograms.

Supporting Figure 8.19 shows the 3D CL tomograms at wavelengths between 470 nm and 950 nm. In these figures, the intensity of the reconstructed function

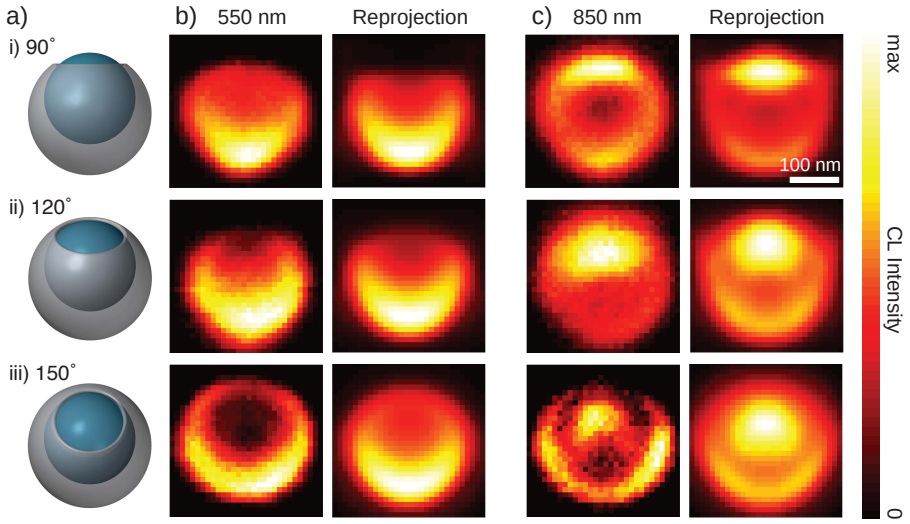

Figure 8.20 – Reprojections of multi-crescent tomogram (a) Schematics of crescents at various orientations, where the angle between the crescent's axis of symmetry and the electron beam is (i) 90°, (ii) 120°, and (iii) 150°. (b) and (c) original experimental CL maps of crescents (left columns) alongside reprojections of the multi-crescent tomogram (right columns) at wavelengths of 550 nm and 850 nm, respectively. Scale bar of 100 nm applies to all images.

corresponds to both the color scale and the transparency of the figure. These CL tomograms agree remarkably well with the CL tomograms shown in the main text, generated from the single crescent virtual tilt series. Most importantly, for shorter wavelengths we see that the CL signal is concentrated primarily in the metallic shell of the crescent, as expected for radiation from the Au. At longer wavelengths, efficient excitation of the gap mode can be seen clearly towards the top of the tomograms, near the tips of the crescent, as predicted by theory.

To confirm the quality of this multi-crescent reconstruction, we re-project the reconstructed volumes at the same angles as were obtained in the experiment. These reprojections, along with the original 2D CL maps of crescents at various angles, are provided in Supporting Figure 8.20. The excellent agreement between the original maps and the reprojections across all wavelengths and angles is indicative of the high fidelity of the multi-crescent reconstruction. This comparison is also useful in demonstrating the validity of generating a tomogram from many different nearly identical particles. Recall that the tomograms and thus the reprojections are based on 7 different crescents at 14 different angles. The strong agreement between these reprojections and the 2D CL maps of individual crescents is an indication of the similarity between the particles as well as the validity of the assumptions made.

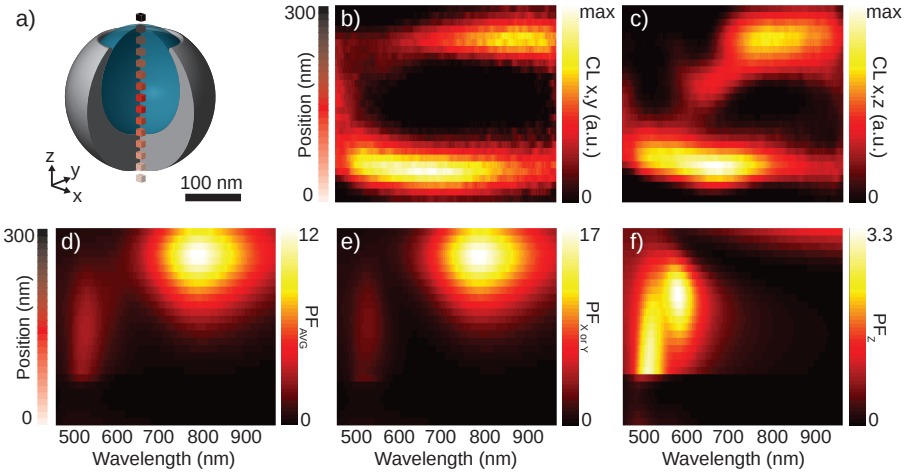

Figure 8.21 – CL reconstructions and Purcell factor calculations (a) Schematic of voxel positions within the crescent along its central axis. Darker colors correspond to higher z positions. (b) Voxel spectra from CL reconstruction based on single CL map (reconstruction in (x, y) planes). (c) Voxel spectra from CL reconstruction based on experimental tilt-series consisting of 7 crescents (reconstruction in (x, z) planes). Purcell factor calculated with FDTD for (d) average of x, y, and z components; (e) x or y component (equivalent due to symmetry); and (f) z component.

8.7.10 Purcell factor calculations

A comparison of the single- and multi-crescent reconstructions to Purcell factor (PF) calculations was provided in Figure 8.5 of the main text. A more detailed analysis is provided in Supporting Figure 8.21. Reconstructed CL spectra at voxels along the central axis of the crescent for the single- and multi-crescent reconstructions are shown in Supporting Figures 8.21(b,c). The spectral color maps show excellent agreement for the plasmonic tip mode at wavelengths around 850 nm, as well as for the material luminescence in the base of the crescent at shorter wavelengths. In the dielectric core of the crescent, however, the multi-crescent reconstruction reveals a peak at around 650 nm not present in the single-crescent reconstruction.

To identify this feature, we calculate the Purcell factor (PF) within the crescent. The average PF is shown in Supporting Figure 8.21(d). By comparing the PF for x- or y-oriented dipoles in Supporting Figure 8.21(e) with the PF for a z-oriented dipole in Supporting Figure 8.21(f), we determine that the peak in the center of the dielectric core in the multi-crescent reconstruction is due to a mode that is not efficiently excited at 90°, and thus does not show up in the single-crescent reconstruction, which ignores modes that require a z-oriented electron beam for efficient excitation. Recall that this mode is also excited by a plane wave, but only when the electric field is oriented in the z direction.

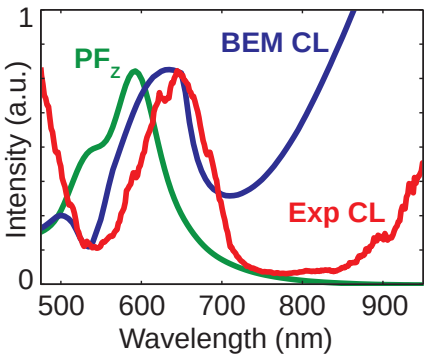

Figure 8.22 – Identification of the mode in the center of the crescent. Spectral comparison of the BEM CL intensity at the center of a crescent oriented at 0° (blue line), the z-component of the Purcell factor (PF_z) at the center of the dielectric core (green line), and the experimental CL intensity at the center of the dielectric core from the multi-crescent reconstruction (red line).

Additional insight into this feature is provided by BEM CL simulations of a crescent oriented at 0° (with the crescent's axis of symmetry parallel to the electron beam). Supporting Figure 8.22 shows a spectrum of the BEM CL intensity for an electron beam at the center of the crescent, along with the experimental CL intensity at the center of the dielectric core from the multi-crescent reconstruction. For comparison, the figure also includes the z-component of the PF at the same position. Note that the blue-shift of the simulated spectra with respect to the experimental spectrum is likely due to the substrate, which is not considered in the simulations. The agreement between these three spectra confirms that the peak at the center of the core of the crescent is, in fact, a mode that requires a z-oriented source for efficient excitation. This comparison also demonstrates the ability of the multi-crescent reconstruction to probe all modes of the system.

9

Near-infrared spectroscopic cathodoluminescence imaging polarimetry on silicon photonic crystal waveguides

We measure polarization- and wavelength-resolved spectra and spatial emission intensity distributions from silicon photonic crystal waveguides in the near-infrared spectral range using spectroscopic cathodoluminescence imaging polarimetry. A 30 keV electron beam acts as an ultra-broadband and deeply subwavelength excitation source. For a photonic crystal waveguide with a period of 420 nm and a hole radius of 120 nm, we observe a dominant emission intensity distribution that is confined to the waveguide for a wavelength of 1425 nm. The polarization-resolved measurements demonstrate that this feature is fully linearly polarized along the waveguide axis. Both the modal pattern and polarization correspond to the odd TE waveguide mode of the system, which is confirmed by good qualitative agreement with calculations of the modal field profiles. From the emission directionality, we conclude that we sample a leaky portion of the odd waveguide mode and that it is not fully guided within the photonic crystal waveguide.

9.1 Introduction

Photonic crystals, materials with a periodically varying dielectric function, can manipulate the propagation of light in a controlled way. They create a photonic band gap that prevents light from propagating in certain directions for certain frequencies [12, 16, 319–321]. Photonic crystal cavities can reach very high Q-factors to achieve strong light-matter interactions [15, 322, 323] and can be used for low threshold lasers [47, 324, 325]. Photonic crystal waveguides can serve as building blocks in photonic integrated circuits, such as splitters, switches, and multiplexers [326–328]. The modes is such waveguides are strongly dispersive and can slow down light, enhancing light-matter interactions [13, 14, 328–333]. To fully exploit the many applications of photonic crystal waveguides, it is essential to measure the propagation and confinement of light at a subwavelength scale. This cannot be achieved by conventional microscopy techniques. Near-field scanning optical microscopy (NSOM), which uses subwavelength probes or apertures to detect or scatter the near field of these structures [334–339], has enabled measurements of the field components of the optical near field just above the waveguide [77, 340, 341].

Here, we use cathodoluminescence (CL) spectroscopy to study silicon photonic crystal waveguides in the near-infrared (NIR) spectral range, coupling to and probing the field distributions inside the waveguide. In CL, a high-energy electron beam is used as a nanoscale optical excitation source in which the time-varying field of the electron couples to the local modes of the system as it traverses the sample [92, 124] (see Chapter 3). In CL, light scattered from these modes to the far field is then detected. The short interaction time of the electron with the structure (a few fs) results in a broadband excitation spectrum. The high excitation resolution of CL is only limited by the extent of the electric field about the electron trajectory and the spread of the beam in the sample. This allows one to explore the radiative local density of states (LDOS) at deeply subwavelength scales [105, 124]. Recently, it has become possible to measure the full polarization distribution of CL emission as a function of angle by using polarimetry [132, 259]. These properties have made CL a powerful, deeply subwavelength characterization technique [101, 102, 139, 179, 181, 182, 185, 194, 196], allowing measurements of the confinement and dispersion of plasmonic and dielectric photonic crystal cavities in the visible spectral range [124, 136, 195, 342].

In this article, we apply spectroscopic cathodoluminescence imaging polarimetry in the NIR spectral range to study the confinement and polarization of propagating photonic crystal waveguide modes. These structures possess different band structures for TE and TM polarization and support two modes for TE polarization, denoted as even and odd [321, 343, 344]. We demonstrate that CL imaging polarimetry enables direct identification and spatial mapping of the modal field distribution in the photonic crystal waveguides. The measurements show good agreement with calculations of the modal field intensities. We find that the CL emission is dominated by the odd TE waveguide mode. The results presented here

demonstrate the ability of CL to measure the spatial, spectral and polarization dependence of emission from complex nanophotonic structures in the near-infrared spectral range.

9.2 Experiment

Silicon photonic crystal waveguides (PCWGs) were fabricated on silicon-on-insulator (SOI) wafers with a 220 nm thick silicon layer on top of a 1 μm silica layer on a silicon substrate. Electron beam lithography was used to pattern the waveguides, followed by reactive ion etching to etch through the top silicon layer. A wet HF etch was used to remove part of the silica layer and obtain a suspended PCWG. Reference measurements in the visible and near-infrared spectral ranges demonstrate that a residual silica layer remains, since we observe characteristic silica defect-related emission peaks. Two different samples were studied; here we only discuss sample 1, showing data for sample 2 in the Supporting information. Figure 9.1(a) shows a SEM image of one of the PCWGs on sample 1 examined here, with a length of 90 μm and a total width of the photonic crystal section of 10 μm (25 periods). The PCWG is composed of a hexagonal array of holes with one missing row of holes (W1 waveguide) [321, 344, 345]. Five waveguides were made on sample 1 with the same period a=420 nm and hole radii varying in the range ~105–125 nm. Figure 9.1(b) shows a close-up of the waveguide section for the most studied structure (denoted as WG2), which has a period a=420 nm and a hole radius r=120 nm.

The TE band structure of WG2 is shown in Figure 9.1(c), calculated using the MPB software [346]. TE polarization corresponds to electric fields that are oriented in the plane of the waveguide slab at z=0. The gray bands represent modes that make up a continuum below and above the photonic band gap, which opens up between normalized frequencies of ~0.25–0.32, corresponding to free space wavelengths of $\sim\lambda_0$=1300–1700 nm. The discrete bands at the lower right are index-guided bands [321]. These are confined by total internal reflection in the slab in all directions since the waveguide itself has a higher average permittivity than the surrounding environment. The band structure is very sensitive to the period, hole size and slab thickness [347].

Removing rows of holes leads to allowed modes within this bandgap [343–345, 348], that are confined vertically by index-guiding (total internal reflection), but horizontally by the band gap of the photonic crystal. For a single row of missing holes there are two TE waveguide modes in the band gap: an even mode with a symmetric field distribution and an odd mode with an anti-symmetric distribution for the in-plane electric field component perpendicular to the propagation direction [329, 343]. The even mode has been studied intensely due to its anomalous dispersion and vanishing group velocity at the edge of the Brillouin zone [13, 326, 328–330, 332]. The odd mode is less well studied, but also displays slow light over a broad range of wavevectors. The dashed line in the figure represents the light

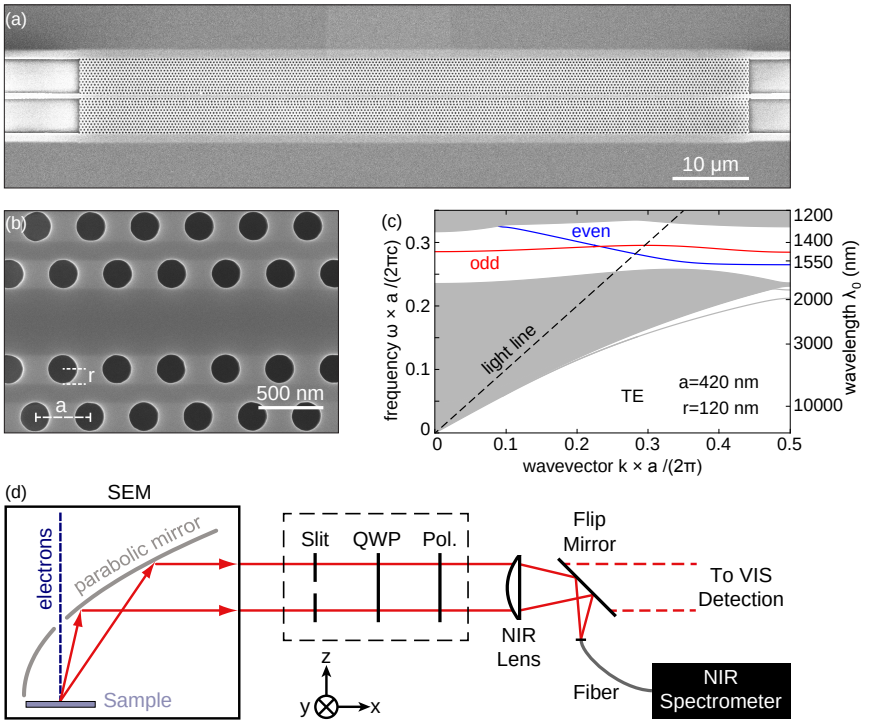

Figure 9.1 – (a) Scanning electron micrograph of one of the silicon photonic crystal waveguides on sample 1 studied here. A 90 µm long, 10 µm wide, and 220 nm thick waveguide with a hexagonal lattice of holes is suspended above a substrate of silica on silicon. (b) Close-up micrograph of waveguide WG2, with a period of a=420 nm and a hole radius of r=120 nm. (c) Band diagram of the waveguide from (b), for TE polarization, showing a selection of modes. The gray lines denote modes that are in the continuum of available modes above and below the photonic band gap. Within the band gap we distinguish an even (blue) and odd (red) waveguide mode. The black dashed line corresponds to the light line of air. (d) Schematic of the cathodoluminescence spectroscopy system. The 30 keV electron beam excites the sample, a parabolic mirror collects the emitted radiation and directs it to an optical setup where we can focus the light onto a fiber connected to a NIR spectrometer. We can also filter the emitted beam with a slit and measure the full polarization state using a QWP and linear polarizer. The coordinate system is also shown, with the PCWGs oriented along the y-axis for all measurements in the main text.

line in air; modes to the left will be leaky and modes to the right are guided in the waveguide slab.

In addition to TE modes, the photonic crystal possesses TM modes, with an electric field perpendicular to the waveguide slab at z=0. Such modes are usually excited efficiently by CL, since the moving electron acts as a vertically polarized source. In Figure 9.9 of the Supporting information we show the band structure for

TM polarization. We find that there is a small photonic band gap for wavelengths in the range ~ λ_0=1100–1200 nm with two waveguide modes within. In the spectral range of the TE band gap, the TM band structure exhibits a continuum of modes. Modes inside or near the band gap are usually localized to the waveguide, while modes in the continuous bands are more delocalized over the photonic crystal [321, 343]. The PCWGs studied here are specifically designed for high quality TE modes rather than TM modes. There are thus multiple possible sources of emission, for both TE and TM polarization, when exciting these Si PCWGs with swift electrons.

Figure 9.1(d) shows a schematic representation of the CL setup [124, 128, 183]. The 30 keV electron beam excites the sample and a parabolic mirror collects the subsequent emission and directs it onto a fiber connected to a NIR spectrometer. The small size of the electron probe and precise scanning capabilities of the SEM allow us to perform spectrally- and spatially-resolved scans of the PCWGs. We also measure the spectrally-resolved polarization of the emission by adding a movable, vertical slit to the optical path. In general, the polarization of the emitted radiation can change as it reflects off the mirror, due to its curved shape. The slit selects the central part of the mirror and thus conserves the emission polarization [129, 130], integrating over zenithal angles for a narrow range of azimuthal angles. We perform measurements for different positions of the slit and orientations of the waveguide with respect to the mirror to determine the polarization state and emission directionality (see Supporting information). We combine a quarter-wave plate (QWP) and linear polarizer (Pol.) to determine the Stokes parameters, which fully describe the polarization state of the emitted light [131, 132]. This allows for the separation of polarized and unpolarized light, as well as the retrieval of different field components and the relative phase difference between them [131]. The Methods Section describes the experimental setup and measurement protocol in more detail. For the measurements described in the main text, all waveguides are oriented along the y-axis, as defined by the coordinate system in Figure 9.1(d).

9.3 Near-infrared spatially-resolved cathodoluminescence

Figure 9.2 shows 2D spatial CL intensity maps from WG2, at wavelengths of λ_0=1170 nm (a), λ_0=1185 nm (b), λ_0=1400 nm (c), and λ_0=1425 nm (d), all averaged over a 20 nm bandwidth. Combining the raw data with the spectral response of the system and in-situ beam current measurements allow us to determine the CL emission probability (number of photons emitted per incoming electron, per unit bandwidth of nm^{-1}) [119]. We additionally correct the data for the dark response of the detector as well as for signal from the remaining silica and the silicon substrate, which contributes a broadband response and a peak at λ_0=1275 nm. To do so, we use a reference spectrum measured in one of the holes, which has no contribution from the waveguide or photonic crystal modes. In the Supporting information, we show additional measurements for a sample with a different period (Figure 9.6),

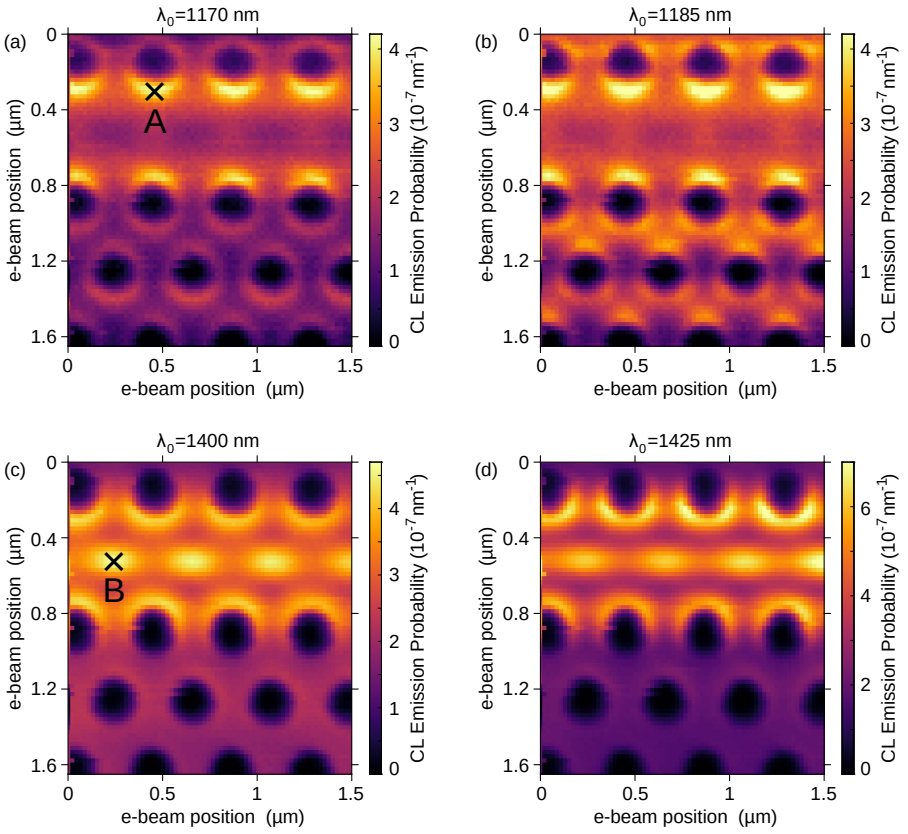

Figure 9.2 – Measured CL emission probability of WG2, as a function of wavelength and excitation position, for center wavelengths of λ_0=1170 nm (a), λ_0=1185 nm (b), λ_0=1400 nm (c), and λ_0=1425 nm (d) (20 nm bandwidth). Black crosses denote the two locations for which we show spectra in Figure 9.4.

for the input section of WG2 (Figure 9.7) and for WG2 in the visible spectral range (Figure 9.8).

The measurements at λ_0=1170 nm and λ_0=1185 nm (Figures 9.2(a,b)), exhibit an overall similarity, with high intensity at the inner edges of the holes lining the waveguide and darker spots along the waveguide at positions in between four holes. These two positions are denoted as A and B in Figures 9.2(a,c). Figure 9.2(b) exhibits a distinct enhanced intensity at the edges of the holes outside of the waveguide, compared to Figure 9.2(a). Figures 9.2(c,d) show data at λ_0=1400 nm and λ_0=1425 nm, displaying a high intensity at the inner edges of the holes lining the waveguide, which wrap around the hole edges more than for the data at shorter wavelengths. The center of the waveguide exhibits high intensity features

at positions that were dark for λ_0=1170 nm and λ_0=1185 nm. At λ_0=1425 nm these peaks are most intense, while the region around the waveguide has a lower relative intensity than for λ_0=1400 nm. The fact that the signal for λ_0=1425 nm is very strongly confined to the waveguide suggests it is related to a waveguide mode.

The features at λ_0=1170 nm and λ_0=1185 nm occur in the upper band of the TE band structure (see Figure 9.1(c)), that represent modes that are delocalized over the waveguide and surrounding holes [321, 343], as seen in Figures 9.2(a,b). In addition to the TE modes, the TM modes can also be responsible for this measured emission. As Figure 9.9 of the Supporting information shows, there is a small TM photonic band gap for wavelengths in the range $\sim \lambda_0$=1100–1200 nm with two waveguide modes within. The emission patterns at λ_0=1400 nm and λ_0=1425 nm occur in the middle of the TE photonic band gap, where the even and odd waveguide modes are present. For TM polarization these wavelengths are in the continuum of modes below the band gap, where one expects modes that are more delocalized from the waveguide, unlike the patterns observed here that are quite strongly confined to the waveguide. In order to distinguish between TE and TM modes, we perform polarization-resolved measurements and calculations of the different electric field components.

Figure 9.3 shows calculations of the electric field intensity distributions (summed over all ω and k within the given frequency range) for the odd and even TE polarized modes at λ_0=1450 nm, using the MIT Photonics Band (MPB) code. For more details about the calculation procedure, see the Methods Section.

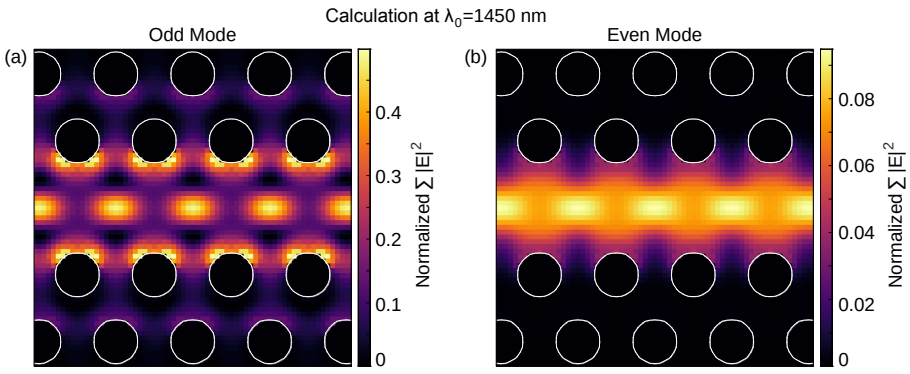

Figure 9.3 – Calculation of the modal intensity distributions of the two waveguide modes in the photonic band bap shown in the band structure diagram of Figure 9.1, for λ_0=1450 nm. (a) displays the odd mode and (b) the even mode. We calculate the E_x, E_y and E_z field components as a function of position and wavevector within a small frequency range, then integrate over all k and field components to obtain $\sum |E|^2$. The modal field intensities are normalized to the maximum intensity for all polarizations and wavelengths (obtained for TE at λ_0=1500 nm, not shown here). We note the strong difference in intensity between the two modes. The white circles show the positions of the holes.

Excellent agreement is observed between the data and the odd TE waveguide mode. TM-polarized calculations in the range λ_0=1430–1500 nm are shown in Figure 9.9 of the Supporting information, but exhibit no sharp features such as the ones on display in the measurements. Calculations in the range of the TM band gap (λ_0=1100–1200 nm) were not possible due to computational constraints related to higher order modes in the vertical direction.

The electron beam principally couples to field components that are parallel to the electron trajectory. For electrons propagating along z, this should lead to preferential coupling to the TM modes, yet we clearly observe TE modes. Our 2D calculations for TE polarization are performed at z=0, where E_z is strictly zero. The membrane does have a finite thickness, however, so E_z has nonzero components for other heights [321]. We can, for example, expect vertical components at the edges of the holes [77]. Considering the high intensity in the middle of the waveguide, the even mode is symmetric with respect to the center, for the in-plane field component perpendicular to the waveguide axis, so it is expected to remain in-plane. The odd mode however is anti-symmetric, exhibiting a field gradient and a pole at the very center where the field switches sign. This flip in the fields can be accompanied by a nonzero E_z component in the center for different heights, explaining why we preferentially measure the odd mode.

Another source of coupling between the electrons and the TE modes is the fact that scattering of the incident electrons inside the silicon membrane leads to a spread in their propagation directions, allowing for direct coupling to in-plane field components [124]. The scattering increases for lower electron energies, which should result in stronger coupling to the in-plane components. We do indeed observe higher intensities from the modal peaks using 10 keV instead of 30 keV (not shown here), indicating that the broadening electron distribution increases the coupling to TE modes.

9.4 Spectroscopic polarimetry

To further confirm the TE nature of the measured modes, we study the polarization-filtered spectral response of the waveguide. First, we show in Figure 9.4 the CL spectra at the inner edge of the hole lining the waveguide (position A in Figure 9.2(a), in red) and in the center of the waveguide between four holes (position B in Figure 9.2(c), in blue). Both positions are dominated by a peak at λ_0 ~1425 nm. The spectrum for position A also exhibits smaller peaks at λ_0 ~1225 nm and 1175 nm, for which the CL distribution was plotted in Figures 9.2(a,b).

The modal structure of PCWGs is extremely sensitive to small changes in the geometry, which is demonstrated in Figure 9.4(b), where we have measured the spectra for five different waveguides (WG1–WG5) with increasing hole sizes, all measured for excitation position A. We observe a clear redshift of the spectral features for decreasing hole size. We note a variability in the intensity as well as an

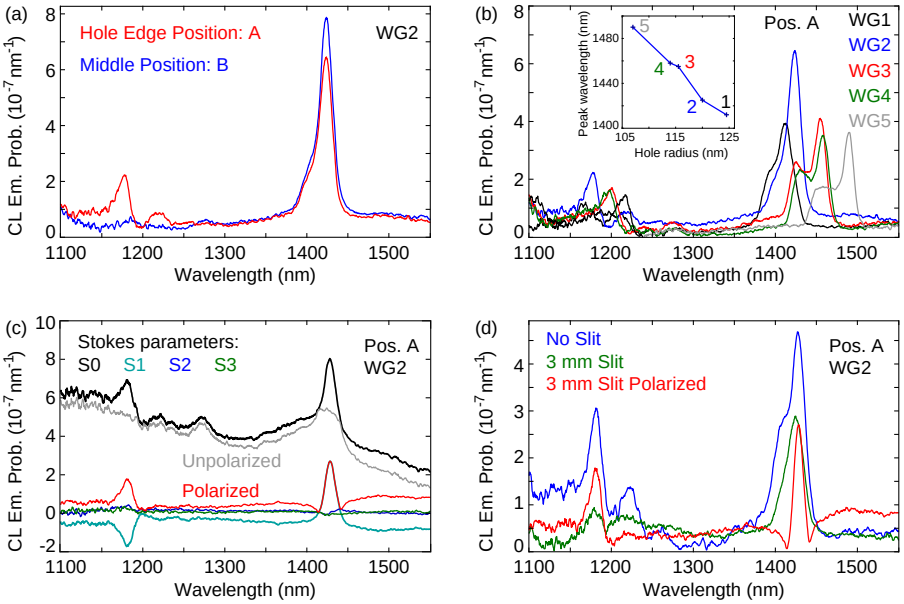

Figure 9.4 – (a) CL emission probability as a function of wavelength, measured on WG2, comparing the spectra obtained for two different excitations positions A (red) and B (blue) indicated in Figure 9.2. (b) CL spectra obtained for excitation position A on five different waveguides (WG1–WG5) with different hole size. The inset shows the wavelength of the dominant peak as a function of hole radius. (c) Polarization-filtered spectra measured on WG2 for excitation position A. We determine the Stokes parameters S0 (black), S1 (turquoise), S2 (blue) and S3 (green) and use them to separate the polarized contribution (red) from the unpolarized contribution that is due to the background luminescence from the substrate (gray). We note that S1 and the polarized contribution overlap at λ_0 ~1425 nm. (d) CL spectra for excitation position A on WG2 for different detection schemes: without a slit (blue), with a 3 mm wide slit filtering the emitted radiation (green), and the polarized spectrum measured with the slit, QWP and linear polarizer. We note there is a certain variability in the exact excitation position and thus on the measured intensity.

increasing contribution of a second peak on the blue side of the main emission peak, for decreasing hole size. The inset of Figure 9.4(b) shows the main peak resonance wavelength as a function of the hole radius, as determined from SEM images. A ~20 nm change in hole radius leads to a ~80 nm shift in the resonance wavelength, underlining the extreme sensitivity of the modal fields to geometrical parameters [347].

To measure the polarization-resolved spectra, we first place the movable slit with a width of 3 mm in the optical path. We find that both peaks at λ_0 ~1175 nm and λ_0 ~1425 nm in the spectra from Figure 9.4(a) exhibit maximum intensity in the middle of the mirror, for orthogonal orientations of the waveguide relative to the

mirror, indicating that the emission direction is close to the surface normal. We can now use polarimetry to determine the polarization state of the emitted radiation. More details on the implementation can be found in the Methods Section and the Supporting information.

We display the Stokes parameters for excitation position A on WG2 oriented along the y-axis in Figure 9.4(c). S0 corresponds to the total intensity, where we have not corrected for the emission from the substrate. S3 determines the ellipticity and handedness of the polarization and we find that S3≈0 for all wavelengths. This demonstrates that the slit is well-aligned to the center of the parabolic mirror since we expect that only the curvature of the mirror will contribute to that component. S2, which indicates the orientation of the principal axes of linearly polarized light, is also close to 0 over all wavelengths. All of the polarized contribution is contained in S1, meaning that the polarization is fully linear and either horizontal (S1>0) or vertical (S1<0). Horizontal polarization corresponds to emission polarized along the y-axis and vertical polarization corresponds to emission polarized along either the z-axis or the x-axis of the coordinate system (see Figure 9.1). We find that the dominant peak at λ_0=1425 nm is polarized along the waveguide orientation (y-axis for data shown here). In fact, measurements using different orientations of the waveguide (see Figure 9.10 of the Supporting information) demonstrate that all of the measured peaks are fully polarized in-plane rather than along the z-axis. This indicates that none of them are due to TM modes, since those are polarized out-of-plane.

Using polarimetry allows us to separate the polarized (in red) and unpolarized (in gray) contributions to the spectra from Figure 9.4(c). Compared to the total intensity S0 we can clearly see that a majority of the signal, including the small peak at λ_0 ~1275 nm, is unpolarized. We can ascribe this unpolarized emission to the luminescence from the substrate. The peaks in the polarized contribution all correspond to modal features in Figure 9.2 (for both excitation positions A and B).

Figure 9.4(d) compares spectra without the slit (blue), with the slit (green), and the polarization-filtered spectra (red). The main peaks at λ_0 ~1175 nm and λ_0 ~1425 nm are well-preserved in all cases, only decreasing in intensity by up to a factor of two. Given that we only collect emission from the 3 mm wide slit, compared to the 23 mm width of the mirror, this implies that the emitted radiation is relatively directional towards the surface normal.

Figures 9.5(a,b) show measurements of the polarization-filtered CL emission intensity distributions from WG2, at λ_0=1425 nm, for x and y polarization. Clearly, the emission is polarized along the waveguide axis y. Figures 9.5(c,d) show the calculated modal field intensity distributions (summed over k) at λ_0=1450 nm for the E_y (c) and E_x (d) components. We observe good qualitative agreement between the calculations and the measurements, especially for the E_y component, while the calculated E_x intensity is more intense than the x-polarized data. At this wavelength the mode is very close to the light line, but is still guided. The emission directionality towards the surface normal ($k \sim 0$) suggests that there is a contribution from the leaky part of the odd mode that can radiate out.

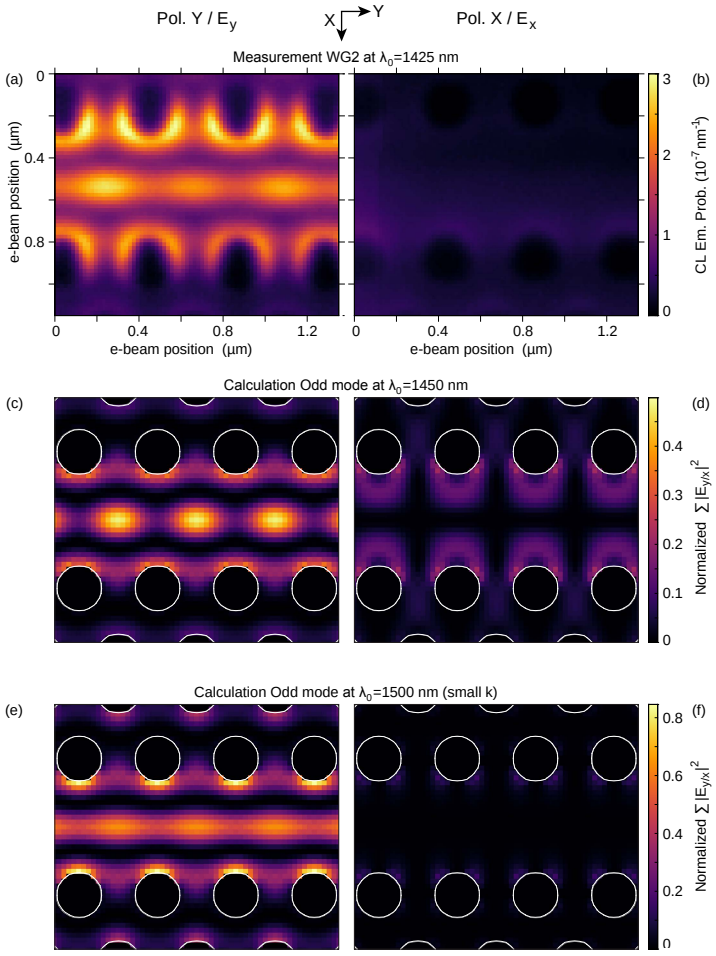

Figure 9.5 – Polarization-filtered 2D excitation maps of WG2, showing the CL emission probability as a function of the electron beam position for a center wavelength of λ_0=1425 nm, averaged over a 20 nm bandwidth. Only a linear polarizer was used here. The polarization is horizontal along the waveguide (along y) for (a) and vertical (along x) for (b) and the two are shown on the same intensity scale. (c) Calculation of the E_y field intensity for the odd waveguide mode at λ_0=1450 nm and the corresponding calculation for E_x (d), integrated over k within the frequency range, both shown on the same scale normalized to the overall total maximum intensity for all the calculations. We show E_y (e) and E_x (f) on the same scale for the odd mode calculated at λ_0=1500 nm, integrated (within the frequency range) over a range of k close to 0, above the light line. The distributions for k below the light line can be seen in Figure 9.11 of the Supporting information.

For this reason we also calculate the field profiles at λ_0=1500 nm, where the dispersion relation of odd mode intersects the frequency window of the calculation for regions of k both above the light line (close to k=0) and below the light line. The modal intensity distributions for k above the light line show very good agreement with the data, as we can observe in Figure 9.5(e) for the E_y intensity and in Figure 9.5(f) for the E_x intensity. The intensity profiles for k below the light line differ more from the measured emission profiles (see Figure 9.11 of the Supporting information). Comparing the measurements to the calculations, we find that the intensity distributions and relative intensities (for both polarizations) show agreement for both calculations, but there is clearly a better match with the leaky distributions at λ_0=1500 nm. The discrepancy in wavelength between measurement and calculation can be attributed to variations between the measured and calculated geometrical parameters, which we have shown to very strongly impact the resonance wavelength. We note that the calculations are not designed to determine field profiles in the leaky region above the light line, since they do not take into account nonzero values of k_z, which necessarily exist for leaky modes that radiate out of the waveguide to free space. Calculations in other systems that do fully take leaky contributions into account have shown that the mode can retain its overall field profile, even if it does becomes more lossy [257, 258]. In our case this is advantageous, as the mode is radiating out of the structure more freely, allowing us to measure it directly.

9.5 Conclusions

In conclusion, we have applied spectroscopic cathodoluminescence imaging polarimetry in the near-infrared spectral range to identify waveguide modes in silicon photonic crystal waveguides. These waveguides are designed to have highly confined modes inside the photonic band gap for TE polarization. Accordingly, the most striking feature that we observe is the odd TE waveguide mode of the structure, which exhibits a highly localized emission intensity distribution. Using spectroscopic polarimetry we demonstrate that this mode is fully linearly polarized along the direction of the waveguide. This is supported by calculations of the electric field intensities which show good qualitative agreement with both the measured intensity distributions and polarization. The vertically-polarized electron beam can couple to this in-plane mode as a result of nonzero contributions from the out-of-plane field component at different heights within the waveguide. A redistribution of the electron trajectories due to scattering also plays a role. The emission peak corresponding to the odd waveguide mode is directional towards the surface normal, indicating that we sample a leaky part of the waveguide mode that radiates out of the structure. Overall, we have demonstrated that spectroscopic cathodoluminescence imaging polarimetry is a powerful tool to measure light confinement and propagation in photonic crystal waveguides.

9.6 Methods

Cathodoluminescence measurements: The measurements were performed in a FEI XL-30 SFEG (10–30 keV electron beam, ~30–46 nA current) equipped with a home-built CL system [124, 128, 183]. An aluminium parabolic mirror collects the emitted light and directs it outside of the microscope to an optical setup. We can measure the spectrum in the λ_0=350–1000 nm spectral range with a liquid-nitrogen-cooled back-illuminated silicon CCD array (Princeton Instruments Spec-10 100B) and in the λ_0=900–1600 nm spectral range with a liquid-nitrogen-cooled InGaAs photodiode array (Princeton Instruments OMA V). Due to the readout noise of the individual pixels, we smooth the spectra with a moving filter over a 2 nm bandwidth. We correct for the system response of the setup by using transition radiation from single crystal aluminium as a reference [119]. A Faraday cup integrated in the sample holder measures the current of the electron beam, which in combination with the system response allows us to determine the CL emission probability. A quarter-wave plate (QWP, Thorlabs AQWP10M-1600) and linear polarizer (Pol., Moxtek PUBB01A50M) are used together to measure the full polarization state of the emitted radiation [132]. To measure the polarization we place a 3 mm wide slit in the beam path followed by the QWP and Pol., which offers a good balance between signal intensity and polarization contrast [129, 130]. Because we focus all of the light passing through the slit onto the spectrometer, the measured polarization is momentum averaged over the zenithal angles that are collected. A series of six measurements for different combinations of the QWP and Pol. (horizontal/90°, vertical/0°, 45°, 135°, right- and left-handed circular) determine the Stokes parameters, which fully describe the polarization state of the light. For all spectral measurements we collect a dark reference spectrum where we blank the electron beam, subtracting this from the data in the post-processing stage. Measurement errors can occur due to drift of the electron beam across the sample, bleaching or contamination leading to a reduction in the measured intensity, as well as fluctuations in the current and optical alignment of the mirror.

Calculations: To calculate the modal fields of the photonic crystal waveguide, we calculated the eigenfrequencies and complex field amplitudes E(r) using the MIT Photonics Band (MPB) code [346], which is a plane-wave method that uses periodic boundary conditions to calculate the eigenfrequencies and eigenmodes of our PCWGs. The band structure diagrams were calculated with the full 3D version. In order to conserve computational resources, we implemented a 2D version of the calculation using an effective index approximation to determine the field profiles. The effective index of the slab was chosen to be that of a 220 nm thick slab of silicon with the refractive index appropriate for each frequency range considered (for example for wavelengths around λ_0=1450 nm, we used 3.484). This procedure yields an effective index of 2.873 for TE modes and 1.831 for TM modes at λ_0=1450 nm. We determine the eigenvalues between 99 % and 101 % of the desired frequency. The E_x, E_y, and E_z field profiles (or eigenmodes) are calculated on a rectangular grid of

points separated by a/16, ensuring that the eigenfrequencies are converged to better than 0.1 %. The modes are normalized such that $\int_{\text{unit cell}} \epsilon(r) * |E(r)|^2 dr = 1$. The calculations are performed for wavevectors in the first irreducible Brillouin zone, after which we use symmetry arguments to add the fields for different wavevectors with the correct weighting factor, over the full first Brillouin zone. Essentially, we sum the field intensities over all wavevectors of the modes that occur within the frequency range of the calculation. The total field intensity is then determined by summing over all three field components. All of the resulting field intensity distributions are normalized to the maximum total intensity value for all wavelengths and polarizations (TE at λ_0=1500 nm).

9.7 Supporting information

9.7.1 Reproducibility for different geometrical parameters

The measurements in the main text were all performed on sample 1, containing waveguides with a 420 nm pitch and slightly different hole sizes, which shifted the resonance by ~4 nm per nanometer change in hole radius. To study how robust the measured features are to other changes in the geometry, we examine a second sample with a much smaller period, a=300 nm instead of 420 nm. The hole size is variable again, with a radius between 94 nm and 107 nm. Figure 9.6 shows the experimental results in the NIR for sample 2. We first examine 2D spatial scans of the PCWG with a hole radius of r=94 nm, finding distinct emission patterns for wavelengths much shorter than for the previous sample, namely λ_0=925 nm for Figure 9.6(a) and λ_0=1140 nm for Figure 9.6(b). The double row of bright spots at λ_0=925 nm is very different from any pattern measured on the other sample, which can be related to different dispersion, especially since there are more possible modes in the vertical direction of the slab at these short wavelengths. This measurement highlights the deeply subwavelength resolution of CL, since we can resolve this pattern so clearly at this scale. For a wavelength of λ_0=1140 nm we find the same emission distribution as the dominant mode at λ_0=1425 nm for WG2. The resonance wavelength of this peak shifts with hole size as in the previous sample, reaching λ_0=1080 nm for a hole radius of r=107 nm. This demonstrates that the main features of these PCWGs scale with both period and hole size, as expected.

Figure 9.6(c) shows spectra for three characteristic positions of bright features in the spatial maps, denoted by C, D and E. We observe the same peaks at λ_0=1140 nm, λ_0=1100 nm and λ_0=925 nm for all three positions, but with varying relative intensities, as was already clear from the emission patterns. We can examine the polarization behavior for this waveguide in the same fashion as in the main text, finding similar behavior. When orienting the waveguide along the y-axis and measuring the Stokes parameters for excitation position E, we obtain the spectra shown in Figure 9.6(d). Similarly to Figure 9.4(c), S2 and S3 are close to 0, while S1 dominates the polarized intensity, with the main emission peak

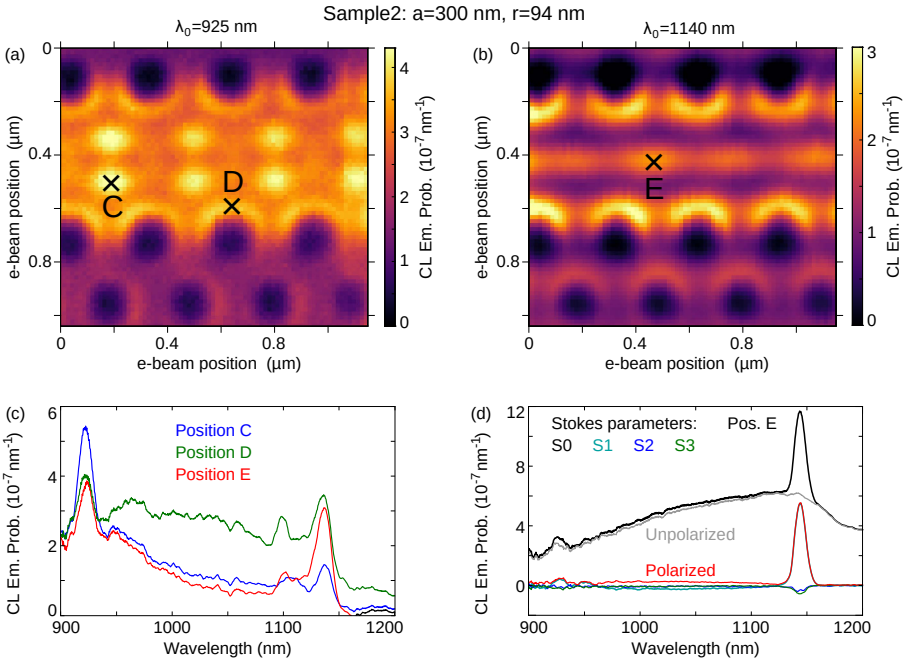

Figure 9.6 – CL emission probability as a function of excitation position for a center wavelength of λ_0=925 nm (a) and λ_0=1140 nm (b), averaged over a 20 nm bandwidth, measured on sample 2. Here the period is much smaller (a=300 nm) with a slightly smaller hole size (r=94 nm), leading to a significant blue shift of same type of mode profile measured on sample 1 in Figures 9.1–9.5. (c) CL spectra for different excitation positions C (blue), D (green), and E (red), denoted by the black crosses in (a) and (b). (d) Polarization-filtered spectra for excitation position E, showing the Stokes parameters S0 (black), S1 (turquoise), S2 (blue) and S3 (green) as well as the polarized (red) and unpolarized (gray) contributions, as for Figure 9.4(c). We note that S1 and the polarized contribution almost fully overlap.

corresponding to the modal pattern of the odd mode being strongly linearly (horizontally) polarized. The majority of the CL emission is due to an unpolarized contribution from the background, leaving a very clean polarized spectrum with an excellent signal-to-noise ratio. These measurements show that the PCWGs reproducibly possess highly localized waveguide modes that are very strongly polarized and exhibit distinct emission profiles, both of which we can measure accurately with infrared spectroscopic CL imaging polarimetry.

9.7.2 Input waveguide and short NIR-wavelength measurements

The majority of the PCWG exhibits a periodically repeating response, but at the interface with the input waveguide, the symmetry of the periodicity is broken,

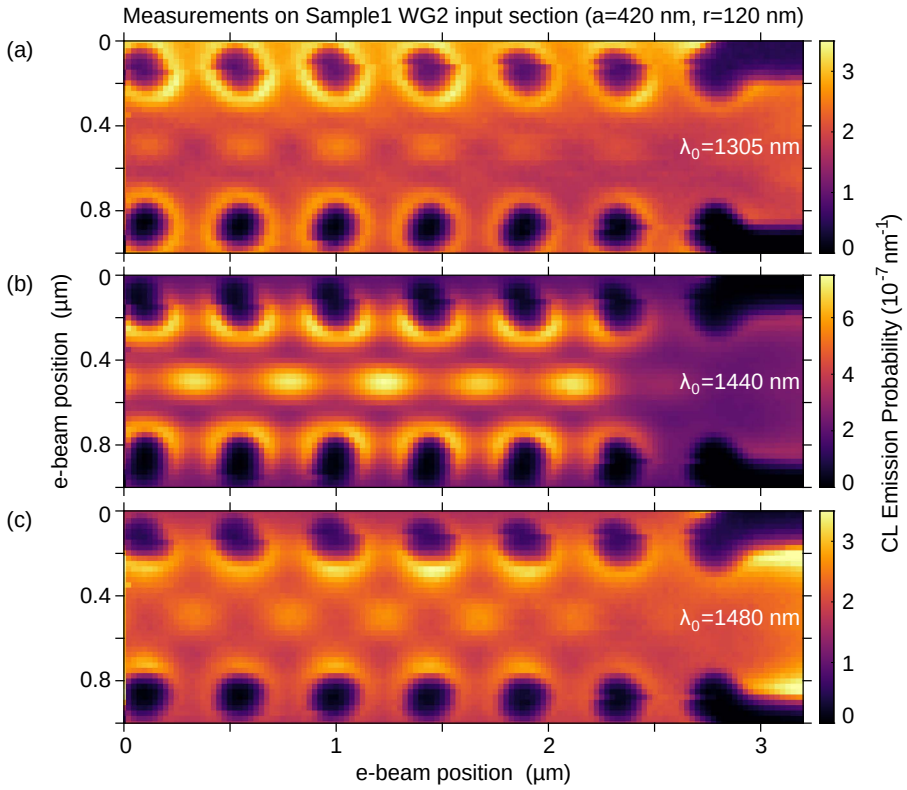

Figure 9.7 – CL emission probability as a function of excitation position on the input section of WG2 (sample 1), for a center wavelength of λ_0=1305 nm (a), λ_0=1440 nm (b), and λ_0=1480 nm (c). The emission probability is averaged over a 20 nm bandwidth.

strongly modifying the band structure. Figure 9.7 displays a 2D spatial intensity distribution measurement on the input section of WG2, the structure most studied in the main text, with a period of 420 nm and a hole radius of 120 nm. We show the CL emission probability for λ_0=1305 nm (a), λ_0=1440 nm (b), and λ_0=1480 nm (c), averaged over a 20 nm bandwidth. At λ_0=1440 nm we clearly recognize the emission distribution of the odd mode measured at λ_0=1425 nm in Figure 9.2(d). The wavelength is slightly different here because the holes are a little smaller at the edges of the structure, which redshifts the resonances. For λ_0=1305 nm we distinguish a different modal pattern from the previous cases, with this time a bright feature along the middle of the waveguide directly between two holes. At λ_0=1480 nm we observe a pattern slightly similar to that at λ_0=1440 nm, but now there are alternating bright and dark spots along the center of the waveguide, with much rounder bright features. This last emission pattern actually resembles the calculated electric

field profile at λ_0=1500 nm for the high k values shown in Figure 9.11(a).

In addition to the spectral measurements in the λ_0=900–1600 nm range presented above, we also measure in the λ_0=400–1000 nm range. Figure 9.8 shows the CL emission probability averaged over a 20 nm bandwidth, as a function of electron beam excitation position, for wavelengths of λ_0=865 nm (a), λ_0=920 nm (b), λ_0=935 nm (c), and λ_0=990 nm (d). We observe complex and distinct emission distributions even for wavelengths only 15 nm apart. At these shorter wavelengths there appear to be many higher order modes with very intricate modal patterns. These are beyond the scope of the research presented here, but the data attest to the high resolution attainable with CL as well as the broadband excitation and detection capabilities.

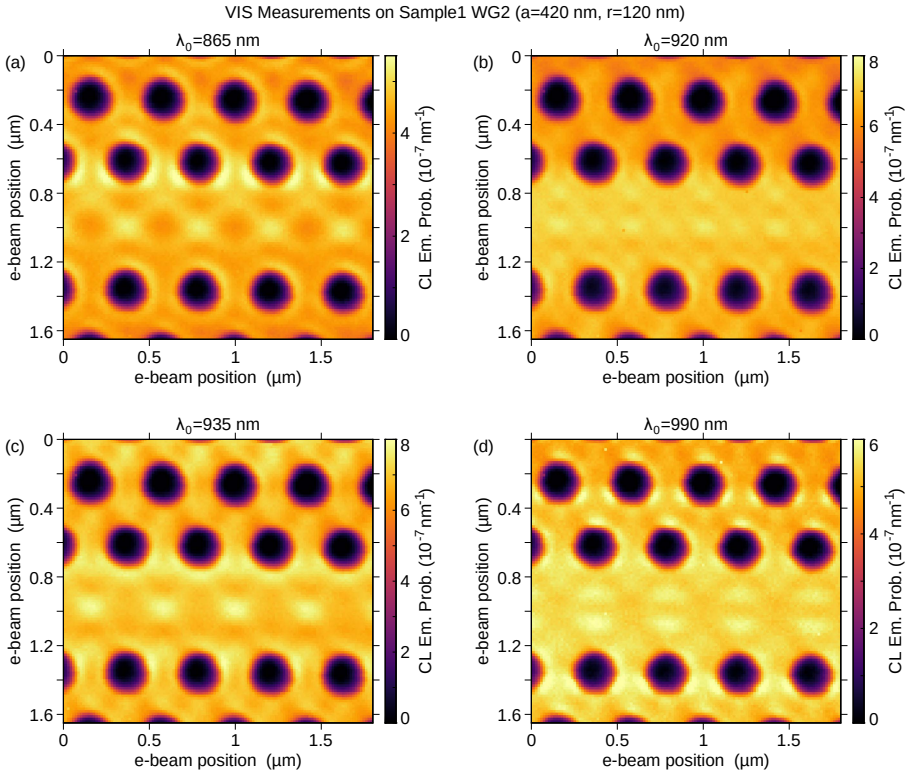

Figure 9.8 – CL emission probability as a function of excitation position on WG2 (sample 1), measured for a center wavelength of λ_0=865 nm (a), λ_0=920 nm (b), λ_0=935 nm (c), and λ_0=990 nm (d). The emission probability is averaged over a 20 nm bandwidth.

9.7.3 TM polarized calculations

The measurements and calculations in the main text have focused on TE polarization, since the waveguides are specifically designed to have well-defined, high-quality modes for that polarization. The TM modes can also contribute to the emission properties however, so they should not be ignored. Figure 9.9(a) displays the band structure for TM polarization with the geometrical parameters used in the main text (period a=420 nm and hole radius r=120 nm). As in Figure 9.1(c), we show the normalized frequency $\omega \times a/2\pi c$ as a function of the normalized wavevector $k \times a/2\pi$ along the propagation direction of the waveguide. The dashed line indicates the light line in air. The continuum of modes dominates nearly the entire band

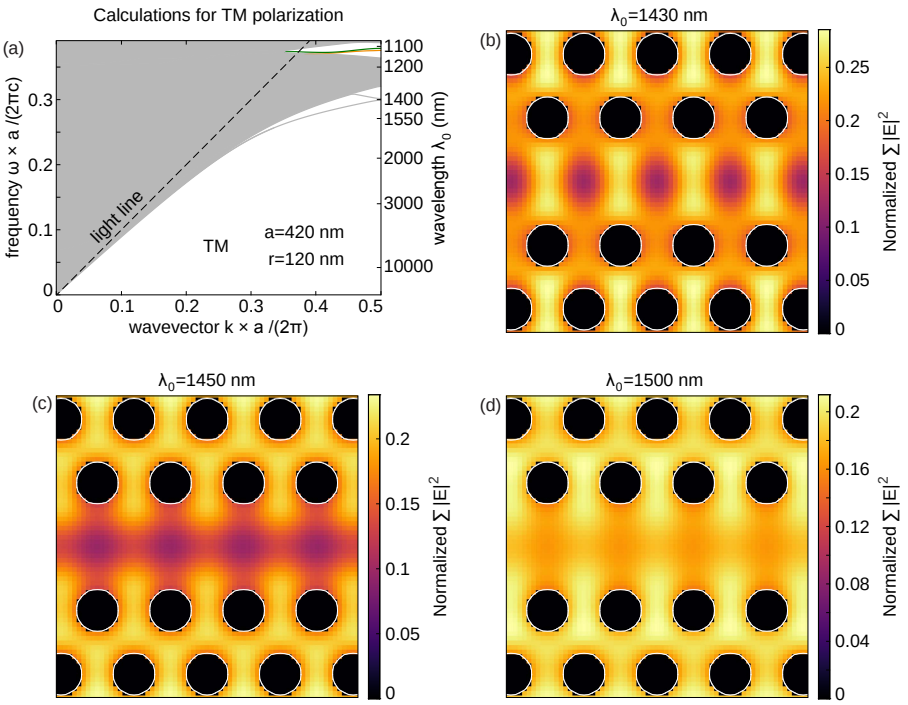

Figure 9.9 – (a) Band structure diagram for a waveguide with a=420 nm and r=120 nm, corresponding to sample 1, WG2, for TM polarization. The frequency ω and the wavevector k are shown in normalized units using the period a. The gray lines denote modes that are in the continuum of available modes above and below the photonic band gap, which display two waveguide modes close to λ_0=1150 nm. The black dashed line indicates the light line in air. We calculate the total $|E|^2$ field profiles, integrating over all available modes and k for λ_0=1430 nm (b), λ_0=1450 nm (c), and λ_0=1500 nm (d). The intensities are normalized to the overall maximum intensity of all the calculations (as in the main text).

diagram. Just below the continuum at high values of k there is a discrete band related to total internal reflection inside the slab. Unlike the TE polarization, there is no large photonic band gap here that extends across a broad range of frequencies and wavevectors, but only a small gap between ~1080–1170 nm for high values of k below the light line. Within this small gap we can distinguish two waveguide modes. These waveguide modes and band edges are in the same spectral range as the modal features observed in Figures 9.2(a,b), so those could be due to TM modes, but we cannot determine the field profiles in that spectral range to confirm this.

Instead we calculate in Figure 9.9 the total electric field intensities for wavelengths of λ_0=1430 nm (b), λ_0=1450 nm (c), and λ_0=1500 nm (d). The intensities are normalized to the maximum total intensity for all wavelengths and polarizations, as in the main text, so that we can compare the values of the color scale. We find that for all wavelengths the field profiles do not show the high confinement and localization in or near the waveguide that is present in the TE calculations at these wavelengths. Indeed the intensities are actually lowest inside the waveguide. This is logical because in the band structure we are deep in the continuum of modes, which are typically delocalized over the entire photonic crystal and not confined to the waveguide. We can conclude that the measured emission patterns in this wavelength range agree with the TE calculations and not with the TM ones.

9.7.4 Implementation of spectroscopic polarimetry

Using polarimetry to measure spectra proves to be a powerful way to determine which spectral features are (strongly) polarized, what their polarization state is, and to separate them from unpolarized background contributions. This allows detailed analysis of the resulting polarized spectra which provides strong insight into the processes generating the radiation. Figure 9.10 describes in more detail how the spectroscopic polarimetry is implemented. The method is based on using a rotating-plate polarimeter composed of a quarter-wave plate (QWP) and linear polarizer (Pol.), taking six measurements for different settings of the polarimeter (horizontal/90°, vertical/0°, 45°, 135°, right- and left-handed circular). These can then be combined to determine the Stokes parameters (S0=$I_H + I_V$, S1=$I_H - I_V$, S2=$I_{45} + I_{135}$, and S3=$I_{RHC} - I_{LHC}$). Figure 9.10(a) displays these six measurements when exciting WG2 (aligned along the y-axis) at excitation position B (in the middle of the waveguide). We observe that below λ_0=1400 nm there is no difference between the six spectra, indicating the emission is unpolarized. The peak at λ_0=1425 nm however is very strongly horizontally polarized, being entirely visible for 90° and absent for 0° (so S1 is large). The left- and right-handed measurements have very similar intensity (S3~0), demonstrating there is no circular polarization, while the similarity between 45° and 135° (S2~0) indicates that the orientation of the polarization is indeed fully horizontal.

To determine how polarized or unpolarized the emission is in an intuitive way, we can use the Stokes parameters to determine the different degrees of polariza-

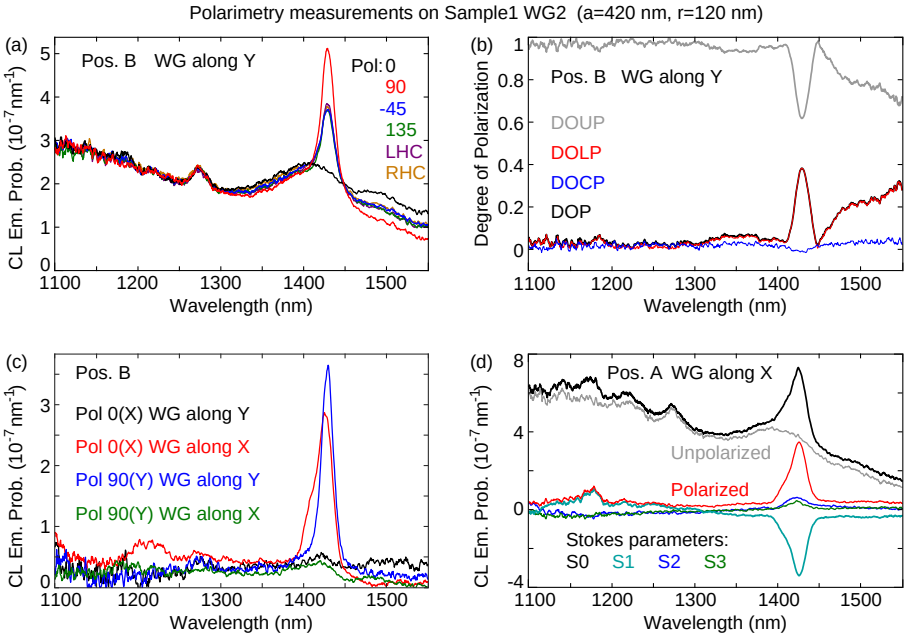

Figure 9.10 – (a) CL emission probability for polarization-filtered spectra excited at position B (in the middle of the waveguide) on WG2, with the waveguide oriented along the y-axis. We show the six spectra corresponding to all the combinations of QWP and linear polarizer settings needed to determine the Stokes parameters (vertical/0°, horizontal/90°, 45°, 135°, left-handed circular and right-handed circular). (b) Degree of polarization as a function of wavelength determined from the spectra shown in (a). The degree of linear polarization (DOLP, red) is nearly indistinguishable from the total degree of polarization (DOP, black). (c) CL spectra excited at position B on sample 1, WG2 for vertical/0°/x polarization and horizontal/90°/y polarization for two different orientations of the waveguide, along x or y as defined by the coordinate system shown in Figure 9.1(d) of the main text. (d) Polarization-filtered spectra for excitation position A on sample 1 WG2 oriented along the x-axis. We show the Stokes parameters S0 (black), S1 (turquoise), S2 (blue) and S3 (green) as well as the polarized (red) and unpolarized (gray) contributions, as for Figure 9.4(c) of the main text. We note that S1 and the polarized contribution overlap for the shorter wavelengths.

tion, which are defined as the ratios of polarized, linearly or circularly polarized light to the total intensity. The degree of polarization ($DOP = \sqrt{S_1^2 + S_2^2 + S_3^2}/S_0$), degree of linear polarization ($DOLP = \sqrt{S_1^2 + S_2^2}/S_0$), and degree of circular polarization ($DOCP = S_3/S_0$) are most commonly used. We can also define a ratio of unpolarized light to total intensity as the "degree of unpolarized light" $DOUP = 1 - DOP$. We show all of these ratios in Figure 9.10(b), determined from the spectra in Figure 9.10(a). As expected from the comparison of the spectra, the DOUP is close to 1 for most of the wavelength range, the DOCP is close to 0, and the DOP

and DOLP are nearly identical. Only the emission peak at λ_0=1425 nm and a broad feature for the highest wavelengths are strongly polarized. We are not certain about the nature of the polarized contribution at these highest wavelengths, but it can be related to polarized modes in the continuum of the upper band in the band structure which are not clearly separated.

These measurements for the waveguide oriented along the y-axis, exhibiting horizontal polarization for the main emission peak at λ_0=1425 nm, indicate that it is in any case not a TM contribution with electric fields normal to the sample surface (along the z-axis). Additionally, polarization along the x-axis should, upon reflection by the mirror, become vertically polarized, which we do not observe. This leads us to conclude that the emission process we measure here is polarized along the waveguide axis (here the y-axis). To confirm this, we also perform measurements after rotating the waveguide by 90° so it is aligned with the x-axis of the coordinate system. Figure 9.10(c) compares spectra measured for horizontal and vertical polarization for the two waveguide orientations, when exciting WG2 at position B. We observe that when the waveguide is oriented along the x-axis, the polarization flips, as expected. In this case no peak is observed at λ_0=1425 nm for horizontal polarization (along y, 90°), instead a peak is clearly observed for vertical polarization (0°) which corresponds to polarization along x. This confirms that this emission peak is entirely polarized along the propagation direction of the waveguide, which agrees with the odd waveguide mode as shown in Figure 9.5 of the main text.

Figure 9.10(d) shows the Stokes parameters as well as the polarized and unpolarized intensities for excitation position A on WG2 oriented along the x-axis, which we can compare to the same measurement for the waveguide oriented along the y-axis (Figure 9.4(c)). As in the previous cases, we observe that the majority of the emission is unpolarized, S2 and S3 are close to 0 so that the polarized intensity very closely follows S1. The only difference is the sign of S1, which is positive for horizontal polarization and negative for vertical polarization. Comparing the peaks at λ_0=1175 nm and λ_0=1425 nm, we note that the first one is positive and the second one in negative. This is exactly the opposite in Figure 9.4(c), confirming the flip in polarization expected from the different orientation that was just discussed for Figure 9.10(c). It also confirms that the emission peaks at these two wavelengths indeed display an opposite polarization. Since the peak at λ_0=1175 nm does not exhibit vertical polarization for both waveguide orientations, it makes it less likely that it is caused by TM modes, which are dominated by the E_z field component.

9.7.5 Polarization of the even and odd waveguide modes

In Figure 9.5 of the main text, we compared the polarization-filtered measurements to electric field profiles of the odd waveguide mode for TE polarization. For λ_0=1500 nm, we found that two separate regions of wavevectors k contribute and that there is good agreement for the range of small k above the light line, where the mode is leaky. For comparison, we show here the normalized field intensi-

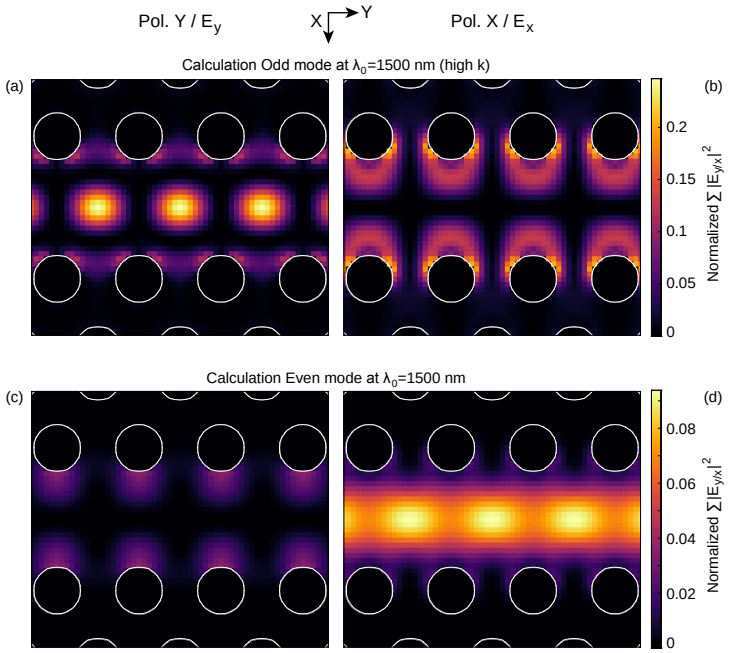

Figure 9.11 – Calculation of the E_y (a) and E_x (b) field intensities for the odd waveguide mode from Figure 9.1(c) of the main text, for λ_0=1500 nm. Here we show the field profiles, on the same scale, obtained after integrating over the range of k values below the light line, as opposed to the range above the light line shown in Figures 9.5(e,f). We also show the field profiles of the even mode, summed over all contributing k, with E_y (c) and E_x (d) on the same scale, at λ_0=1500 nm. As before, the intensities are all normalized to the maximum total intensity of all the calculations.

ties summed over the range of k below the light line, for the E_y component (Figure 9.11(a)) and the E_x component (Figure 9.11(b)). Similarly to the previous calculations, we show the two components on the same intensity scale, normalized to the maximum overall intensity obtained for all wavelengths and polarizations. We find bright features in the middle of the waveguide separated by dark sections for $|E_y|^2$ and enhanced intensity at the inner edges of the holes for $|E_x|^2$. Compared to the measurements in Figures 9.5(a,b), the qualitative agreement is not as good as for the field profiles in the leaky region, even though the latter are less accurate. The brightness in the center of the waveguide for $|E_y|^2$ is much more continuous than that shown here and $|E_x|^2$ is much darker than what we observe here. The total intensity (summed over all field components) does, however, show strong similarities with the measured emission profile at λ_0=1480 nm in Figure 9.7(c), suggesting the guided portion of the mode can play a role at slightly different wavelengths from those dominated by the leaky portion.

We found the same polarization and field profiles for the measurements and the odd waveguide mode, leading us to discount the even waveguide mode. Verifying the expected opposite symmetry and polarization of the modes allows us to confirm this. We show in Figures 9.11(c,d) that the even mode is dominated by $|E_x|^2$ (d) while $|E_y|^2$ (c) is dark, completely opposite to the measurements and the calculations of the odd mode. We only display the modal intensity distributions at λ_0=1500 nm, but find that for wavelengths of 1430, 1450 and 1550 nm there is very little difference in the field profiles and intensities.

References

[1] V. Ronchi, *Histoire de la lumière*, SEVPEN, 1956.

[2] D. A. Park, *The fire within the eye: a historical essay on the nature and meaning of light*, Princeton University Press, 1997.

[3] B. S. Eastwood, *Astronomy and optics from Pliny to Descartes: texts, diagrams and conceptual structures*, volume 291, Variorum, 1989.

[4] *Al Hazen, Father of optical physiology; www.fravahr.org/spip.php?article80.*

[5] J. C. Maxwell, *A dynamical theory of the electromagnetic field*, Phil. Trans. R. Soc. , 459 (1865).

[6] A. Einstein, *The photoelectric effect*, Ann. Phys. **17**, 4 (1905).

[7] A. F. Koenderink, A. Alù, and A. Polman, *Nanophotonics: Shrinking light-based technology*, Science **348**, 516 (2015).

[8] N. Engheta, *Circuits with Light at Nanoscales: Optical Nanocircuits Inspired by Metamaterials*, Science **317**, 1698 (2007).

[9] N. Yu, P. Genevet, M. A. Kats, F. Aieta, J.-P. Tetienne, F. Capasso, and Z. Gaburro, *Light Propagation with Phase Discontinuities: Generalized Laws of Reflection and Refraction*, Science **334**, 333 (2011).

[10] X. Ni, N. K. Emani, A. V. Kildishev, A. Boltasseva, and V. M. Shalaev, *Broadband Light Bending with Plasmonic Nanoantennas*, Science **335**, 427 (2012).

[11] A. Silva, F. Monticone, G. Castaldi, V. Galdi, A. Alù, and N. Engheta, *Performing Mathematical Operations with Metamaterials*, Science **343**, 160 (2014).

[12] E. Yablonovitch, *Photonic band-gap structures*, J. Opt. Soc. Am. B: Opt. Phys. **10**, 283 (1993).

[13] H. Gersen, T. Karle, R. Engelen, W. Bogaerts, J. Korterik, N. Van Hulst, T. Krauss, and L. Kuipers, *Real-space observation of ultraslow light in photonic crystal waveguides*, Phys. Rev. Lett. **94**, 073903 (2005).

[14] M. Notomi, K. Yamada, A. Shinya, J. Takahashi, C. Takahashi, and I. Yokohama, *Extremely large group-velocity dispersion of line-defect waveguides in photonic crystal slabs*, Phys. Rev. Lett. **87**, 253902 (2001).

[15] Y. Akahane, T. Asano, B.-S. Song, and S. Noda, *High-Q photonic nanocavity in a two-dimensional photonic crystal*, Nature **425**, 944 (2003).

[16] A. Blanco, E. Chomski, S. Grabtchak, M. Ibisate, S. John, S. W. Leonard, C. Lopez, F. Meseguer, H. Miguez, J. P. Mondia, G. A. Ozin, O. Toader, and H. M. van Driel, *Large-scale synthesis of a silicon photonic crystal with a complete three-dimensional bandgap near 1.5 micrometres*, Nature **405**, 437 (2000).

[17] H. Raether, *Surface plasmons on smooth and rough surfaces and on gratings*, Springer, 1988.

[18] W. L. Barnes, A. Dereux, and T. W. Ebbesen, *Surface plasmon subwavelength optics*, Nature **424**, 824 (2003).

[19] J. A. Schuller, E. S. Barnard, W. Cai, Y. C. Jun, J. White, and M. L. Brongersma, *Plasmonics for extreme light concentration and manipulation*, Nat. Mater. **9**, 193 (2010).

[20] H. T. Miyazaki and Y. Kurokawa, *Squeezing visible light waves into a 3-nm-thick and 55-nm-long plasmon cavity*, Phys. Rev. Lett. **96**, 097401 (2006).

[21] G. Dolling, C. Enkrich, M. Wegener, C. M. Soukoulis, and S. Linden, *Simultaneous negative phase and group velocity of light in a metamaterial*, Science **312**, 892 (2006).

[22] E. Verhagen, M. Spasenović, A. Polman, and L. Kuipers, *Nanowire plasmon excitation by adiabatic mode transformation*, Phys. Rev. Lett. **102**, 203904 (2009).

[23] R. F. Oulton, V. J. Sorger, T. Zentgraf, R.-M. Ma, C. Gladden, L. Dai, G. Bartal, and X. Zhang, *Plasmon lasers at deep subwavelength scale*, Nature **461**, 629 (2009).

[24] E. Feigenbaum and M. Orenstein, *Ultrasmall volume plasmons, yet with complete retardation effects*, Phys. Rev. Lett. **101**, 163902 (2008).

[25] R. Maas, J. Parsons, N. Engheta, and A. Polman, *Experimental realization of an epsilon-near-zero metamaterial at visible wavelengths*, Nat. Photonics **7**, 907 (2013).

[26] L. Novotny and N. van Hulst, *Antennas for light*, Nat. Photonics **5**, 83 (2011).

[27] A. G. Curto, G. Volpe, T. H. Taminiau, M. Kreuzer, R. Quidant, and N. F. van Hulst, *Unidirectional emission of a quantum dot coupled to a nanoantenna*, Science **329**, 930 (2010).

[28] G. M. Akselrod, C. Argyropoulos, T. B. Hoang, C. Ciracì, C. Fang, J. Huang, D. R. Smith, and M. H. Mikkelsen, *Probing the mechanisms of large Purcell enhancement in plasmonic nanoantennas*, Nat. Photonics (2014).

[29] A. I. Kuznetsov, A. E. Miroshnichenko, Y. H. Fu, J. B. Zhang, and B. Luk'yanchuk, *Magnetic light*, Sci. Rep. **2**, 492 (2012).

[30] L. Novotny, *Effective wavelength scaling for optical antennas*, Phys. Rev. Lett. **98**, 266802 (2007).

[31] M. L. Brongersma, *Plasmonics: Engineering optical nanoantennas*, Nat. Photonics **2**, 270 (2008).

[32] E. Plum, X.-X. Liu, V. Fedotov, Y. Chen, D. Tsai, and N. Zheludev, *Metamaterials: optical activity without chirality*, Phys. Rev. Lett. **102**, 113902 (2009).

[33] I. Sersic, M. A. van de Haar, F. Bernal Arango, and A. F. Koenderink, *Ubiquity of optical activity in planar metamaterial scatterers*, Phys. Rev. Lett. **108**, 223903 (2012).

[34] M. Schäferling, D. Dregely, M. Hentschel, and H. Giessen, *Tailoring enhanced optical chirality: design principles for chiral plasmonic nanostructures*, Phys. Rev. X **2**, 031010 (2012).

[35] J. K. Gansel, M. Thiel, M. S. Rill, M. Decker, K. Bade, V. Saile, G. von Freymann, S. Linden, and M. Wegener, *Gold Helix Photonic Metamaterial as Broadband Circular Polarizer*, Science **325**, 1513 (2009).

[36] J. B. Pendry, *Negative refraction makes a perfect lens*, Phys. Rev. Lett. **85**, 3966 (2000).

[37] J. B. Pendry, Y. Luo, and R. Zhao, *Transforming the optical landscape*, Science **348**, 521 (2015).

[38] S. P. Burgos, R. de Waele, A. Polman, and H. A. Atwater, *A single-layer wide-angle negative index metamaterial at visible frequencies*, Nat. Mater. **9**, 407 (2010).

[39] D. Lin, P. Fan, E. Hasman, and M. L. Brongersma, *Dielectric gradient metasurface*

optical elements, Science **345**, 298 (2014).
[40] H. J. Kimble, *The quantum internet*, Nature **453**, 1023 (2008).
[41] T. D. Ladd, F. Jelezko, R. Laflamme, Y. Nakamura, C. Monroe, and J. L. O'Brien, *Quantum computers*, Nature **464**, 45 (2010).
[42] K. J. Savage, M. M. Hawkeye, R. Esteban, A. G. Borisov, J. Aizpurua, and J. J. Baumberg, *Revealing the quantum regime in tunnelling plasmonics*, Nature **491**, 574 (2012).
[43] J. S. Fakonas, H. Lee, Y. A. Kelaita, and H. A. Atwater, *Two-plasmon quantum interference*, Nat. Photonics **8**, 317 (2014).
[44] M. Arcari, I. Söllner, A. Javadi, S. L. Hansen, S. Mahmoodian, J. Liu, H. Thyrrestrup, E. H. Lee, J. D. Song, S. Stobbe, and P. Lodahl, *Near-unity coupling efficiency of a quantum emitter to a photonic crystal waveguide*, Phys. Rev. Lett. **113**, 093603 (2014).
[45] D. Englund, A. Majumdar, M. Bajcsy, A. Faraon, P. Petroff, and J. Vučković, *Ultrafast photon-photon interaction in a strongly coupled quantum dot-cavity system*, Phys. Rev. Lett. **108**, 093604 (2012).
[46] W. Challener, C. Peng, A. Itagi, D. Karns, W. Peng, Y. Peng, X. Yang, X. Zhu, N. Gokemeijer, Y.-T. Hsia, G. Ju, R. E. Rottmayer, M. A. Seigler, and E. C. Gage, *Heat-assisted magnetic recording by a near-field transducer with efficient optical energy transfer*, Nat. Photonics **3**, 220 (2009).
[47] K. Hirose, Y. Liang, Y. Kurosaka, A. Watanabe, T. Sugiyama, and S. Noda, *Watt-class high-power, high-beam-quality photonic-crystal lasers*, Nat. Photonics **8**, 406 (2014).
[48] G. Lozano, D. J. Louwers, S. R. Rodríguez, S. Murai, O. T. Jansen, M. A. Verschuuren, and J. Gómez Rivas, *Plasmonics for solid-state lighting: enhanced excitation and directional emission of highly efficient light sources*, Light. Sci. Appl. **2**, e66 (2013).
[49] P. Spinelli, M. A. Verschuuren, and A. Polman, *Broadband omnidirectional antireflection coating based on subwavelength surface mie resonators*, Nat. Commun. **3**, 692 (2012).
[50] J. Wallentin, N. Anttu, D. Asoli, M. Huffman, I. Åberg, M. H. Magnusson, G. Siefer, P. Fuss-Kailuweit, F. Dimroth, B. Witzigmann, H. Q. Xu, L. Samuelson, K. Deppert, and M. T. Borgström, *InP Nanowire Array Solar Cell Achieving 13.8% Efficiency by Exceeding the Ray Optics Limit*, Science **339**, 1057 (2013).
[51] H. A. Atwater and A. Polman, *Plasmonics for improved photovoltaic devices*, Nat. Mater. **9**, 205 (2010).
[52] K. Catchpole and A. Polman, *Design principles for particle plasmon enhanced solar cells*, Appl. Phys. Lett. **93**, 191113 (2008).
[53] K. Nakayama, K. Tanabe, and H. A. Atwater, *Plasmonic nanoparticle enhanced light absorption in GaAs solar cells*, Appl. Phys. Lett. **93**, 121904 (2008).
[54] M. W. Knight, H. Sobhani, P. Nordlander, and N. J. Halas, *Photodetection with active optical antennas*, Science **332**, 702 (2011).
[55] F. De Angelis, M. Patrini, G. Das, I. Maksymov, M. Galli, L. Businaro, L. C. Andreani, and E. Di Fabrizio, *A hybrid plasmonic-photonic nanodevice for label-free detection of a few molecules*, Nano Lett. **8**, 2321 (2008).
[56] S. P. Burgos, S. Yokogawa, and H. A. Atwater, *Color imaging via nearest neighbor hole coupling in plasmonic color filters integrated onto a complementary metal-oxide semiconductor image sensor*, ACS Nano **7**, 10038 (2013).
[57] R. J. Walters, R. V. A. van Loon, I. Brunets, J. Schmitz, and A. Polman, *A silicon-based electrical source of surface plasmon polaritons*, Nat. Mater. **9**, 21 (2009).
[58] N. Liu, M. Hentschel, T. Weiss, A. P. Alivisatos, and H. Giessen, *Three-dimensional plasmon rulers*, Science **332**, 1407 (2011).

[59] L. Langguth, D. Punj, J. Wenger, and A. F. Koenderink, *Plasmonic band structure controls single molecule fluorescence*, ACS Nano **7**, 8840 (2013).

[60] R. Bardhan, S. Lal, A. Joshi, and N. J. Halas, *Theranostic nanoshells: from probe design to imaging and treatment of cancer*, Acc. Chem. Res. **44**, 936 (2011).

[61] B. McNally, A. Singer, Z. Yu, Y. Sun, Z. Weng, and A. Meller, *Optical recognition of converted DNA nucleotides for single-molecule DNA sequencing using nanopore arrays*, Nano Lett. **10**, 2237 (2010).

[62] D. Punj, M. Mivelle, M. Satish Babu, T. S. van Zanten, H. Rigneault, N. F. van Hulst, M. F. García-Parajó, and J. Wenger, *A plasmonic 'antenna-in-box' platform for enhanced single-molecule analysis at micromolar concentrations*, Nat. Nanotechnol. **8**, 512 (2013).

[63] R. Adato and H. Altug, *In-situ ultra-sensitive infrared absorption spectroscopy of biomolecule interactions in real time with plasmonic nanoantennas*, Nat. Commun. **4**, 2154 (2013).

[64] A. M. Gobin, M. H. Lee, N. J. Halas, W. D. James, R. A. Drezek, and J. L. West, *Near-infrared resonant nanoshells for combined optical imaging and photothermal cancer therapy*, Nano Lett. **7**, 1929 (2007).

[65] B. Kang, M. M. Afifi, L. A. Austin, and M. A. El-Sayed, *Exploiting the nanoparticle plasmon effect: Observing drug delivery dynamics in single cells via Raman/fluorescence imaging spectroscopy*, ACS Nano **7**, 7420 (2013).

[66] J. Chan, T. M. Alegre, A. H. Safavi-Naeini, J. T. Hill, A. Krause, S. Gröblacher, M. Aspelmeyer, and O. Painter, *Laser cooling of a nanomechanical oscillator into its quantum ground state*, Nature **478**, 89 (2011).

[67] B. J. Hausmann et al., *Integrated diamond networks for quantum nanophotonics*, Nano Lett. **12**, 1578 (2012).

[68] M. T. Sheldon, J. van de Groep, A. M. Brown, A. Polman, and H. A. Atwater, *Plasmoelectric potentials in metal nanostructures*, Science **346**, 828 (2014).

[69] L. D. Tzuang, K. Fang, P. Nussenzveig, S. Fan, and M. Lipson, *Non-reciprocal phase shift induced by an effective magnetic flux for light*, Nat. Photonics **8**, 701 (2014).

[70] D. L. Sounas, C. Caloz, and A. Alú, *Giant non-reciprocity at the subwavelength scale using angular momentum-biased metamaterials*, Nat. Commun. **4** (2013).

[71] M. C. Rechtsman, J. M. Zeuner, Y. Plotnik, Y. Lumer, D. Podolsky, F. Dreisow, S. Nolte, M. Segev, and A. Szameit, *Photonic Floquet topological insulators*, Nature **496**, 196 (2013).

[72] F. H. L. Koppens, D. E. Chang, and F. J. García de Abajo, *Graphene Plasmonics: A Platform for Strong Light-Matter Interactions*, Nano Lett. **11**, 3370 (2011).

[73] A. Vakil and N. Engheta, *Transformation Optics Using Graphene*, Science **332**, 1291 (2011).

[74] E. Abbe, *Beiträge zur Theorie des Mikroskops und der mikroskopischen Wahrnehmung*, Arch. Mikrosk. Anat. **9**, 413 (1873).

[75] E. Betzig and J. K. Trautman, *Near-field optics: microscopy, spectroscopy, and surface modification beyond the diffraction limit*, Science **257**, 189 (1992).

[76] J. Chen, M. Badioli, P. Alonso-González, S. Thongrattanasiri, F. Huth, J. Osmond, M. Spasenović, A. Centeno, A. Pesquera, P. Godignon, A. Zurutuza Elorza, N. Camara, F. J. García de Abajo, R. Hillenbrand, and F. H. L. Koppens, *Optical nano-imaging of gate-tunable graphene plasmons*, Nature **487**, 77 (2012).

[77] B. Le Feber, N. Rotenberg, D. M. Beggs, and L. Kuipers, *Simultaneous measurement of nanoscale electric and magnetic optical fields*, Nat. Photonics **8**, 43 (2014).

[78] E. Goldstein, *Vorläufige Mittheilungen über elektrische Entladungen in verdünnten Gasen*, Berlin Akd. Monatsber. , 279 (1876).

[79] W. Hittorf, *Ueber die Elektricitätsleitung der Gase*, Ann. Phys. **136**, 1 (1869).

[80] W. Crookes, *Contributions to Molecular Physics in High Vacua. Magnetic Deflection of Molecular Trajectory. Laws of Magnetic Rotation in High and Low Vacua. Phosphorogenic Properties of Molecular Discharge*, Phil. Trans. R. Soc. **170**, 641 (1879).

[81] J. J. Thomson, *Cathode rays*, Philos. Mag. **44**, 293 (1897).

[82] N. Bohr, *I. On the constitution of atoms and molecules*, Philos. Mag. **26**, 1 (1913).

[83] E. Ruska, *Die elektronenmikroskopische Abbildung elektronenbestrahlter Oberflächen*, Z. Phys. **83**, 492 (1933).

[84] M. Knoll, *Aufladepotentiel und sekundäremission elektronenbestrahlter körper*, Z. Tech. Phys. **16**, 467 (1935).

[85] M. v Ardenne, *Das Elektronen-Rastermikroskop, Theoretische Grundlagen*, Z. Phys. **109**, 553 (1938).

[86] M. v Ardenne, *Das Elektronen-Rastermikroskop, Praktische Ausführung*, Z. Tech. Phys. **19**, 407 (1938).

[87] D. McMullan, *Scanning electron microscopy 1928–1965*, Scanning **17**, 175 (1995).

[88] R. Egerton, *Physical Principles of Electron Microscopy: An Introduction to TEM, SEM, and AEM*, Springer, 2005.

[89] J. Goldstein, D. E. Newbury, P. Echlin, D. C. Joy, A. D. Romig Jr, C. E. Lyman, C. Fiori, and E. Lifshin, *Scanning electron microscopy and X-ray microanalysis: a text for biologists, materials scientists, and geologists*, Springer Science & Business Media, 2nd edition, 1992.

[90] J. J. Bozzola and L. D. Russell, *Electron microscopy: principles and techniques for biologists*, Jones & Bartlett Learning, 1999.

[91] T. Arabatzis, *Cathode Rays*, in *Compendium of Quantum Physics*, edited by D. Greenberger, K. Hentschel, and F. Weinert, pages 89–92, Springer Berlin Heidelberg, 2009.

[92] F. J. García de Abajo, *Optical excitations in electron microscopy*, Rev. Mod. Phys. **82**, 209 (2010).

[93] I. Frank and I. Tamm, *Coherent visible radiation from fast electrons passing through matter*, CR Acad. Sci. USSR **14**, 109 (1937).

[94] V. L. Ginzburg, *Radiation by uniformly moving sources (Vavilov-Cherenkov effect, transition radiation, and other phenomena)*, Phys. Usp. **39**, 973 (1996).

[95] A. Potylitsyn, *Transition radiation and diffraction radiation. Similarities and differences*, Nucl. Instrum. Methods Phys. Res., Sect. B **145**, 169 (1998).

[96] S. J. Smith and E. Purcell, *Visible light from localized surface charges moving across a grating*, Phys. Rev. **92**, 1069 (1953).

[97] I. Frank and V. Ginzburg, *Radiation of a uniform moving electron due to its transition from one medium into another*, J. Phys. (USSR) **9**, 353 (1945).

[98] P. Goldsmith and J. Jelley, *Optical transition radiation from protons entering metal surfaces*, Philos. Mag. **4**, 836 (1959).

[99] M. Kuttge, E. J. R. Vesseur, A. F. Koenderink, H. J. Lezec, H. A. Atwater, F. J. García de Abajo, and A. Polman, *Local density of states, spectrum, and far-field interference of surface plasmon polaritons probed by cathodoluminescence*, Phys. Rev. B **79**, 113405 (2009).

[100] E. J. R. Vesseur, F. J. García de Abajo, and A. Polman, *Modal decomposition of surface-plasmon whispering gallery resonators*, Nano Lett. **9**, 3147 (2009).

[101] M. W. Knight, L. Liu, Y. Wang, L. Brown, S. Mukherjee, N. S. King, H. O. Everitt, P. Nordlander, and N. J. Halas, *Aluminum plasmonic nanoantennas*, Nano Lett. **12**, 6000 (2012).

[102] T. Coenen, F. Bernal Arango, A. F. Koenderink, and A. Polman, *Directional emission from a single plasmonic scatterer*, Nat. Commun. **5**, 3250 (2014).

[103] T. Coenen, J. van de Groep, and A. Polman, *Resonant Modes of Single Silicon Nanocavities Excited by Electron Irradiation*, ACS Nano **7**, 1689 (2013).

[104] A. Losquin, L. F. Zagonel, V. Myroshnychenko, B. Rodríguez-González, M. Tencé, L. Scarabelli, J. Förstner, L. M. Liz-Marzán, F. J. García de Abajo, O. Stéphan, and M. Kociak, *Unveiling nanometer scale extinction and scattering phenomena through combined electron energy loss spectroscopy and cathodoluminescence measurements*, Nano Lett. **15**, 1229 (2015).

[105] A. Losquin and M. Kociak, *Link between cathodoluminescence and electron energy loss spectroscopy and the radiative and full electromagnetic local density of states*, ACS Photonics **2**, 1619 (2015).

[106] B. G. Yacobi and D. B. Holt, *Cathodoluminescence scanning electron microscopy of semiconductors*, J. Appl. Phys. **59**, R1 (1986).

[107] B. G. Yacobi and D. B. Holt, *Cathodoluminescence microscopy of inorganic solids*, Springer Science & Business Media, 1990.

[108] R. Sauer, H. Sternschulte, S. Wahl, K. Thonke, and T. R. Anthony, *Revised Fine Splitting of Excitons in Diamond*, Phys. Rev. Lett. **84**, 4172 (2000).

[109] Z. Mahfoud, A. T. Dijksman, C. Javaux, P. Bassoul, A. L. Baudrion, J. Plain, B. Dubertret, and M. Kociak, *Cathodoluminescence in a scanning transmission electron microscope: A nanometer-scale counterpart of photoluminescence for the study of II-VI quantum dots*, J. Phys. Chem. Lett. **4**, 4090 (2013).

[110] L. H. G. Tizei and M. Kociak, *Spatially resolved quantum nano-optics of single photons using an electron microscope*, Phys. Rev. Lett. **110**, 153604 (2013).

[111] K. Thonke, I. Tischer, M. Hocker, M. Schirra, K. Fujan, M. Wiedenmann, R. Schneider, M. Frey, and M. Feneberg, *Nanoscale characterisation of semiconductors by cathodoluminescence*, IOP Conf. Ser.: Mater. Sci. Eng. **55**, 012018 (2014).

[112] B. Dierre, X. Yuan, and T. Sekiguchi, *Low-energy cathodoluminescence microscopy for the characterization of nanostructures*, Sci. Technol. Adv. Mater. **11**, 043001 (2010).

[113] P. R. Edwards and R. W. Martin, *Cathodoluminescence nano-characterization of semiconductors*, Semicond. Sci. Technol. **26**, 064005 (2011).

[114] A. Leto and G. Pezzotti, *Cathodoluminescence study of off-stoichiometry and residual stresses in advanced dielectrics and related devices*, Phys. Status Solidi A **208**, 1119 (2011).

[115] M. A. S. Kalceff, *Cathodoluminescence microcharacterization of the defect structure of irradiated hydrated and anhydrous fused silicon dioxide*, Phys. Rev. B **57**, 5674 (1998).

[116] C. Ton-That, L. Weston, and M. Phillips, *Characteristics of point defects in the green luminescence from Zn- and O-rich ZnO*, Phys. Rev. B **86**, 115205 (2012).

[117] H.-J. Fitting, A. N. Trukhin, T. Barfels, B. Schmidt, and A. V. Czarnowski, *Radiation induced defects in SiO_2*, Radiat. Eff. Defect. S. **157**, 575 (2002).

[118] E. F. Schubert, *Light emitting diodes, 2^{nd} edition*, Cambridge University press, 2006.

[119] B. J. M. Brenny, T. Coenen, and A. Polman, *Quantifying coherent and incoherent cathodoluminescence in semiconductors and metals*, J. Appl. Phys. **115**, (2014).

[120] T. E. Everhart and P. H. Hoff, *Determination of Kilovolt Electron Energy Dissipation vs Penetration Distance in Solid Materials*, J. Appl. Phys. **42**, 5837 (1971).

[121] C. A. Klein, *Bandgap Dependence and Related Features of Radiation Ionization Energies in Semiconductors*, J. Appl. Phys. **39**, 2029 (1968).

[122] H. Demers, N. Poirier-Demers, A. R. Couture, D. Joly, M. Guilmain, N. de Jonge, and D. Drouin, *Three-dimensional electron microscopy simulation with the CASINO Monte Carlo software*, Scanning **33**, 135 (2011).

[123] M. Kuttge, *Cathodoluminescence plasmon microscopy*, PhD thesis, Utrecht University, 2009.

[124] R. Sapienza, T. Coenen, J. Renger, M. Kuttge, N. F. van Hulst, and A. Polman, *Deep-subwavelength imaging of the modal dispersion of light*, Nat. Mater. **11**, 781 (2012).

[125] N. M. Haegel, T. J. Mills, M. Talmadge, C. Scandrett, C. L. Frenzen, H. Yoon, C. M. Fetzer, and R. R. King, *Direct imaging of anisotropic minority-carrier diffusion in ordered GaInP*, J. Appl. Phys. **105**, 023711 (2009).

[126] E. J. R. Vesseur, *Electron beam imaging and spectroscopy of plasmonic nanoantenna resonances*, PhD thesis, Utrecht University, 2011.

[127] T. Coenen, *Angle-resolved cathodoluminescence nanoscopy*, PhD thesis, University of Amsterdam, 2014.

[128] T. Coenen, E. J. R. Vesseur, and A. Polman, *Angle-resolved cathodoluminescence spectroscopy*, Appl. Phys. Lett. **99**, 143103 (2011).

[129] T. Coenen and A. Polman, *Polarization-sensitive cathodoluminescence Fourier microscopy*, Opt. Express **20**, 18679 (2012).

[130] E. J. R. Vesseur and A. Polman, *Plasmonic whispering gallery cavities as optical antennas*, Nano Lett. **11**, 5524 (2011).

[131] M. Born and E. Wolf, *Principles of Optics: Electromagnetic Theory of Propagation, Interference and Diffraction of Light, 7^{th} ed.*, Cambridge University Press, 1997.

[132] C. I. Osorio, T. Coenen, B. J. M. Brenny, A. Polman, and A. F. Koenderink, *Angle-resolved cathodoluminescence imaging polarimetry*, ACS Photonics **3**, 147 (2016).

[133] O. G. Rodríguez-Herrera and N. C. Bruce, *Confined three-dimensional plasmon modes inside a ring-shaped nanocavity on a silver film imaged by cathodoluminescence microscopy*, Opt. Eng. **45**, 053602 (2006).

[134] O. G. Rodríguez-Herrera, M. Rosete-Aguilar, and N. C. Bruce, *Change in the polarization state by reflection in an elliptical mirror*, Rev. Mex. Fis. **E50**, 33 (2004).

[135] T. Suzuki and N. Yamamoto, *Cathodoluminescent spectroscopic imaging of surface plasmon polaritons in a 1-dimensional plasmonic crystal*, Opt. Express **17**, 23664 (2009).

[136] K. Takeuchi and N. Yamamoto, *Visualization of surface plasmon polariton waves in two-dimensional plasmonic crystal by cathodoluminescence*, Opt. Express **19**, 12365 (2011).

[137] G. Adamo, K. F. MacDonald, Y. H. Fu, C. M. Wang, D. P. Tsai, F. J. García de Abajo, and N. I. Zheludev, *Light well: a tunable free-electron light source on a chip*, Phys. Rev. Lett. **103**, 113901 (2009).

[138] K. Kimoto, T. Asaka, T. Nagai, M. Saito, Y. Matsui, and K. Ishizuka, *Element-selective imaging of atomic columns in a crystal using STEM and EELS*, Nature **450**, 702 (2007).

[139] M. V. Bashevoy, F. Jonsson, K. F. MacDonald, Y. Chen, and N. I. Zheludev, *Hyperspectral imaging of plasmonic nanostructures with nanoscale resolution*, Opt. Express **15**, 11313 (2007).

[140] J. A. Scholl, A. L. Koh, and J. A. Dionne, *Quantum plasmon resonances of individual metallic nanoparticles*, Nature **483**, 421 (2012).

[141] F. J. García de Abajo and M. Kociak, *Probing the photonic local density of states with*

electron energy loss spectroscopy, Phys. Rev. Lett. **100**, 106804 (2008).

[142] U. Hohenester, H. Ditlbacher, and J. R. Krenn, *Electron-energy-loss spectra of plasmonic nanoparticles*, Phys. Rev. Lett. **103**, 106801 (2009).

[143] W. Cai, R. Sainidou, J. Xu, A. Polman, and F. J. García de Abajo, *Efficient Generation of Propagating Plasmons by Electron Beams*, Nano Lett. **9**, 1176 (2009).

[144] A. Asenjo-Garcia and F. J. García de Abajo, *Plasmon electron energy-gain spectroscopy*, New J. Phys. **15**, 103021 (2013).

[145] A. Hörl, A. Trügler, and U. Hohenester, *Tomography of particle plasmon fields from electron energy loss spectroscopy*, Phys. Rev. Lett. **111**, 086801 (2013).

[146] A. Feist, K. E. Echternkamp, J. Schauss, S. V. Yalunin, S. Schäfer, and C. Ropers, *Quantum coherent optical phase modulation in an ultrafast transmission electron microscope*, Nature **521**, 200 (2015).

[147] L. Piazza, T. T. A. Lummen, E. Quinonez, Y. Murooka, B. W. Reed, B. Barwick, and F. Carbone, *Simultaneous observation of the quantization and the interference pattern of a plasmonic near-field*, Nat. Commun. **6** (2015).

[148] C. Matyssek, J. Niegemann, W. Hergert, and K. Busch, *Computing electron energy loss spectra with the Discontinuous Galerkin Time-Domain method*, Phot. Nano. Fund. Appl. **9**, 367 (2011).

[149] K. Busch, M. König, and J. Niegemann, *Discontinuous Galerkin methods in nanophotonics*, Laser Photon. Rev. **5**, 773 (2011).

[150] J. D. Jackson, *Classical electrodynamics, 3^{rd} edition*, John Wiley and Sons, 1999.

[151] M. Abramowitz and I. A. Stegun, *Handbook of mathematical functions*, volume 55, Courier Corporation, 1964.

[152] F. J. García De Abajo, A. Rivacoba, N. Zabala, and N. Yamamoto, *Boundary effects in Cherenkov radiation*, Phys. Rev. B **69**, 155420 (2004).

[153] Y.-Y. Teng and E. A. Stern, *Plasma radiation from metal grating surfaces*, Phys. Rev. Lett. **19**, 511 (1967).

[154] D. Heitmann, *Radiative decay of surface plasmons excited by fast electrons on periodically modulated silver surfaces*, J. Phys. C: Solid State Phys. **10**, 397 (1977).

[155] M. V. Bashevoy, F. Jonsson, A. V. Krasavin, N. I. Zheludev, Y. Chen, and M. I. Stockman, *Generation of traveling surface plasmon waves by free-electron impact*, Nano Lett. **6**, 1113 (2006).

[156] J. van Wijngaarden, E. Verhagen, A. Polman, C. Ross, H. J. Lezec, and H. A. Atwater, *Direct imaging of propagation and damping of near-resonance surface plasmon polaritons using cathodoluminescence spectroscopy*, Appl. Phys. Lett. **88**, 221111 (2006).

[157] G. W. Ford and W. H. Weber, *Electromagnetic interactions of molecules with metal surfaces*, Phys. Rep. **113**, 195 (1984).

[158] M. L. Ter-Mikaelian, *High-energy electromagnetic processes in condensed media*, volume 29, John Wiley & Sons, 1972.

[159] E. Kröger, *Calculations of the energy losses of fast electrons in thin foils with retardation*, Zeitschrift für Physik **216**, 115 (1968).

[160] T. A. Swift, M. Martin, and Shellback, *Shake it off*, Big Machine **1989** (2014).

[161] E. M. Purcell, *Electricity and magnetism*, McGraw-Hill, 1983.

[162] B. M. Bolotovskii and A. V. Serov, *On representation of electromagnetic radiation in the picture of force lines*, Nucl. Instrum. Methods Phys. Res., Sect. B **145**, 31 (1998).

[163] A. Serov and B. M. Bolotovskii, *Application of the method of images in the problems of transition radiation in a dihedral angle*, J. Exp. Theor. Phys. **104**, 866 (2007).

[164] L. Van Hove, *The occurrence of singularities in the elastic frequency distribution of a crystal*, Phys. Rev. **89**, 1189 (1953).

[165] F. Bassani and G. P. Parravicini, *Electronic states and optical transitions in solids*, Pergamon, 1975.

[166] R. A. Ferrell, *Predicted radiation of plasma oscillations in metal films*, Phys. Rev. **111**, 1214 (1958).

[167] E. A. Stern, *Transition radiation from metal films*, Phys. Rev. Lett. **8**, 7 (1962).

[168] N. Yamamoto, A. Toda, and K. Araya, *Imaging of Transition Radiation from Thin Films on a Silicon Substrate Using a Light Detection System Combined with TEM*, J. Electron Microsc. **45**, 64 (1996).

[169] W. Kuhn, *Über die gesamtstärke der von einem zustande ausgehenden absorptionslinien*, Z. Phys. **33**, 408 (1925).

[170] F. Reiche and W. Thomas, *Über die zahl der dispersionselektronen, die einem stationären zustand zugeordnet sind*, Z. Phys. **34**, 510 (1925).

[171] Z.-J. Yang, T. J. Antosiewicz, R. Verre, F. J. García de Abajo, S. P. Apell, and M. Käll, *Ultimate Limit of Light Extinction by Nanophotonic Structures*, Nano Letters **15**, 7633 (2015).

[172] M. Pagel, V. Barbin, P. Blanc, and D. Ohnenstetter, *Cathodoluminescence in geosciences*, Springer, 2000.

[173] D. J. Marshall and A. N. Mariano, *Cathodoluminescence of geological materials*, Unwin Hyman, 1988.

[174] S. Myhajlenko, *Cathodoluminescence*, Springer US, 1998.

[175] S. Koizumi, K. Watanabe, M. Hasegawa, and H. Kanda, *Ultraviolet emission from a diamond pn junction*, Science **292**, 1899 (2001).

[176] G. Li, D. Geng, M. Shang, C. Peng, Z. Cheng, and J. Lin, *Tunable luminescence of Ce^{3+}/Mn^{2+}-coactivated $Ca_2Gd_8(SiO_4)_6O_2$ through energy transfer and modulation of excitation: Potential single-phase white/yellow-emitting phosphors*, J. Mater. Chem. **21**, 13334 (2011).

[177] M. Avella, J. Jiménez, F. Pommereau, J. Landesman, and A. Rhallabi, *Cathodoluminescence study of inductively coupled plasma (ICP) etched InP waveguide structures: Influence of the ridge dimension and dielectric capping*, Mat. Sci. Eng. B **147**, 136 (2008).

[178] F. A. Ponce, D. P. Bour, W. Götz, and P. J. Wright, *Spatial distribution of the luminescence in GaN thin films*, Appl. Phys. Lett. **68**, 57 (1996).

[179] D. Spirkoska, J. Arbiol, A. Gustafsson, S. Conesa-Boj, F. Glas, I. Zardo, M. Heigoldt, M. Gass, A. Bleloch, S. Estrade, M. Kaniber, J. Rossler, F. Peiro, J. Morante, G. Abstreiter, L. Samuelson, and A. Fontcuberta i Morral, *Structural and optical properties of high quality zinc-blende/wurtzite GaAs nanowire heterostructures*, Phys. Rev. B **80**, 245325 (2009).

[180] C.-W. Chen, K.-H. Chen, C.-H. Shen, A. Ganguly, L.-C. Chen, J.-J. Wu, H.-I. Wen, and W.-F. Pong, *Anomalous blueshift in emission spectra of ZnO nanorods with sizes beyond quantum confinement regime*, Appl. Phys. Lett. **88**, (2006).

[181] V. Myroshnychenko, J. Nelayah, G. Adamo, N. Geuquet, J. Rodríguez-Fernández, I. Pastoriza-Santos, K. F. MacDonald, L. Henrard, L. M. Liz-Marzán, N. I. Zheludev, M. Kociak, and F. J. García de Abajo, *Plasmon spectroscopy and imaging of individual gold nanodecahedra: a combined optical microscopy, cathodoluminescence, and electron energy-loss spectroscopy study*, Nano Lett. **12**, 4172 (2012).

[182] A. I. Denisyuk, G. Adamo, K. F. MacDonald, J. Edgar, M. D. Arnold, V. Myroshnychenko,

J. Ford, F. J. García de Abajo, and N. I. Zheludev, *Transmitting hertzian optical nanoantenna with free-electron feed*, Nano Lett. **10**, 3250 (2010).

[183] T. Coenen, E. J. R. Vesseur, A. Polman, and A. F. Koenderink, *Directional emission from plasmonic Yagi Uda antennas probed by angle-resolved cathodoluminescence spectroscopy*, Nano Lett. **11**, 3779 (2011).

[184] A. Kumar, K.-H. Fung, J. C. Mabon, E. Chow, and N. X. Fang, *Excitation and imaging of resonant optical modes of Au triangular nanoantennas using cathodoluminescence spectroscopy*, J. Vac. Sci. Technol. B **28**, C6C21 (2010).

[185] X. L. Zhu, J. S. Ma, Y. Zhang, X. F. Xu, J. Wu, Y. Zhang, X. B. Han, Q. Fu, Z. M. Liao, L. Chen, and D. P. Yu, *Confined three-dimensional plasmon modes inside a ring-shaped nanocavity on a silver film imaged by cathodoluminescence microscopy*, Phys. Rev. Lett. **105**, 127402 (2010).

[186] M. Kuttge, F. J. García de Abajo, and A. Polman, *How grooves reflect and confine surface plasmon polaritons*, Opt. Express **17**, 10385 (2009).

[187] N. Yamamoto, S. Bhunia, and Y. Watanabe, *Polarized cathodoluminescence study of InP nanowire by transmission electron microscopy*, Appl. Phys. Lett. **88**, 153106 (2006).

[188] E. J. R. Vesseur, T. Coenen, H. Caglayan, N. Engheta, and A. Polman, *Experimental Verification of n = 0 Structures for Visible Light*, Phys. Rev. Lett. **110**, 013902 (2013).

[189] A. C. Narváez, I. G. C. Weppelman, R. J. Moerland, N. Liv, A. C. Zonnevylle, P. Kruit, and J. P. Hoogenboom, *Cathodoluminescence Microscopy of nanostructures on glass substrates*, Opt. Express **21**, 29968 (2013).

[190] E. D. Palik, *Handbook of optical constants*, Academic Press, New York, 1985.

[191] P. B. Johnson and R. W. Christy, *Optical constants of the noble metals*, Phys. Rev. B **6**, 4370 (1972).

[192] N. Yamamoto, A. Toda, and K. Araya, *Imaging of Transition Radiation from Thin Films on a Silicon Substrate Using a Light Detection System Combined with TEM*, J. Electron Microsc. **45**, 64 (1996).

[193] D. Drouin, A. R. Couture, D. Joly, X. Tastet, V. Aimez, and R. Gauvin, *CASINO V2.42 - A Fast and Easy-to-use Modeling Tool for Scanning Electron Microscopy and Microanalysis Users*, Scanning **29**, 92 (2007).

[194] G. Adamo, J. Y. Ou, J. S. So, S. D. Jenkins, F. De Angelis, K. F. MacDonald, E. Di Fabrizio, J. Ruostekoski, and N. I. Zheludev, *Electron-beam-driven collective-mode metamaterial light source*, Phys. Rev. Lett. **109**, 217401 (2012).

[195] X. Ma, M. Grüßer, and R. Schuster, *Angular Dependence of Cathodoluminescence of Linear and Circular Au Gratings: Imaging the Coupling Angles between Surface Plasmon Polaritons and Light*, J. Phys. Chem. C **118**, 23247 (2014).

[196] N. Yamamoto, S. Ohtani, and F. J. García de Abajo, *Gap and Mie plasmons in individual silver nanospheres near a silver surface*, Nano Lett. **11**, 91 (2011).

[197] Y. Gorodetski, A. Drezet, C. Genet, and T. W. Ebbesen, *Generating Far-Field Orbital Angular Momenta from Near-Field Optical Chirality*, Phys. Rev. Lett. **110**, 203906 (2013).

[198] L. Lu, J. D. Joannopoulos, and M. Soljacic, *Topological photonics*, Nat. Photonics **8**, 821 (2014).

[199] M. Onoda, S. Murakami, and N. Nagaosa, *Hall Effect of Light*, Phys. Rev. Lett. **93**, 083901 (2004).

[200] X. Yin, Z. Ye, J. Rho, Y. Wang, and X. Zhang, *Photonic Spin Hall Effect at Metasurfaces*, Science **339**, 1405 (2013).

[201] G. Li, M. Kang, S. Chen, S. Zhang, E. Y.-B. Pun, K. W. Cheah, and J. Li, *Spin-Enabled*

Plasmonic Metasurfaces for Manipulating Orbital Angular Momentum of Light, Nano Lett. **13**, 4148 (2013).

[202] D. O'Connor, P. Ginzburg, F. J. Rodríguez-Fortuño, G. A. Wurtz, and A. V. Zayats, *Spin–orbit coupling in surface plasmon scattering by nanostructures*, Nat. Commun. **5** (2014).

[203] C. Fallet, T. Novikova, M. Foldyna, S. Manhas, B. H. Ibrahim, A. D. Martino, C. Vannuffel, and C. Constancias, *Overlay measurements by Mueller polarimetry in back focal plane*, J. Micro/Nanolith **10**, 033017 (2011).

[204] O. Arteaga, B. M. Maoz, S. Nichols, G. Markovich, and B. Kahr, *Complete polarimetry on the asymmetric transmission through subwavelength hole arrays*, Opt. Express **11**, 13719 (2014).

[205] S. S. Kruk, M. D. I. Staude, S. Schlecht, M. Greppmair, D. N. Neshev, and Y. S. Kivshar, *Spin-Polarized Photon Emission by Resonant Multipolar Nanoantennas*, ACS Photonics **1**, 1218 (2014).

[206] C. I. Osorio, A. Mohtashami, and A. F. Koenderink, *K-space polarimetry of bullseye plasmon antennas*, Sci. Rep. **5**, 9966 (2015).

[207] M. Lieb, J. Zavislan, and L. Novotny, *Single-molecule orientations determined by direct emission pattern imaging*, J. Opt. Soc. Am. B: Opt. Phys. **21**, 1210 (2004).

[208] T. Kosako, Y. Kadoya, and H. F. Hofmann, *Directional control of light by a nano-optical Yagi-Uda antenna*, Nat. Photonics **4**, 312 (2010).

[209] H. Aouani, O. Mahboub, N. Bonod, E. Devaux, E. Popov, H. Rigneault, T. W. Ebbesen, and J. Wenger, *Bright unidirectional fluorescence emission of molecules in a nanoaperture with plasmonic corrugations*, Nano Lett. **11**, 637 (2011).

[210] I. Sersic, C. Tuambilangana, and A. F. Koenderink, *Fourier microscopy of single plasmonic scatterers*, New J. Phys. **13**, 083019 (2011).

[211] C. Belacel, B. Habert, F. Bigourdan, F. Marquier, J. P. Hugonin, S. Michaelis de Vasconcellos, X. Lafosse, L. Coolen, C. Schwob, C. Javaux, B. Dubertret, J. J. Greffet, P. Senellart, and A. Maitre, *Controlling spontaneous emission with plasmonic optical patch antennas*, Nano Lett. **13**, 1516 (2013).

[212] H. G. Berry, G. Gabrielse, and A. E. Livingston, *Measurement of the Stokes parameters of light*, Appl. Opt. **16**, 3200 (1977).

[213] R. A. Chipman, *Polarimetry*, in *Handbook of Optics, Third Edition Volume I: Geometrical and Physical Optics, Polarized Light, Components and Instruments*, edited by M. Bass, C. DeCusatis, J. Enoch, V. Lakshminarayanan, G. Li, C. Macdonald, V. Mahajan, and E. Van Stryland, McGraw-Hill, Inc., 2010.

[214] H. J. Lezec, A. Degiron, E. Devaux, R. A. Linke, L. Martín-Moreno, F. J. Garcia-Vidal, and T. W. Ebbesen, *Beaming light from a subwavelength aperture*, Science **297**, 820 (2002).

[215] Y. C. Jun, K. C. Y. Huang, and M. L. Brongersma, *Plasmonic beaming and active control over fluorescent emission*, Nat. Commun. **2**, 283 (2011).

[216] S. Han and D. Norris, *Beaming thermal emission from hot metallic bull's eyes*, Opt. Express **18**, 4829 (2010).

[217] G. Rui, D. C. Abeysinghe, R. L. Nelson, and Q. Zhan, *Demonstration of beam steering via dipole-coupled plasmonic spiral antenna*, Sci. Rep. **3**, 2237 (2013).

[218] A. Mohtashami, T. Coenen, A. Antoncecchi, A. Polman, and A. F. Koenderink, *Nanoscale excitation mapping of plasmonic patch antennas*, ACS Photonics (2014).

[219] G. Brucoli and L. Martín-Moreno, *Effect of defect depth on surface plasmon scattering by subwavelength surface defects*, Phys. Rev. B **83**, 075433 (2011).

[220] D. T. Schoen, T. Coenen, F. J. García de Abajo, M. L. Brongersma, and A. Polman, *The*

planar parabolic optical antenna, Nano Lett. **13**, 188 (2013).

[221] L. Novotny and B. Hecht, *Principles of nano-optics*, Cambridge University press, 2006.

[222] A. Drezet, C. Genet, J.-Y. Laluet, and T. W. Ebbesen, *Optical chirality without optical activity: How surface plasmons give a twist to light*, Opt. Express **16**, 12559 (2008).

[223] G. Rui, W. Chen, D. C. Abeysinghe, R. L. Nelson, and Q. Zhan, *Beaming circularly polarized photons from quantum dots coupled with plasmonic spiral antenna*, Opt. Express **20**, 19297 (2012).

[224] G. Rui, R. L. Nelson, and Q. Zhan, *Circularly polarized unidirectional emission via a coupled plasmonic spiral antenna*, Opt. Lett. **36**, 4533 (2011).

[225] K. Haraguchi, T. Katsuyama, and K. Hiruma, *Polarization dependence of light emitted from GaAs p-n junctions in quantum wire crystals*, J. Appl. Phys. **75**, 4220 (1994).

[226] C. P. T. Svensson, T. Mårtensson, J. Trägårdh, C. Larsson, M. Rask, D. Hessman, L. Samuelson, and J. Ohlsson, *Monolithic GaAs/InGaP nanowire light emitting diodes on silicon*, Nanotechnology **19**, 305201 (2008).

[227] M. H. Huang, S. Mao, H. Feick, H. Yan, Y. Wu, H. Kind, E. Weber, R. Russo, and P. Yang, *Room-temperature ultraviolet nanowire nanolasers*, Science **292**, 1897 (2001).

[228] Y. Cui, J. Wang, S. R. Plissard, A. Cavalli, T. T. T. Vu, R. P. J. van Veldhoven, L. Gao, M. Trainor, M. A. Verheijen, J. E. M. Haverkort, and E. P. A. M. Bakkers, *Efficiency enhancement of InP nanowire solar cells by surface cleaning*, Nano Lett. **13**, 4113 (2013).

[229] J. Wang, M. S. Gudiksen, X. Duan, Y. Cui, and C. M. Lieber, *Highly polarized photoluminescence and photodetection from single indium phosphide nanowires*, Science **293**, 1455 (2001).

[230] A. V. Maslov and C. Z. Ning, *Far-field emission of a semiconductor nanowire laser.*, Opt. Lett. **29**, 572 (2004).

[231] A. V. Maslov, M. I. Bakunov, and C. Z. Ning, *Distribution of optical emission between guided modes and free space in a semiconductor nanowire*, J. Appl. Phys. **99**, 024314 (2006).

[232] J. Motohisa, Y. Kohashi, and S. Maeda, *Far-field emission patterns of nanowire light-emitting diodes*, Nano Lett. **14**, 3653 (2014).

[233] G. Grzela, R. Paniagua-Domínguez, T. Barten, Y. Fontana, J. A. Sánchez-Gil, and J. Gómez Rivas, *Nanowire antenna emission*, Nano Lett. **12**, 5481 (2012).

[234] D. van Dam, D. R. Abujetas, R. Paniagua-Domínguez, J. A. Sánchez-Gil, E. P. A. M. Bakkers, J. E. M. Haverkort, and J. Gómez Rivas, *Directional and polarized emission from nanowire arrays*, Nano Lett. **15**, 4557 (2015).

[235] R. Yan, D. Gargas, and P. Yang, *Nanowire photonics*, Nat. Photonics **3**, 569 (2009).

[236] X. Duan, Y. Huang, Y. Cui, J. Wang, and C. M. Lieber, *Indium phosphide nanowires as building blocks for nanoscale electronic and optoelectronic devices*, Nature **409**, 66 (2001).

[237] M. S. Gudiksen, L. J. Lauhon, J. Wang, D. C. Smith, and C. M. Lieber, *Growth of nanowire superlattice structures for nanoscale photonics and electronics*, Nature **415**, 617 (2002).

[238] M. Björk, B. Ohlsson, T. Sass, A. Persson, C. Thelander, M. Magnusson, K. Deppert, L. Wallenberg, and L. Samuelson, *One-dimensional steeplechase for electrons realized*, Nano Lett. **2**, 87 (2002).

[239] J. Claudon, J. Bleuse, N. S. Malik, M. Bazin, P. Jaffrennou, N. Gregersen, C. Sauvan, P. Lalanne, and J.-M. Gérard, *A highly efficient single-photon source based on a quantum dot in a photonic nanowire*, Nat. Photonics **4**, 174 (2010).

[240] H. J. Joyce, C. J. Docherty, Q. Gao, H. H. Tan, C. Jagadish, J. Lloyd-Hughes, L. M. Herz, and M. B. Johnston, *Electronic properties of GaAs, InAs and InP nanowires studied by terahertz spectroscopy*, Nanotechnology **24**, 214006 (2013).

[241] J. Claudon, N. Gregersen, P. Lalanne, and J.-M. Gérard, *Harnessing light with photonic nanowires: fundamentals and applications to quantum optics*, ChemPhysChem **14**, 2393 (2013).

[242] D. J. Traviss, M. K. Schmidt, J. Aizpurua, and O. L. Muskens, *Antenna resonances in low aspect ratio semiconductor nanowires*, Opt. Express **23**, 22771 (2015).

[243] H. Acar, T. Coenen, A. Polman, and L. Kuipers, *Dispersive ground plane core-shell type optical monopole antennas fabricated with electron beam induced deposition*, ACS Nano **6**, 8226 (2012).

[244] F. Bernal Arango, A. Kwadrin, and A. F. Koenderink, *Plasmonic antennas hybridized with dielectric waveguides*, ACS Nano **6**, 10156 (2012).

[245] J. Wallentin, P. Wickert, M. Ek, A. Gustafsson, L. R. Wallenberg, M. H. Magnusson, L. Samuelson, K. Deppert, and M. T. Borgström, *Degenerate p-doping of InP nanowires for large area tunnel diodes*, Appl. Phys. Lett. **99**, 253105 (2011).

[246] D. Vanmaekelbergh and L. K. van Vugt, *ZnO nanowire lasers*, Nanoscale **3**, 2783 (2011).

[247] R. Röder, D. Ploss, A. Kriesch, R. Buschlinger, S. Geburt, U. Peschel, and C. Ronning, *Polarization features of optically pumped CdS nanowire lasers*, J. Phys. D: Appl. Phys. **47**, 394012 (2014).

[248] P. Krogstrup, H. I. Jørgensen, M. Heiss, O. Demichel, J. V. Holm, M. Aagesen, J. Nygard, and A. Fontcuberta i Morral, *Single-nanowire solar cells beyond the Shockley-Queisser limit*, Nat. Photonics **7**, 306 (2013).

[249] O. L. Muskens, J. Gómez Rivas, R. E. Algra, E. P. A. M. Bakkers, and A. Lagendijk, *Design of light scattering in nanowire materials for photovoltaic applications*, Nano Lett. **8**, 2638 (2008).

[250] M. Heiss, Y. Fontana, A. Gustafsson, G. Wüst, C. Magen, D. O'Regan, J. Luo, B. Ketterer, S. Conesa-Boj, A. Kuhlmann, J. Houel, E. Russo-Averchi, J. R. Morante, M. Cantoni, N. Marzari, J. Arbiol, A. Zunger, R. J. Warburton, and A. Fontcuberta i Morral, *Self-assembled quantum dots in a nanowire system for quantum photonics*, Nat. Mater. **12**, 439 (2013).

[251] G. Bulgarini, M. E. Reimer, M. Bouwes Bavinck, K. D. Jöns, D. Dalacu, P. J. Poole, E. P. A. M. Bakkers, and V. Zwiller, *Nanowire waveguides launching single photons in a gaussian mode for ideal fiber coupling.*, Nano Lett. (2014).

[252] M. E. Reimer, G. Bulgarini, N. Akopian, M. Hocevar, M. Bouwes Bavinck, M. A. Verheijen, E. P. A. M. Bakkers, L. P. Kouwenhoven, and V. Zwiller, *Bright single-photon sources in bottom-up tailored nanowires*, Nat. Commun. **3**, 737 (2012).

[253] R. Paniagua-Domínguez, D. R. Abujetas, and J. A. Sánchez-Gil, *Ultra low-loss, isotropic optical negative-index metamaterial based on hybrid metal-semiconductor nanowires*, Sci. Rep. **3**, 1507 (2013).

[254] M. Ramezani, A. Casadei, G. Grzela, F. Matteini, G. Tütüncüoglu, D. Rüffer, A. Fontcuberta i Morral, and J. Gómez-Rivas, *Hybrid semiconductor nanowire-metallic Yagi-Uda antennas*, Nano Lett. **15**, 4889 (2015).

[255] C. Thelander, P. Agarwal, S. Brongersma, J. Eymery, L. Feiner, A. Forchel, M. Scheffler, W. Riess, B. Ohlsson, U. Gösele, and L. Samuelson, *Nanowire-based one-dimensional electronics*, Mater. Today **9**, 28 (2006).

[256] L. Cao, J. S. White, J. Park, J. A. Schuller, B. M. Clemens, and M. L. Brongersma, *Engineering light absorption in semiconductor nanowire devices*, Nat. Mater. **8**, 643

(2009).

[257] R. Paniagua-Domínguez, G. Grzela, J. Gómez Rivas, and J. Sánchez-Gil, *Enhanced and directional emission of semiconductor nanowires tailored through leaky/guided modes*, Nanoscale **5**, 10582 (2013).

[258] D. R. Abujetas, R. Paniagua-Domínguez, and J. A. Sánchez-Gil, *Unraveling the janus role of Mie resonances and leaky/guided modes in semiconductor nanowire absorption for enhanced light harvesting*, ACS Photonics **2**, 921 (2015).

[259] B. J. M. Brenny, D. van Dam, C. I. Osorio, J. Gómez Rivas, and A. Polman, *Azimuthally polarized cathodoluminescence from InP nanowires*, Appl. Phys. Lett. **107**, 201110 (2015).

[260] E. Russo-Averchi, M. Heiss, L. Michelet, P. Krogstrup, J. Nygard, C. Magen, J. R. Morante, E. Uccelli, J. Arbiol, and A. Fontcuberta i Morral, *Suppression of three dimensional twinning for a 100% yield of vertical GaAs nanowires on silicon*, Nanoscale **4**, 1486 (2012).

[261] F. Matteini, G. Tütüncüoglu, H. Potts, F. Jabeen, and A. Fontcuberta i Morral, *Wetting of Ga on SiO_x and its impact on GaAs nanowire growth on silicon*, Cryst. Growth Des. **15**, 3105 (2015).

[262] J. A. Stratton, *Electromagnetic theory*, Read Books, 1941.

[263] E. D. Palik, *Handbook of optical constants of solids*, volume 3, Academic press, 1998.

[264] H.-J. Hagemann, W. Gudat, and C. Kunz, *Optical constants from the far infrared to the x-ray region: Mg, Al, Cu, Ag, Au, Bi, C, and Al_2O_3*, J. Opt. Soc. Am. **65**, 742 (1975).

[265] S. R. Arridge, *Optical tomography in medical imaging*, Inverse Prob. **15**, R41 (1999).

[266] W. Munk, P. Worcester, and C. Wunsch, *Ocean Acoustic Tomography*, Cambridge University Press, 2009.

[267] G. Nolet, editor, *Seismic Tomography*, Springer Netherlands, 1987.

[268] R. A. Crowther, D. J. DeRosier, and A. Klug, *The Reconstruction of a Three-Dimensional Structure from Projections and its Application to Electron Microscopy*, Proc. R. Soc. A **317**, 319 (1970).

[269] N. Yao and Z. L. Wang, *Handbook of Microscopy for Nanotechnology*, Springer, 2006.

[270] P. A. Midgley and R. E. Dunin-Borkowski, *Electron tomography and holography in materials science*, Nat. Mater. **8**, 271 (2009).

[271] D. De Winter, M. N. Lebbink, D. F. Wiggers De Vries, J. A. Post, and M. R. Drury, *FIB-SEM cathodoluminescence tomography: practical and theoretical considerations*, J. Microsc. **243**, 315 (2011).

[272] S. Van Aert, K. J. Batenburg, M. D. Rossell, R. Erni, and G. Van Tendeloo, *Three-dimensional atomic imaging of crystalline nanoparticles*, Nature **470**, 374 (2011).

[273] M. C. Scott, C. C. Chen, M. Mecklenburg, C. Zhu, R. Xu, P. Ercius, U. Dahmen, B. C. Regan, and J. Miao, *Electron tomography at 2.4-Ångström resolution*, Nature **483**, 444 (2012).

[274] G. Möbus, R. C. Doole, and B. J. Inkson, *Spectroscopic electron tomography*, Ultramicroscopy **96**, 433 (2003).

[275] M. H. Gass, K. K. K. Koziol, A. H. Windle, and P. A. Midgley, *Four-Dimensional Spectral Tomography of Carbonaceous Nanocomposites*, Nano Lett. **6**, 376 (2006).

[276] K. Jarausch, P. Thomas, D. N. Leonard, R. Twesten, and C. R. Booth, *Four-dimensional STEM-EELS: Enabling nano-scale chemical tomography*, Ultramicroscopy **109**, 326 (2009).

[277] G. Haberfehlner, P. Bayle-Guillemaud, G. Audoit, D. Lafond, P. H. Morel, V. Jousseaume, T. Ernst, and P. Bleuet, *Four-dimensional spectral low-loss energy-filtered transmission*

electron tomography of silicon nanowire-based capacitors, Appl. Phys. Lett. **101**, 063108 (2012).

[278] B. Huang, W. Wang, M. Bates, and X. Zhuang, *Three-Dimensional Super-Resolution Imaging by Stochastic Optical Reconstruction Microscopy*, Science **319**, 810 (2008).

[279] S. R. P. Pavani, M. A. Thompson, J. S. Biteen, S. J. Lord, N. Liu, R. J. Twieg, R. Piestun, and W. E. Moerner, *Three-dimensional, single-molecule fluorescence imaging beyond the diffraction limit by using a double-helix point spread function*, Proc. Natl. Acad. Sci. U.S.A. **106**, 2995 (2009).

[280] T. Klar, M. Perner, S. Grosse, G. von Plessen, W. Spirkl, and J. Feldmann, *Surface-Plasmon Resonances in Single Metallic Nanoparticles*, Phys. Rev. Lett. **80**, 4249 (1998).

[281] M. Schnell, A. García-Etxarri, A. J. Huber, K. Crozier, J. Aizpurua, and R. Hillenbrand, *Controlling the near-field oscillations of loaded plasmonic nanoantennas*, Nat. Photonics **3**, 287 (2009).

[282] Z. Fei, A. S. Rodin, G. O. Andreev, W. Bao, A. S. McLeod, M. Wagner, L. M. Zhang, Z. Zhao, M. Thiemens, G. Dominguez, M. M. Fogler, A. H. Castro Neto, C. N. Lau, F. Keilmann, and D. N. Basov, *Gate-tuning of graphene plasmons revealed by infrared nano-imaging*, Nature **487**, 82 (2012).

[283] J. Michaelis, C. Hettich, J. Mlynek, and V. Sandoghdar, *Optical microscopy using a single-molecule light source*, Nature **405**, 325 (2000).

[284] J. N. Farahani, D. W. Pohl, H. J. Eisler, and B. Hecht, *Single Quantum Dot Coupled to a Scanning Optical Antenna: A Tunable Superemitter*, Phys. Rev. Lett. **95**, 017402 (2005).

[285] M. Frimmer, Y. Chen, and A. F. Koenderink, *Scanning emitter lifetime imaging microscopy for spontaneous emission control*, Phys. Rev. Lett. **107**, 123602 (2011).

[286] F. Dolde, H. Fedder, M. W. Doherty, T. Nöbauer, F. Rempp, G. Balasubramanian, T. Wolf, F. Reinhard, L. C. L. Hollenberg, F. Jelezko, and J. Wrachtrup, *Electric-field sensing using single diamond spins*, Nat. Phys. **7**, 459 (2011).

[287] M. Geiselmann, M. L. Juan, J. Renger, J. M. Say, L. J. Brown, F. J. García de Abajo, F. Koppens, and R. Quidant, *Three-dimensional optical manipulation of a single electron spin*, Nat. Nanotechnol. **8**, 175 (2013).

[288] N. Yamamoto, K. Araya, and F. J. García de Abajo, *Photon emission from silver particles induced by a high-energy electron beam*, Phys. Rev. B **64**, 205419 (2001).

[289] O. Nicoletti, F. de la Peña, R. K. Leary, D. J. Holland, C. Ducati, and P. A. Midgley, *Three-dimensional imaging of localized surface plasmon resonances of metal nanoparticles*, Nature **502**, 80 (2013).

[290] A. Aubry, D. Y. Lei, A. I. Fernandez-Dominguez, Y. Sonnefraud, S. A. Maier, and J. Pendry, *Plasmonic Light-Harvesting Devices over the Whole Visible Spectrum*, Nano Lett. **10**, 2574 (2010).

[291] A. I. Fernandez-Dominguez, Y. Luo, A. Wiener, J. Pendry, and S. A. Maier, *Theory of three-dimensional nanocrescent light harvesters*, Nano Lett. **12**, 5946 (2012).

[292] Y. Luo, D. Y. Lei, S. A. Maier, and J. Pendry, *Broadband Light Harvesting Nanostructures Robust to Edge Bluntness*, Phys. Rev. Lett. **108**, (2012).

[293] Y. Lu, G. Liu, J. Kim, Y. Mejia, and L. Lee, *Nanophotonic crescent moon structures with sharp edge for ultrasensitive biomolecular detection by local electromagnetic field enhancement effect*, Nano Lett. **5**, 119 (2005).

[294] G. L. Liu, Y. Lu, J. Kim, J. C. Doll, and L. P. Lee, *Magnetic Nanocrescents as Controllable Surface-Enhanced Raman Scattering Nanoprobes for Biomolecular Imaging*, Adv. Mater. **17**, 2683 (2005).

[295] B. Ross and L. Lee, *Plasmon tuning and local field enhancement maximization of the*

nanocrescent, Nanotechnology **19**, 275201 (2008).

[296] M. W. Knight and N. J. Halas, *Nanoshells to nanoeggs to nanocups: optical properties of reduced symmetry core–shell nanoparticles beyond the quasistatic limit*, New J. Phys. **10**, 105006 (2008).

[297] A. C. Atre, A. García-Etxarri, H. Alaeian, and J. A. Dionne, *Toward high-efficiency solar upconversion with plasmonic nanostructures*, J. Opt. **14**, 024008 (2012).

[298] M. Cortie and M. Ford, *A plasmon-induced current loop in gold semi-shells*, Nanotechnology **18**, 235704 (2007).

[299] N. A. Mirin and N. J. Halas, *Light-Bending Nanoparticles*, Nano Lett. **9**, 1255 (2009).

[300] A. C. Atre, A. García-Etxarri, H. Alaeian, and J. A. Dionne, *A Broadband Negative Index Metamaterial at Optical Frequencies*, Adv. Opt. Mater. **1**, 327 (2013).

[301] F. J. García de Abajo and A. Howie, *Relativistic electron energy loss and electron-induced photon emission in inhomogeneous dielectrics*, Phys. Rev. Lett. **80**, 5180 (1998).

[302] F. J. García de Abajo and A. Howie, *Retarded field calculation of electron energy loss in inhomogeneous dielectrics*, Phys. Rev. B **65**, 115418 (2002).

[303] R. Gómez-Medina, N. Yamamoto, M. Nakano, and F. J. García de Abajo, *Mapping plasmons in nanoantennas via cathodoluminescence*, New J. Phys. **10**, 105009 (2008).

[304] A. Mooradian, *Photoluminescence of metals*, Phys. Rev. Lett. **22**, 185 (1969).

[305] X. Wu, T. Ming, X. Wang, P. Wang, J. Wang, and J. Chen, *High-photoluminescence-yield gold nanocubes: for cell imaging and photothermal therapy*, ACS Nano **4**, 113 (2009).

[306] M. Yorulmaz, S. Khatua, P. Zijlstra, A. Gaiduk, and M. Orrit, *Luminescence Quantum Yield of Single Gold Nanorods*, Nano Lett. **12**, 4385 (2012).

[307] G. A. George, *The phosphorescence spectrum and photodegradation of polystyrene films*, J. Appl. Polym. Sci. **18**, 419 (1974).

[308] K. M. Hanson, *Special Topics in Test Methodology: Tomographic reconstruction of axially symmetric objects from a single radiograph*, Prog. Astronaut. Aeronaut. **155**, 1 (1993).

[309] X. Y. Wang, R. Lockwood, M. Malac, H. Furukawa, P. Li, and A. Meldrum, *Reconstruction and visualization of nanoparticle composites by transmission electron tomography*, Ultramicroscopy **113**, 96 (2012).

[310] M. Lyra and A. Ploussi, *Filtering in SPECT Image Reconstruction*, Int. J. Biomed. Imaging **2011**, 1 (2011).

[311] I. Arslan, J. R. Tong, and P. A. Midgley, *Reducing the missing wedge: High-resolution dual axis tomography of inorganic materials*, Ultramicroscopy **106**, 994 (2006).

[312] M. van Heel, B. Gowen, R. Matadeen, E. V. Orlova, R. Finn, T. Pape, D. Cohen, H. Stark, R. Schmidt, and M. Schatz, *Single-particle electron cryo-microscopy: towards atomic resolution*, Q. Rev. Biophys. **33**, 307 (2000).

[313] D. Cai, A. Neyer, R. Kuckuk, and H. M. Heise, *Raman, mid-infrared, near-infrared and ultraviolet–visible spectroscopy of PDMS silicone rubber for characterization of polymer optical waveguide materials*, J. Mol. Struct. **976**, 274 (2010).

[314] A. C. Atre, B. J. M. Brenny, T. Coenen, A. García-Etxarri, A. Polman, and J. A. Dionne, *Nanoscale optical tomography with cathodoluminescence spectroscopy*, Nat. Nanotechnol. **10**, 429 (2015).

[315] M. B. Mohamed, V. Volkov, S. Link, and M. A. El-Sayed, *The lightning gold nanorods: fluorescence enhancement of over a million compared to the gold metal*, Chem. Phys. Lett. **317**, 517 (2000).

[316] M. R. Beversluis, A. Bouhelier, and L. Novotny, *Continuum generation from single gold nanostructures through near-field mediated intraband transitions*, Phys. Rev. B **68**,

115433 (2003).
[317] E. Dulkeith, T. Niedereichholz, T. A. Klar, J. Feldmann, G. von Plessen, D. I. Gittins, K. S. Mayya, and F. Caruso, *Plasmon emission in photoexcited gold nanoparticles*, Phys. Rev. B **70**, 205424 (2004).
[318] H. Hu, H. Duan, J. K. W. Yang, and Z. X. Shen, *Plasmon-Modulated Photoluminescence of Individual Gold Nanostructures*, ACS Nano **6**, 10147 (2012).
[319] E. Yablonovitch, *Inhibited spontaneous emission in solid-state physics and electronics*, Phys. Rev. Lett. **58**, 2059 (1987).
[320] M. Fujita, S. Takahashi, Y. Tanaka, T. Asano, and S. Noda, *Simultaneous inhibition and redistribution of spontaneous light emission in photonic crystals*, Science **308**, 1296 (2005).
[321] J. D. Joannopoulos, S. G. Johnson, J. N. Winn, and R. D. Meade, *Photonic crystals: molding the flow of light*, Princeton University Press, 2011.
[322] T. Yoshie, A. Scherer, J. Hendrickson, G. Khitrova, H. M. Gibbs, G. Rupper, C. Ell, O. B. Shchekin, and D. G. Deppe, *Vacuum Rabi splitting with a single quantum dot in a photonic crystal nanocavity*, Nature **432**, 200 (2004).
[323] S. Hughes, *Enhanced single-photon emission from quantum dots in photonic crystal waveguides and nanocavities*, Opt. Lett. **29**, 2659 (2004).
[324] S. Noda, M. Yokoyama, M. Imada, A. Chutinan, and M. Mochizuki, *Polarization mode control of two-dimensional photonic crystal laser by unit cell structure design*, Science **293**, 1123 (2001).
[325] H.-G. Park, S.-H. Kim, S.-H. Kwon, Y.-G. Ju, J.-K. Yang, J.-H. Baek, S.-B. Kim, and Y.-H. Lee, *Electrically driven single-cell photonic crystal laser*, Science **305**, 1444 (2004).
[326] A. Opheij, N. Rotenberg, D. M. Beggs, I. H. Rey, T. F. Krauss, and L. Kuipers, *Ultracompact (3 μm) silicon slow-light optical modulator*, Sci. Rep. **3** (2013).
[327] D. M. Beggs, T. P. White, L. O'Faolain, and T. F. Krauss, *Ultracompact and low-power optical switch based on silicon photonic crystals*, Opt. Lett. **33**, 147 (2008).
[328] D. M. Beggs, I. H. Rey, T. Kampfrath, N. Rotenberg, L. Kuipers, and T. F. Krauss, *Ultrafast tunable optical delay line based on indirect photonic transitions*, Phys. Rev. Lett. **108**, 213901 (2012).
[329] T. F. Krauss, *Slow light in photonic crystal waveguides*, J. Phys. D: Appl. Phys. **40**, 2666 (2007).
[330] T. F. Krauss, M. Richard, and S. Brand, *Two-dimensional photonic-bandgap structures operating at near-infrared wavelengths*, Nature **383**, 699 (1996).
[331] Y. A. Vlasov, M. O'Boyle, H. F. Hamann, and S. J. McNab, *Active control of slow light on a chip with photonic crystal waveguides*, Nature **438**, 65 (2005).
[332] D. M. Beggs, T. F. Krauss, L. Kuipers, and T. Kampfrath, *Ultrafast tilting of the dispersion of a photonic crystal and adiabatic spectral compression of light pulses*, Phys. Rev. Lett. **108**, 033902 (2012).
[333] T. Baba, *Slow light in photonic crystals*, Nat. Photonics **2**, 465 (2008).
[334] D. W. Pohl, W. Denk, and M. Lanz, *Optical stethoscopy: Image recording with resolution λ/20*, Appl. Phys. Lett. **44**, 651 (1984).
[335] E. Betzig, J. K. Trautman, T. D. Harris, J. S. Weiner, and R. L. Kostelak, *Breaking the diffraction barrier: optical microscopy on a nanometric scale*, Science **251**, 1468 (1991).
[336] R. C. Reddick, R. J. Warmack, and T. L. Ferrell, *New form of scanning optical microscopy*, Phys. Rev. B **39**, 767 (1989).
[337] C. Chicanne, T. David, R. Quidant, J.-C. Weeber, Y. Lacroute, E. Bourillot, A. Dereux, G. Colas des Francs, and C. Girard, *Imaging the local density of states of optical corrals*,

Phys. Rev. Lett. **88**, 097402 (2002).

[338] G. Colas des Francs, C. Girard, J.-C. Weeber, and A. Dereux, *Relationship between scanning near-field optical images and local density of photonic states*, Chem. Phys. Lett. **345**, 512 (2001).

[339] H. Gersen, T. Karle, R. Engelen, W. Bogaerts, J. Korterik, N. Van Hulst, T. Krauss, and L. Kuipers, *Direct observation of Bloch harmonics and negative phase velocity in photonic crystal waveguides*, Phys. Rev. Lett. **94**, 123901 (2005).

[340] L. Novotny, *The history of near-field optics*, Prog. Optics **50**, 137 (2007).

[341] M. Burresi, D. van Oosten, T. Kampfrath, H. Schoenmaker, R. Heideman, A. Leinse, and L. Kuipers, *Probing the magnetic field of light at optical frequencies*, Science **326**, 550 (2009).

[342] M. Honda and N. Yamamoto, *Size dependence of surface plasmon modes in one-dimensional plasmonic crystal cavities*, Opt. Express **21**, 11973 (2013).

[343] H. Benisty, *Modal analysis of optical guides with two-dimensional photonic band-gap boundaries*, J. Appl. Phys. **79**, 7483 (1996).

[344] S. G. Johnson, P. R. Villeneuve, S. Fan, and J. D. Joannopoulos, *Linear waveguides in photonic-crystal slabs*, Phys. Rev. B **62**, 8212 (2000).

[345] G. Lecamp, J.-P. Hugonin, and P. Lalanne, *Theoretical and computational concepts for periodic optical waveguides*, Opt. Express **15**, 11042 (2007).

[346] S. G. Johnson and J. D. Joannopoulos, *Block-iterative frequency-domain methods for Maxwell's equations in a planewave basis*, Opt. Express **8**, 173 (2001).

[347] D. M. Beggs, L. O'Faolain, and T. F. Krauss, *Accurate determination of the functional hole size in photonic crystal slabs using optical methods*, Phot. Nano. Fund. Appl. **6**, 213 (2008).

[348] M. Lončar, D. Nedeljković, T. P. Pearsall, J. Vučković, A. Scherer, S. Kuchinsky, and D. C. Allan, *Experimental and theoretical confirmation of Bloch-mode light propagation in planar photonic crystal waveguides*, Appl. Phys. Lett. **80**, 1689 (2002).

Scientific summary

Light is ubiquitous, both in everyday life (sunlight, lamps, laser pointers) and in scientific research. Whether in biology, medicine, chemistry or physics, it is an essential tool to probe and characterize different structures and processes. Light allows us to better understand the world around us and improve or invent useful applications. Throughout the last decades, science has been probing both the biological and physical worlds in ever greater detail, delving deeper and deeper to the smallest length scales. Improvements in microscopy have played a major role in these advances, with each successive increase in resolution revealing previously hidden features. Nanophotonics, the study of light at the nanoscale, is a vibrant field of research with a wide variety of important applications, such as new solar cells, LEDs, sensors, and integrated optical chips. To mold and control light at the nanoscale, it is essential to measure and characterize nanostructures and their interaction with light at that scale. For this reason, techniques which allow us to determine optical properties at subwavelength length scales are critical to advances in the field.

Electrons prove to be useful to achieve this goal, because they can attain much higher momenta and correspondingly smaller wavelengths than photons in the optical spectral range. Electron microscopes have already been used for decades to determine the size or morphology of nanostructures, but high-energy electrons can also generate electromagnetic radiation. As a result, electron-light-matter interactions can be studied at deep subwavelength scales by using electron spectroscopy techniques. We focus on one such method, cathodoluminescence (CL) spectroscopy. This thesis describes a variety of CL techniques, adding new capabilities to the existing angle-resolved CL imaging spectroscopy (ARCIS) setup. Integrating optical and electron microscopy allows us to reach an excitation resolution on the order of 10 nm. The spectral, angular and polarization properties of light emitted by nanophotonic structures as well as bulk materials can all be measured. Chapter 2 describes the different detection methods used throughout this thesis to measure all of these degrees of freedom of light.

In Chapter 3, we develop a theoretical framework which allows us to determine the time evolution of electron-matter interactions. A moving electron has an electric field that varies with time and space. Studying these dependencies is critical to understanding how electrons can interact with matter to create electromagnetic radiation. We first examine the fields of a moving electron in vacuum. Next, we study the coherent CL processes that occur when a swift electron penetrates a metal surface. Surface plasmon polaritons (SPPs) can be excited and guided along the surface, forming wave packets a few hundred femtoseconds in duration. High-frequency components close to the plasmon resonance are strongly damped, so lower frequencies dominate as the wave packets propagate further from the point of excitation. Transition radiation (TR) is emitted to the far field – as ultrashort wave packets a few tens of femtoseconds in duration – which are strongly dependent on the emission angle and the material properties.

With the theoretical framework in place, we can now move on to experiments using these new CL methods to explore nanoscale light-matter interactions. Chapter 4 demonstrates how angle-resolved cathodoluminescence measurements can be used to separate coherent and incoherent radiation processes. Metals such as aluminium display a dipolar angular radiation profile due to coherent transition radiation. The emission from luminescent materials such as gallium arsenide is dominated (at the band gap energy) by incoherent radiation with a Lambertian angular distribution. In silicon, transition radiation and incoherent luminescence are similar in magnitude, but the exact ratio depends on wavelength. The angular data can be fitted to determine the ratio between these processes to separate their spectral contributions. Using polarization, however, could provide a more general method to separate these different mechanisms in more complex structures and geometries.

Chapter 5 introduces angle-resolved CL imaging polarimetry as a new method to determine the *full* polarization state of CL emission. Combining 6 measurements for different settings of a quarter-wave plate and linear polarizer establishes the Stokes parameters, which fully characterize the polarization of light. The technique is benchmarked using transition radiation, after which we apply it to metallic bullseye and spiral nanostructures. Both nanoscale changes in excitation position and structure handedness lead to significant modifications in the ellipticity and helicity of the polarization. Polarimetry distinguishes polarized from unpolarized light, allowing us to separate coherent (polarized) from incoherent (unpolarized) emission from gold, gallium arsenide and silicon surfaces, in greater detail than was achieved through the method described in Chapter 4.

Chapter 6 describes how the CL polarimetry developed in Chapter 5 can measure the angle- and polarization-dependent emission from vertically grown indium phosphide nanowires of different heights. The electron beam excites band gap emission from the wires, which in turn displays azimuthally polarized rings, with the number of rings depending on the nanowire height. These results are well-described by a model in which emission from the top of the nanowire interferes with the reflection off of the substrate. The measurements and calculations deter-

mine the size of the emission region, enabling an assessment of the carrier diffusion length.

Chapter 7 presents the use of CL polarimetry to study horizontal gallium arsenide nanowires of different diameters. Band gap luminescence excited by the electron beam couples to waveguide modes that depend on nanowire diameter and determine the directionality and polarization of the emission. Polarimetry measurements demonstrate that the emission behavior is dominated by the TM01 waveguide mode for all wires. However, thin and thick nanowires exhibit opposite emission directionality when exciting them close to their end facets. This results from a transition in the waveguide mode from leaky behavior for the thin nanowire to guided behavior for the thick one, in agreement with a simple line current model and numerical simulations.

The measurements in the previous chapters provide only spatial information about light emission in 2D. Chapter 8 introduces spectroscopic CL tomography, a new method to characterize the 3D optical properties of structures at the nanoscale. We measure 2D CL intensity maps of a metal-dielectric resonator for various orientations and use the method of filtered back projection to reconstruct a 3D image of the CL emission. Studying this spectrally-resolved 3D CL distribution allows us to recognize and distinguish material luminescence from electromagnetic eigenmodes that correlate with the radiative local density of optical states, as they are separated both spatially and spectrally.

All chapters thus far have discussed experiments performed in and close to the visible spectral range (λ_0=400–1000 nm). Finally, in Chapter 9, we measure CL spectroscopy in the near-infrared spectral range (λ_0=1000–1600 nm) to examine silicon photonic crystal waveguides. 2D CL intensity scans display sharp spectral resonances with distinct spatial distributions and a strong linear polarization along the waveguide propagation direction. The dominant resonance correlates with calculations for the odd TE waveguide mode in the structure. CL usually couples most strongly to out-of-plane (TM) modes. Our findings demonstrate that it is also possible to couple to TE modes that govern the measured emission.

This thesis demonstrates that cathodoluminescence spectroscopy is a powerful and innovative nanoscale characterization technique, able to determine a wide variety of optical properties of nanophotonic structures. The broad range of experiments and novel theoretical ideas presented in this thesis provide several new fundamental insights into electron-light-matter interactions and the behavior of light at the nanoscale.

Wetenschappelijke samenvatting

Licht is alomtegenwoordig, in het dagelijks leven (denk aan zonlicht, lampen of laser pointers) alsook in wetenschappelijk onderzoek. Zij het in de biologie, geneeskunde, scheikunde of natuurkunde, licht is een essentieel deel van meetmethodes om verschillende structuren en processen te karakteriseren. Dankzij licht kunnen wij de wereld om ons heen beter begrijpen en toepassingen die nuttig zijn voor de samenleving ontdekken of verbeteren. In de laatste decennia heeft de wetenschap de biologische en fysische werelden in steeds meer detail onderzocht, steeds weer de grenzen verleggend naar kleinere lengteschalen. Verbeteringen in de microscopie hebben een grote rol gespeeld in deze ontwikkelingen; elke toename in resolutie gaat gepaard met het ontrafelen van eerder onbekende kenmerken. Nanofotonica, het bestuderen van licht op de nanoschaal, is een levendig onderzoeksgebied met veel belangrijke toepassingen, zoals nieuwe zonnecellen, LEDs, gevoeligere sensoren en geïntegreerde optische chips. Om licht op nanoschaal te kunnen controleren en manipuleren, is het van essentieel belang om nanostructuren, en hun interactie met licht, op diezelfde schaal te meten en te karakteriseren. Om deze reden zijn technieken nodig die optische eigenschappen kunnen bepalen op een lengteschaal kleiner dan de golflengte van licht.

Elektronen zijn nuttige handlangers om dit doel te bereiken, omdat ze een veel hogere kinetische energie en veel kleinere golflengtes kunnen hebben dan fotonen in het optische spectrale gebied. Elektronenmicroscopen zijn al decennia in gebruik om de afmeting en vorm van nanostructuren te bepalen, maar hoogenergetische elektronen kunnen ook worden gebruikt om elektromagnetische straling te genereren. Hierdoor kan men de interacties tussen elektronen, licht en materie onderzoeken op lengteschalen veel kleiner dan de golflengte van licht, met behulp van elektronenspectroscopietechnieken. In dit proefschrift wordt gebruik gemaakt van een van deze methodes, kathodeluminescentie (CL) spectroscopie. We beschrijven verschillende CL technieken en voegen nieuwe meetmethodes toe aan de bestaande hoekopgeloste CL beeldvorming spectroscopie opstelling (ARCIS). Door elektronenmicroscopie te integreren met optische microscopie kunnen we een excitatie resolutie halen in de orde van 10 nm. De spectrale-, hoekafhankelijke- en

polarisatie-eigenschappen van licht dat is uitgezonden door nanofotonische structuren of macroscopische materialen kunnen worden gemeten. Hoofdstuk 2 beschrijft de verschillende detectiemethodes die in dit proefschrift worden gebruikt om alle vrijheidsgraden van licht te meten.

In Hoofdstuk 3 ontwikkelen we een theoretisch model om de tijdsafhankelijkheid van elektron-materie interacties te ontrafelen. Een bewegend elektron heeft een elektrisch veld dat verandert in tijd en ruimte. Het bestuderen van deze eigenschappen is van cruciaal belang om te begrijpen hoe de interactie tussen elektronen en materie kan leiden tot elektromagnetische straling. Om dit te bereiken bekijken we eerst de velden van een bewegend elektron in vacuüm. Vervolgens bestuderen we coherente CL processen die plaatsvinden als een elektron door een metaaloppervlak indringt. Oppervlakteplasmonpolaritonen (SPPs) worden aangemaakt en propageren over het oppervlak, als golfpakketten die maar een paar honderd femtosecondes lang duren. Hoogfrequente componenten dichtbij de plasmon resonantie worden sterk gedempt, dus lagere frequenties domineren wanneer de golfpakketten verder van de excitatiepositie komen. Transitiestraling (TR) is een ander proces, dat uitstraalt naar het verre veld, in de vorm van ultrasnelle golfpakketten die maar een paar tientallen femtosecondes lang duren, en die sterk afhankelijk zijn van de emissiehoek en de permitiviteit van het medium.

Met dit theoretisch kader kunnen we nu experimenten uitvoeren die gebruik maken van nieuwe CL methodes om nanoschaal-licht-materie interacties te bestuderen. Hoofdstuk 4 toont aan dat hoekopgeloste kathodeluminescentiemetingen gebruikt kunnen worden om coherente en incoherente stralingsprocessen van elkaar te scheiden. Metalen zoals aluminium vertonen hetzelfde hoekafhankelijke emissiepatroon als een verticale dipool, als gevolg van transitiestraling. De emissie van luminescerende materialen zoals galliumarseen (GaAs) wordt (bij de bandgapenergie) gedomineerd door incoherente straling met een Lambertiaans hoekprofiel. Voor silicium zijn transitiestraling en luminescentie vergelijkbaar in sterkte, maar de precieze verhouding tussen de twee is afhankelijk van de golflengte. We kunnen de hoekopgeloste metingen fitten om de verhouding van deze processen te bepalen, en op die manier kunnen we hun bijdrage aan het gemeten spectrum van elkaar scheiden. Polarisatie gebruiken zou echter een meer algemene manier opleveren om deze verschillende stralingsprocessen te scheiden.

In Hoofdstuk 5 introduceren we hoekopgeloste CL-beeldvormingpolarimetrie als een nieuwe methode om de volledige polarisatietoestand van CL emissie te bepalen. Het combineren van 6 metingen voor verschillende instellingen van een kwart-lambda faseplaat en een lineaire polarisator leidt tot het vaststellen van de Stokes parameters, die volledig de polarisatie van licht karakteriseren. We testen de techniek met transitiestraling, en passen het daarna toe op metallische “bullseye”- en spiraalantennes. We laten zien dat nanoschaalveranderingen in de excitatiepositie en de draairichting van de structuren leiden tot grote veranderingen in de ellipticiteit en heliciteit van de polarisatie. Polarimetrie maakt het ook mogelijk om gepolariseerd en ongepolariseerd licht van elkaar te scheiden. Hierdoor kunnen we met meer detail dan in Hoofdstuk 4 coherente (gepolariseerde) en incoherente

(ongepolariseerde) emissie onderscheiden, voor oppervlaktes van goud, galliumarseen en silicium.

Hoofdstuk 6 gebruikt de CL-polarimetrietechniek die ontwikkeld is in Hoofdstuk 5 om de hoek- en polarisatieafhankelijke emissie te meten van verticale indiumfosfidenanodraden met verschillende lengtes. De elektronenbundel exciteert bandgapluminescentie in de nanodraden, en de resulterende emissie naar het verre veld vertoont azimutaal gepolariseerde ringen, waarbij het aantal ringen afhangt van de hoogte van de draad. We vinden een goede overeenkomst tussen de metingen en een model waarin de emissie van de bovenkant van de draad interfereert met de reflectie vanaf het substraat. De metingen en berekeningen geven een schatting van de grootte van de emissieregio, wat tot een nieuwe manier leidt om de diffusielengte van ladingsdragers te bepalen.

In Hoofdstuk 7 gebruiken we CL polarimetrie om horizontale galliumarseennanodraden met verschillende diameters te bestuderen. Bandgapluminescentie, die geëxciteerd wordt door de elektronenbundel, koppelt met golfgeleidermodes die afhankelijk zijn van de diameter van de nanodraad en die de directionaliteit en polarisatie van de emissie bepalen. De polarimetriemetingen tonen aan dat voor alle draden de TM01 golfgeleidermode het emissiegedrag domineert. Er is echter wel een duidelijk verschil in directionaliteit tussen dikke en dunne nanodraden als we ze dicht bij de uiteinden exciteren. Dit komt door een overgang in de golfgeleidermode van een gedrag dat licht lekt voor de dunne draad tot een gedrag dat licht geleid voor de dikke draad, wat overeenkomt met een simpel lijnstroommodel en numerieke simulaties.

De metingen in de voorgaande hoofdstukken geven alleen ruimtelijke informatie over lichtemissie in 2D. Hoofdstuk 8 introduceert spectroscopische CL-tomografie, een nieuwe methode om de 3D optische eigenschappen van structuren op de nanoschaal te karakteriseren. We meten 2D CL intensiteitsverdelingen van een metaal-diëlektrische nanostructuur voor verschillende oriëntaties en gebruiken daarna de methode van “gefilterde terugprojectie” om een 3D beeld van de CL emissie te reconstrueren. Door de 3D CL distributie te bestuderen voor meerdere golflengtes kunnen we materiaalluminescentie en elektromagnetische eigentoestanden herkennen en onderscheiden, omdat ze ruimtelijk en spectraal van elkaar verschillen.

Tot nu toe hebben we experimenten beschreven die in of dichtbij het zichtbare spectrale gebied zijn uitgevoerd (λ_0=400–1000 nm). In Hoofdstuk 9 voeren we CL spectroscopie uit in het nabij-infrarood spectrale gebied (λ_0=1000–1600 nm) om silicium fotonische kristal golfgeleiders te bestuderen. 2D CL intensiteitsverdelingen vertonen scherpe resonanties met gedetailleerde ruimtelijke verdelingen en een sterke lineaire polarisatie. De dominante resonantie correleert met berekeningen voor een oneven TE golfgeleidermode in de structuur. CL koppelt het meest efficiënt aan verticale (TM) modes, maar onze metingen tonen aan dat het ook mogelijk is om aan TE modes te koppelen, zodanig dat deze de gemeten emissie domineren.

Dit proefschrift toont aan dat kathodeluminescentiespectroscopie een krachtige nanoschaal karakterisatietechniek is waarmee een grote verscheidenheid aan optische eigenschappen van nanofotonische structuren kan worden bepaald. Het brede scala van experimenten en nieuwe theoretische ideeën die gepresenteerd worden in dit proefschrift verschaffen nieuwe fundamentele inzichten in de interacties tussen elektronen, materie en licht, alsmede in het gedrag van licht op de nanoschaal.

Résumé scientifique

La lumière est omniprésente dans la vie quotidienne (le soleil, lampes, pointeurs laser). Que cela ne soit en biologie, médecine, chimie ou en physique, la lumière fournit un outil essentiel pour examiner et caractériser différentes structures et différents processus. Elle nous permet de mieux comprendre le monde qui nous entoure, de réaliser des inventions technologiques ou d'améliorer des technologies existantes. Au cours des dernières décennies, la science n'a cessé de chercher à comprendre plus en détail la biologie et la physique, en atteignant les meilleurs niveaux de résolution possibles. Les innovations dans le domaine de la microscopie ont notamment joué un rôle important ; chaque raffinement de la résolution révélant des caractéristiques et informations invisibles voire inconnus auparavant concernant la matière. La nanophotonique, l'étude de la lumière à l'échelle du nanomètre, est un domaine de recherche en pleine expansion, donnant naissance à de nombreuses améliorations technologiques essentielles à notre société. On peut citer les panneaux solaires, les diodes électroluminescentes (DELs), les capteurs, et les circuits photoniques intégrés parmi ceux-ci. Pour contrôler la lumière à l'échelle du nanomètre, il est essentiel de fabriquer et caractériser des nanostructures, afin de dévoiler leurs interactions avec la lumière à cette même échelle. Il est donc indispensable d'avoir à notre disposition des techniques permettant de déterminer les propriétés optiques de ces structures avec une meilleure précision que celle de la longueur d'onde de la lumière.

Les électrons permettent d'atteindre ce but. Grâce à leur masse, les électrons ont une quantité de mouvement bien supérieure aux photons du spectre visible. Ils sont donc beaucoup plus énergétiques et ont une longueur d'onde associée plus courte. Les microscopes électroniques sont utilisés depuis des décennies afin de quantifier la taille et la morphologie de nanostructures. Mais ces électrons à hautes énergies sont aussi exploités parce qu'ils peuvent eux-mêmes générer un rayonnement électromagnétique. Par conséquent, les interactions électron-lumière-matière peuvent être étudiées à des échelles beaucoup plus petites que les longueurs d'onde lumineuses en utilisant des techniques de spectroscopies à base d'électrons. Nous allons nous intéresser tout particulièrement à l'une de ces méthodes, la cathodoluminescence (CL).

Cette thèse présente différentes techniques reposant sur la CL, obtenues en incorporant de nouvelles fonctionnalités à un dispositif expérimental déjà existant (imagerie hyperspectrale de cathodoluminescence résolue angulairement). Grâce à cette combinaison d'une excitation électronique et d'un dispositif de détection optique efficace, nous sommes capables de caractériser les propriétés optiques des matériaux avec une précision de l'ordre de 10 nm. Les propriétés spectrales, angulaires ainsi que la polarisation de la lumière émise peuvent être mesurées. Le Chapitre 2 décrit les différentes méthodes de détection utilisées tout au long de la thèse afin de déterminer toutes ces propriétés de la lumière.

Dans le Chapitre 3, nous développons un modèle théorique qui nous permet de déterminer l'évolution temporelle des interactions entre les électrons et la matière. En effet, un électron en mouvement induit un champ électromagnétique qui varie dans l'espace et le temps. Il est essentiel d'étudier ces variations afin de comprendre comment les électrons peuvent interagir avec la matière pour générer un rayonnement. Dans un premier temps, nous étudions les champs électromagnétiques induits par un électron en mouvement dans le vide. Ensuite nous examinons les processus de CL dits cohérents qui se produisent lorsqu'un électron de haute énergie traverse une interface entre le vide et un métal. Des plasmons de surface peuvent être excités et guidés à cette interface, formant des paquets d'ondes d'une durée de vie de quelques centaines de femtosecondes. Les composantes de hautes fréquences proches de la résonance plasmonique sont fortement amorties, par conséquent ce sont les composantes de basses fréquences qui dominent lorsque les paquets d'ondes s'éloignent du point d'origine de l'excitation. Ensuite nous étudions le rayonnement de transition, qui est émis dans le champ lointain, sous forme de paquets d'ondes d'une durée de quelques dizaines de femtosecondes. Ces paquets dépendent très fortement de l'angle d'émission et des propriétés du matériau pénétré par les électrons.

Après cette étude théorique, nous allons, tout au long des chapitres suivants, étudier expérimentalement comment les nouvelles méthodes de spectroscopie mises en œuvre permettent d'explorer les interactions entre la lumière et la matière à l'échelle du nanomètre. Le Chapitre 4 montre comment des mesures angulaires peuvent être utilisées pour séparer des processus de radiation cohérente et incohérente. Les métaux, comme l'aluminium, émettent principalement le rayonnement de transition. Celui-ci est cohérent et possède une distribution angulaire toroïdale, similaire à celle d'un dipôle vertical. Par contre, l'émission de semiconducteurs comme l'arséniure de gallium est dominée par une luminescence incohérente (principalement dû à la recombinaison de paires électron-trou proche de l'énergie du gap) avec une distribution orthotrope ou Lambertienne. Pour le silicium, les intensités du rayonnement de transition et de la luminescence incohérente ont une amplitude similaire, mais le rapport entre les deux dépend de la longueur d'onde. Nous utilisons les données expérimentales collectées pour extraire cette proportion entre les deux processus et séparer leurs contributions spectrales. Utiliser la polarisation de la lumière permettrait de surcroît de séparer ces mécanismes de radiation d'une façon plus générale, dans des structures et

géométries plus complexes.

Dans le Chapitre 5 nous introduisons l'imagerie de polarimétrie de CL résolue angulairement, une nouvelle méthode pour déterminer l'état complet de la polarisation du signal de CL. La combinaison de six mesures pour différentes orientations d'une lame quart d'onde et d'un polariseur permet d'établir les paramètres de Stokes, qui caractérisent complètement la polarisation de la lumière. On utilise le rayonnement de transition comme référence pour tester cette technique. Nous appliquons ensuite cette méthode sur des nanostructures métalliques en forme de "bullseye" et de spirales. Des modifications de la chiralité de la structure ou de la position d'excitation à l'échelle du nanomètre engendrent des changements importants dans l'ellipticité et l'helicité de la polarisation. La polarimétrie permet de distinguer la lumière polarisée et non-polarisée, pour séparer l'émission cohérente (polarisée) et incohérente (non-polarisée) de surfaces en or, en arséniure de gallium ou en silicium. Grâce à cette méthode on peut alors augmenter la sélection de la mesure par rapport à la méthode exposée dans le Chapitre 4.

Dans le Chapitre 6 nous décrivons comment la méthode de polarimétrie développée dans le Chapitre 5 peut être utilisée pour mesurer la polarisation et la distribution angulaire de la lumière émise par des nanofils de phosphure d'indium orthogonaux au substrat, de longueurs différentes. Le faisceau d'électrons excite des paires électron-trou à l'énergie du gap, qui en se recombinant émettent une lumière ayant une distribution angulaire annulaire avec une forte polarisation azimutale. Le nombre d'anneaux visibles dépend de la hauteur des nanofils. Ces résultats corroborent un modèle dans lequel l'émission du sommet du fil interfère avec la réflexion du substrat de l'échantillon. Les expériences, associées à des calculs numériques, donnent accès à la taille de la zone d'excitation associée à l'émission, ce qui permet d'évaluer la longueur de diffusion des porteurs de charge.

Le Chapitre 7 présente l'utilisation de la polarimétrie de CL pour étudier des nanofils d'arséniure de gallium avec des diamètres différents, qui reposent horizontalement sur le substrat. La luminescence à l'énergie du gap qui est excitée par le faisceau d'électrons peut se coupler à des modes de guide d'onde. Ces modes dépendent du diamètre du nanofil et déterminent la directionnalité et la polarisation de l'émission. Les mesures de polarimétrie prouvent que le comportement de l'émission est dominé par le mode de guide d'onde TM01 pour tous les nanofils. Cependant nous observons que, lorsqu'ils sont excités à proximité de leurs terminaisons, les nanofils minces et épais ont une directionnalité de l'émission opposée. Ceci est dû à une transition d'un comportement de mode à fuite pour le nanofil mince vers un comportement de mode guidé pour le nanofil épais. Nous montrons que cela peut être expliqué avec un simple modèle de courant linéique associé à des simulations numériques.

Les mesures présentées dans les chapitres précédents fournissent seulement des informations spatiales en deux dimensions (2D) sur l'émission de la lumière. Dans le Chapitre 8 nous introduisons la tomographie spectroscopique de CL, une nouvelle méthode permettant de caractériser en 3D les propriétés optiques de structures à l'échelle du nanomètre. Pour cela, on mesure la carte (2D) de

la distribution d'intensité du signal de CL émis par un résonateur métallo-diélectrique, et ce, pour différentes orientations du résonateur. Nous utilisons ensuite la méthode de "rétroprojection filtrée" pour reconstruire par tomographie l'image de l'émission en 3D. En étudiant ces distributions de la CL en 3D en fonction des longueurs d'onde de la lumière, nous pouvons reconnaître et distinguer la luminescence du matériau et les modes propres électromagnétiques du résonateur, qui sont en corrélation avec la partie radiative de la densité locale d'état. Cette distinction est possible parce que les deux sources d'émissions sont séparées spectralement et spatialement.

Tous les chapitres précédents ont traité d'expériences réalisées dans, ou proche du spectre visible (λ_0=400–1000 nm). Dans le Chapitre 9 en revanche, nous étendons les mesures de CL à la lumière proche infrarouge (λ_0=1000–1600 nm), afin d'étudier les guides d'onde à cristaux photoniques en silicium. La distribution spatiale de l'intensité de l'émission montre des pics qui sont bien définis spectralement et spatialement, avec une forte polarisation linéaire. La résonance principale est associée, grâce à des calculs, au mode guidé TE antisymétrique. L'émission de CL est habituellement dominée par des modes perpendiculaires à la surface (TM). Nos mesures prouvent que c'est aussi possible de mesurer les modes TE de ces guides d'onde à cristaux photoniques.

Nous montrons tout au long de cette thèse que les méthodes de spectroscopies basées sur la CL sont des techniques de caractérisation puissantes, capables de déterminer une grande partie des propriétés optiques de nanostructures adaptées à la photonique. Les nombreuses expériences et nouvelles idées théoriques présentées dans cette thèse ont permis d'atteindre un nouveau niveau de compréhension sur les interactions électron-lumière-matière et le comportement de la lumière à l'échelle du nanomètre.

Layperson's summary

Light is everywhere around us and allows for many essential everyday applications. Lasers in our pointers and DVD players, lamps that free us to work or have fun anytime and anywhere, solar cells that produce electricity, optical fibers that transport digital information – these are but a few examples of the many ways light plays an important role in our daily lives. Scientific research has made great advances in the last decades to better understand how light works and how to manipulate it to our advantage.

Light is a complex phenomenon; it is both a particle (a photon) and a wave (an electromagnetic field). We can describe a beam of light as separate photons traveling through space, but also as a wave of electric and magnetic fields that oscillate through space. This light wave has many similarities with other waves such as water waves in the sea, moving up and down in a regular fashion, repeating over a distance we call the wavelength. For light, the wavelength corresponds to color: the longest visible wavelengths (650–750 nanometers) are perceived as red, the shortest (400–450 nanometers) are blue, and light with intermediate wavelengths fills the rainbow with green, yellow, and orange. One nanometer is a billionth (10^{-9}) of a meter. For comparison, a human hair is roughly 100,000 nanometers thick while most cells and bacteria are 1,000 to 10,000 nanometers in size.

Strange and interesting things begin to happen when light, or any wave, interacts with objects that are similar in size to the wave itself. For light, this means we need to make structures that are several hundred nanometers in size or smaller (the nanoscale) and since they are smaller than the wavelength, we speak of subwavelength dimensions. The study of light at the nanoscale is called nanophotonics and has developed tremendously in the last decades due to developments in the ability to make and measure such small objects.

As we improve our ability to characterize and understand the interaction between light and nanostructures, we enhance our ability to engineer such structures for specific applications. Since light is usually "larger" than these objects, we cannot use light directly to study these structures with high resolution. Scientists have developed optical (light-based) tricks and techniques to get around this problem, but in this thesis we take a different approach.

Instead of using light to probe the structures of interest we use electrons, the negatively charged elementary particles that fly around the nucleus of each atom and which are the fundamental elements of electricity. An electrical current is simply a moving "train" of electrons. It so happens that electrons have a much smaller wavelength than photons. As a result, we can "see" much smaller things by using electrons in an electron microscope than with light in a conventional optical microscope. Additionally, electrons can also generate light inside materials and structures, through several different processes.

The light produced by electrons – called "*cathodoluminescence*" – is the cornerstone of the work presented in this thesis. We have used electrons to generate this cathodoluminescence (referred to below as "CL" for short) and built a setup with different functionalities to measure various properties of the light that is emitted by nanostructures. The main components of the setup are an electron microscope that excites the nanostructures of interest and a rounded (parabolic) metal mirror that we place inside the microscope to collect the emitted light and send it to various detectors. When we hit a structure with an electron, the matter becomes "excited" and can "relax" by emitting light, which we collect and measure. Because of the small wavelength of the electron we can excite objects with a much higher resolution than is possible with traditional light-based methods: typically 10 to 30 nanometers instead of several hundreds of nanometers. This is the primary advantage of cathodoluminescence: it allows us to measure the light radiated by objects at the nanoscale, inspiring the title of this thesis: "Probing light emission at the nanoscale with cathodoluminescence".

When a fast electron hits a material, different light-emitting processes can take place. Just like a photon, an electron is accompanied by an electric field that changes in time and space, with some differences due to the mass and charge of the electron. The electron can, for example, generate a type of light which "sticks" to the surface in the case of a metal and is known as a surface plasmon polariton. At the same time, the electron has to adapt to its new environment after it transits into a material. This change leads to light that is called transition radiation. We theoretically study the time-dependence of these processes and they turn out to be very fast, disappearing in less than a trillionth ($< 10^{-12}$) of a second (roughly equivalent to a minute relative to the age of the universe).

We then perform different CL experiments that study the interactions between matter and light at the nanoscale. We can for example measure the direction in which light is emitted, the angular distribution pattern or "shape" of the emitted light. It turns out that different materials can exhibit various types of CL emission, which have a different shape, like a doughnut or ball for instance. Measuring the shape of the light allows you to tell which processes have occurred and in what ratio.

A new addition to the setup is a method called polarimetry, which measures the polarization of CL emission. Polarization describes the orientation of the electric field of light as it oscillates through space. It can, for example, move up and down vertically, or it can move horizontally, or it can even move in a circular fashion.

We measure this orientation of light emitted by different nanostructures. In metal nanoantennas we find that even small changes in the exact location where the electron beam strikes can lead to large differences in the polarization. We also measure on vertically-grown nanoscale wires (nanowires) made of a material called indium phosphide, which is used in many applications that combine light and electronics. We find that they emit light in the shape of multiple rings and that the number of rings depends on the nanowire height. Horizontal nanowires of another much-used material (gallium arsenide) also show interesting behavior. We find that thin and thick wires behave differently; they emit light in opposite directions when we hit them near one of the end facets.

Another new technique, CL tomography, allows us to visualize the optical properties of nanostructures in three dimensions (3D). The method consists of combining many 2D measurements of the same structure for different orientations to reconstruct a 3D image of the light emission, giving more information about the object of interest.

Finally, we study photonic crystal waveguides, channels that can confine light very efficiently. They are made of silicon, the same material used in many electronic chips and solar cells. We measure a specific state of light which travels through the waveguide at infrared wavelengths. The human eye cannot see these wavelengths but they are important due to their use in telecommunications traffic.

This thesis shows that we can expand the previously demonstrated capabilities of cathodoluminescence microscopy to observe new properties of the light emitted by nanostructures. The experiments and theoretical ideas provide new insights into the interactions between electrons, matter and light at the nanoscale. Cathodoluminescence has provided us with an improved understanding of light that will allow more targeted engineering of applications. Structures such as the ones studied here can be used to improve solar cells and LED lamps, develop new sensitive sensors for all sorts of measurements (including medical tests), or to develop optical chips that use light to achieve faster computers. Thanks to nanophotonics and cathodoluminescence, there are still many exciting discoveries to be made and uses of light to be explored.

Samenvatting voor allen

Licht bevindt zich overal om ons heen en maakt veel essentiële, alledaagse toepassingen mogelijk. Lampen die altijd en overal voor verlichting zorgen, lasers in laserpennen en in DVD-spelers, zonnecellen die elektriciteit produceren en optische fibers die digitale informatie over de hele wereld geleiden. Dit zijn maar een paar van de vele toepassingen waarin licht een belangrijke rol speelt en ons leven verrijkt. In de laatste decennia hebben wetenschappelijk onderzoekers grote vorderingen gemaakt in het doorgronden van het subtiele gedrag van licht en van de manier waarop het met materie reageert. Hoe beter we licht begrijpen, des te beter we het kunnen manipuleren om er optimaal gebruik van te maken.

Licht is een complex fenomeen: het is zowel een deeltje (een foton) als een golf (een elektromagnetisch veld). We kunnen een lichtbundel beschrijven als een groep fotonen die door de ruimte vliegt, maar ook als een golf van elektrische en magnetische velden die snel door de ruimte oscilleren (trillen). De lichtgolf deelt veel karakteristieke eigenschappen met andere soorten golven zoals watergolven: hij deint op en neer terwijl hij zich voortbeweegt, zich steeds opnieuw herhalend over een afstand die we de golflengte noemen. Voor zichtbaar licht kunnen we de golflengte koppelen aan een bepaalde kleur. De kortste zichtbare golflengtes (400–450 nanometer) komen overeen met blauw licht, terwijl de langste (650–750 nanometer) overeenkomen met rood licht, en de golflengtes ertussenin de andere kleuren van de regenboog (groen, geel en oranje) vertegenwoordigen. Een nanometer is een miljardste van een meter. Ter vergelijking: een haar is ruwweg 100.000 nanometers dik, terwijl de meeste cellen en bacteriën tussen 1000 en 10.000 nanometers groot zijn.

Bijzonder en interessant gedrag kan plaatsvinden wanneer een golf interactie heeft met objecten die even groot of kleiner zijn dan de golf zelf. In het geval van licht betekent dit dat structuren maximaal een paar honderd nanometers groot moeten zijn. We noemen deze lengteschaal de nanoschaal en het bestuderen van licht op deze schaal heet nanofotonica. Dit onderzoeksveld heeft een grote ontwikkeling doorgemaakt in de afgelopen decennia, door verbeteringen in de technieken die ons in staat stellen om zulke kleine nanostructuren te maken en te meten. Hoe beter het samenspel tussen licht en materie op de nanoschaal gekarakteriseerd en

begrepen kan worden, des te beter kunnen we gerichte toepassingen ontwikkelen om de eigenschappen van licht optimaal te benutten. Aangezien de golflengte van licht meestal groter is dan de nanostructuren, kunnen we licht zelf niet gebruiken om deze objecten met hoge resolutie te bestuderen. Wetenschappers hebben verschillende optische technieken en trucjes ontwikkeld om dit probleem aan te pakken, maar in dit proefschrift gebruiken we een andere aanpak.

In plaats van licht gebruiken we elektronen om nanostructuren te onderzoeken. Elektronen zijn de negatief geladen elementaire deeltjes die rond de kern van een atoom vliegen. Het zijn ook de bestanddelen van elektriciteit, die simpelweg uit een "treintje" van elektronen bestaat. Elektronen hebben een veel kleinere golflengte dan fotonen. Hierdoor kunnen we met behulp van elektronen in een elektronenmicroscoop veel kleinere objecten zien dan met licht in een gewone optische microscoop. Een extra voordeel is dat elektronen op verschillende manieren licht kunnen opwekken in allerlei materialen en structuren.

Met behulp van energetische elektronen kan licht geproduceerd worden; dit heet "*kathodeluminescentie*" en dit proces ligt aan de basis van het onderzoek in dit proefschrift. We hebben een opstelling verbeterd om met allerlei technieken van kathodeluminescentie (afgekort CL) de verschillende eigenschappen van de lichtemissie van nanostructuren te meten. Wanneer we een structuur aanslaan met elektronen, raakt de materie "geëxciteerd" en kan deze vervolgens "vervallen" door licht uit te sturen; dit vangen wij op en meten we. De belangrijkste componenten van de CL-opstelling zijn een elektronenmicroscoop die de nanostructuren aanslaat en een metalen spiegel met een afgeronde (parabolische) vorm die we in de microscoop plaatsen om het licht op te vangen en naar verschillende detectoren te sturen. Door de veel kleinere golflengte van elektronen kunnen we objecten exciteren met een veel hogere resolutie dan met gewone optische technieken: ongeveer 10 tot 30 nanometers in plaats van een paar honderd nanometers. Dit is het grootste voordeel van CL: het stelt ons in staat om op de nanoschaal licht te meten dat uitgestraald is door nanostructuren. Dat is ook de inspiratie voor de titel van dit proefschrift: "Meten van lichtemissie op de nanoschaal met kathodeluminescentie".

Wanneer een hoogenergetisch elektron neerslaat op een materiaaloppervlak kunnen verschillende processen plaatsvinden die licht uitstralen. Evenals een foton heeft een elektron een elektrisch veld dat oscilleert in de tijd en de ruimte, met een paar verschillen die worden veroorzaakt door de massa en de lading van het elektron. Het inkomende elektron kan een speciale straling genereren die aan het materiaaloppervlak blijft plakken in het geval van een metaal. Dit noemen we een oppervlakteplasmonpolariton. Tegelijkertijd moet het elektron zich aanpassen aan zijn nieuwe omgeving wanneer het doordringt in een materiaal. Deze verandering leidt tot een lichtemissie die we transitiestraling noemen. We bestuderen deze processen theoretisch en tonen aan dat beiden heel snel verlopen (binnen een duizendmiljardste van een seconde).

Nu kunnen we verschillende CL experimenten uitvoeren om de interacties tussen licht en materie te onderzoeken op nanoschaal. We kunnen bijvoorbeeld me-

ten in welke richting licht uitstraalt: het hoekafhankelijke emissiepatroon of simpelweg de “vorm” van het uitstralende licht. Het blijkt dat verschillende materialen verschillende soorten lichtemissie kunnen vertonen, die elk een unieke vorm hebben, zoals een donut of een bal. Door de vorm van het licht te meten kunnen we bepalen welke processen plaatsvinden en in welke verhouding dat geschiedt.

We hebben ook een nieuwe methode ontwikkeld om de volledige polarisatietoestand van CL emissie te bepalen: CL polarimetrie. Polarisatie beschrijft de bewegingsrichting van het elektrisch veld van licht terwijl het door de ruimte golft. Het kan bijvoorbeeld verticaal op en neer bewegen, maar ook horizontaal, onder elke willekeurige hoek, of zelfs in cirkels ronddraaien. We meten deze richting van licht voor verschillende nanostructuren. In metalen nanoantennes vinden we dat heel kleine veranderingen in de locatie waar we ze aanslaan tot grote verschillen in de polarisatie kunnen leiden. We bestuderen ook verticale nanoschaal draden (nanodraden) van het materiaal indiumfosfide, dat veel wordt gebruikt in toepassingen die licht en elektronica combineren. We meten lichtemissie in de vorm van meerdere ringen, waarbij het aantal ringen afhangt van de hoogte van de draad. Ook horizontaal liggende nanodraden van het materiaal galliumarseen vertonen interessant gedrag. Dikke en dunne draden zijn namelijk erg verschillend: ze sturen licht uit in tegengestelde richting als we ze bij de uiteinden aanslaan.

Een andere, nieuwe techniek, CL tomografie, maakt het mogelijk om de optische eigenschappen van nanostructuren in drie dimensies (3D) te meten. De methode combineert een groot aantal tweedimensionale (2D) metingen voor verschillende oriëntaties van een structuur om een 3D beeld van de lichtemissie te reconstrueren. Dit levert extra informatie op over de eigenschappen van het gemeten object.

Tot slot bestuderen we fotonische kristal golfgeleiders: kanalen die heel efficiënt licht kunnen opsluiten. Ze zijn gemaakt van silicium, hetzelfde materiaal dat gebruikt wordt in veel elektronische chips en zonnecellen. We meten een specifieke toestand van licht dat door de golfgeleider voortbeweegt voor infrarood golflengtes. Het menselijk oog kan deze golflengtes niet waarnemen; ze worden gebruikt voor telecommunicatie.

Dit proefschrift toont aan dat we de krachtige kathodeluminescentietechniek hebben kunnen uitbreiden om veel verschillende eigenschappen van de lichtemissie van nanostructuren te bepalen. De experimenten en theoretische ideeën verschaffen nieuwe fundamentele inzichten in de interacties tussen elektronen, materie en licht op nanoschaal. Geholpen door CL kunnen we doelgerichter en efficiënter toepassingen ontwikkelen. Nanostructuren kunnen op veel manieren worden gebruikt, bijvoorbeeld: het verbeteren van zonnecellen en LED-verlichting, het ontwerpen van gevoeligere sensoren voor allerlei metingen (onder andere voor medische tests), en het ontwikkelen van optische chips die licht gebruiken om computers sneller te maken. Dankzij de nanofotonica en kathodeluminescentie valt er nog veel te leren en ontdekken om licht beter te kunnen benutten.

Résumé pour tous

La lumière fait partie de notre quotidien, on s'en sert pour de nombreuses applications. Outre l'utilisation basique qui est l'éclairage, nous pouvons citer par exemple l'application des lasers comme sonde dans les lecteurs DVD, la lumière comme source d'énergie par le biais des panneaux solaires qui la transforment en électricité, ou encore un moyen de communiquer l'information grâce aux fibres optiques. C'est depuis plusieurs décennies, au moyen d'une étude approfondie de son fonctionnement et de la meilleure façon de la manipuler, que nous pouvons aujourd'hui utiliser la lumière de manière si efficace et variée.

En elle-même, la lumière est un concept intéressant et complexe ; c'est à la fois une particule (un photon) et une onde (un champ électromagnétique). C'est-à-dire que l'on peut décrire un rayon lumineux soit comme un groupe de photons en mouvement, soit comme une propagation d'une onde de champs électriques et magnétiques. Cette onde lumineuse a beaucoup de similitudes avec d'autres types d'ondes comme les vagues à la surface de l'eau ; elles se propagent toutes par oscillations. La distance sur laquelle une onde se répète s'appelle la longueur d'onde. Pour la lumière, à chaque longueur d'onde correspond une couleur. Par exemple 650 nanomètres est perçu comme rouge, alors que 450 nanomètres serait bleu (un nanomètre représente un milliardième de mètre), et les longueurs d'onde entre les deux correspondent aux autres couleurs de l'arc-en-ciel (vert, jaune et orange). Par comparaison, un cheveu a une épaisseur de 100 000 nanomètres, alors que la plupart des cellules et bactéries ont une taille entre 1000 et 10 000 nanomètres.

Des phénomènes intéressants et étranges peuvent se produire lorsqu'une onde interagit avec des objets de la taille de sa longueur d'onde, voire même plus petits. Dans le cas de la lumière, pour observer ces effets, il nous faut construire des structures aux dimensions ne dépassant pas quelques centaines de nanomètres. L'étude de la lumière à cette échelle est le domaine de la "nano-optique" ou "nanophotonique". Depuis plusieurs dizaines d'années, ce domaine de recherche est en pleine expansion, grâce au développement de nouvelles technologies permettant de fabriquer et de mesurer des objets toujours plus petits.

L'amélioration de notre compréhension des interactions entre la lumière et les nanostructures permet de mieux optimiser ces structures pour des applications

spécifiques. Puisque la longueur d'onde de la lumière est plus grande que ces objets, il n'est pas possible d'utiliser la lumière elle-même pour les étudier. Malgré cette limitation, les scientifiques ont trouvé des solutions pour améliorer la meilleure résolution atteignable avec des mesures optiques. Néanmoins, on peut également utiliser d'autres outils que la lumière pour s'affranchir de cette limite ; c'est dans ce cadre que s'inscrit cette thèse. En effet, au lieu d'utiliser la lumière pour caractériser les nanostructures qui nous intéressent, nous utilisons des électrons qui sont des particules élémentaires qui gravitent autour du noyau de l'atome. Les électrons sont aussi à l'origine de l'électricité, qui est simplement un "train" d'électrons en mouvement. Il se trouve que les électrons ont une longueur d'onde bien inférieure à celle de la lumière. Par conséquent, il est possible de "voir" des objets beaucoup plus petits avec un microscope spécial utilisant les électrons qu'avec un microscope traditionnel qui utilise la lumière. Les électrons peuvent exciter certaines structures qui, tout comme le filament d'une lampe, émettent de la lumière pour se désexciter.

Cette lumière émise par la matière grâce aux électrons est appelée "*la cathodoluminescence*", et elle constitue la base de la recherche présentée dans cette thèse. Nous avons apporté des améliorations à un dispositif de cathodoluminescence (CL) préexistant en y ajoutant de multiples fonctionnalités afin de mesurer les différentes propriétés de la lumière émise par les nanostructures. Les principales composantes de ce système sont un microscope électronique pour exciter les nanostructures étudiées et un miroir métallique parabolique (courbé) placé à l'intérieur du microscope pour capter la lumière émise et ensuite l'envoyer sur les différents détecteurs. Grâce à la courte longueur d'onde des électrons, il est possible d'exciter des objets avec une meilleure résolution que celle atteinte avec les techniques optiques traditionnelles : environ 10 à 30 nanomètres contre quelques centaines de nanomètres. C'est le plus grand avantage de la CL ; elle nous permet de caractériser la lumière émise à l'échelle des nanostructures, d'où le titre de la thèse : "Mesurer l'émission de la lumière à l'échelle du nanomètre avec la cathodoluminescence".

Lorsqu'un électron à haute énergie traverse la surface d'un matériau, différents types de rayonnements lumineux peuvent être produits. Tout comme le photon, l'électron est associé à un champ électrique qui varie dans le temps et l'espace, et qui est déterminé en grande partie par la masse et la charge électrique de l'électron. L'électron peut générer un type de rayonnement particulier en traversant l'interface entre l'air et un métal, où la lumière reste "collée" à la surface du métal. La particule associée à ce rayonnement est appelée un plasmon de surface. Une fois dans un matériau, l'électron doit s'adapter au nouvel environnement en modifiant son champ électromagnétique, ce qui engendre un rayonnement lumineux que l'on appelle le rayonnement de transition. Nous étudions à travers une recherche théorique le comportement temporel de ces rayonnements et trouvons qu'ils ont une évolution très rapide (un millième de milliardième de seconde).

Dans la suite nous examinons des expériences qui tirent parti des différentes fonctionnalités du dispositif de CL afin d'étudier les interactions entre la matière et

la lumière à l'échelle du nanomètre. Nous pouvons par exemple mesurer les directions dans lesquelles la lumière est émise, ce qui nous donne la distribution angulaire (ou la "forme") de la lumière. Différents matériaux peuvent manifester différents types de signaux de CL, chacun pouvant avoir une direction d'émission différente, en forme toroïdale (comme un donut) ou en forme sphérique par exemple. Mesurer ces formes nous permet de déterminer quels genres de processus sont responsables de l'émission, et dans quelles proportions.

Nous introduisons une nouvelle technique, "polarimétrie de CL", qui permet de mesurer la polarisation complète du signal de CL émit par l'échantillon. La polarisation décrit l'orientation de la lumière, plus précisément l'orientation du champ électrique de la lumière pendant qu'elle se propage à travers l'espace. Cette orientation peut, par exemple, être verticale, horizontale, ou bien même tourner d'une façon circulaire. Nous avons mesuré cette orientation de la lumière émise par différentes nanostructures. Dans le cas de nanoantennes métalliques, la polarisation dépend très fortement de la position d'excitation. Nous utilisons aussi la polarimétrie de CL afin d'étudier des fils à l'échelle du nanomètre (des nanofils) orientés verticalement et constitués de phosphure d'indium, un matériau qui est très utile pour les applications mêlant lumière et électronique. Nous trouvons que la lumière est émise en forme d'anneaux et que le nombre d'anneaux augmente avec la hauteur du fil. Des nanofils différents orientés horizontalement et composés d'arséniure de gallium ont aussi un comportement intéressant. Des fils minces ou épais agissent différemment : ils émettent la lumière dans des directions opposées lorsqu'ils sont excités à proximité de leurs extrémités.

Une autre nouvelle technique que nous avons développée, la "tomographie de CL", permet de visualiser les propriétés optiques de nanostructures en trois dimensions (3D). Cette méthode consiste à collecter des données via la visualisation en 2D d'une structure pour un grand nombre de points de vue différents. La tomographie permet alors de combiner toutes ces données afin de reconstruire une image en 3D de l'émission de la lumière à l'échelle du nanomètre, ce qui nous donne encore d'avantage d'informations sur les propriétés de l'objet.

Enfin, nous étudions des guides d'onde à cristaux photoniques, des objets qui agissent comme des tubes pour guider la lumière et la piéger très efficacement. Ils sont constitués de silicium, le même matériau que celui utilisé dans beaucoup de circuits électroniques et panneaux solaires. Nous mesurons un état spécifique de la lumière qui se déplace à travers le guide d'onde, avec une longueur d'onde dans le domaine infrarouge que l'œil humain ne peut pas percevoir, mais qui est certes très utilisée dans les télécommunications.

Cette thèse prouve que la cathodoluminescence est une technique puissante qui permet de déterminer de nombreuses propriétés de la lumière émise par des nanostructures. Les expériences et idées théoriques qui y sont présentées ont permis d'atteindre un meilleur niveau de compréhension sur les interactions entre les électrons, la matière et la lumière à l'échelle du nanomètre. Cette meilleure compréhension nous permettra de développer des applications d'une manière plus efficace. Les nanostructures étudiées ici peuvent par exemple être utilisées pour

améliorer les panneaux solaires et les LEDs, développer de nouveaux capteurs sensibles pour toutes sortes de mesures (y compris des tests médicaux), ou bien de développer des circuits photoniques qui utilisent la lumière à la place de l'électricité pour rendre nos ordinateurs et calculateurs encore plus rapides.

La lumière est étudiée par l'humanité depuis des millénaires, mais grâce à la nanophotonique et à la cathodoluminescence, elle dévoile de nouvelles potentialités et ouvre ainsi une ère où beaucoup de découvertes restent à faire.

List of publications

This thesis is based on the following publications:

- *Femtosecond plasmon and photon wave packets excited by a high-energy electron on a metal or dielectric surface*, B. J. M. Brenny, A. Polman, and F. J. García de Abajo, submitted. **(Chapter 3)**
- *Quantifying coherent and incoherent cathodoluminescence in semiconductors and metals*, B. J. M. Brenny, T. Coenen, and A. Polman, J. Appl. Phys. **115**, 244307 (2014). **(Chapter 4)**
- *Angle-resolved cathodoluminescence imaging polarimetry*, C. I. Osorio*, T. Coenen*, B. J. M. Brenny*, A. Polman, and A. F. Koenderink, ACS Photonics **3**, 147-154 (2016). (*equal author contribution) **(Chapter 5)**
- *Azimuthally polarized cathodoluminescence from InP nanowires*, B. J. M. Brenny, D. van Dam, C. I. Osorio, J. Gómez Rivas, and A. Polman, Appl. Phys. Lett. **107**, 201110 (2015). **(Chapter 6)**
- *Directional emission from leaky and guided modes in GaAs nanowires measured by cathodoluminescence*, B. J. M. Brenny, D. R. Abujetas, D. van Dam, J. A. Sánchez-Gil, J. Gómez Rivas, and A. Polman, ACS Photonics **3**, 677–684 (2016). **(Chapter 7)**
- *Nanoscale optical tomography with cathodoluminescence spectroscopy*, A. C. Atre, B. J. M. Brenny, T. Coenen, A. Garcia-Etxarri, A. Polman, and J. A. Dionne, Nat. Nanotechnol. **10**, 429 (2015). **(Chapter 8)**
- *Near-infrared cathodoluminescence spectroscopic polarimetry on silicon photonic crystal waveguides*, B. J. M. Brenny, D. M. Beggs, L. Kuipers, and A. Polman, in preparation. **(Chapter 9)**

Other publications by the author:

- *Gallium plasmonics : deep subwavelength spectroscopic imaging of single and interacting gallium nanoparticles*, M. W. Knight, T. Coenen, Y. Yang, B. J. M. Brenny, M. Losurdo, A. S. Brown, H. O. Everitt, and A. Polman, ACS Nano **9**, 2049 – 2060 (2015).

- *Robustness of plasmon phased array antennas to disorder*, F. Bernal Arango, R. Thijssen, B. J. M. Brenny, T. Coenen, and A. F. Koenderink, Sci. Rep. **5**, 10911: 1-9 (2015).
- *Cathodoluminescence microscopy: Optical imaging and spectroscopy with deep-subwavelength resolution*, T. Coenen, B. J. M. Brenny, E. J. R. Vesseur, and A. Polman, MRS Bulletin **40**, 359-365 (2015).
- *Nanoscale spatial coherent control over the modal excitation of a coupled plasmonic resonator system*, T. Coenen, D. T. Schoen, B. J. M. Brenny, S. R. K. Rodriguez, S. Mann, A. Polman, and M. L. Brongersma, Nano Lett. **15**, 7666–7670 (2015).
- *Controlling magnetic and electric dipole modes in hollow silicon nanocylinders*, M. A. van de Haar, J. van de Groep, B. J. M. Brenny, and A. Polman, Opt. Express **24**, 2047-2064 (2016).
- *Surface plasmon polariton modes in coaxial metal-dielectric-metal waveguides*, M. A. van de Haar, R. Maas, B. J. M. Brenny, and A. Polman, New J. Phys. **18**, 043016 (2016).
- *Combined electron energy-loss and cathodoluminescence spectroscopy on individual and composite plasmonic nanostructures*, T. Coenen, D. T. Schoen, B. J. M. Brenny, A. Polman, and M. L. Brongersma, Phys. Rev. B **93**, in press (2016).
- *White light emitting silicon nanocrystals – engineering emission by e-beam irradiation*, B. Bruhn, B. J. M. Brenny, S. Dekker, Ilker Dogan, P. Schall, and K. Dohnalova, in preparation.

Acknowledgements

Obtaining a PhD is an interesting and exciting task, but also a challenging and arduous one. A lot of time and effort has been spent over the past years, resulting in this thesis. I certainly cannot take all of the credit for the work presented here, since many people have been essential in bringing this project to completion. I would like to thank all of you for the help and support, both professionally and personally.

Allereerst wil ik mijn promotor Albert Polman bedanken. Ik heb veel geleerd van jouw optimisme, de capaciteit om de juiste kritische vragen te stellen die de essentie van een experiment blootstellen en jouw vaardigheden in het communiceren van de wetenschap aan anderen. Bedankt voor de kans om samen te werken met veel verschillende groepen in alle hoeken van de wereld.

Toon, mijn CL-broeder en mentor van het eerste uur, ik wil je erg bedanken voor alles wat je me geleerd hebt de afgelopen jaren. We hebben veel mooie momenten beleefd, in het SEM-lab en daarbuiten. Jouw scherpe blik, goede ideëen en rustige instelling waren van grote hulp. Bedankt dat je mijn paranimf wilt zijn om dit CL hoofdstuk af te sluiten. I would also like to thank all my other CL-companions. Ernst Jan, bedankt voor het delen van je ervaring in het begin van mijn traject. Philip, it was a pleasure to introduce you to the world of CL and to help supervise your project. Sophie, it has been great to have you join the CL-team, merci pour ton aide et pour avoir lu mes résumés en Français.

The Photonic Materials group has been full of fun people over the years, all of you have been invaluable in contributing to productive discussions and for the gezelligheid that always made for a great atmosphere. Toon Coenen, Claire van Lare, Jorik van de Groep, Ruben Maas, Pierpaolo Spinelli, Rutger Thijssen and Marie Anne van de Haar, we were quite the PhD generation! James Parsons, Bonna Newman, Lourens van Dijk, Hugo Doeleman, Bas Zegers, Julia Attevelt, Verena Neder, Philip Heringlake, Philipp Tockhorn, Teresa Ortmann and Bas Onokiewicz thanks for the good times. Mark, my last two years at AMOLF would not have been the same without you. Thank you for your help with experiments, photography, proofreading, consuming various beverages and fine chocolate! Claire, bedankt voor alle lol die we hebben gehad. Jorik, Ruben en Rutger, bedankt voor alle hulp met uitleg, in het lab en met code voor berekeningen. Marie Anne, bedankt voor de vele jaren

vol babbels over wetenschap, paarden en allerlei onzin. I wish each of our Master students all the best for their next step!

Next to the research group, the office is a very important part of life at AMOLF. Without all of my office members from 2.51 it would have been a very boring time. Ramy El-Dardiry, Grzegorz Grzela, Hugo Doeleman, Beniamino Sciacca, Said Rodriguez, Mohammad Ramezani, Janika van Moergestel, Leffert Lansink, Teresa Ortmann and Philip Heringlake, thanks for the discussions about science and daily life. Beniamino, it is still funny to me that we share an office, the mino and maxi Benis.

The Center for Nanophotonics is a fantastic and productive environment, where the colloquium and communal activities create a cohesive group that stimulates gezelligheid, feedback and collaborations. I have learned a lot from all these discussions and critical questions. Due to the dynamic nature of AMOLF I have seen too many come and go to name everyone, but my thanks go to all group members and leaders.

During my PhD I have had the chance to collaborate with many different people. I would like to show my gratitude to Javier García de Abajo for his immense knowledge and patience, as well as for hosting me at ICFO. Our theory project is an important cornerstone of the thesis. Clara Osorio and Femius Koenderink, I had a great time working together with you and Toon in developing CL polarimetry, which contributed to several chapters in the thesis, thank you. Jaime Gómez Rivas, Dick van Dam, Diego Abujetas and José Sánchez-Gil, thank you for the collaboration on the semiconductor nanowire projects. Ashwin Atre, Aitzol García-Etxarri and Jennifer Dionne, we had a very productive month three years ago that led to CL tomography, many thanks! Daryl Beggs, Ruben van der Wel and Kobus Kuipers, our work on silicon photonic crystal waveguides was a big project spread out over several years, I am very happy we managed to bring everything together on time, thank you. Next to the projects that feature in this thesis, there were others that also played an important part of my research. Felipe Bernal, it was a pleasure to teach you to become a CL monkey. Toon, Ernst Jan, Rutger, Marie Anne, Jorik, Ruben, Mark Knight, David Schoen, Mark Brongersma, Sander Mann, Said Rodríguez, Katerina Dohnalova, Benjamin Bruhn, Sidoeri Dekker, Nader Engheta, Sassan Sheikholeslami, Andrea Baldi, Jonathan Scholl, Harry Atwater, Siying Peng, Freddy Rabouw, Flavio Mariani, Ren-Min Ma, Erik Garnett, Sebastian Oener, Beniamino Sciacca, Forrest Bradbury and Linda van der Waart, thank you for all the interesting experiments! Kévin Cognée et Alexei Halpin, merci à vous pour la lecture de mes résumés. Thanks to everyone who took the time to read and give feedback on the contents of the thesis.

In developing the cathodoluminescence setup, we closely collaborated with DELMIC. I would like to thank Sander den Hoedt, Andries Effting, Éric Piel, Martijn Haring and Lennard Voortman. You are bringing the power of CL to a bigger audience, best of luck!

A quintessential part of any acknowledgments section in an AMOLF PhD thesis is to honor the fantastic contributions from the support departments of AMOLF. They play a very important role on many different levels and I am very grateful for

that. Dion, bedankt voor alle technische ondersteuning van onze groep. Ik heb het meest samengewerkt met de technici van de cleanroom. Hans Zeijlemaker, Andries Lof, Dimitry Lamers en Johan Derks, ontzettend bedankt voor al jullie bijdragen. Iliya Cerjak, hartelijk dank voor het ontwerpen van de opstelling. Henk-Jan Boluijt, ontzettend bedankt voor het ontwerpen van figuren in het proefschrift en op de kaft. Sjoerd Wouda en Sander van de Haar, ik dank jullie voor het ontwikkelen van software voor de pinhole scanner. Ronald Buijs en de anderen van E&I, bedankt voor de elektronische ondersteuning. Wim Brouwer en het team van de werkplaats, bedankt voor het maken van veel onderdelen van de opstelling. Ik wil ook graag de ICT afdeling bedanken, met name Wiebe de Boer, voor het helpen met verschillende computer problemen.

Niet alleen de technische ondersteuning is uitmuntend, ook de administratieve afdelingen zijn onmisbaar. Petra Rodriguez, Karelia Wrona en Floortje van den Berg, heel erg bedankt voor alle secretariële ondersteuning. Floortje, dank voor al ons ander goed teamwerk. Erny Lammers en Sabine Penning, dank voor het helpen organiseren van de EBSN workshop, dat was een groot succes! Sabine, ook bedankt voor je haviksogen die geen detail ongemerkt voorbij laten gaan en het delen van Nederlandse kennis en goede series. Valeska de Graaf en Roos Luthart, dank voor de HR ondersteuning. Ik wil jullie allemaal, ook Esther van Leeuwen, ontzettend bedanken voor de gezellige babbels over alles en nog wat. Iedereen van de Facilities, Finance, Inkoop en Safety afdelingen, dank voor het zorgen dat AMOLF soepel kan functioneren.

Help with the content was essential, but help on a personal and social level was also very important to finish this journey. At AMOLF I have greatly enjoyed the (almost) weekly jogs with the AMOLF Runners, thank you Mark, Sabine, Sophie, Verena, Hinke Schokker, Rick Leijssen, Wouter den Hollander and Alessandro Antoncecchi. For a post-work drink and other borrels in the weekends I could always count on Sander, Sebastian, Mark, Sophie, Andrea, Alexei, Eric Johlin, Giorgos Georgiou, and Juha Muhonen, thanks guys! Marie Anne, Hinke en Freddy, we hebben al jaren veel leuke momenten meegemaakt, bedankt voor alle koediekoedies. Hinke, het was me een waar genoegen om alle tijden van de dag en nacht te kunnen praten en eten te delen.

Ik wil ook graag mijn natuurkunde groepsgenoten van Groepje W bedanken: Dick Abma, Sander Mann, Nivard Kagie, Thijs Krijger, Miekee Lam, Maarten van der Steen en Remco van den Dungen. Zonder jullie was de studie niet zo leuk geweest en had ik dit niet bereikt. Al mijn vrienden van AEGEE zijn ook onmisbaar geweest de afgelopen jaren. Mijn mentorkindjes Marleen Dijkhoff, Karin Rozendal, Linda Groot Wassink, Arne Prüst, Joline Heusinkveld en Annemieke Visscher, wat zijn jullie toch een koningsgroepje! Schuimbroeders Thijs de Wolff, Casper Wolf en Tim de Jong, bedankt voor onze bijeenkomsten. Yvonne Antonovic, Dennis Huizing, Gerben Swaan, Isabella van Batenburg, Aleida Weegenaar, Sanne la Grouw, Donald Krol, Jelle Bauer, Casper Halffman en nog teveel anderen om te noemen, dank voor jullie vriendschap. Nicole van Doorn, bedankt voor de mooie tijd samen. Rodolfo Navarrete, thank you for all the salsa lessons. Erik Spande, Adil Chaudry and Kasia

Stokowska, thank you for all the great tastings at Chocolatl. Marcia Schaasberg, dank je voor de bootcamp lessen die me fit hebben gemaakt.

J'ai tellement de bons souvenirs de mon temps à Madagascar, je suis très heureux de toujours pouvoir compter sur mes chers amis Paul Grandjean et Alessandro Del Fiore. Alessandro mon pote, merci pour la competitivité au Lycée et pour les bons moments depuis. Paul, my brother from another mother, merci pour ton amitié toutes ces années et j'espère que l'on continuera d'avoir des fous rires ensembles encore longtemps. Ça me fait plaisir que tu sois à mes côtés pendant la défense en tant que paranymphe. Dominique et Blanche, merci pour les liens forts entre nos familles. Tante Geeta en Tante Sieta, bedankt aan jullie en de familie voor alle steun door de jaren heen, jullie zijn gewoon familie voor mij! Galja, thank you for our curious dance, I look forward to seeing where it leads us.

Finally (yes really, I promise!) I want to thank my family. Growing up abroad, moving from one country to another, family was always the one constant, you all mean the world to me. Tante Sterre, Uncle Satish, Samir, and Sharika (and kids!); Tante Engelien, Uncle Paul (McGowan), Aidan, Liam, and Lily; Auntie Lynn, Uncle Tom, Meghan, and Rachel; Auntie Cheryl and Uncle Chuck; Auntie Tina, Uncle Paul (Billimoria), Josh and Kennan; the rest of the Zegers and ten Horn families, thank you all! Last of all, my love and thanks to my parents Mei and Patrick and my sister Sophie for their unwavering support and encouragement.

About the author

Benjamin Joseph Maarten Brenny was born in Amsterdam, The Netherlands, on August 27, 1987. After receiving his high school degree from the Lycée Français International de Bangkok in 2005, he studied physics at Utrecht University. He graduated in 2011, with a thesis on gain characteristics of ZnO crystals at low temperatures and ZnO nanowire growth and manipulation, supervised by prof. dr. Jaap Dijkhuis and prof. dr. Daniël Vanmaekelbergh. He started as a PhD student in the Photonic Materials group of prof. dr. Albert Polman at the FOM Institute AMOLF in 2011, working on cathodoluminescence spectroscopy. The results of his research are shown in this thesis.

In his free time, Benjamin enjoys reading, laughing with friends, playing sports, savoring good food (fine chocolate in particular), traveling, and going to cultural performances (of as many countries and cultures as possible).

The work described in this thesis was performed at the FOM-Institute AMOLF, Science Park 104, 1098 XG Amsterdam, The Netherlands.